

**Experiments and Modeling of the Onset of Gas Entrainment into Small
Branches from a Co-Currently Flowing Stratified Gas-Liquid Regime**

Robert Constantinos Bowden

A Thesis
in
The Department
of
Mechanical and Industrial Engineering

Presented in Partial Fulfillment of the Requirements

For the Degree of Doctor of Philosophy

Concordia University

Montréal, Québec, Canada

November 2010

© Robert Constantinos Bowden, 2010

CONCORDIA UNIVERSITY
SCHOOL OF GRADUATE STUDIES

This is to certify that the thesis prepared

By: **Robert Constantinos Bowden**

Entitled: **Experiments and Modeling of the Onset of Gas Entrainment into Small Branches from a Co-Currently Flowing Stratified Gas-Liquid Regime**

and submitted in partial fulfillment of the requirements for the degree of

DOCTOR OF PHILOSOPHY (Mechanical Engineering)

complies with the regulations of the University and meets the accepted standards with respect to originality and quality.

Signed by the final examining committee:

_____ Chair
Dr. O.A. Pekau

_____ External Examiner
Dr. A. Soulaïmani

_____ External to Program
Dr. A. Youssef

_____ Examiner
Dr. G. Vatistas

_____ Examiner
Dr. W. Ghaly

_____ Thesis Supervisor
Dr. I. Hassan

Approved by _____
Dr. W-F. Xie, Graduate Program Director

November 26, 2010

Dr. Robin A.L. Drew, Dean
Faculty of Engineering & Computer Science

Abstract

Experiments and Modeling of the Onset of Gas Entrainment into Small Branches from a Co-Currently Flowing Stratified Gas-Liquid Regime

Robert Constantinos Bowden, Ph.D.

Concordia University, 2011

The discharge of two-phase flow from a co-currently flowing gas-liquid region through single or multiple branches is an important process in many industrial applications including oil-gas production and nuclear power plants. Accurate physical descriptions of the flow phenomena involved, along with the quality and mass flow rate of the discharging streams, is necessary to adequately predict the different phenomena associated with the process.

A test facility was developed, consisting of a horizontal pipe with an inlet diameter of 50.8 mm and three 6.35 mm diameter branches located at a distance of 1.8 m from the pipe inlet. The branches were machined perpendicularly into the test section wall, and oriented at 0, 45, and 90 degrees down from horizontal. Air and water, operating at 206 kPa, were used to provide a two-phase flow regime. Both fluids flowed co-currently within the inlet, and mainly in the stratified regime, but transitions to wavy and slug regimes were observed.

Extensive experimental data are reported for the three branch orientations. The relation between the air-water interface height, the inlet superficial gas and liquid velocities, and the branch two-phase quality and mass flow rate are presented for each branch orientation. The critical inlet conditions leading to beginning of two-phase flow in the branch, the onsets of gas and liquid entrainment, respectively, were reported in both single and dual branch cases. Effects of inlet measurement location, the secondary branch Froude number, and branch fluid phase on the critical conditions were investigated. A novel map relating the dual discharge branch Froude numbers, the inlet superficial liquid velocity, and the related dual branch phenomena was developed. The map presented the three observed modes of gas entrainment during dual discharge.

A two-fluid separated theoretical model was developed in order to predict the critical height at the onset of gas entrainment in a bottom branch. Potential flow theory lead to the branch being simulated by a point-sink, while the flowing liquid upstream of the branch was simulated by a uniform constant crossflow velocity. Two analytical criteria were used to predict the dip position (height and offset distance) relative to the branch. Inaccuracies with experiments lead to the inclusion of empirical terms to satisfy the local crossflow velocities within the inlet. A digital imaging technique was also developed in order to record local interface profiles at the onset of gas entrainment, and was used to satisfy the relationship between the dip height and offset distance. The semi-empirical approach provided a significant improvement over the purely analytical model, and demonstrated that the critical height to be predicted within a reasonable error.

Acknowledgments

My sincerest appreciation and gratitude goes to my thesis advisor and mentor Professor Ibrahim Hassan, for his continual encouragement, support, and for guiding me to realize a life long dream.

I have shared many memories with members of the Micro Scale Heat Transfer Group over the years, and I will look back in fond admiration of these times as I move on from Concordia. Special thanks to my friends and colleagues Wael, Roland, Mohamed Gaber, Chad, Tarek , Dr.Sung In-Kim, Patricia, Tariq, Minmin, Minh, Fan, Ayman, Mohamed Rahman, Tina, Othman, Carole, Ling, Ming and Amen.

To my parents, siblings, extended family and friends, thank you for your kind words encouragement, advice, and for always being there for me.

Financial support and awards provided by the Natural Sciences and Engineering Research Council of Canada's Alexander Graham Bell Post-graduate scholarship program, les Fonds de Recherche sur la Nature et Technologies du Québec, and la Bourse d'études Hydro-Québec - Faculté de Génie et d'Informatique, are gratefully acknowledged.

To my wife Tamlyn, thank you for being by my side, and never doubting...

Contents

List of Figures	xi
List of Tables	xix
Nomenclature	xxi
1 Introduction	1
1.1 Motivation	2
1.2 Organization	4
2 Literature Review	5
2.1 Stratified Two-phase Flow in Horizontal Pipes and Channels	5
2.2 Two-phase Gas-Liquid Flow in Equal Sided and Reduced T-Junctions	15
2.3 Small Branches Exposed to a Stratified Gas-Liquid Region	21
2.3.1 Experiments and Modeling in Stratified Two-Phase Reservoirs	21
2.3.2 Experiments in Stratified Horizontal Channels	30
2.4 Summary	32
3 Experimental Investigations	34

3.1	Problem Description	34
3.2	Reduction of Variables: Dimensional Analysis	37
3.2.1	Scaling a Single Simulated Feeder Bank	37
3.2.2	Beginning of Two-phase Flow in a Single Branch	38
3.2.3	Two-phase Flow in a Single Branch	43
3.3	Test Section	45
3.3.1	Design	47
3.4	Test Facility and Flow Loop	49
3.5	Methodologies	52
4	Experiments with Co-current Stratified Gas-Liquid Flow in a Single Reduced T-Junction	56
4.1	Chapter Overview	56
4.2	Experimental Methodology	57
4.2.1	Procedures	59
4.2.2	Test Matrix	61
4.2.3	Estimates of Uncertainty	63
4.3	Results and Discussion	64
4.3.1	Co-current Air-water Flow without an Active Branch	64
4.3.2	Bottom Branch	70
4.3.3	Inclined Branch	82
4.3.4	Side Branch	90
4.4	Summary	94

5	Experiments with Dual Discharging Branches at Low to Moderate Froude Numbers	96
5.1	Chapter Overview	96
5.2	Experimental Methodology	97
5.2.1	Procedures	98
5.2.2	Test Matrix	98
5.3	Results and Discussion	99
5.3.1	Flow Visualization	99
5.3.2	Critical Conditions at the Onset of Gas Entrainment	123
5.3.3	Comparison with Existing Studies	152
5.4	Summary	168
6	Theoretical Analysis of the Onset of Gas Entrainment	169
6.1	Chapter Overview	169
6.2	Single Branch on a Semi-infinite Horizontal Plane	170
6.2.1	Problem Description	170
6.2.2	Results and Discussion	179
6.3	The OGE Criterion in Crossflow	197
6.3.1	Problem Description	197
6.3.2	Results and Discussion	200
6.4	The OGE Criterion for Two Branches	208
6.4.1	Results and Discussion	214
6.5	Summary	225

7	Semi-Empirical Modeling of the Onset of Gas Entrainment	226
7.1	Chapter Overview	226
7.2	Feasibility Study: Semi-Empirical Methods	227
7.2.1	Problem Description	227
7.2.2	Analysis and Results	228
7.3	Reduced T-Junction With Co-current Stratified Gas-Liquid Flow . . .	233
7.3.1	Theoretical Analysis	233
7.3.2	Experimental Methodology	244
7.3.3	Results and Discussion	252
7.4	Summary	274
8	Conclusions and Future Directions	275
8.1	Conclusions and Contributions	275
8.2	Future Directions	279
	References	283
A	Experimental Data	295
A.1	Co-Current Air-Water Flow	296
A.2	Single Discharging Branch	298
A.3	The OGE in Dual Discharging Branches	305

List of Figures

3.1	Problem description	36
3.2	Single feeder bank problem description.	39
3.3	Estimated dimensionless numbers of liquid flow in a feeder branch.	42
3.4	Qualitative description of two-phase flow in a single discharging branch.	43
3.5	Test section.	48
3.6	Manufactured test section.	50
3.7	Schematic of the experimental facility.	53
3.8	Experimental facility assembly.	54
3.9	Schematic of the two-phase flow separator.	55
4.1	Calibration of branch hydraulic lines.	58
4.2	Inlet conditions during co-current air-water flow in the horizontal pipe.	66
4.3	Wave propagation during gas entrainment in the bottom branch.	67
4.4	Slug development during gas entrainment in the bottom branch.	68
4.5	Observed inlet regime as compared with Mandhane et al. (1974)'s map.	69
4.6	Flow visualization of the onset of gas entrainment in the bottom branch.	71

4.7	Critical conditions at the onset of gas entrainment in the bottom branch at $\lambda/D = -5$	73
4.8	Critical liquid flow distribution between the bottom branch and run. .	74
4.9	Critical conditions at the onset of gas entrainment in the bottom branch.	75
4.10	Two-phase distribution at the bottom branch in relation to the inter- face height at $\lambda/D = -5$	78
4.11	Sketches of observed air spout development during two-phase flow in the bottom branch with decreasing interface height from (a) to (c). .	79
4.12	Comparison of two-phase quality in the bottom branch with Smoglie and Reimann (1986) and Hassan et al. (1997).	81
4.13	Critical conditions at the onset of gas entrainment in the inclined branch at $\lambda/D = -5$	84
4.14	Critical liquid flow distribution between the inclined branch and run.	85
4.15	Sketches of observed air/water spout development during two-phase flow in the inclined branch with decreasing interface height from (a) to (c).	87
4.16	Two-phase distribution at the inclined branch in relation to the inter- face height at $\lambda/D = -5$	88
4.17	Comparison of two-phase quality in the inclined branch with Hassan et al. (1997).	89
4.18	Two-phase distribution at the side branch in relation to the interface height at $\lambda/D = -5$	91

4.19	Comparison of the present critical height $\lambda/D = -5$ at the OLE in the side branch with available models and experimental data.	93
4.20	Comparison of the two-phase quality in the side branch with Smoglie and Reimann (1986) and Hassan et al. (1997).	94
5.1	Sketches of the onset of gas entrainment at the inclined branch with constant values of V_{SL1} and V_{SG1}	102
5.2	Sample image of the onset of gas entrainment at the inclined branch with a low value of Fr_C	103
5.3	Sketches of the onset of gas entrainment at the bottom branch with constant values of V_{SL1} and V_{SG1}	104
5.4	Sample images of the local air-water interface development with increasing $Fr_B = Fr_C$ and constant V_{SL1} and V_{SG1}	107
5.5	Sketches of the onset of gas entrainment at the inclined branch with a moderate value of Fr_C and constant values of V_{SL1} and V_{SG1} (Mode 1).	109
5.6	Sketches of the onset of gas entrainment at the bottom branch with a low value of Fr_B and constant values of V_{SL1} and V_{SG1} (Mode 2).	111
5.7	Sketches of the onset of gas entrainment at both the inclined and bottom branches with constant values of V_{SL1} and V_{SG1} (Mode 3).	112
5.8	Sample image of the onset of gas entrainment at both the inclined and bottom branches (Mode 3).	113
5.9	Sketches of the onset of gas entrainment at the inclined branch with a low value of Fr_A and variable inlet conditions.	116

5.10	Sketches of the onset of gas entrainment at the inclined branch with a moderate value of Fr_A and variable inlet conditions.	118
5.11	Sketches of the onset of gas entrainment at the bottom branch with a moderate value of Fr_A and variable inlet conditions.	121
5.12	Sketches of the inlet flow during wavy to slug regime transition.	122
5.13	The onset of gas entrainment at the inclined branch demonstrating the effect of measurement location, λ	126
5.14	The onset of gas entrainment at the bottom branch demonstrating the effect of measurement location, λ	127
5.15	Effect of branch orientation and measurement methodology on the critical conditions at the onset of gas entrainment.	131
5.16	Effect of measurement location, λ , on the OGE in the inclined branch with $Fr_C = 1$ (Mode 1).	133
5.17	Effect of measurement location, λ , on the OGE in the inclined branch with $Fr_C = Fr_B$ (Mode 1).	135
5.18	Effect of measurement location, λ , on the OGE in the inclined branch with $Fr_C = 10$ (Mode 1).	136
5.19	Effect of Fr_C on the OGE in the inclined branch at $\lambda/D = -5$ (Mode 1).	138
5.20	Effect of measurement location, λ , on the OGE in the bottom branch with $Fr_B = 1$ (Mode 2).	140
5.21	Effect of measurement location, λ , on the OGE in the bottom branch with $Fr_B = 2$ (Mode 2).	141

5.22	Effect of Fr_B on the OGE in the bottom branch at $\lambda/D = -5$ (Mode 2).	142
5.23	Critical conditions at the simultaneous OGE in the inclined and bottom branches (Mode 3).	144
5.24	Map of dual onset conditions in the inclined and bottom branches (Modes 1, 2 and 3).	145
5.25	Effect of measurement location, λ on the OGE in the inclined branch with $Fr_A = 1$	149
5.26	Effect of measurement location, λ on the OGE in the inclined branch with $Fr_A = 10$	150
5.27	Effect of Fr_A on the OGE in the inclined branch at $\lambda/D = -5$	151
5.28	Effect of measurement location on the OGE in the bottom branch with $Fr_A = 1$	153
5.29	Effect of measurement location on the OGE in the bottom branch with $Fr_A = 10$	154
5.30	Effect of Fr_A on the OGE in the bottom branch at $\lambda/D = -5$	155
5.31	Effect of branch orientation on the OGE in comparison to Bartley et al. (2008).	158
5.32	Effect of Fr_C on the OGE in the inclined branch at $\lambda/D = -5$ in comparison to published models and data (Mode 1).	163
5.33	The OGE in the inclined branch with $Fr_B = Fr_C$ at $\lambda/D = -5$ in comparison to published models and data (Mode 1).	164

5.34	Effect of Fr_B on the OGE in the bottom branch at $\lambda/D = -5$ in comparison to published models and data (Mode 2).	166
5.35	Comparison of simultaneous gas entrainment in the inclined and bottom branches with published models and data (Mode 3).	167
6.1	Geometry and coordinate system.	175
6.2	Effect of Fr_U on the critical height H_{OGE}/d	181
6.3	Variation of the dip height, h/d	183
6.4	Variation of H_{OGE}/h	184
6.5	Variation of the dip offset distance, b/d	185
6.6	Variation of the offset distance, b , with the dip height, h	186
6.7	Example of critical values causing flow reversal ($d/W = 0.05$).	190
6.8	Comparison of the special case model ($Fr_U = 0$) with theoretical work of (1)Andaleeb et al. (2006), (2) and experimental work of (2)Bowden and Hassan (2007), (3)Ahmad and Hassan (2006), (4)Hassan et al. (1997), (5)Abdalla and Berenyi (1969), and (6)Lubin and Springer (1967).	192
6.9	Effect of crossflow with comparison to experimentally derived correlations by (1)Smoglie and Reimann (1986), (2)Schrock et al. (1986), (3)Kowalski and Krishnan (1987), (4)Maciaszek and Micaelli (1990), and (5)Yonomoto and Tasaka (1991).	194
6.10	Comparison of the point-sink model with experimentally derived correlation compensating for crossflow effects (Maciaszek and Micaelli, 1990).	195

6.11 Comparison with Yonomoto and Tasaka (1991)'s correlation compensating for crossflow effects.	196
6.12 Evaluating Craya (1949)'s criterion at two different dip angles under crossflow $U = 0.25 \text{ m/s}$	202
6.13 Predicted critical points using Craya (1949)'s criterion.	203
6.14 Location of critical points obtained using Craya (1949)'s criterion within the flow field.	204
6.15 Vertical acceleration field including the gradients in the x-direction.	207
6.16 Geometry and flow conditions.	209
6.17 Effect of Fr_I on the vertical acceleration for a single branch.	216
6.18 Vertical acceleration resulting from two branches in the same horizontal plane, with $Fr_I = 1$, $Fr_{II} = 20$ and $L_s/d = 2$	218
6.19 Onset of gas entrainment in branch I with $Fr_{II} = 56.7$ compared with Parrott et al. (1991)'s experiments.	221
6.20 Acceleration field of two branches in the same vertical plane with $L_s/d = 5$	222
6.21 Acceleration field of two branches in the same vertical plane with $L_s/d = 1$	223
7.1 Steady dip in a stagnant two-phase reservoir at a bottom oriented branch.	229
7.2 Theoretical problem description.	234
7.3 Image calibration.	247
7.4 Comparison between imaging and transducer measurements under smooth-stratified conditions.	249

7.5	Digitization of the critical dip profile.	251
7.6	Critical liquid flow distribution between run and branch.	254
7.7	Example of the development of the steady OGE dip profile.	255
7.8	Air-water interface at the onset of gas entrainment including the steady dip.	257
7.9	Relationship between the dip angle and dip momentum flux ratio. . .	258
7.10	Problem description for OGE in a bottom branch from a cylindrical channel.	259
7.11	Calculated horizontal velocities at the dip.	261
7.12	Prediction of the critical dip with $Fr_d = 15$	263
7.13	Comparison between predictions at the critical dip and experiments. .	264
7.14	Comparing the dip kinetic energy obtained from Eq. (7.9) and (7.32). .	268
7.15	Inlet flow conditions at $\lambda/D = -5$	270
7.16	Critical height prediction.	271
7.17	Effect of channel geometry on the critical height prediction.	273

List of Tables

3.1	Saturation properties of D_2O at 300° and 10 MPa	40
4.1	Test matrix for experiments without an active branch.	62
4.2	Test matrix for experiments with an active branch.	62
5.1	Test matrix of dual branch experiments.	100
7.1	Saleh et al. (2009)'s data for OGE in a bottom branch	232
7.2	Test matrix.	248
7.3	Measured critical dip location for OGE in a bottom branch	260
7.4	Calculated Dip Velocities	260
7.5	Calculation of the critical height using Eq.(7.9)	272
A.1	Case SS-1 data	296
A.2	Case SS-2 data	297
A.3	Case SB-1 data	298
A.4	Case IB-1 data	299
A.5	Case IB-2 data	299
A.6	Case IB-3 data	300
A.7	Case BB-1 data	300

A.8 Case BB-2 data	301
A.9 Case BB-3 data	301
A.10 Data for the OGE in the inclined branch	302
A.11 Data for the OGE in the bottom branch	302
A.12 Dip profile data from Fig. 7.8(a) ($Fr_d = 18, 13$)	303
A.13 Dip profile data from Fig. 7.8(a) ($Fr_d = 11.4, 7.9$)	304
A.14 Dual case 1 data: OGE in the inclined branch ($Fr_C = 1$)	305
A.15 Dual case 1 data: OGE in the inclined branch ($Fr_C = 10$)	306
A.16 Dual case 1 data: OGE in the inclined branch ($Fr_C = Fr_B$)	306
A.17 Dual case 2 data: OGE in the bottom branch ($Fr_B = 1$)	307
A.18 Dual case 2 data: OGE in the bottom branch ($Fr_B = 2$)	307
A.19 Dual case 3 data: OGE in the inclined and bottom branches	308
A.20 Dual case 4 data: OGE in the inclined branch ($Fr_A = 1$)	308
A.21 Dual case 4 data: OGE in the inclined branch ($Fr_A = 10$)	308
A.22 Dual case 5 data: OGE in the bottom branch ($Fr_A = 1$)	309
A.23 Dual case 5 data: OGE in the bottom branch ($Fr_A = 10$)	309

Nomenclature

A	Point on the gas-liquid interface within the inlet
A_G	Gas side cross-sectional flow area, m^2
a_I	Vertical acceleration due to Branch I, m/s^2
a_{II}	Vertical acceleration due to Branch II, m/s^2
A_L	Liquid side cross-sectional flow area, m^2
a_y	Vertical acceleration, m/s^2
B	Point on the gas-liquid interface at the bottom of the OGE dip
b	OGE dip offset distance, m
B_I	Lowest point of the OGE dip caused by Branch I
b_I	Offset distance of the OGE dip caused by Branch I
B_{II}	Lowest point of the OGE dip caused by Branch II
b_{II}	Offset distance (x -direction) of the OGE dip induced by Branch II
	II
C_1, C_2	Correlation coefficients in Eq. (2.5)

C_G	Gas side friction coefficient in Eq.(2.2)
C_L	Liquid side friction coefficient in Eq.(2.2)
D_2O	Chemical equation for deuterium
D	Inlet and run diameter, m
d	Branch diameter, m
$(\frac{dP}{dx})_{SG}$	Gas side superficial pressure gradient, N/m^3
$(\frac{dP}{dx})_{SL}$	Liquid side superficial pressure gradient, N/m^3
Fr_A	Froude number in branch A
Fr_B	Froude number in branch B
Fr_C	Froude number in branch C
Fr_d	Branch Froude number, $Fr_d = \frac{4\dot{m}_{L3}}{\sqrt{gd^5\rho_L(\rho_L-\rho_G)}}$
Fr_I	Froude number in Branch I
Fr_{II}	Froude number in Branch II
Fr_U	Crossflow Froude number, $Fr_U = \frac{U}{\sqrt{gd}}(\frac{\rho_L}{\Delta\rho})^{\frac{1}{2}}$
Fr_{UA}	Inlet crossflow Froude number, $Fr_{UA} = \frac{U_{LA}}{\sqrt{gH_{OGE}}}$
Fr_{UB}	Dip crossflow Froude number, $Fr_{UB} = \frac{U_{LB}}{\sqrt{gh}}$
g	Gravitational acceleration, m/s^2
H	Liquid height (general), m
h	OGE dip height, m
H_f	Critical height referenced to the gas-liquid interface free surface, m

h_I	Vertical height (y -direction) of the OGE dip induced by Branch I
h_{II}	Vertical height (y -direction) of the OGE dip induced by Branch II
H_{L1}	Inlet liquid height, m
H_{L2}	Run liquid height, m
H_m	Critical height referenced to the top of the meniscus, m
$\mathbf{i}, \mathbf{j}, \mathbf{k}$	Unit vectors in x , y and z -directions
L	Inlet and run pipe length, m
l	Vertical separating distance between two branches, m
L_S	Branch center-to-center separating distance, m
\dot{m}	Mass flow rate, kg/s
\tilde{X}	Lockhart-Martinelli parameter, $\tilde{X}^2 = \frac{(\frac{dP}{dx})_{SL}}{(\frac{dP}{dx})_{SG}}$
\dot{m}_{G1}	Inlet gas mass flow rate, kg/s
\dot{m}_{G2}	Run gas mass flow rate, kg/s
\dot{m}_{G3}	Branch gas mass flow rate, kg/s
\dot{m}_i	Initial liquid mass flow rate in Eq. (2.3), kg/s
\dot{m}_{L1}	Inlet liquid mass flow rate, kg/s
\dot{m}_{L2}	Run liquid mass flow rate, kg/s
\dot{m}_{L3}	Branch liquid mass flow rate, kg/s
\dot{m}_{L3-I}	Liquid mass flow rate in Branch I, kg/s
\dot{m}_{L3-II}	Liquid mass flow rate in Branch II, kg/s

\dot{m}_{TP1}	Inlet two-phase mass flow rate, $\dot{m}_{TP1} = \dot{m}_{L1} + \dot{m}_{G1}$, kg/s
\dot{m}_{TP2}	Run two-phase mass flow rate, $\dot{m}_{TP2} = \dot{m}_{L2} + \dot{m}_{G2}$, kg/s
\dot{m}_{TP3}	Two-phase branch mass flow rate, $\dot{m}_{TP3} = \dot{m}_{G3} + \dot{m}_{L3}$, kg/s
n_1, n_2	Exponents in Eq. (2.2)
p	General point in the liquid side flow field with (x, y, z) coordinates
P_{GA}	Gas side pressure on the gas-liquid interface at point A, N/m^2
P_{GB}	Gas side pressure on the gas-liquid interface at point B, N/m^2
P_{LA}	Liquid side pressure on the gas-liquid interface at point A, N/m^2
P_{LB}	Liquid side pressure on the gas-liquid interface at point B, N/m^2
P	Pressure, N/m^2 or Pa
r	Point-sink radius, m
Re_d	Branch Reynolds number, $Re_d = \frac{4\dot{m}_{L3}}{\mu_L \pi d}$
R	Branch hydraulic resistance, $(kg - m)^{-1/2}$, $R = \frac{\sqrt{\Delta P}}{\dot{m}_{L3, OGE}}$
S_G	Gas side wetted perimeter, m
S_i	Interfacial chord length, m
S_L	Liquid side wetted perimeter, m
t	Time, s
T1, T2	Turrets in Fig. 3.1
U	Crossflow velocity, m/s
u	Velocity component in x -direction, m/s
u_{LB}	Liquid velocity component in x -direction at point B, m/s

\mathbf{V}	Velocity vector, $\mathbf{V} = u\mathbf{i} + v\mathbf{j} + w\mathbf{k}$, m/s
v	Velocity component in y -direction, m/s
v_I	Vertical velocity due to Branch I, m/s
v_{II}	Vertical velocity due to Branch II, m/s
V_{L1}	Average inlet liquid crossflow velocity, m/s
V_{L2}	Average run liquid crossflow velocity, m/s
V_{L3}	Branch average liquid velocity in a cylindrical branch of diameter d , $V_{L3} = 4\dot{m}_{L3}/(\rho_L\pi d^2)$, m/s
V_{LA}	Liquid velocity of the gas-liquid interface at point A, m/s
V_{LB}	Liquid velocity of the gas-liquid interface at point B, m/s
v_{LB}	Liquid velocity component in y -direction at point B, m/s
V_{Ld}	Point-sink radial velocity, m/s
V_{SG1}	Inlet gas superficial velocity, m/s
V_{SL1}	Inlet liquid superficial velocity, m/s
V_{SL2}	Run superficial liquid velocity in a cylindrical pipe of diameter D , $V_{SL2} = 4\dot{m}_{L2}/(\pi\rho_L D^2)$, m/s
W	Wall width in z -direction, m
w	Velocity component in z -direction, m/s
We_d	Branch Weber number, $We_d = \frac{16\dot{m}_{L3}^2}{\sigma\rho_L\pi^2 d^3}$
w_{LB}	Liquid velocity component in z -direction at point B, m/s
X_1	Inlet two-phase flow quality, $X_1 = \frac{\dot{m}_{G1}}{\dot{m}_{G1} + \dot{m}_{L1}}$
X_3	Branch two-phase quality, $X_3 = \frac{\dot{m}_{G3}}{\dot{m}_{G3} + \dot{m}_{L3}}$

X	Flow quality
x	Longitudinal coordinate, m
y	Vertical coordinate, m
z	Lateral coordinate, m

Abbreviations

AECL	Atomic Energy of Canada Limited
CANDU	Canada Deuterium and Uranium
CATHENA	Canadian Algorithm for Thermal Hydraulic Network Analysis
DOE	Department of Energy
FB	Feeder bank
GIF	Generation IV International Forum
HEM	Homogeneous Equilibrium Model
ILG	Interfacial Liquid Gradient
INL	Idaho National Laboratory
LOCA	Loss-of-Coolant Accident
NRC	Nuclear Regulatory Commission
OGE	Onset of Gas Entrainment
OLE	Onset of Liquid Entrainment
PIV	Particle Image Velocimetry
SCWR	Super Critical Water Reactor

Greek Letters

α	Angle of channel from horizontal, <i>radian</i>
β	Branch angle shown in Fig. 3.1
$\Delta\rho$	Difference in density between liquid and gas phases, $\Delta\rho = \rho_L - \rho_G$, kg/m^3
λ	Horizontal distance between branch and location where H is recorded, m
μ	Dynamic viscosity, $N \cdot s/m^2$
∇	Differential operator, Eq. (6.5)
ν_G	Gas kinematic viscosity, m^2/s
ν_L	Liquid kinematic viscosity, m^2/s
ϕ	Total potential function, m^2/s
ϕ_I	Potential function of a point-sink, m^2/s
ϕ_{II}	Potential function of a uniform crossflow velocity or second point-sink, m^2/s
ρ	density, kg/m^3
ρ_{G1}	Inlet gas density, kg/m^3
σ	surface tension, N/m
τ_i	Interfacial shear stress, N/m^2
τ_{WG}	Gas side wall shear stress, N/m^2

τ_{WL} Liquid side wall shear stress, N/m^2

Subscripts

1	Inlet
2	Run
3	Branch
A	Horizontal branches located at $\beta = 0^\circ$, and 180°
B	Inclined branches located at $\beta = 45^\circ$, and 135°
C	Downward branch located at $\beta = 90^\circ$
G	Gas phase
L	Liquid phase
mod	Model scale
prot	Prototype scale
TP	Two-phase fluid

Chapter 1

Introduction

Two-phase flow in branching conduits is a widely studied topic with a variety of motivating applications which include oil-gas production and nuclear power generation. During the refinement of petroleum products T-junctions have been used as fluid separators in order to improve plant efficiency and performance (Azzopardi, 1999). These simple compact devices can be incorporated within pipelines and offer low cost alternatives to large reservoir type separators. In normally single phase systems however, such as the header-feeder coolant distribution system of a Canada Deuterium and Uranium (CANDU) nuclear power plant, prior knowledge of two-phase operating conditions are important in the prediction of postulated accident scenarios. A more detailed description of the CANDU application is provided in the next section in order to outline some of the motivations driving this study. It is emphasized however that this study is not limited to CANDU type applications. It was designed to serve a wider audience with interests in dividing gas-liquid flow in reduced T-junctions, or two-phase flow in multi-branch type headers.

1.1 Motivation

The CANDU nuclear power plant uses natural uranium fuel coupled with deuterium, also referred to as heavy water, to produce electrical power (Banerjee and Nieman, 1982). The heavy water transports thermal energy produced in the fuel channels to a steam turbine generator. The coolant delivery system is arranged in a “figure-of-eight”, with heavy water traveling to and from the fuel channels through a network of pipes (*feeders*) connected to four large reservoirs (*headers*). The headers both supply (*inlet header*) and receive (*outlet header*) coolant to and from the fuel channels, respectively. A rupture in the network or a failure of a mechanical device, such as a valve or pump, can cause a sudden reduction in the coolant inventory, which is referred to as a loss-of-coolant accident (LOCA). Some of the most infamous and well documented nuclear power plant disasters caused by the coolant distribution system occurred at Three-Mile Island in 1979, and Chernobyl in 1986. The health and environmental risks associated with these accidents has spurred global initiatives by governing agencies to improve the safety of nuclear power stations.

One of the by-products of these initiatives has been the development of sophisticated commercial codes, for example the Canadian Algorithm for Thermal Hydraulic Network Analysis (CATHENA) developed by the Atomic Energy of Canada Limited (AECL) (Hanna, 1998) or the RELAP5-3D code developed at the Idaho National Laboratory (INL) through sponsorship by the U.S. Department of Energy (DOE) and Nuclear Regulatory Commission (NRC) (Riemke et al., 2006). These codes use experimentally or analytically derived thermohydraulic models in their simulations.

For example, the stratification/entrainment model incorporated in the RELAP5-3D code is used to predict the two-phase phenomena in a stratified gas-liquid pipe at a side or bottom oriented discharging branch (Ardron and Bryce, 1990) and is based on experimental correlations developed by Smogle and Reimann (1986). These types of empirical models can result in incorrect simulations, as Riemke et al. (2006) recently pointed out in their study of a small break LOCA, and are limited in applicability.

Going forward, as part of the long term strategy established by participating countries at the Generation IV International Forum (GIF) on nuclear energy, the Super Critical Water Reactor (SCWR) has the potential to achieve higher thermal efficiencies than its predecessors. The CANDU-SCWR is projected to achieve up to 48-50% efficiency based on preliminary design constraints (Torgerson et al., 2006), but this will come at the cost of higher thermodynamic operating conditions. The potential consequences of a postulated LOCA are cause enough for thermalhydraulics and safety to be at the forefront of research and development. As CANDU-SCWR is expected to employ a header/feeder arrangement in its heat transport system (Torgerson et al., 2006), it is important to further explore the effects of postulated LOCAs, particularly where the stratification/entrainment problem is concerned. A break on the side of the inlet header, a break upstream of the turrets, or a pump failure, are only a few scenarios that may cause the nominally single phase liquid inventory within the inlet header to become two-phase (gas-liquid). In effect, there are underlying areas that can be explored in the stratification/entrainment problem, and not only where the nuclear industry is concerned but from a fundamental perspective, in order to expand the knowledge base of this intriguing engineering problem.

1.2 Organization

This document is organized into eight chapters. In Chapter 2, a comprehensive literature review is provided. The chapter provides details regarding the state-of-the-art of the stratification/entrainment problem and concludes with a summary of the main areas requiring further investigation. The experimental investigation is described in Chapter 3, and provides details regarding the problem description, dimensional analysis and similitude, facility design, instrumentation, procedures and analysis. The experimental results are divided into two chapters. In Chapter 4, the two-phase results obtained from single branch experiments are provided. These results detail the related phenomena, as well as the two-phase mass flow rate and quality in a small diameter branch at three distinct orientations. The second set of experimental results are provided in Chapter 5, and details the effect of two discharging branches on the related phenomena. The knowledge obtained from experiments provides the basis to the theoretical modeling presented in Chapter 6. This chapter investigates the onset of gas entrainment in single and dual discharging branches, and evaluates the performance of selected boundary conditions. Through use of digital imaging, the interfacial liquid gradient and gas-core profile are recorded under limited flow conditions. The data is used in Chapter 7 to further improve the theoretical model through the application of empirical boundary conditions. The outcomes from the study are summarized in Chapter 8, highlighting the conclusions and future directions.

Chapter 2

Literature Review

2.1 Stratified Two-phase Flow in Horizontal Pipes and Channels

Two-phase flow is a generic term that encompasses a broad spectrum of fluidic applications with *phase* being analogous to the thermodynamic state, i.e. a gas/liquid/solid. The two *phases* could be of the same species, for example water and saturated steam (water's vapour phase), or two different species, for example air and water. Gas-liquid fluidic systems are found in both the natural sciences (e.g. oceanography) and engineering applications (e.g. industrial petrochemical processing plants). The two fluids can flow separately, sharing a common interface, or as a mixture - the *flow regime* distinguishes the physical characteristics of the two-fluid system. For example, an ocean and surrounding atmosphere form two fluid layers, or *strata* - this is

commonly referred to as the *stratified* flow regime. The physical nature of the two-fluid interface further defines the stratified regime into sub-categories, these being the *smooth-* or *wavy-* stratified regimes. For example, a flat horizontal interface is likely defined as smooth-stratified, while an undulating interface may be characterized as wavy-stratified. Two-phase flow regimes have been investigated by Baker (1954) and Sakaguchi et al. (1979). These authors developed flow pattern maps that describe the transition of two-phase flow regimes from smooth-stratified to wavy-stratified, intermittent, annular, and dispersed-bubble for flow within a circular pipe.

Mandhane et al. (1974) presented a review of the flow regimes in gas-liquid flow within a horizontal channel. A comprehensive flow map was developed, which included over 14,000 experimental data points from a variety of published sources. They pointed out that flow regime identification was subjective, based solely on the experimenter's visual observations, which resulted in a variety of flow descriptions; they classified these into six widely accepted regimes. These were characterized as the stratified, wavy, bubble, elongated bubble, slug, and annular regimes. The simple two-dimensional map represented the flow regime transitions which were presented as functions of the gas and liquid phase superficial velocities. They found that their map outperformed previously presented flow regime maps and recently Ghiaasiaan (2008) pointed out it is still a widely used reference by engineers in the field, and particularly in oil-gas production.

Taitel and Dukler (1976) provided an analytical model to predict the equilibrium liquid level for given two-phase conditions in a horizontal or inclined pipe with co-currently flowing stratified layers of gas and liquid phases. They applied a momentum

balance on the liquid and gas side which yielded an equation in the form,

$$\tau_{WG} \frac{S_G}{A_G} - \tau_{WL} \frac{S_L}{A_L} + \tau_i S_i \left(\frac{1}{A_L} + \frac{1}{A_G} \right) + (\rho_L - \rho_G) g \sin \alpha = 0. \quad (2.1)$$

The wall shear stresses produced in the gas and liquid phases were defined as τ_{WG} and τ_{WL} , respectively, while interfacial shear was defined by τ_i . The geometrical terms in Eq. (2.1) included the fluid flow cross-sectional areas of the gas, A_G , and liquid, A_L , phases. The wetted perimeter of the gas phase was defined by S_G , and that of the liquid phase as S_L , with S_i defining the chord length of the gas-liquid interface. The authors found a dimensionless form of Eq. (2.1) that incorporated the Lockhart-Martinelli parameter, \tilde{X}^2 , as,

$$\tilde{X}^2 = \frac{|(dP/dx)_{SL}|}{|(dP/dx)_{SG}|} = \frac{\frac{4C_L}{D} \left(\frac{V_{SL} D}{\nu_L} \right)^{-n_1} \frac{\rho_L V_{SL}^2}{2}}{\frac{4C_G}{D} \left(\frac{V_{SG} D}{\nu_G} \right)^{-n_2} \frac{\rho_G V_{SG}^2}{2}}. \quad (2.2)$$

The superficial pressure gradient of the gas and liquid phases, $(dP/dx)_{SG}$ and $(dP/dx)_{SL}$, respectively, was defined as the pressure gradient the fluid would experience if it flowed alone in the pipe. The superficial velocities of the gas and liquid phases were defined according to V_{SG} and V_{SL} , and the kinematic viscosity of the gas and liquid fluid phases are defined as ν_G and ν_L , respectively. The authors investigated turbulent-gas and turbulent-liquid regimes and cited friction coefficients for the gas and liquid phase as, $C_G = C_L = 0.046$ with exponents $n_1 = n_2 = 0.2$. The liquid height could be found by defining the superficial liquid velocities of each fluid phase however, the authors pointed out that two-phase regime transitions are dependent on these velocities and

provided analytical criteria to define these transitions.

Wallis (1980) reviewed the models for the prediction of critical two-phase flow. These models are classified as the homogeneous equilibrium model (HEM), and non-equilibrium models. The HEM model treats the two fluid phases as a single pseudo-fluid, where the two phases are everywhere in equilibrium with equal velocities and temperatures. Of the non-equilibrium models, the two-fluid separated flow approach applies the conservation equations to each of the two fluid phases. Additional terms are incorporated to describe the inter-phase heat, mass, and momentum transfer. Wallis (1980) argued that this approach to modeling two-phase critical flow is highly complex, particularly when describing the interactions between phases.

Persen (1984) theoretically investigated gas-liquid flow in a horizontal pipe using a two-fluid separated flow approach. A one-dimensional (1-D) model was developed by applying the energy equation to both fluid phases and the head loss terms incorporated frictional terms associated with the wall and gas-liquid interface. The author identified three key physical scenarios. The first and most simple was uniform flow in both fluid phases, indicating a steady level at any position along the pipe. The second was steady but accelerated flow, where the flow at any cross-section is independent of time but not of the axial position along the pipe (i.e. interfacial liquid level gradients form along the length of the pipe), and the third was wholly unsteady flow in the pipe. Through dimensional analysis the author was able to establish a refined general energy equation that could be evaluated based on physical principles. The condition for uniform flow was recognized in the general equation, and the author was able to parametrically evaluate the equation to determine the conditions for uniform flow

depth and pressure gradient. The study did not consider the evolution of certain terms, for example determining the friction factor from physical principles, but did provide insight into the challenges associated with modeling.

Taitel and Dukler (1987) investigated co-current gas-liquid flow in horizontal pipes and explored the effects of pipe length on the flow regime boundaries both experimentally and theoretically. The authors noted that the flow conditions near and at the pipe's exit were vital in the development of their theoretical model. In their study, the pipe exit was a free discharge, with the liquid phase emptying into a containment reservoir. Three key liquid level regions were identified along the pipe length, the equilibrium, stability, and critical levels. The critical level was said to exist at the pipe exit, with the equilibrium level located far upstream. The stability level was located in between the critical and equilibrium locations. The authors developed a 1-D theoretical model by applying the steady-state momentum equation on either fluid phase. Depending on the relative level of each of the three positions the flow regime can be stratified and independent of pipe length, stratified but unstable at the exit, in which case a transition regime will occur, and also independent of pipe length, or transitioning into intermittent or annular flow but dependent on the pipe length. The authors also point out that for low-viscosity fluids, such as water, the flow pattern transition will be independent of pipe length in the stratified regime. Their model predicted the flow regime transitions of their own experiments reasonably well, and showed some agreement with selected data in open literature.

Gardner (1988) investigated the flow of two fluids from a stagnant reservoir into a short horizontal pipe and dealt with the effects of the pipe entrance geometry on the

inlet height (liquid height in the stagnant reservoir). The two fluids were water and air operating at atmospheric pressure. The horizontal pipe was 84 mm in diameter and 590 mm long and discharged as a free stream at its exit. The inlet geometries tested included square-cut, bell-mouth, and PWR entry - named because it modeled a typical entry from the upper plenum of a pressurized water reactor (PWR). Two locations along the pipe length were selected to measure the liquid height and static pressure using differential and static pressure transducers, and were located at 140 mm and 420 mm from the inlet, respectively. The liquid height in the reservoir was recorded using a liquid filled manometer. The experimental results included a visual identification of flow regime boundaries, which were cited as: small occasional waves, large waves, and droplets in air phase. For all intents and purposes the author's description of the small occasional wave regime could be interpreted as nearly smooth stratified. The authors also developed a theoretical model to predict the liquid height within the reservoir, assuming that the flow becomes critical at some location along the length of the pipe, and before the exit. They applied Bernoulli's equation on either side of the gas liquid interface and assumed uniform flow in each fluid phase. Their model predicted their experiments reasonably well, and they also compared it with experiments conducted by Smoglie and Reimann (1986). There was a stark contrast with the theoretical prediction and the latter's experimental data. The effect of orifice diameter, (6 mm and 20mm) was evident, although it lead the authors to speculate on its significance without any clear conclusion. The experimental data for the smaller diameter orifices were not well predicted; in fact all data were over-predicted, and the author's speculated that there was some phenomenological occurrence in one of the

fluid phases that caused this difference.

Sadatomi et al. (1993) conducted smooth-stratified two-phase experiments in a horizontal channel using air and kerosene at room temperature and atmospheric pressure. Their test section consisted of a 7.2 meter long rectangular duct (50.8 mm high by 101.6 mm wide) connected between two reservoirs. The gas and liquid phases flowed co-currently within the duct from the first reservoir and into the second reservoir. The objective of their experiments was to determine the void fraction, which is the ratio of the gas phase flow area to the total flow area, at two selected locations along the channel. Distances of 1.3 and 3.3 m from the test section exit were used to record the liquid height. Their results demonstrated that a strong interfacial liquid gradient (ILG), defined as a change in liquid height with change in distance along the channel, was present. The authors then developed a theoretical model to account for the effects of the ILG. They considered co-current two-phase flow in a horizontal pipe with a circular cross-section. The main difference between their work and that of Taitel and Dukler (1976) was the inclusion of the ILG term. They argued that Taitel and Dukler (1976)'s model was representative of well-developed stratified two-phase flows, which result in a negligible ILG. They further found that the solution depended on the boundary condition at the exit reservoir and defined the concept of critical exit heights. They found that a set of imposed flow and geometrical conditions produced a set of critical heights - two critical and one normal. The normal height denotes a well-developed stratified flow, while the two critical heights are dependent on the exit boundary conditions.

Lorenz Gonzalez (1994) experimentally investigated gas-liquid flow in a horizontal rectangular channel and reported velocity and turbulence fields in each fluid phase as well as at their interface. They studied three configurations: open channel (un-sheared interface), co-current, and counter-current flows. The author used photochromic dye activation, a non-invasive flow visualization technique, to record the flow structure local to the gas-liquid interface and hot-film anemometry in the bulk fluid. The test facility consisted of a 7.2 m long rectangular channel (50 mm high by 100 mm wide). The two fluids used were liquid kerosene and air at atmospheric pressure. The liquid height was recorded at 2.5, 3.5, and 4.5 m from the inlet while the velocity field was recorded in the vicinity of 4.4 m from the inlet, which the author considered to be in the fully developed region. The author performed a series of experiments, including turbulent-gas laminar-liquid cases, and turbulent-gas turbulent-liquid cases. As the gas phase Reynolds number increased the author observed a transformation in the interface geometry from smooth-stratified to wavy-stratified. They considered that a hydraulically smooth regime coincided to a wave height less than 0.5 mm and observed that the liquid gradient decreased with increasing gas flow rate. They presented velocity and turbulence fields in both the gas and liquid fluid phases. The author compared the turbulent velocity profile with the universal profile (Nikuradse, 1932) and found that they closely followed the *Law of the Wall* in the buffer region and turbulent core until the neighborhood of the maximum velocity was reached. To characterize the gas streamwise velocity near the interface using interfacial parameters, the author found it necessary to estimate the interfacial shear stress. The interfacial shear stress and interfacial friction velocity

were determined following a method outlined by Sadatomi et al. (1993). In all cases, the author observed that the vertical velocity was dampened at the upper wall and did not vanish near the interface. The shear imposed by the gas flow on the interface transformed gradually the nearly laminar liquid velocity profile into a turbulent one. In the smooth-stratified data the authors observed that the velocity near the interface adopted a Couette-type flow, since the top layers of liquid were undergoing an intense shear. They observed that vertical motion was dampened by either the lower wall or the liquid interface.

Rodriguez and Oliemans (2006) experimentally investigated liquid-liquid flow in an inclined pipe over a wide range of flow regimes, including separated and dispersed flow patterns. The main application of their research was in oil/gas production. The two fluids used were oil and water, and the test section was a 15 m long, 76.2 mm diameter pipe which incorporated a 1.5 m clear viewing section. The measurements were conducted with the test section oriented horizontally, and angled up to 5 degrees from the horizontal. Data was reported for two-phase pressure gradient, volumetric fraction of liquid phase (referred to as holdup), and flow patterns using digital imaging. The authors used a two-fluid model for stratified flow and a homogeneous model for dispersed flow. They observed that as a result of the pipe inclination the smooth-stratified flow pattern was visibly absent, and was replaced by a stratified-wavy pattern. The authors found that the two-fluid separated flow model was able to predict the holdup of the stratified flow patterns within 15% and pressure gradients to within 35%.

Ullmann and Brauner (2006) theoretically modeled stratified gas-liquid flow in an inclined pipe using the two-fluid approach. The model applied the momentum equation on each fluid phase in order to predict the in-situ liquid holdup and pressure gradient. One of the main criteria of this approach was to consider the gas-liquid interface as flat along the pipe length, which implied a fully developed profile. Several closure relationships, which included empirical correlations, were used to determine the wall and interfacial shear stress terms of the momentum equations. The pressure gradient term was considered to include the hydrostatic and frictional terms. The authors tested the model on experimental data and obtained reasonably good agreement which was within 20% of the liquid holdup and pressure gradient measurements.

Summary

A selection of studies dealing with two-phase flow in horizontal or near horizontal pipes/channels that focused on the stratified flow regime were surveyed. The studies provided a basis for two-phase flow regime identification (Mandhane et al., 1974), showed the influence of design parameters including entrance and exit effects (Taitel and Dukler, 1987; Gardner, 1988; Sadatomi et al., 1993; Lorencez Gonzalez, 1994; Rodriguez and Oliemans, 2006), and demonstrated important parameters and analytical approaches for modeling stratified two-phase flow (Taitel and Dukler, 1976; Wallis, 1980; Persen, 1984; Taitel and Dukler, 1987; Sadatomi et al., 1993; Ullmann and Brauner, 2006). The two-phase flow regime is routinely cited as an important factor in the distribution of fluid phases in T-junctions, as will be presented in the next section.

2.2 Two-phase Gas-Liquid Flow in Equal Sided and Reduced T-Junctions

Efficient two-phase flow separation is one of the areas that can lead to improved performance of oil-gas production plants Azzopardi (1999). The use of a T-junction as a phase separator has been extensively investigated under a variety of conditions for this purpose. The topic of phase distribution in T-Junctions includes experimental studies in impacting junctions (El-Shaboury et al., 2007), small diameter junctions (Das et al., 2005), and analytical modeling (Margaris, 2007). One of the main geometric identities found in the T-junction studies is that the ratio of the branch (d) to inlet diameter (D), d/D , typically varies between around 0.5 and 1. An extensive review by Azzopardi (1999), including horizontal stratified and annular flow in T-Junctions, pointed out that the majority of these studies were in this classification. A few used a ratio lower than 0.5 with the smallest being $d/D = 0.084$. Azzopardi (1999) pointed out that these smaller branch studies were typically motivated by the nuclear industry and related to the small-break LOCA.

Generally speaking these studies adopted a particular nomenclature when describing the T-junction problem. Two-phase flow enters a horizontal T-junction through the *inlet* and splits either into the *branch*, oriented perpendicular to the inlet, or flows past the branch into the *run*. The inlet and run are typically the same size and shape with the branch having an equal or reduced size. With a horizontally oriented inlet the branch may direct the separated flow anywhere from vertically down to vertically up. The operating conditions upstream of the branch, particularly the flow regime,

have been shown to be highly influential on the phase separation characteristics. A brief historical look at some of the work done in this area follows.

Oranje (1973) first observed that particular stations in a natural gas transmission network contained varying levels of condensate. Upon further experimental investigation using a T-junction the author found that several factors influenced how the inlet flow was distributed between the branch and run. These included the T-junction geometry, flow regime, liquid inertia, and branch pressure. A wide variety of studies were later conducted in order to understand the behavior of two-phase flow within T-junctions, and there have been notable developments in the state-of-the art since this seminal work.

Henry (1981) conducted experiments in a horizontal T-junction with a side oriented branch. The test section consisted of 100 mm diameter (D) horizontal pipe with a 20 mm branch diameter (d). The inlet pipe length between the two-phase mixer and the branch inlet was 30 pipe diameters (3 m). Water and air operating at near ambient conditions were used. The authors described the dependency of the branch two-phase mass flow rate on the upstream conditions, and more specifically, the mass flow rate of each constituent phase. Their investigation was conducted with annular flow in the inlet but also provided some measurements in the stratified regime. The authors correlated the annular regime results using the inlet two-phase flow quality, X_1 , and found that it did not predict the stratified regime data well. They argued that that the branch liquid mass flow rate prior to gas entrainment, \dot{m}_i , is likely dependent on the liquid depth in the pipe. They suggested that \dot{m}_i is better predicted

as a function of the Lockhart-Martinelli parameter, \tilde{X} as,

$$\dot{m}_i = 544 - 491\tilde{X}. \quad (2.3)$$

Honan and Lahey Jr. (1981) performed two-phase experiments in vertically oriented Y and T-junctions using air and water. The T-junction was equal sided with an inlet diameter of 38.1 mm and was operated at a pressure of 0.7 MPa with a maximum air flow rate of $0.47 \text{ m}^3/\text{s}$ and water mass flow rate of 4.43 kg/s. The authors recorded the inlet and branch flow rates of each fluid phase and then presented the phase distribution in terms of the phase separation ratio (X_3/X_1), inlet quality X_1 , and the ratio between the run and inlet mass flow rates, $\dot{m}_{TP2}/\dot{m}_{TP1}$. They found that the fluid phases did not separate equally between the run and branch, but rather, a higher portion of gas flowed through the branch. This was particularly true with higher inlet qualities, which approached the complete phase separation line that the authors defined as,

$$\frac{X_3}{X_1} = \frac{1}{1 - \frac{\dot{m}_{TP2}}{\dot{m}_{TP1}}}. \quad (2.4)$$

Azzopardi and Whaley (1982) Performed experiments in vertical and horizontal T-junctions and investigated the effects of the flow pattern on the two-phase characteristics. The annular regime was tested in both horizontal and vertical cases, while the churn and bubbly regimes were only tested in the vertical arrangement. The

horizontal tests were conducted with an inlet diameter of 32 mm, a branch diameter of 12.7 mm, and an inlet length of 3.6 m. Water and air operating at 250 kPa in the T-junction were used. The gas and liquid inlet mass flow rates were 0.064 kg/s and 0.051 kg/s, respectively. They tested branch orientations ranging between 0 to 180 degrees from the vertical. Results demonstrated that the liquid flow in the branch increased dramatically with the branch angle. Following this Azzopardi (1984) focused on the effect of geometry, specifically the ratio between the branch and run diameters of the T-junction. They experimented with d/D equal to 0.8 and 1. The study focused only on the vertical pipe arrangement in the annular flow regime. They found that the larger the diameter ratio, the higher the amount of each phase extracted through the branch.

Saba and Lahey Jr. (1984) studied two-phase separation in a horizontal equal sided T-junction. Experiments were conducted across a variety of flow regimes, including stratified, wavy-stratified and slug. The inlet diameter was 38.1 mm, and experiments were conducted using air up to a volume flow rate of $0.47 \text{ m}^3/\text{s}$ and water up to a mass flow rate of $4.42 \text{ kg}/\text{s}$. The pressure drop in each of the three legs of the T-Junction were recorded using pressure transducers and the authors were able to quantify the pressure drop due to the T-junction. They developed a phase separation model, which included mixture and vapor phase continuity equations, mixture linear momentum equations for the branch and run flows, as well as the vapor phase linear momentum equation. Empirical relations were required to close the system, but the authors found the model provided reasonably good predictability of the inlet and branch qualities. The authors do point out that for separated flow their model could

not accurately predict phase separation.

Marti and Shoham (1997) experimentally and analytically investigated the fluid phase distribution in a reduced T-junction. The test section had a 50.8 mm inlet and a 25.4 mm diameter branch. Experiments were carried out using water and air operating at 194 kPa within the stratified-wavy regime. An inlet superficial gas velocity of 6.1 m/s was used while the inlet superficial liquid velocity ranged between 0.059, 0.03, 0.015, and 0.0051 m/s. The branch orientation was varied between 20 degrees upwards to 60 degrees downward from the horizontal. They presented the phase distribution in terms of the liquid and gas fractions between branch and run. The authors described that when the interface was below the branch inlet the liquid phase must “climb up” into the branch. They also indicated that the axial momentum of the liquid phase caused it to bypass the branch and used this observation in the development of their model. Their approach was a two-fluid model that considered two streamlines, one for each fluid phase, and applied a one-dimensional momentum equation between two convenient points. The momentum equation considered a direction parallel to the branch (perpendicular to the inlet), which was convenient since far upstream the flow was considered to flow parallel to the inlet. This assumption resulted in the inlet velocity term to decay to zero. The resulting equation required that a second location be defined; the authors used points at the branch center and the downstream branch edge. In the solution the authors used experimentally recorded values of the liquid holdup to determine the in-situ velocities of each fluid phase. In some cases good agreement was found between the experimental and analytical phase distribution, however in other cases differences of up to 200% were evident but the

reasons for these discrepancies were not discussed.

Rea and Azzopardi (2001) experimentally investigated the phase split of gas and liquid phases in a large diameter T-junction. An equal sided T-junction test section, with a 127 mm diameter circular cross-section, was machined into a block of clear acrylic resin. The sides of the test section were machined flat, with overall outside dimensions of 200 by 200 mm, in order to reduce optical distortions due to refraction. The test section was located 3.5 m downstream of a two-phase mixing unit which translated into an entrance length of approximately $27.5D$. The authors used a capacitive two-wire technique to record the lateral liquid height distribution across the pipe cross-section. Experiments were conducted primarily in the stratified regime using air and water operating at near atmospheric conditions. They reported the effects of the inlet superficial velocities of the two fluids on the fractions of each fluid entrained into the branch. They compared the phase splitting with selected models, one in particular by Shoham et al. (1987), and found poor agreement with their experimental results. They modified the model by including several empirical functions based on their experimental data, and showed an improvement in the model prediction.

2.3 Small Branches Exposed to a Stratified Gas-Liquid Region

A large number of studies have been conducted on the topic of two-phase flow in small diameter branches. These investigations are typically either phenomenological in nature, as in the study of incipience of two-phase entrainment, or on the topic of two-phase flow characteristics. A brief historical review of these studies is presented here.

2.3.1 Experiments and Modeling in Stratified Two-Phase Reservoirs

Zuber (1980) reviewed the two-phase phenomena at a small branch on the side of a large reservoir containing stratified layers of gas and liquid fluid phases. The location of the gas-liquid interface relative to the branch was a key factor in determining the phenomena. With single phase gas flowing initially into the branch a critical distance between the gas-liquid interface and branch exists where the branch flow will become two-phase - called the onset of liquid entrainment (OLE). On the other hand, with single phase liquid flow in the branch the critical distance to cause two-phase flow is called the onset of gas entrainment (OGE). The OGE was described by mechanisms that included either vortex induced or vortex-free gas entrainment, with the latter dramatically affecting the branch two-phase mass flow rate and quality. The critical liquid height, H_{OGE} at which vortex-free OGE occurred was found to be related to

the branch flow Froude number, Fr_d as,

$$\frac{H_{OGE}}{d} = C_1 Fr_d^{C_2} \quad (2.5)$$

where,

$$Fr_d = \frac{4\dot{m}_{L3}}{\pi\sqrt{gd^5\rho_L(\rho_L - \rho_G)}} \quad (2.6)$$

The branch diameter is defined as d , the single phase liquid mass flow rate in the branch as \dot{m}_{L3} , the liquid and gas densities as ρ_L and ρ_G , respectively, and the acceleration due to gravity as g . The coefficients C_1 and C_2 were found to be correlated with $C_1 = 0.574$ and $C_2 = 0.667$ for $H_{OGE}/d < 1$ and $C_1 = 0.624$ and $C_2 = 0.4$ for $H_{OGE}/d > 1$ from transient experiments (Lubin and Hurwitz, 1966). Similar transient experiments were also performed using a range of reservoir and branch sizes with two stratified fluids of varying densities, viscosities, and surface tension coefficients. The fluid combinations included air-water, kerosene-water, corn oil-water, turpentine-water, and silicone oil-water (Lubin and Springer, 1967) as well as air and liquid ethanol (Abdalla and Berenyi, 1969). Both studies described the flow field as being vortex-free at the onset of gas entrainment in the branch. This is in contrast to the vortex induced air entrainment phenomenon which is traditionally associated with this type of “draining” flow (Baum and Cook, 1975; Takahashi et al., 1988; Andersen et al., 2003).

CANDU Type Header-Feeder under Postulated LOCA Conditions

Kowalski and Krishnan (1987) performed full scale experiments in a test facility that is typical of a CANDU primary cooling loop. Two horizontal headers were connected to each other by 30 feeder branches. The experiments consisted of single and two turret injection tests with two-phase mass flow rates ranging between 30 to 60 kg/s of water, and 0.05 to 2.4 kg/s of steam. The authors observed that even a small amount of injected steam caused flow stratification within the header. Under these conditions the injected two-phase flow impinged on the steam-water interface causing an axial velocity (crossflow) within the header. Correlations for the critical height in a single branch were presented as a function of the branch location. Later, Teclemariam et al. (2003) performed experiments in a scaled down test section typical of a CANDU-type header. These authors presented the two-phase flow distribution in the header under single and dual injection tests through the turrets. Like Kowalski and Krishnan (1987), these authors showed that two branches on opposing sides of the header had similar two-phase flow characteristics. These authors presented qualitative sketches of their observations showing the complex nature of the two-phase flow distribution during injection tests. Their observations depict an axial flow within the header with a varying liquid level between feeder banks.

In order to isolate the particular effects of geometry and flow conditions in complex multi-branch header-feeder systems a variety of quasi-steady experiments were conducted with one or two branches on a flat vertical wall (Parrott et al., 1991; Hassan et al., 1996a,b, 1998; Maier et al., 2001b; Bartley et al., 2008, 2010) or with up

to three branches on a curved surface (Hassan et al., 1997; Ahmad and Hassan, 2006; Bowden and Hassan, 2007, 2008) exposed to large stagnant stratified gas-liquid reservoir. These studies reported the critical height at the onset of liquid entrainment and vortex-free gas entrainment for a variety of geometries and flow configurations (single or multiple branches), and corroborated the relationship between the critical height and the branch Froude number. With interface heights below the OGE or above the OLE, the flow into the small branch becomes a two-phase gas-liquid mixture. The relationship between the interface height and the two-phase branch characteristics, e.g. the two-phase mass flow rate and quality, have also been investigated in a few of these studies (Hassan et al., 1997; Bartley et al., 2010).

Modeling the Onset of Liquid Entrainment (OLE)

Since 1990 several studies have been conducted to model the critical height at the onsets of gas and liquid entrainment in either single or multiple branches. These studies consider branches exposed to a large stratified gas-liquid region. An analytical model for the onset of liquid entrainment in a side oriented branch was first derived by Craya (1949), and verified experimentally by Gariel (1949). The model considered two immiscible fluids, a gas and a liquid phase, with Bernoulli's equation applied along the gas-liquid interface between two convenient points. The first point was assumed to be sufficiently far from the branch where the fluid velocity was considered negligible (stagnant). The vertical distance between this stagnant point and the branch center is defined as the critical height. The author considered the tip of a liquid spout that formed in the interface just below the branch as the second point. Potential theory

was used to describe the motion of the lighter fluid entering the branch, with the branch's velocity field approximated by a point-sink. The kinetic energy at the spout tip could be defined through the point-sink equation as well as Bernoulli's equation. The spout height was found as a single solution where these two equations were equal and tangent to each other. The simplified model demonstrated reasonable accuracy with Gariel (1949)'s experimental results.

Following from Craya (1949)'s theory the onset of liquid entrainment was investigated for a side slot of finite width (Soliman and Sims, 1991) and a branch with a finite diameter (Soliman and Sims, 1992). Their analysis provided an improvement in the prediction in the critical height, particularly at low branch Froude numbers. Armstrong et al. (1992) provided an analytical model for the onset of liquid entrainment for two branches on the side of a flat vertical wall. They found that the flow in the branches could be simulated as point-sinks, which resulted in relatively good agreement with their experimental data. Hassan et al. (1999), and later Maier et al. (2001a), improved the dual branch models for a variety of branch configurations by considering each branch to have a finite diameter. Better agreement was found at low branch Froude numbers, and these models were shown to more appropriately predict the physical limits of the branch edges.

Modeling the Onset of Gas Entrainment (OGE)

Ahmed et al. (2003) modeled the onset of gas entrainment in a single discharging side branch installed on a flat vertical wall exposed to a smooth-stratified gas-liquid environment. Two models were proposed by the authors, first a simplified model that

treated the branch as a three-dimensional point sink, and a second more complex model that assumed the branch to have a finite diameter. They treated each fluid phase independently and assumed incompressible, inviscid, irrotational, and quasi-steady flow conditions with negligible surface tension. These assumptions directed the authors to a potential flow problem, and considered the gas-liquid interface to be the link between both fluid phases. To that end they applied Bernoulli's equation along the interface between two convenient points. The first point was selected far from the branch where the liquid kinetic energy was negligible. The vertical distance between this point and the branch was considered to be the critical height. The second point was established by considering that a steady dip forms in the gas-liquid interface just prior to the OGE. The tip of this steady dip was considered to be the second point. The authors considered that at the OGE the dip would become unstable and used a criterion based on the work of Taylor (1950) who investigated the instability of inviscid liquid surfaces when accelerated vertically. It was stated that a liquid surface would become unstable if accelerated vertically at a rate greater than or equal to gravity. A simplification of the point-sink approach reduced their model to the form found in Eq. (2.5) with $C_1 = 0.625$ and $C_2 = 0.4$, which is consistent with Lubin and Hurwitz (1966). For the second finite branch model the authors accounted for the branch diameter by solving Laplace's three-dimensional equation. This was a result of applying a potential function to the continuity equation with the appropriate boundary conditions. A solution was found by a Fourier integral method using appropriate sine and cosine transformations. This second model was found to be more representative of the physical limits with a branch Froude number of less

than 10. At this point, the difference between both the point-sink and finite-branch models was approximately 5%. With the Froude number decreased to approximately one the difference between the point-sink and finite-branch predictions increased to nearly 20%. The authors followed this by modeling the onset of gas entrainment in two branches on a flat wall in the same vertical plane (Ahmed et al., 2004) and the same inclined plane (Ahmed, 2006).

Andaleeb et al. (2006) used a similar point-sink approach to model the onset of gas entrainment in single branch on a curved surface exposed to a large stratified gas-liquid environment. Saleh (2008) modeled the onset of gas entrainment in single, dual, and triple discharging branches on the side or bottom of a semi-cylindrical wall. These models showed reasonably good agreement with experimental data provided by Ahmad and Hassan (2006) at moderate and high branch Froude numbers. In dual branch configurations Saleh (2008) identified that the OGE could occur in each branch separately or both branches simultaneously. These modes of entrainment had been earlier classified experimentally by Parrott et al. (1991). At low branch Froude numbers the point-sink models showed poor agreement with experimental values; Saleh et al. (2009) proposed that this was due to the effect of surface tension. To address this point, the authors incorporated a term in their point-sink model that compensated for surface tension effects using the dip radius of curvature. They argued that an analytical expression for the dip radius of curvature could not be established, and opted instead for an empirical approach. The authors used a digital imaging technique to record the OGE dip radius of curvature and produced a semi-empirical model for the critical height. The results showed an improvement at low branch

Froude numbers in comparison to experimental data by Ahmad and Hassan (2006) over existing point-sink models.

Particle Image Velocimetry and Semi-Empirical Modeling of the OGE

One of the underlying challenges in modeling either the onset of liquid or gas entrainment is in determining a suitable potential function to describe the flow field local to the branch. The finite branch approach is known to be particularly complex to solve, with limited solutions being attained to date. An alternative to an analytical expression of the potential function is to obtain localized whole field measurements of the fluid velocity through experimental investigation. The technique referred to as particle image velocimetry (PIV) has been thoroughly discussed (Willert and Gharib, 1991; Raffel et al., 1998; Adrian, 2005). It is a non-intrusive velocity field mapping technique that uses particles immersed in the fluid to enable flow tracking and determination of the local fluid velocity. The basic components are a digital camera to capture the particle displacement and a light source to illuminate the particles at two instants in time. Image analysis of two sequential images of the particles, taken within a known time interval, can be correlated to produce velocity vectors. Earlier PIV systems were developed to provide two-component fluid velocity measurements (2d-PIV), but more recent advances using two-camera systems have produced three-component velocity fields (Prasad, 2000). This three-component technique is commonly referred to as stereoscopic PIV (3d-PIV) and it has been used successfully to record velocity fields in single liquid phase systems (Zhang and Hugo, 2006) or even two-phase systems (Hassan et al., 2001).

Bowden and Hassan (2007) used 2d-PIV to study the OGE phenomena in a single downward branch by recording the liquid phase velocity field local to the branch in a large air-water reservoir. They divided the three-dimensional flow field into three horizontal and a single vertical image plane. The authors developed a control volume conservation of mass validation technique to determine the relative error of the PIV measurements. Their analysis demonstrated that the PIV measurements resulted in high error near the branch. They speculated that this was due, in part, to the two-phase air-water dip distorting the images in this region. Saleh et al. (2010a) thoroughly evaluated the use of 3d-PIV for measurement of the liquid side velocity field at the OGE in a side oriented branch. They improved the control volume approach to estimate the measurement error, and concluded that the high error near the branch was due mainly to out-of-plane motion which resulted in a loss of velocity vectors. Spatial and temporal factors were also found to affect the measurement error. These included the control volume discretization technique and imaging frequency. The authors compared experimental velocity measurements with the analytical prediction obtained from their previous point-sink analysis (Saleh, 2008) and showed good agreement at a distance of 15 mm from the branch. Saleh et al. (2010b) followed this with a parametric investigation of the liquid side velocity field using 3d-PIV at the OGE during dual discharge.

2.3.2 Experiments in Stratified Horizontal Channels

The relationship between the critical height and branch Froude number in studies involving horizontal pipes with a co-currently flowing stratified gas-liquid regime was found to be significantly different from that obtained in large stratified gas-liquid reservoirs. A few studies have been done that investigate the related two-phase phenomena in a small branch on the side or bottom of horizontal pipe with a co-currently flowing stratified gas-liquid regime.

Reimann and Khan (1984) investigated the critical height at the onset of vortex-free gas entrainment and correlated their results in the form of Eq. (2.5) yielding $C_1 = 0.9625$ and $C_2 = 0.4$. Their air-water experiments were conducted at pressures up to 0.5 MPa in a 206 mm internal diameter horizontal pipe with a single downward or side oriented branch having a diameter of 6, 12, or 20 mm. The inlet water mass flow rate ranged between 0.2 kg/s and 11 kg/s with heights varying between 14.01 mm and 94.76 mm. The liquid height measurements were conducted at a location approximately 0.5 m upstream of the branch entrance within the inlet. They discussed that water's velocity in the pipe (0.2 to 0.8 m/s) had negligible influence on the critical height since the liquid velocity entering the branch was significantly larger - up to 60 m/s. Smoglie and Reimann (1986) later demonstrated that their fitting coefficients, C_1 and C_2 of 1.06 and 0.4, respectively, were independent of the ratio between run, $\rho_L V_{SL2}^2$, and branch, $\rho_L V_{SL3}^2$ superficial momentum fluxes in the range of $0.1 \times 10^{-4} \leq \rho_L V_{SL2}^2 / \rho_L V_{SL3}^2 \leq 40 \times 10^{-4}$. Smoglie and Reimann (1986) also investigated the branch two-phase mass flow rate and quality, and derived an

empirical expression for the branch quality as a function of the interface height, the critical height at the onset of gas entrainment, and the densities of the gas and liquid phases.

Schrock et al. (1986) experimented with water and steam, as well as water and air at up to 1.07 MPa, flowing co-currently in a 102 mm diameter horizontal pipe with a 4, 6, or 10 mm diameter branch at the side or bottom of the pipe. They found that the critical height at onset of gas entrainment was best fit when the effects of viscosity and surface tension were accounted for. Their OLE experiments did however correlate well with Eq. (2.5) with coefficients of $C_1 = 0.624$ and $C_2 = 0.4$. The authors did not discuss any possible effects of the inlet crossflow velocity on the critical height. They also investigated conditions leading to two-phase flow in the branch, and provided correlations for the branch two-phase quality in relation to the interface height.

Maciaszek and Micaelli (1990) experimented with gas entrainment in a downward branch using inlet diameters of 80 and 135 mm and branch diameters of 12 and 20 mm. Their tests were conducted at operating pressures between 2 and 7 MPa. The authors found that their data was correlated by $C_1 = 0.335$ and $C_2 = 0.4$ and observed that the transverse liquid velocity in the pipe, up to 3 m/s, drastically influenced C_1 .

Yonomoto and Tasaka (1991) reported the critical height at the onset of vortex-free gas entrainment using air and water. Their test facility consisted of a 190 mm square horizontal duct with a single downward branch whose diameter varied between 10, 15, and 20 mm at an operating pressure of between 0.4 and 0.7 MPa. The authors provided a simplified theoretical model in the same form as Eq. (2.5) with $C_1 = 0.555$ and $C_2 = 0.4$. The simplified model considered the discharge to be a point-sink, and

neglected the effects of viscosity, compressibility, and phase change. By comparing their analytical and experimental results the authors were able to provide a correction factor to compensate for the effects of the transverse liquid flow in the pipe as a function of the inlet, \dot{m}_{L1} and run \dot{m}_{L2} , liquid mass flow rates.

2.4 Summary

The literature review was organized into three main topics relating to two-phase flow in straight channels, T-junctions, and small branches. The underlying theme in each topic was the two-phase flow regime; emphasis was placed on separated flows and in particular smooth and wavy-stratified regimes. The discussion was focused to describe pertinent experimental details and provide summaries of relevant analytical, empirical, and semi-empirical models available.

It was found that there are a limited number of studies that describe two-phase flow and related phenomena in small branches exposed to co-currently flowing stratified gas-liquid regimes. These studies showed dramatically different predictions of the critical height at the onset of gas entrainment in comparison to each other, and in comparison to studies dealing with large stratified gas-liquid reservoirs. These differences may be the result of the fluid velocity in the channel, the different test section scales, the measurement location, or methodologies employed. There are also little or no studies dealing with multiple branches exposed to flowing stratified gas-liquid regimes, however two-phase reservoir based studies have demonstrated that a second

or third branch can considerably affect the two-phase mass flow rate and related phenomena. Therefore several questions persist, and the specific objectives of this work are:

- Design and build an experimental facility in order to investigate the stratification/entrainment problem in single and dual branch configurations.
- Investigate two-phase flow (mass flow rate and quality) and phenomena (onset of gas and liquid entrainment, two-phase regime transitions) in a single branch with a stratified co-current gas-liquid flow regime.
- Experiment and report on the onset of gas entrainment phenomenon in dual discharging branches with co-current stratified gas-liquid flow conditions.
- Formulate a theoretical model to predict the critical height at the onset of gas entrainment in a single discharging branch from a stratified gas-liquid region with liquid crossflow.
- Develop appropriate empirical and semi-empirical correlations for use in the prediction of the stratification/entrainment problem.

Chapter 3

Experimental Investigations

3.1 Problem Description

A typical CANDU header can be described as a horizontally oriented pipe with a length-to-diameter ratio of approximately 14 to 17. The header diameter (D) typically ranges between 0.356 and 0.406 m with an overall length of approximately 6 m (Kowalski and Krishnan, 1987). There are multiple inlet (turrets) and exit orifices (feeders) along the header which are used to distribute coolant within the system. Coolant is supplied to the header through the two turrets located at the top of the header; these are referred to here as T1 and T2 in Fig. 3.1. The coolant flows from the header through the feeders and towards the fuel channels; these are referred to here as FB-2, FB-1, FB0, FB+1, FB+2, and FB+3 in the figure. The feeders are arranged in a specific configuration called a feeder bank. A single typical feeder bank has five feeder orifices located around the circumference of the header, two horizontal ($\beta = 0^\circ, 180^\circ$), two inclined at 45° and 135° , and a single downward branch ($\beta = 90^\circ$).

The diameter (d) of each feeder is typically 50.8 mm. The horizontal separating distance between feeder banks is denoted by L_{FB} , and between the feeder bank and turrets as L_T .

Under postulated loss-of-coolant accident conditions the normally liquid phase coolant entering the header through the turrets can become a two-phase gas-liquid mixture. Even a small amount of injected steam has been shown to cause flow stratification within the header (Kowalski and Krishnan, 1987). The liquid level distribution along the header is non-uniform and is influenced by the two-phase mass flow rate of the coolant entering the header through the turrets (Tecler et al., 2003). The turret injection flow may impinge on the gas-liquid interface which may also contribute to the non-uniform liquid level. The complex flow structure will ultimately vary along the header's length. Isolating a single feeder bank denoted by the shaded control volume in Fig. 3.1, at FB-0, the fluid phase mass flow rates at the boundary control surfaces may be defined. The left control surface is denoted as the *inlet* with subscript 1 , the gas and liquid mass flow rates are defined as \dot{m}_{G1} and \dot{m}_{L1} , respectively. Subscripts L and G are used to denote the gas and liquid phases, respectively. The right side control surface is referred to as the *run* using subscript 2 , the gas and liquid mass flow rates through this surface are defined as \dot{m}_{G2} and \dot{m}_{L2} , respectively. The third control surface is referred to as the *branch* using subscript 3 . In Fig. 3.1 the side oriented branches are simply referred to as *branch A*, the inclined branches as *branch B*, and the bottom oriented branch as *C*. The fluid mass flow rates through these branches are defined as \dot{m}_A , \dot{m}_B , and \dot{m}_C .

The consequence of flow stratification within the header is that the conditions

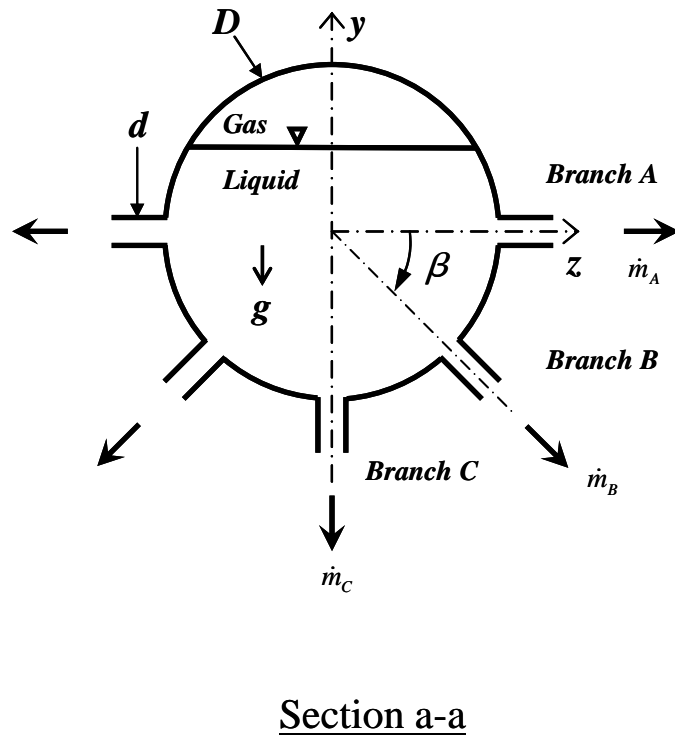
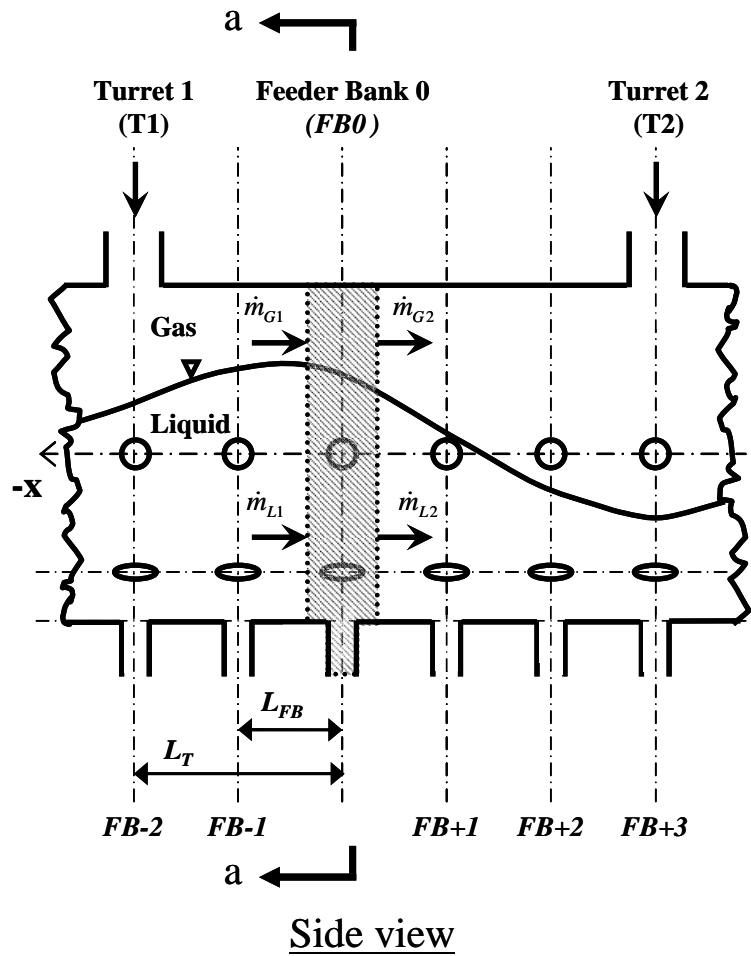


Figure 3.1: Problem description

are favorable for the gas phase to entrain into the normally liquid feeder flow. As a result the various branch mass flow rates, \dot{m}_A , \dot{m}_B and \dot{m}_C , could either be a single phase liquid, a two-phase mixture, or a single phase gas. The location of the interface relative to the branch is an important consideration to determine if the branch mass flow is single phase or two-phase. If the interface is well above the branch the flow is likely to be a single phase liquid. If the interface is well below the branch the flow is likely to be single phase gas. As the interface approaches the branch however, a two-phase gas-liquid mixture is likely flowing in the branch. As a result there are critical interfacial locations where the branch flow transitions between single phase and two-phase. These critical conditions are defined as the onset of gas and liquid entrainment, OGE and OLE, respectively. To formally evaluate the conditions resulting in OGE, OLE, and two-phase flow, a reduction of terms is required to simplify the problem to one that is more manageable.

3.2 Reduction of Variables: Dimensional Analysis

3.2.1 Scaling a Single Simulated Feeder Bank

The problem conditions considered for a single feeder bank, the shaded region at FB0 in Fig.3.1, are presented in Fig.3.2. The relevant geometric and dynamic parameters are presented in the figure in addition to the fluid density (ρ), dynamic viscosity (μ), and interfacial surface tension (σ). The branch orientations considered in this analysis are located at the side ($\beta = 0^\circ$), inclined ($\beta = 45^\circ$), and bottom ($\beta = 90^\circ$).

The branches located at $\beta = 135^\circ$ and 180° will not be considered in this study in order to reduce the number of independent variables.

A geometric scaling factor of 1:8 was selected for the cross-sectional dimensions resulting in a simulated header diameter, D , of 50.8 mm and a branch diameter, d , of 6.35 mm. A suitable inlet length scale was determined by examining earlier experimental studies dealing with stratified flow in reduced T-junctions. It was found that these investigations typically used a longer inlet than run length. A typical inlet length was found to be on the order of $22D$ (Smoglie and Reimann, 1986) and $29D$ (Yonomoto and Tasaka, 1991). Using these studies as guides, the inlet and run lengths (L) were selected as $36D$.

3.2.2 Beginning of Two-phase Flow in a Single Branch

The onset of gas entrainment is characterized when a steady stream of gas begins to flow into the normally liquid branch flow. The onset of liquid entrainment is characterized when the liquid phase ceases to flow into the branch, and the branch mass flow rate is a single phase gas. The critical liquid height at the OGE (H_{OGE}) and the OLE (H_{OLE}) are expected to be functions of several independent parameters which include geometric variables (D , d , L , λ), dynamic variables (g , \dot{m}_{L3} , \dot{m}_{G3} , \dot{m}_{G2} , \dot{m}_{L2}), as well as fluid properties (ρ , μ , σ). The term λ is the position within the inlet where the critical interface height is measured. This is an important parameter since the scaled inlet length is relatively short and an interfacial liquid gradient is expected, as previously discussed by Sadatomi et al. (1993). A reduction of terms

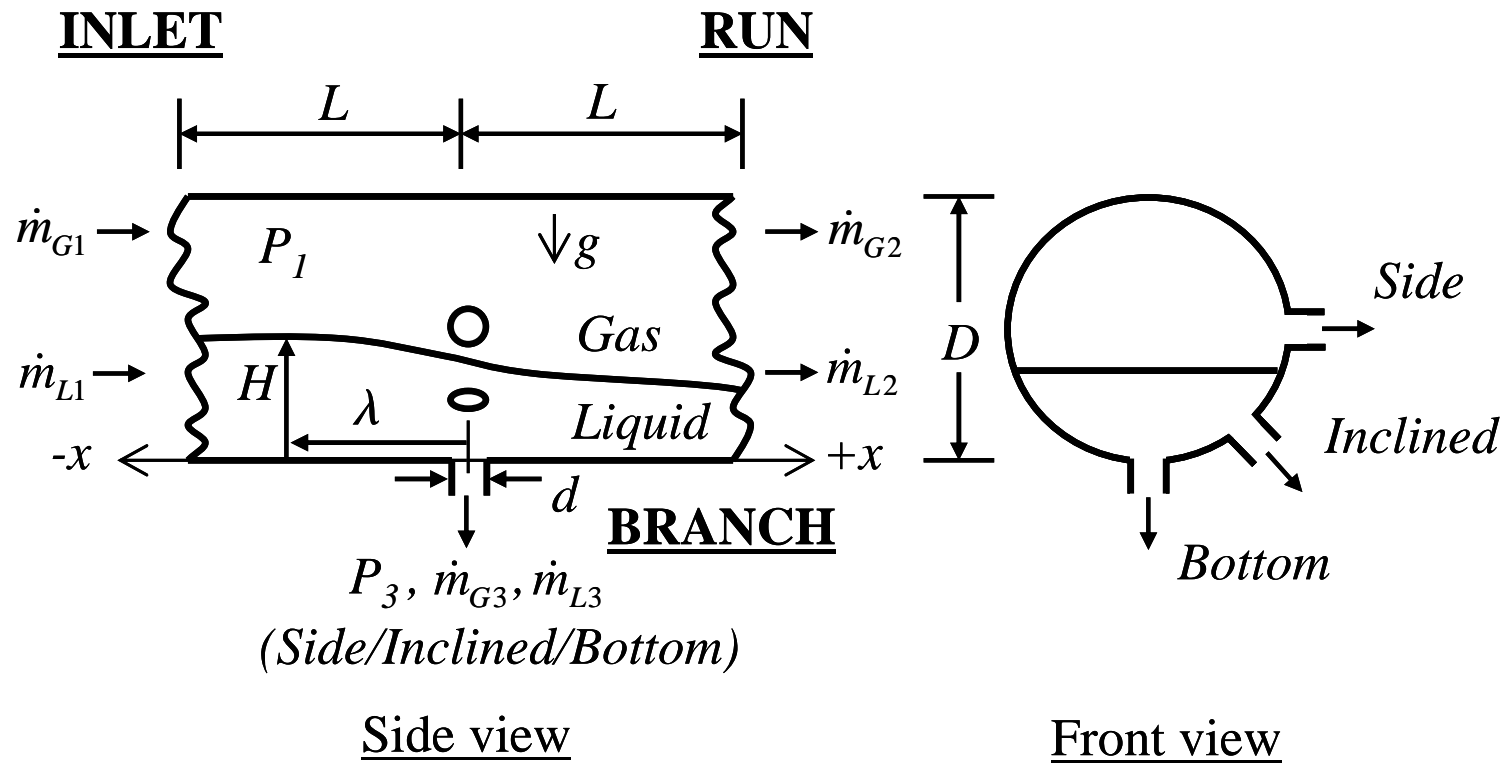


Figure 3.2: Single feeder bank problem description.

therefore provides the following functional relationship,

$$\frac{H_{OGE}}{d} = f\left(\beta, \frac{d}{D}, \frac{L}{D}, \frac{\lambda}{D}, Fr_d, Re_d, We_d, \frac{\rho_L V_{L2}}{\rho_L V_{L3}}\right) \quad (3.1)$$

where,

$$Fr_d = \frac{4\dot{m}_{L3}}{\sqrt{gd^5\rho_L(\rho_L - \rho_G)}}, \quad (3.2)$$

$$Re_d = \frac{4\dot{m}_{L3}}{\mu_L\pi d}, \quad (3.3)$$

and

$$We_d = \frac{16\dot{m}_{L3}^2}{\sigma\rho_L\pi^2d^3}. \quad (3.4)$$

The branch Froude number, Fr_d , is a ratio of inertial and gravitational forces, the branch Reynolds number, Re_d , is a ratio of inertial and viscous forces, and the branch Weber number, We_d , is a ratio of inertial and surface tension forces. The last term on the right hand side represents the ratio of mass fluxes between the run and branch.

Table 3.1: Saturation properties of D_2O at 300° and 10 MPa

	Saturated Liquid	Saturated Vapor
Density (kg/m^3)	784.87	52.64
Viscosity ($N \cdot s/m^2$)	9.36E-05	1.97E-05
Surface Tension (N/m)	1.39E-02	

Dynamic Similarity

A typical CANDU header nominally operates with heavy-water (D_2O) at temperatures and pressures in the range of $300^\circ C$ and 10 MPa (Banerjee and Nieman, 1982).

At $300^\circ C$ the saturation pressure is approximately 8.6 MPa; the saturated liquid and vapor properties are listed in Table 3.1. Dynamic similarity is satisfied by,

$$(Fr_d)_{mod} = (Fr_d)_{prot}, \quad (3.5)$$

$$(Re_d)_{mod} = (Re_d)_{prot}, \quad (3.6)$$

$$(We_d)_{mod} = (We_d)_{prot}, \quad (3.7)$$

$$\left(\frac{\rho_L V_{L2}}{\rho_L V_{L3}}\right)_{mod} = \left(\frac{\rho_L V_{L2}}{\rho_L V_{L3}}\right)_{prot} \quad (3.8)$$

The variation of the idealized liquid branch Froude, Reynolds and Weber numbers were evaluated using $d = 50.8mm$; the results of are presented in Fig. 3.3. The figure presents the magnitude of each dimensionless group as a function of the inertia term, which is represented in the figure by the average liquid velocity in the branch, V_{L3} . For a circular branch this velocity is defined as,

$$V_{L3} = \frac{4\dot{m}_{L3}}{\rho_L \pi d^2}. \quad (3.9)$$

The force of gravity in the branch Froude number is dominant over viscous (Re_d) and surface tension (We_d) forces. The Weber number demonstrates that surface tension effects could be relevant at low values of V_{L3} .

Based on this analysis it is reasonable to assume that the physics of the problem would be governed by the branch Froude number. This also helps to further reduce

the number of dimensionless groups that need to be considered in the problem, and the relationship in Eq. (3.1) can now be rewritten as,

$$\frac{H_{OGE}}{d} = f\left(\beta, \frac{d}{D}, \frac{L}{D}, \frac{\lambda}{D}, Fr_d, \frac{\rho_L V_{L2}}{\rho_L V_{L3}}\right) \quad (3.10)$$

A similar equation may be developed for the onset of liquid entrainment, with the branch flowing gas rather than liquid, and the branch Froude number becomes,

$$Fr_d = \frac{4\dot{m}_{G3}}{\pi\sqrt{gd^5\rho_G(\rho_L - \rho_G)}}. \quad (3.11)$$

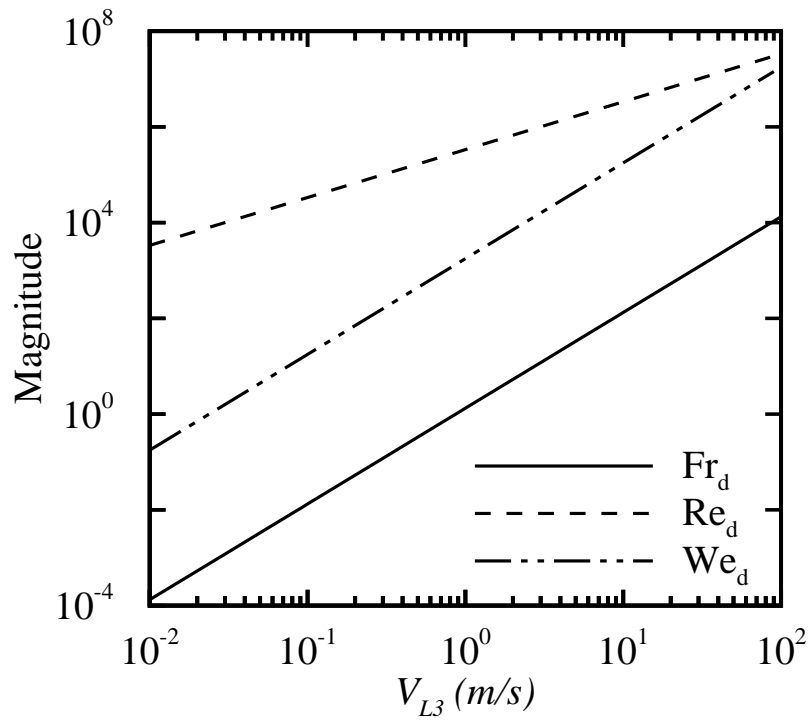


Figure 3.3: Estimated dimensionless numbers of liquid flow in a feeder branch.

3.2.3 Two-phase Flow in a Single Branch

Between the limits defined by H_{OGE} and H_{OLE} the flow in the branch is a two-phase mixture, as illustrated in Fig. 3.4. At H_{OGE} the single phase liquid mass flow rate is defined as $\dot{m}_{L3,OGE}$ while at H_{OLE} the single phase gas mass flow rate is $\dot{m}_{G3,OLE}$. The two-phase branch mass flow rate, \dot{m}_{TP3} , is defined as the sum of gas, \dot{m}_{G3} , and

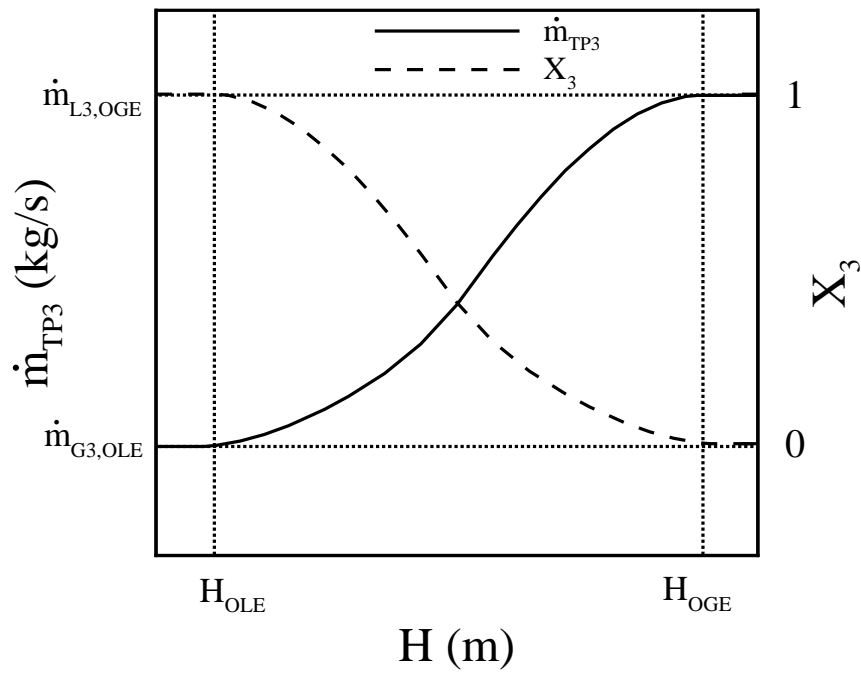


Figure 3.4: Qualitative description of two-phase flow in a single discharging branch.

liquid, \dot{m}_{L3} , mass flow rates as,

$$\dot{m}_{TP3} = \dot{m}_{L3} + \dot{m}_{G3}, \quad (3.12)$$

and the branch flow quality (X_3) represents the ratio of the gas phase in the two-phase mixture as,

$$X_3 = \frac{\dot{m}_{G3}}{\dot{m}_{TP3}}. \quad (3.13)$$

The two-phase branch mass flow rate is expected to be influenced by the pressure difference across the branch, ΔP , assuming that the flow is not choked, as,

$$\Delta P = P_1 - P_3, \quad (3.14)$$

where the inlet gas pressure is defined as P_1 and pressure at the branch outlet is P_3 . Single phase fluid flow through the branch, between boundary pressures P_1 and P_3 , is expected to incur losses attributed to friction, entrance effects, and mechanical fittings (Munson et al., 2002). Hassan et al. (1997) used hydraulic resistance, R , to quantify these losses as a control parameter defined as,

$$R = \frac{\sqrt{\Delta P}}{\dot{m}_{L3,OGE}}, \quad (3.15)$$

which is a ratio of the imposed boundary pressures, P_1 and P_3 , and the branch's single phase liquid mass flow rate at the OGE ($\dot{m}_{L3,OGE}$). The hydraulic resistance is passively controlled through selection of the connecting pipe length, diameter, and material.

The two-phase flow regime within a horizontal channel can be classified using the superficial velocities of each fluid phase. Under co-current flow conditions the inlet

liquid superficial velocity, V_{SL1} , becomes,

$$V_{SL1} = \frac{4(\dot{m}_{L2} + \dot{m}_{L3})}{\rho_L \pi D^2}, \quad (3.16)$$

where the inlet liquid mass flow rate in the numerator is defined through conservation of mass as a sum of the run and branch liquid mass flow rates, \dot{m}_{L2} and \dot{m}_{L3} , respectively. Similarly, the inlet gas superficial velocity, V_{SG1} , is defined using the run and branch mass gas mass flow rates as,

$$V_{SG1} = \frac{4\dot{m}_{G2} + \dot{m}_{G3}}{\rho_{G1} \pi D^2}. \quad (3.17)$$

The inlet gas density is defined as ρ_{G1} , the run gas mass flow rate as \dot{m}_{G2} , and the branch gas mass flow rate as \dot{m}_{G3} .

The six mass flow rates shown in Fig. 3.1, \dot{m}_{L1} , \dot{m}_{G1} , \dot{m}_{L2} , \dot{m}_{G2} , \dot{m}_{L3} , and \dot{m}_{G3} , are therefore reduced to the four parameters, \dot{m}_{TP3} , X_3 , V_{SL1} , and V_{SG1} . Maintaining R , P_1 and P_3 constant, the liquid height, H , can be varied and the corresponding branch and run mass flow rates recorded at each steady value of H .

3.3 Test Section

Dimensional analysis provided a reasonable guide to establishing the important parameters and geometric relations with respect to the CANDU header prototype. Some additional aspects need to be considered in the test section design, the constraints include:

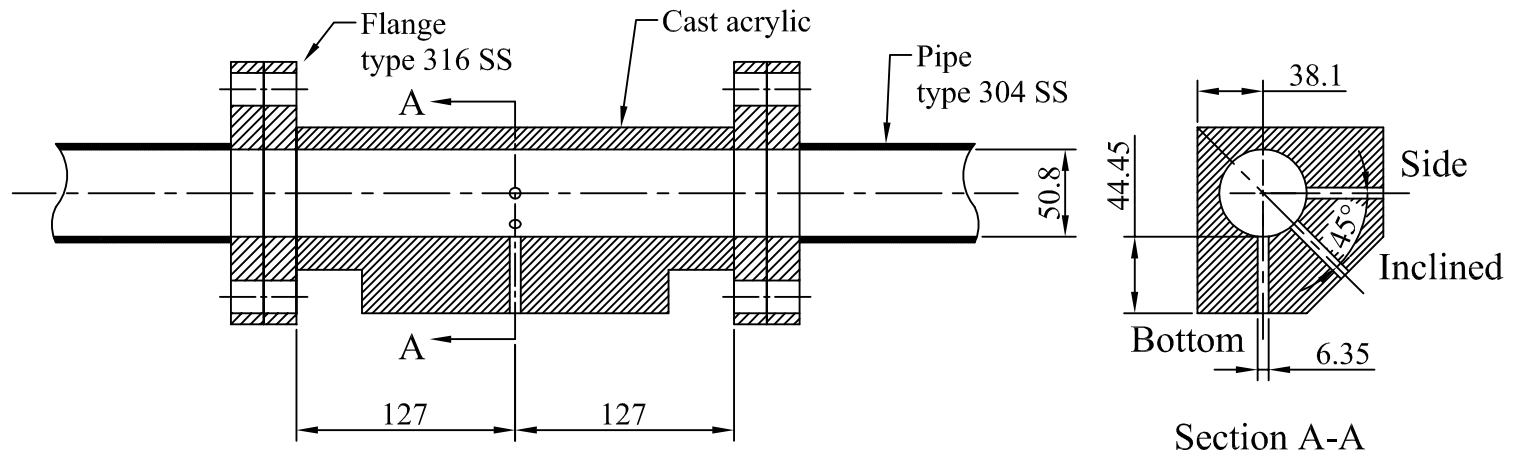
- Geometric and dynamic similarity to the prototype
- Flow visualization
- Pressurized system
- Control over mass flow rates in branch and inlet
- Flexibility of design and components

To achieve the desired branch Froude numbers the operating pressure needs to be high enough to overcome the pressure drop from the pipes, fittings, and accessories. According to the American Society of Mechanical Engineers (ASME) Pressure Vessel Code, strict design requirements and regulations are in place to assure safe operation of a pressurized device containing an expandable fluid. Section VIII - Division 1 of the ASME code outlines the rules for construction of a pressure vessel and outlines the material thickness requirements based on the operating pressure and geometry. Pressurized air is supplied from Concordia at up to 670 kPa. Increasing the design pressure to improve operational safety can lead to an increase in wall thickness, and consequently the trade off is a reduction in optical clarity. Digital imaging technologies, such as particle image velocimetry, rely on recording high resolution images of reflected light off of particles immersed within the fluid. Curved surfaces and fluid interfaces produce local light refractions and reflections, which can result in a loss of image quality. Refractive index matching can be used to reduce the effects of curved surfaces with the imaging path.

3.3.1 Design

The main technical constraints imposed on the test section design were dimensional similarity to the CANDU header-feeder bank problem under smooth-stratified conditions, operate with internal pressure, permit flow visualization, and be modular in construction. The pertinent design features of the test section are presented in Fig. 3.5. The design consists of two elements, the cast acrylic flow visualization test section, and commercially available standardized stainless-steel pipes connecting the acrylic section to the test facility flow loop. The connecting pipes were sized (D , L) based on geometric scaling. A cast acrylic rod (152.4 mm in diameter and 304.8 mm long) was used to produce the test section, as shown in Fig. 3.6. A 50.8 mm diameter hole (D) was machined through the length of the rod. Three 6.35 mm diameter holes were machined perpendicularly to the rod's longitudinal direction, at the mid-span, and penetrating into the larger diameter hole, as shown in Section A-A of Fig. 3.5. These three holes correspond to the three branch orientations shown in Fig. 3.1. The sides of the rod were then machined flat to reduce optical distortions that were expected as a result of the inner wall's relatively small radius of curvature. The cast acrylic material was chosen because its refractive index (1.48 to 1.5) was close to that of water (1.33). The material's mechanical properties were sufficient for handling the design stresses without losing the optical benefit to wall thickness requirements.

The minimum material thickness was estimated from the ASME Pressure Vessel Code using a design pressure rating of 1.05 MPa. Two commercially available stainless-steel flanges were then machined and installed at either end of the acrylic



All dimensions in *mm*

Figure 3.5: Test section.

part using five, 6.35 mm diameter, stainless-steel rods (not shown) connecting them together. Two face seals (O-rings) were installed between the flange and acrylic surface. The part was then thoroughly pressure tested under liquid-filled, and then gas-filled conditions up to 350 kPa (roughly 1/3 of the design limit). The maximum operating pressure was then set at 250 kPa to ensure safe operation, and a pressure relief valve was installed in the test facility to prevent pressurizing beyond this operating limit.

3.4 Test Facility and Flow Loop

A simplified schematic of the test facility is presented in Fig. 3.7 and a image of the facility is presented in Fig. 3.8. The test section was installed horizontally in the facility between two large stainless-steel TEE-shaped reservoirs. Water was stored in an open reservoir and delivered via a pump to the inlet-TEE. Pressurized air flowed through a pressure regulator into the inlet-TEE. A pneumatic feedback to the regulator provided continuous monitoring and control of the set point pressure, P_1 . The water flow rate was regulated using a combination of needle valve and globe valve installed in parallel at the pump outlet. The two fluids flowed co-currently through the test section and connecting pipes, each 1.8 m long, and into the outlet-TEE which acted as a gravity separator. The branch outlet was connected to a second gravity based two-phase flow separator, as shown in Fig. 3.9, that was maintained at pressure, P_3 . Measurements of the liquid height and static pressure were performed using differential pressure and static pressure transducers. The liquid height and pressure

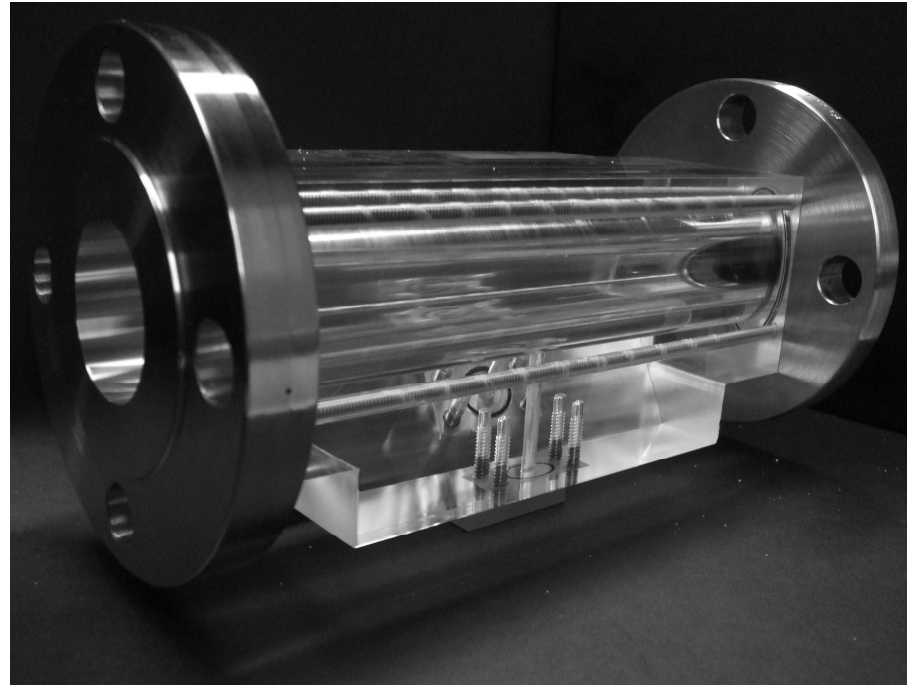


Figure 3.6: Manufactured test section.

measurements could be interchanged between a total of six different locations, λ , along the inlet and run. These distances are $\lambda = \pm 254$ mm, ± 889 mm, and ± 1800 mm. In Fig. 3.7 a single measurement point of H and P_1 is shown at $\lambda = -254$ mm for simplicity.

The branch separator shown in Fig. 3.9 was designed to divide a two-phase air-water mixture of mass flow rate \dot{m}_{TP3} into its constituent components. This was needed in order to measure the branch air and water mass flow rates, \dot{m}_{L3} and \dot{m}_{G3} , respectively. The air-water mixture entered through a hole machined in the top acrylic plate. The separated water stream flowed out through a hole in the bottom acrylic plate and the air stream flowed through a separate hole on the top acrylic plate. The air-water mixture impacted on the diffuser and baffle plates before impinging on the air-water interface. This was necessary in order to achieve a steady air-water interface. The inner, middle, and outer cylinder provided different levels of sensitivity on the liquid mass flow rate measurement. The outlet-TEE separator was a 100 mm diameter 1.5 m long vertical pipe made from stainless steel. A 100 mm to 50.8 mm reducing TEE was welded at its midspan to accommodate connection to the run pipe. Air flowed out through the top flange while water flowed out through the bottom flange. The liquid heights in the outlet-TEE and separator were monitored using sight levels, while the air and water flow rates were recorded using rotameters. A static pressure transducer was installed on the top acrylic plate of the branch separator to record P_3 .

3.5 Methodologies

Descriptions of the procedures, test cases and estimates of uncertainty are provided in detail in each experimental chapter. For example, Chapter 4 discusses two-phase flow in a single branch, Chapter 5 presents experiments conducted with two discharging branches, and Chapter 7 presents the development of a digital imaging technique for semi-empirical analysis.

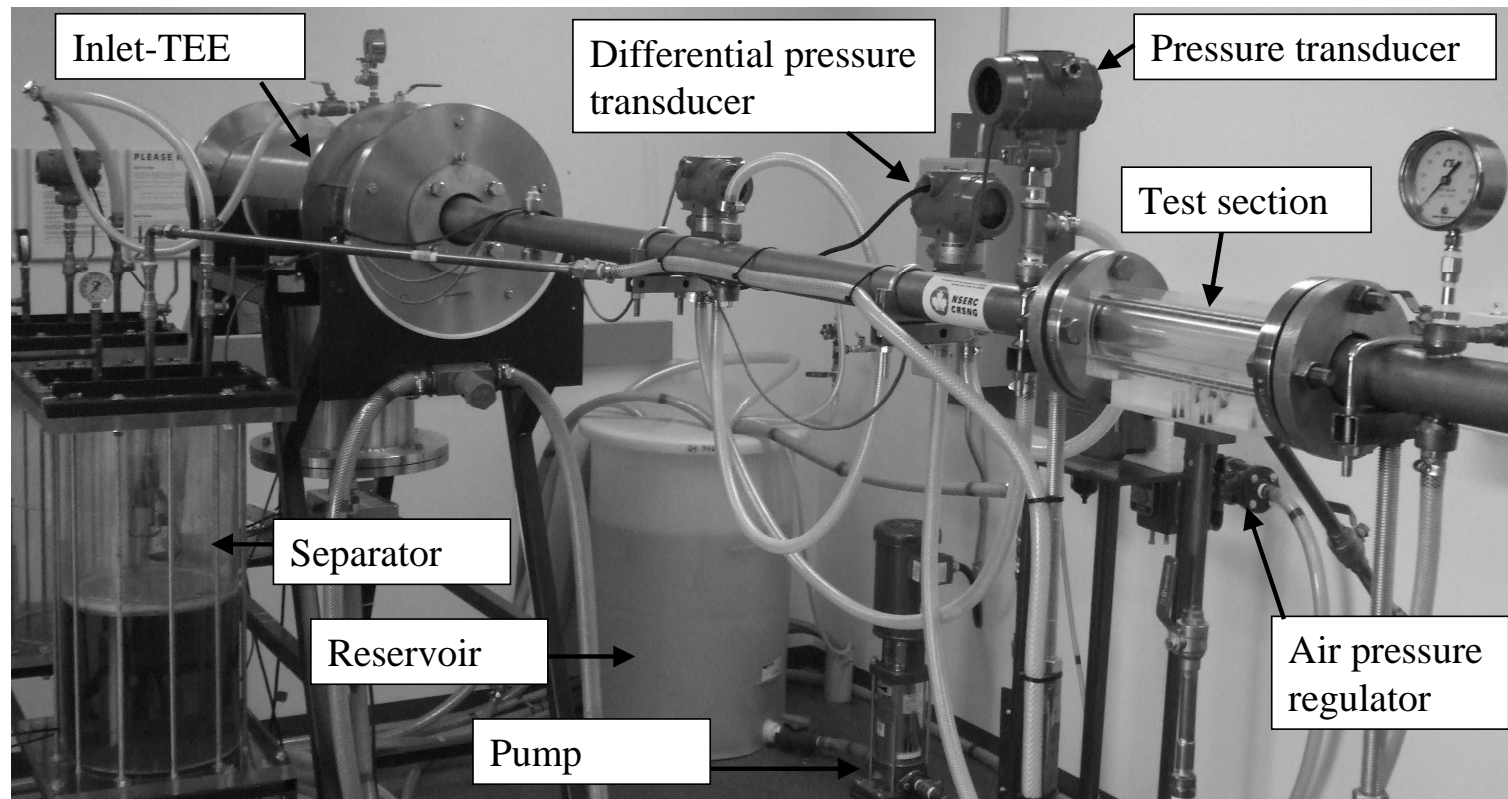


Figure 3.8: Experimental facility assembly.

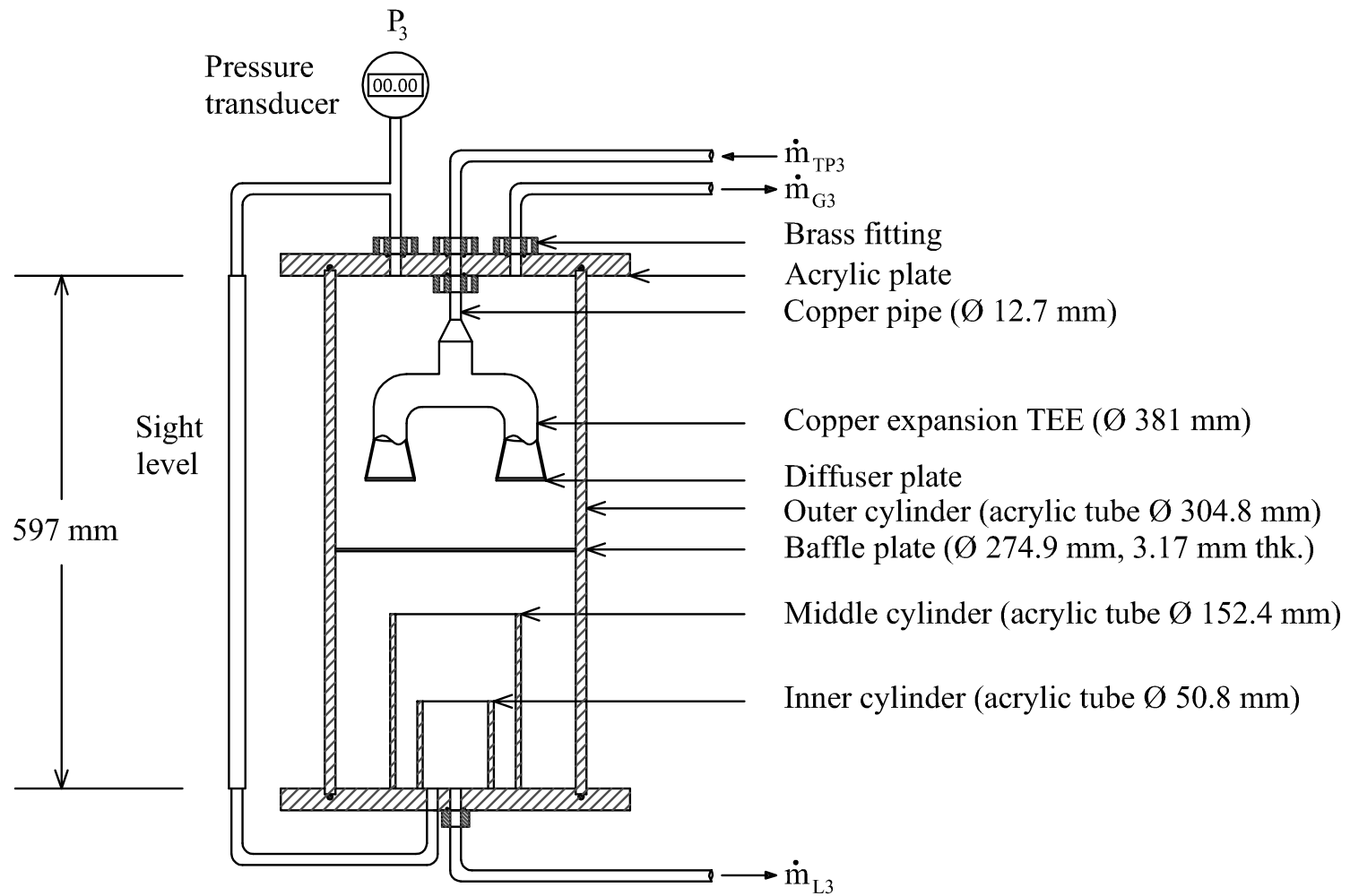


Figure 3.9: Schematic of the two-phase flow separator.

Chapter 4

Experiments with Co-current Stratified Gas-Liquid Flow in a Single Reduced T-Junction

4.1 Chapter Overview

In this chapter an experimental investigation of the two-phase distribution in side (0 degrees), inclined (45 degrees) and bottom (90 degrees) oriented branches under co-current two-phase stratified conditions are presented. The two-phase distribution, defined as the division of the gas and liquid streams between the inlet, branch and run, are reported as a function of the gas-liquid interface height at a well defined location upstream of the branch. The critical height at the onset of two-phase flow (OGE, OLE) is also reported under co-current stratified conditions. The results include descriptions of the branch two-phase mass flow rate and quality, inlet superficial

velocities of the gas and liquid phases, and description of encountered flow regimes as a function of the gas-liquid interface height.

4.2 Experimental Methodology

Air and water flowed co-currently from the inlet-TEE through the test section and connecting pipes, each 1.8 m long, and into the outlet-TEE, which acted as a fluid phase separator. Measurements of the liquid height, H , were performed using a digital differential pressure transducer at a distance of $\lambda/D = -5$, upstream of the branch. Digital pressure transducers were installed at P_1 and P_3 to measure the static pressure in the inlet and branch outlet, the latter of which emptied into an air-water separator. The water level in the outlet-TEE, and branch two-phase phase separator, were monitored using a sight level. The air and water volume flow rates were measured using rotameters.

Calibration of the hydraulic lines between the branch inlet and air-water separator was done to ensure that the hydraulic resistance for each branch (side/inclined/bottom) was the same. The hydraulic resistance of each branch was tested individually, with liquid only flowing in the branch. The relationship between the applied boundary pressures, $\Delta P = P_1 - P_3$, and branch liquid mass flow rate, \dot{m}_{L3} , shown in Fig.4.1 was best fit by,

$$\begin{aligned} \dot{m}_{L3} &= 0.028(\Delta P)^{0.52} \dots (kg/s), \\ 6.2 &\leq \Delta P \leq 91.2 \dots (kPa). \end{aligned} \tag{4.1}$$

From this calibration, the average hydraulic resistance, following Eq. (3.15), was calculated as $R = 1032 (kg - m)^{-1/2}$ with a spread of $50 (kg - m)^{-1/2}$.

Flow visualization was enhanced by digital imaging, and a 3-CCD (charge coupled device) Sony progressive scan digital camera, with 640×3480 pixel resolution, coupled with an objective lens was used. The camera output was connected to a National Instruments image acquisition module and an in house LabVIEW code was used to control the acquisition and storing of the images. The camera was arranged such that the CCD plane was parallel to the flat vertical side of the test section, and a small quantity of blue tracer dye was added to the water to enhance visualization.

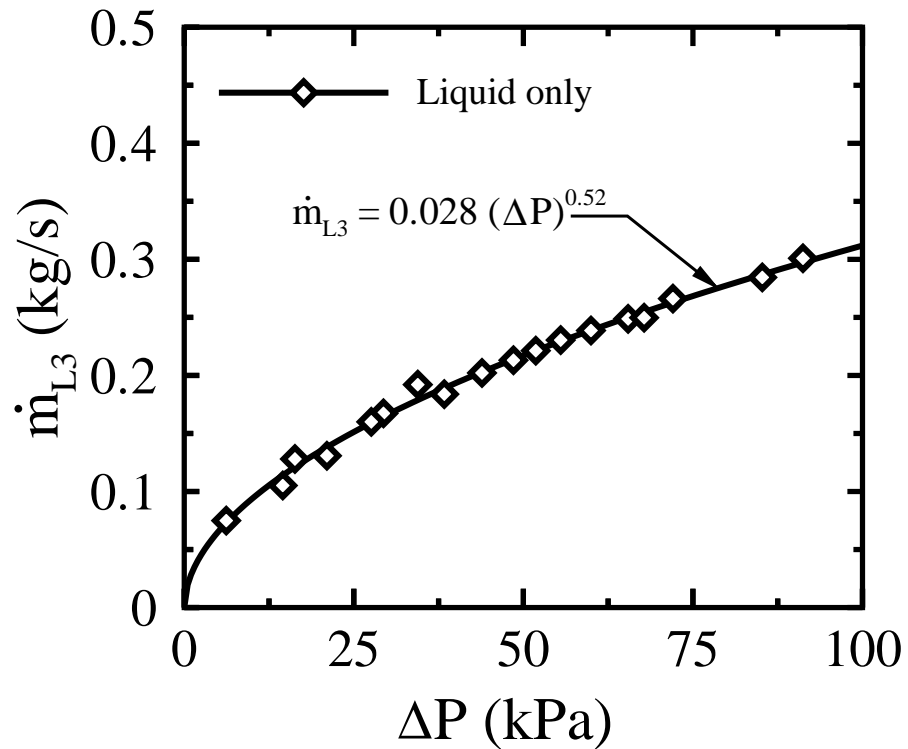


Figure 4.1: Calibration of branch hydraulic lines.

4.2.1 Procedures

Stratified Co-current Air-water Flow

Water was first added to the inlet-TEE until the outlet-TEE was filled to the same level. This starting water level resulted in the horizontal pipe being half-full, with approximately $H/D = 0.5$, and a flat horizontal air-water interface between the inlet-TEE and outlet-TEE. With all rotameter valves closed, air was added to the system through the inlet-TEE to a static set-point pressure of P_1 . Air and water were then permitted to flow out through the outlet-TEE by opening the rotameter valves at \dot{m}_{L2} and \dot{m}_{G2} . This caused the water level in the outlet-TEE to decrease below the initial level, and consequently water began to flow from the inlet-TEE towards the outlet-TEE, within the horizontal pipe. The water level in the outlet-TEE was permitted to drop well below the horizontal pipe level so that its air-water interface was separated from the stream of water being supplied by the run. Water was then supplied to the system, through adjustment of the needle valve connected between the pump and the inlet-TEE, in order to compensate for the outflow of water through the outlet-TEE. Steady-state was achieved when the water level in the outlet-TEE, the liquid height, H , and pressure P_1 were observed to be constant. The value of H could be controlled by adjusting the amount of water supplied to the inlet-TEE.

Two cases were tested in Table 4.1 in order to demonstrate the effect of the gas phase on the liquid phase in cases without branch flow. This was done in order to establish a benchmark to which the active branch experiments could be compared to. These cases are designated as SS-1 and SS-2. In the first case the gas phase is in

the laminar regime and in the second case it is turbulent following the methodology outlined by Taitel and Dukler (1976) which uses the local phase averaged velocities and hydraulic diameters to determine the local gas and liquid Reynolds numbers. In all cases the local liquid Reynolds numbers were found to be in the turbulent regime.

Two-phase Branch Flow

With stratified co-current air water flow established, and H steady at a desired initial value, the separator was pressurized so that P_3 was the same as P_1 . The ball valve between the separator and branch inlet was then opened, and P_3 was slowly decreased by allowing air to flow through the gas rotameter (\dot{m}_{G3}). This decrease in the separator pressure subsequently caused flow, typically a two-phase mixture, to enter into the branch. To maintain the liquid level within the separator water was permitted to flow out through the liquid rotameter (\dot{m}_{L3}), while at the same time the liquid level in the outlet-TEE was maintained by adjusting \dot{m}_{L2} . The separator pressure was slowly decreased, and all subsequent flow rates adjusted continuously, until the desired pressure difference, ΔP , was reached. The liquid levels in the outlet-TEE and separator were maintained by adjusting the various flow rates (branch and run) until steady-state was achieved. The branch air-water separator was considered steady when P_3 and its water level observed through the sight level were constant. The mass flow rates of all streams, pressure drop, and inlet height were then recorded (\dot{m}_{G3} , \dot{m}_{L3} , H , P_1 , P_3 , \dot{m}_{L2} , \dot{m}_{G2}). Once the desired value of ΔP was achieved, H could be varied by changing the quantity of water supplied to the system through adjustment of the needle valve between the pump and inlet-TEE. The change in H

was typically around 0.5 to 1 mm, and then all steady-state quantities were recorded. A total of seven cases were tested with two-phase branch flow, as shown in Table 4.2, one with the side branch (SB-1), three with the inclined branch (IB-1, IB-2, IB-3), and three with the bottom branch (BB-1, BB-2, BB-3).

Onsets of Gas and Liquid Entrainment

The procedure to record the critical heights at the onset of gas entrainment is similar to the one described above for two phase branch flow, however, the branch is connected directly to a rotameter rather than through the separator, which enables much simpler control of the facility. This was done because at the critical conditions (OGE, OLE) the branch flow can be considered single phase. The branch liquid flow rate (\dot{m}_{L3}) was then slowly increased to the desired test value. The interface height was then slowly decreased, by reducing \dot{m}_{L1} , until a small steady stream of air could be seen to entrain into the branch at the OGE. The mass flow rates of all streams, and the water height were then recorded (\dot{m}_{L3} , H , P_1 , \dot{m}_{L2} , \dot{m}_{G2}).

4.2.2 Test Matrix

Experiments without any branch flow are summarized in Table 4.1 and for active branch experiments in Table 4.2. The experiments were performed at room temperature, at approximately 20 to 23 degrees Celsius, using air and water as the two fluid phases. The experiments scanned the maximum and minimum allowable values of H in order to maintain a smooth-stratified flow regime in the inlet. As will be seen, the upper limit of H is defined by either the onset of gas entrainment or a flow regime

Table 4.1: Test matrix for experiments without an active branch.

Case	Description	P_1 (kPa)	λ/D	V_{SG1} (m/s)
SS-1	Laminar Gas - Turbulent Liquid	206	-5, -36	0.3
SS-2	Turbulent Gas - Turbulent Liquid	206	-5, -36	1

transition. The lower limit is defined by dry-out, or the onset of liquid entrainment. The term ‘dry-out’ refers to a reduction in the run water mass flow rate to the point that it could not be measured accurately. For the co-current two-phase experiments listed in Table 4.1 the run gas flow rate was maintained constant so that $V_{SG1} = 0.3$ m/s in case SS-1, and $V_{SG1} = 1$ m/s in case SS-2. The air density was determined by treating it as an ideal gas operating at $P_1 = 206$ kPa. For the three branch orientations (side, inclined, bottom) in Table 4.2, three values of ΔP were tested, these are 34.47 kPa, 51.71 kPa and 68.94 kPa, respectively. The run gas mass flow rate, \dot{m}_{G2} , was maintained constant at 0.0022 kg/s in all cases so that at the OGE, $V_{SG1} = 0.3$ m/s.

Table 4.2: Test matrix for experiments with an active branch.

Case	Description	P_1 (kPa)	ΔP (kPa)	R (kg - m) ^{-1/2}	λ/D	\dot{m}_{G2} (kg/s)
SB-1	Side		34.47	1052		
IB-1	Inclined		34.47	1052		
IB-2	Inclined		51.71	1044		
IB-3	Inclined	206	68.94	1038	-5	0.0022
BB-1	Bottom		34.47	1052		
BB-2	Bottom		51.71	1044		
BB-3	Bottom		68.94	1038		

4.2.3 Estimates of Uncertainty

Experimental uncertainties were evaluated following the methodology outlined by Kline and McClintock (1953) at odds of 20:1 and include both precision and bias estimates. The allowable operating pressure deviation for P_1 was 6.8 kPa and for ΔP was approximately 0.4 kPa, with an instrument uncertainty of 0.83 kPa. The inlet gas density, ρ_{G1} , is calculated to be 3.66 kg/m^3 with an estimated uncertainty of 3.8%. The instrument uncertainty in measuring the liquid height was 0.165 mm, while the uncertainty in the critical heights was estimated as 1 mm. The uncertainty of the air and water flow rates in the branch and run were found to be dominated by level fluctuations in the separator and outlet-TEE combined with the rotameter uncertainty used in the measurement. A bank of rotameters was used in order to have the ability to scan a variety of flow rate ranges. In total, four liquid and four gas rotameters were employed to measure the run flow rates, and five liquid and five gas rotameters were used to measure the branch flow rates. The rotameter instrument errors ranged between 2% and 10% of the full scale value. The uncertainty in the inlet superficial liquid velocity was estimated as 14%, while that of the inlet gas velocity was estimated as 29%. The uncertainty of the branch two-phase mass flow rate was estimated as 22%, and the two-phase branch quality as 38%. The uncertainty in the Froude number with air as the working fluid was estimated to be 11%, while with water as a working fluid the uncertainty was estimated as 5%.

4.3 Results and Discussion

Measurements of the two-phase quantities in the three branch orientations (side, inclined, bottom) were conducted. The results are presented in order to demonstrate the relationship between the two-phase mass distribution (V_{SL1} , V_{SG1} , \dot{m}_{TP3} , X_3) and the interface height, H . It is generally expected that \dot{m}_{TP3} will decrease with decreasing H , between H_{OGE} and H_{OLE} , while accompanied by an increase in the branch quality X_3 . In effect the portion of gas in the total two-phase mass flow rate, \dot{m}_{G3} , increases with decreasing H . One of the consequences of this increase in \dot{m}_{G3} , however, is that the inlet gas superficial velocity increases, since \dot{m}_{G2} is constant, which lead to transition from the smooth-stratified regime to wavy or slug regimes in some instances.

4.3.1 Co-current Air-water Flow without an Active Branch

The results obtained from cases SS-1 and SS-2 are presented in Fig. 4.2 in order to demonstrate the effect of the superficial gas velocity, V_{SG1} , on the superficial liquid velocity, V_{SL1} , and two-phase regime transitions. The liquid level was presented at two distinct locations, $\lambda/D = -5$ and -36 , in order to demonstrate the effect of interfacial gradients within the inlet on H . In both cases as H increases V_{SL1} is shown to increase. In addition, each case shows that H decreases along the length of the inlet. This can be seen by comparing H at the measurement point furthest from the branch ($\lambda/D = -36$) with that closest to the branch ($\lambda/D = -5$). Comparing case SS-1 and SS-2, it is shown that increasing V_{SG1} from 0.3 to 0.1 m/s did not

lead to a substantial increase in V_{SL1} , a difference of less than 6%. This indicates that interfacial shear induced by the gas phase did not dramatically impact the liquid flow rate. In fact in separate tests decreasing V_{SG1} well below 0.3 m/s showed no substantial effect on V_{SL1} . The inlet air-water interface was visibly smooth over the recorded range of H , between the lower limit (dry-out) and the upper limit (two-phase regime transition). In the case of SS-1 the interface remained relatively smooth until around $H/D = 0.57$ ($\lambda/D = -5$), at which point a fast moving slug was observed to propagate from the inlet-TEE towards the outlet-TEE. On the other hand in case SS-2 the air-water interface was observed to become wavy at the upper limit, at $H/D = 0.46$ ($\lambda/D = -5$).

In general, V_{SG1} could be increased at any H to achieve a flow regime transition from smooth to wavy or slug regimes. Figure 4.3 shows the temporal development of waves, flowing from the inlet to the run. The size and frequency of these waves was observed to vary according to H and V_{SG1} . It was observed that small amplitude, higher frequency, waves typically occurred at lower values of H , with relatively high values of V_{SG1} . On the other hand, larger amplitude, shorter frequency, waves were observed at higher values of H , and lower values of V_{SG1} . In some instances the wave amplitude grew sufficiently as to touch the top of the pipe which immediately caused a slug to propagate through the system, as shown in Fig. 4.4. These transient flow regimes caused uncontrollably high fluctuations of the liquid level in the outlet-TEE, and consequently, it was not possible to accurately measure the gas and liquid flow rates within the run. The inlet transition regime was therefore estimated based on the superficial gas and liquid velocities just prior to wave formation, and are presented in

Fig. 4.5 as a dashed line on the two-phase flow regime map developed by Mandhane et al. (1974). The observed smooth-stratified regime is well represented by the regime boundaries described in Mandhane et al. (1974)'s two-phase regime map. Case SS-1 demonstrated that the smooth-stratified regime could be maintained over a larger range of H than case SS-2. Decreasing V_{SG1} below 0.3 m/s ($\dot{m}_{G2} = 0.0022$ kg/s) did not dramatically affect the maximum upper limit of H since slug flow was encountered without noticeable wave formation. As a result, $\dot{m}_{G2} = 0.0022$ kg/s was chosen as a condition for all the active branch experiments listed in Table 4.2.

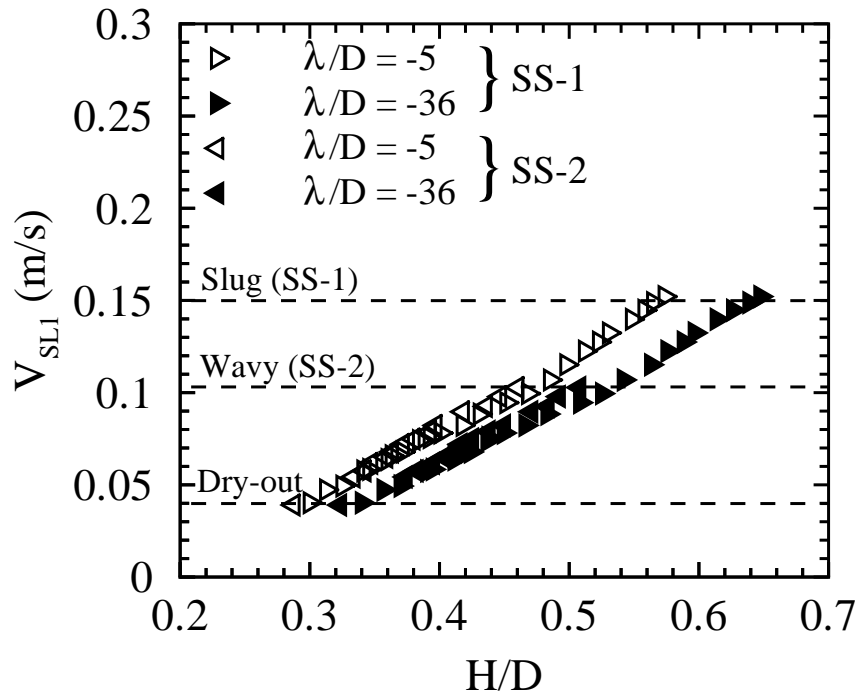


Figure 4.2: Inlet conditions during co-current air-water flow in the horizontal pipe.

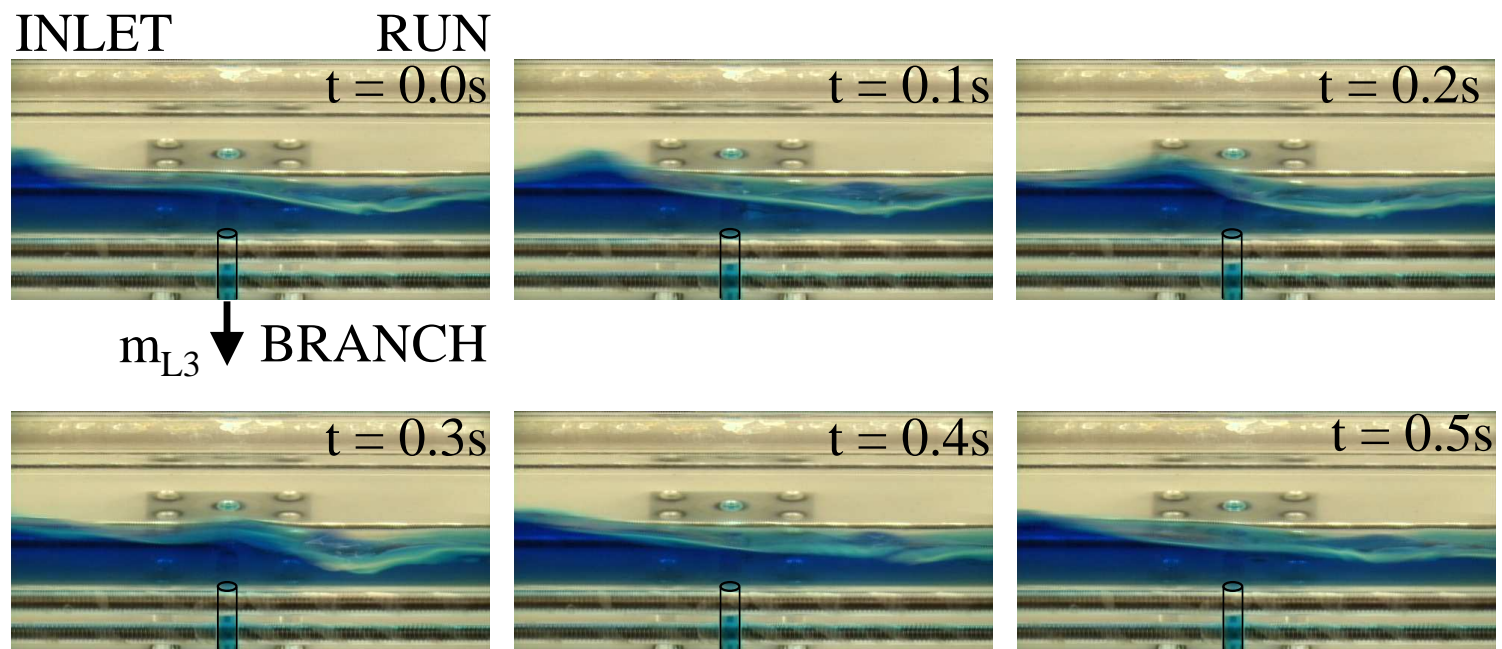


Figure 4.3: Wave propagation during gas entrainment in the bottom branch.

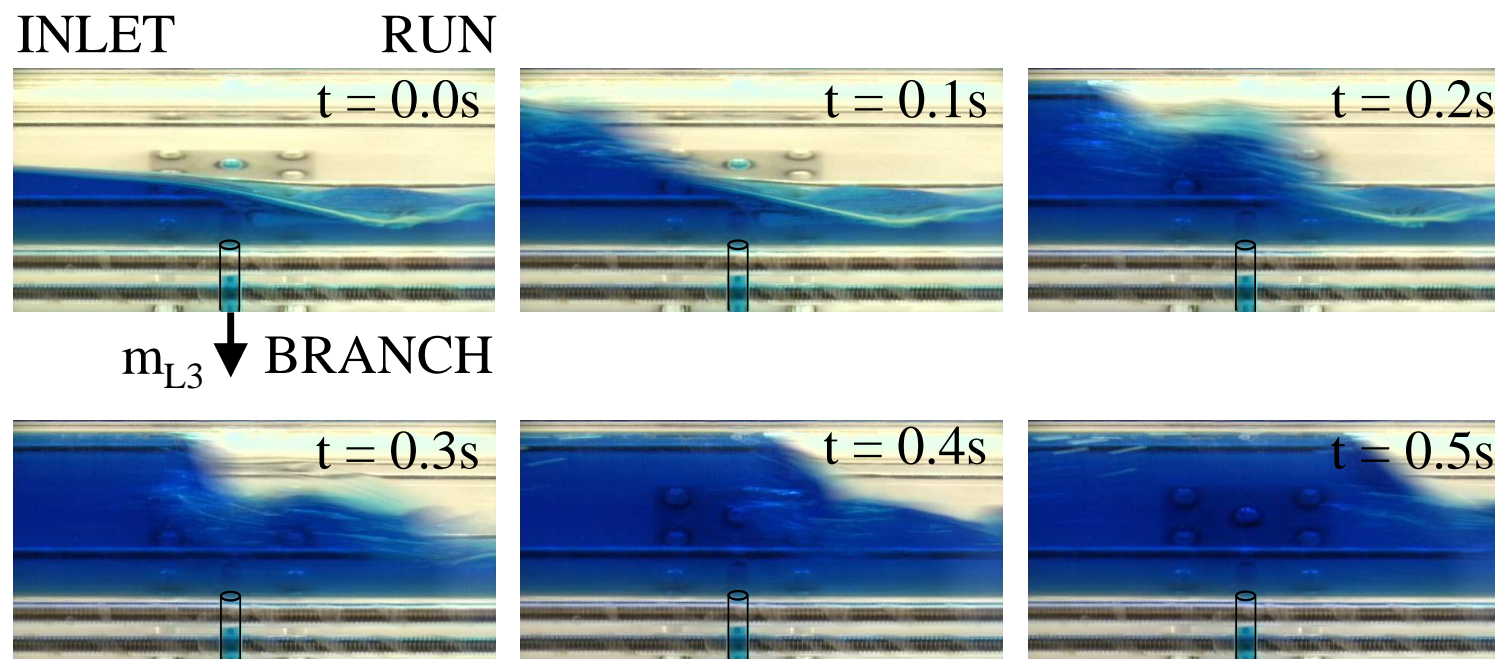


Figure 4.4: Slug development during gas entrainment in the bottom branch.

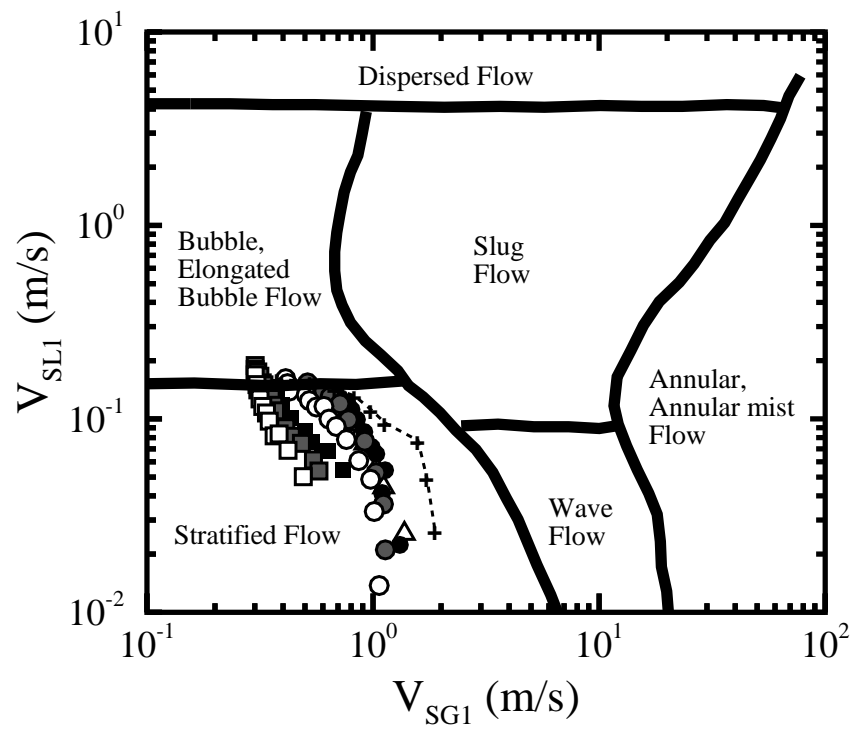


Figure 4.5: Observed inlet regime as compared with Mandhane et al. (1974)'s map.

4.3.2 Bottom Branch

The images presented in Fig. 4.6 show the typical development of the gas entrainment flow structure in the bottom branch. In Fig. 4.6(a) the image depicts the formation of a steady dip in the air-water interface to the right of the branch. The dip is forced downstream (to the right in the image) by the momentum of the inlet liquid flow. By contrast, images of the same phenomenon in a stagnant reservoir demonstrated that the steady dip was almost directly above the branch (Saleh et al., 2009). Slowly increasing the branch mass flow rate caused the air to entrain into the branch, as shown in Fig. 4.6(b). Initially the air entrainment was observed to be transient as the dip experienced a sudden collapse into the branch, and then quickly reformed, but eventually began to steadily entrain. The steady entrainment of air in Fig. 4.6b is characterized as the onset of gas entrainment.

Critical Height

The critical height at the OGE in the bottom branch is presented in Fig. 4.7 as a function of the branch single phase liquid Froude number, Fr_d . In Fig. 4.7(a), the interface was smooth-stratified between the lower dry-out limit, around $H/D = 0.16$, and the upper limit, around $H/D = 0.6$, where slug flow was observed. The inlet conditions are presented in Fig. 4.7(b), with V_{SG1} constant at 0.3 m/s, along with data from case SS-1. The slug regime is encountered at approximately the same interface height, however at a higher value of V_{SL1} . The increase in V_{SL1} is particularly evident where $H/D > 0.4$ and is shown to be up to 20% higher than that of SS-1. Since

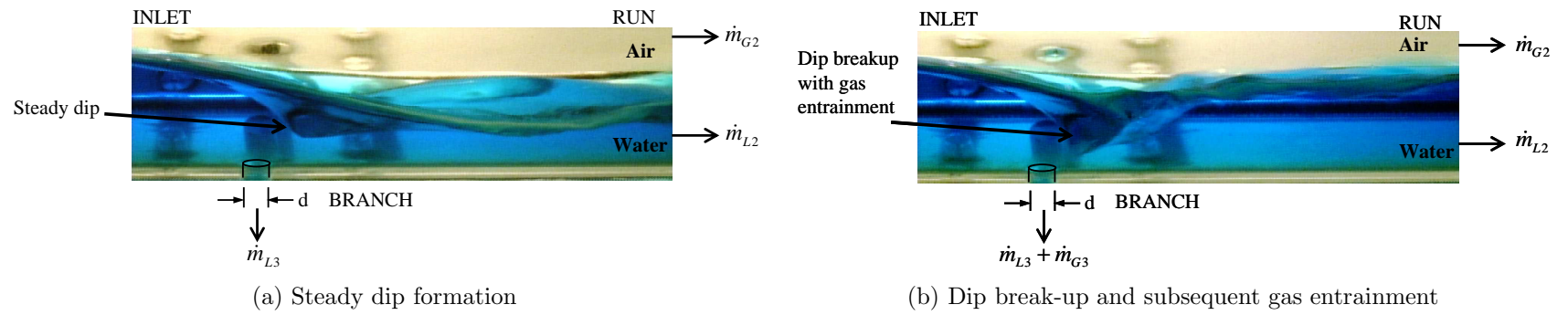


Figure 4.6: Flow visualization of the onset of gas entrainment in the bottom branch.

V_{SG1} is expected to have negligible influence on V_{SL1} , according to Fig. 4.2, the increase in the inlet liquid superficial velocity is attributed primarily to the branch flow. The ratio between the run and branch liquid mass fluxes, $\rho_L V_{SL2}/\rho_L V_{L3}$, is presented in Fig. 4.8. The branch mass flux at the OGE is approximately two orders of magnitude larger than that of the run, and is consistent with Smoglie and Reimann (1986)'s findings. A correlation was developed for the critical height, H_{OGE} , based on Fr_d , as,

$$\frac{H_{OGE}}{D} = 0.134 Fr_d^{0.45}, \quad (4.2)$$

$$\lambda/D = -5.$$

The critical height is compared in Fig. 4.9 with a variety of studies conducted using bottom oriented branches. In this figure the critical height is non-dimensionalized using the branch diameter, d , rather than the pipe diameter, D . These include data obtained in stagnant two-phase reservoirs with test sections in geometrical similarity to the present study (Ahmad and Hassan, 2006; Hassan et al., 1997), correlations developed from liquid-liquid experiments in a quasi-steady draining experiment (Lubin and Springer, 1967), and correlations in horizontal channels (Kowalski and Krishnan, 1987; Smoglie and Reimann, 1986; Schrock et al., 1986; Yonomoto and Tasaka, 1991; Maciaszek and Micaelli, 1990). The best agreement is found with Smoglie and Reimann (1986) and Schrock et al. (1986)'s correlations. The stagnant reservoir studies demonstrate that for the same value of H_{OGE} a substantially higher value of Fr_d is needed to achieve the OGE. In theoretical studies, the criterion for the OGE has been characterized using the total kinetic energy at the lowest point of the dip (Ahmed

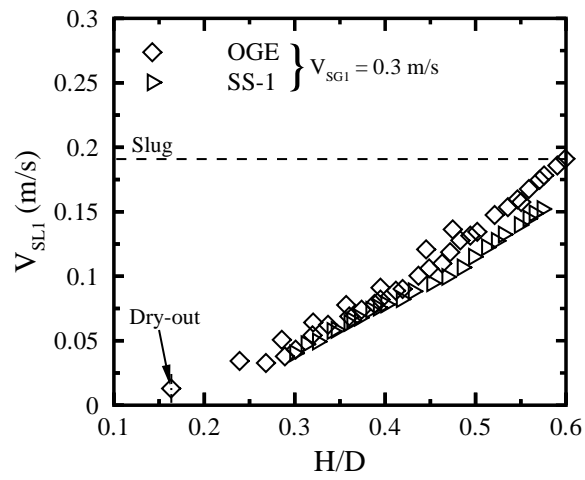
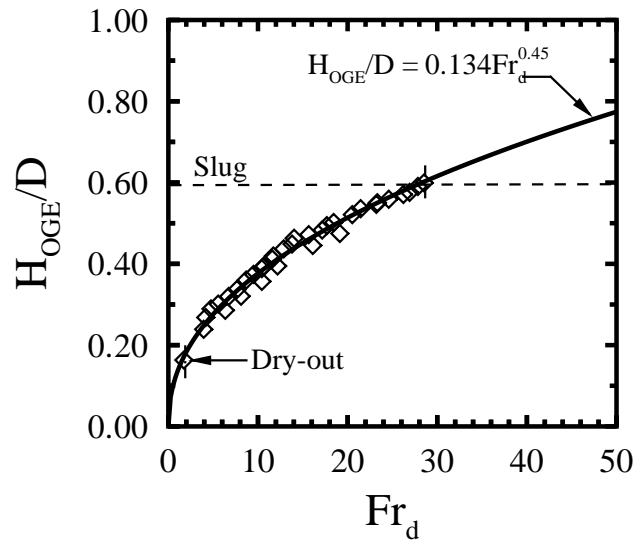


Figure 4.7: Critical conditions at the onset of gas entrainment in the bottom branch at $\lambda/D = -5$.

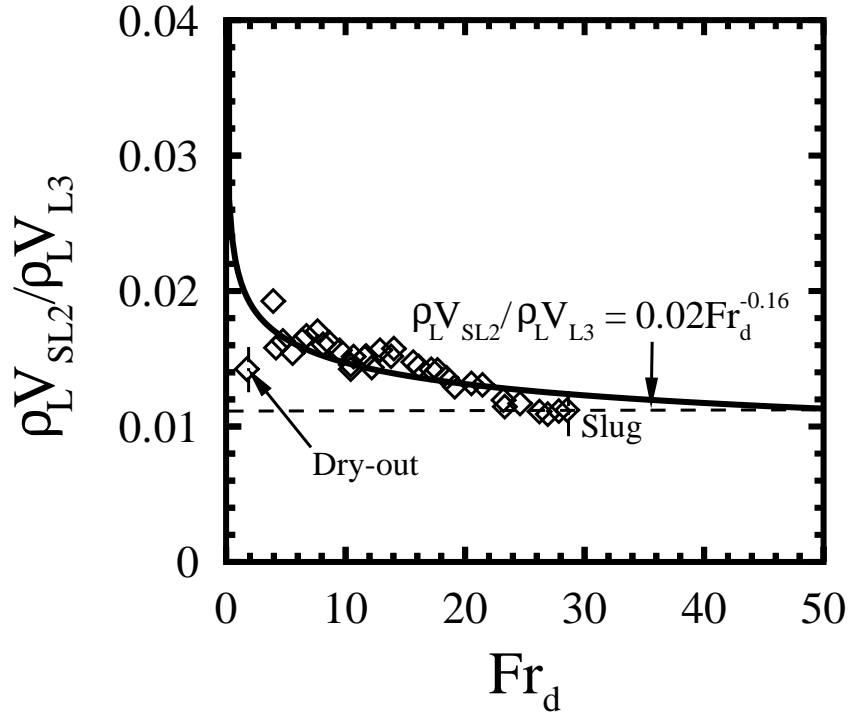


Figure 4.8: Critical liquid flow distribution between the bottom branch and run.

et al., 2003; Andaleeb et al., 2006). With co-currently flowing phases of gas and liquid, the total kinetic energy at the dip is found as summation of contributions from the branch and run (Bowden and Hassan, 2009). Therefore, the branch's contribution to the total kinetic energy at the dip can be lower than the stagnant reservoir case at the OGE. The remaining correlations show very poor agreement with the present data which may be due to the measurement location, λ/D of H_{OGE} . As seen in Fig. 4.6, measurement of the interface height near the branch can be greatly affected by the OGE flow structure, as the dip interface height can be dramatically lower than the inlet height.

Multiplying $\rho_L V_{SL2} / \rho_L V_{L3}$ by the geometric ratio D^2/d^2 , the ratio of mass flow rates between the run and branch, $\dot{m}_{L2} / \dot{m}_{L3}$, is obtained. This ratio shows that

the branch accounts for between 50 to 60% of the total inlet liquid flow rate. The relatively high portion of the liquid flow diverted into the branch, and the branch flow's high velocity compared to the run flow, helps to explain the observed increase in V_{SL1} over case SS-1 data in Fig. 4.7(b). A correlation was provided that can be used to determine the liquid flow distribution between the branch and run as,

$$\frac{\rho_L V_{SL2}}{\rho_L V_{L3}} = 0.02 Fr_d^{-0.16}$$

$$2 \leq Fr_d \leq 30 \quad (4.3)$$

$$\frac{\lambda}{D} = -5.$$

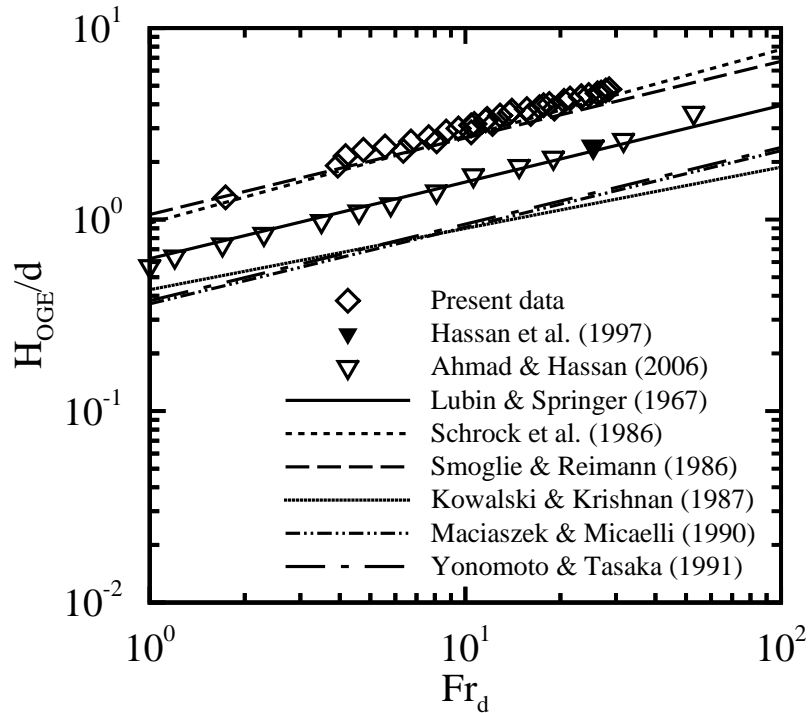


Figure 4.9: Critical conditions at the onset of gas entrainment in the bottom branch.

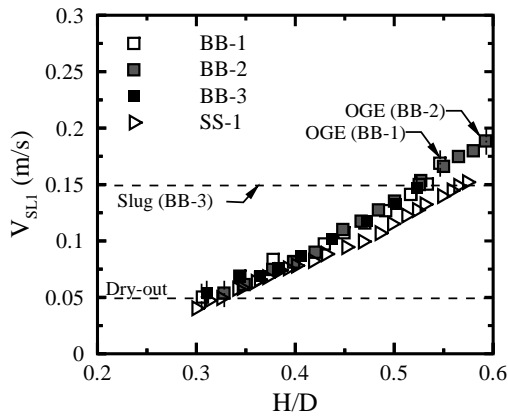
Similar to case SS-1 and SS-2 if V_{SG1} is increased sufficiently the smooth-stratified regime can become wavy, or slugging can occur. Interestingly, with each passing wave or slug the gas entrainment flow structure shown in Fig. 4.6 would dissipate and then reform. The images of the wavy and slug regimes in Fig. 4.3 and 4.4, respectively, were taken with the OGE in the bottom branch to demonstrate this point. The OGE flow structure described in Fig. 4.6(a) is found in the first image of Fig. 4.3 and 4.4, at $t = 0.0$ s. In Fig. 4.3 as a wave approaches the branch ($t = 0.1$ and 0.2 s) the OGE dip slowly begins to recede upwards until the wave is close to the branch ($t = 0.3$ s) subsequently the dip and wave interact and dissipate, as shown at $t = 0.4$ s. At $t = 0.5$ s a new wave begins to form at the left of the image, while the OGE dip also begins to reform in the air-water interface. In Fig. 4.3 the air-water interface within the inlet, to the left of the steady OGE dip at $t = 0.0$ s, is shown to be smooth. A sudden slug forms within the inlet and quickly propagates towards the OGE dip ($t = 0.1$ s). The OGE dip is immediately dissipated as it is impacted by the fast moving slug ($t = 0.2$ s), and then the pipe becomes full behind the slug face ($t = 0.3$ s to 0.5 s). Once the slug completely passes the branch the OGE flow structure observed at $t = 0.0$ s gradually reforms as steady conditions are re-established.

Two-phase Branch Mass Flow Rate and Quality

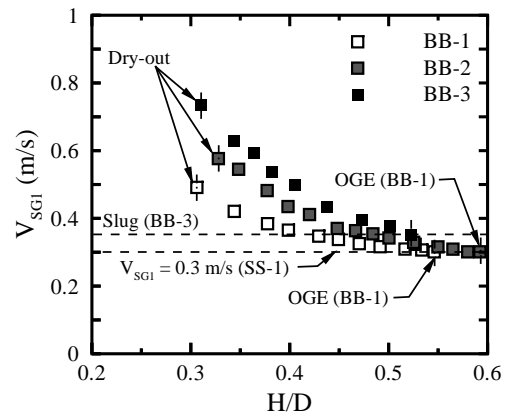
Below H_{OGE} a two-phase mixture of air and water flows in the branch. The two-phase flow distribution at the inlet and branch are presented in Fig. 4.10 as a function of the liquid height, H , at $\lambda/D = -5$ and pressure drop, ΔP . Sketches of the observed flow structure with decreasing H below H_{OGE} , and constant ΔP , specifically the air-spout

relative to the branch, are presented in Fig. 4.11. The beginning of gas entrainment is shown in Fig. 4.11(a), with two-phase branch flow in Fig. 4.11(b) and (c). No appreciable difference in V_{SL1} over the three pressure drops is found in Fig. 4.10(a), however an overall increase is found when compared to case SS-1. As H decreases below H_{OGE} , V_{SG1} increases due to the inception of air into the branch, as shown in Fig. 4.10(b). Increasing V_{SG1} has shown however to cause flow regime transitions in cases SS-1 and SS-2, and in the case of BB-3 the slug regime was encountered well below H_{OGE} with a value of approximately $V_{SG1} = 0.35$ m/s. In this case the slug was initiated due to wave formation in the inlet region. The onset of gas entrainment corresponds to $X_3 = 0$ in Fig. 4.10(d). The relationship between the interface height and the branch two-phase mass flow rate and quality are shown in Fig. 4.10(c) and 4.10(d), respectively. As H decreases below H_{OGE} the two-phase mass flow rate decreases due to the increased amount of air entrained into the branch, which can be observed by the increase of X_3 . It was observed that as H decreased, the air spout increased in size, as shown in Fig. 4.11(a) to (c). This effectively increased the air flow area at the branch inlet while decreasing the water flow area. The higher air flow area at the branch inlet helped to promote a higher mass of air to flow into the branch and is why the decrease in the two-phase mass flow rate with H is accompanied by an increase in the flow quality.

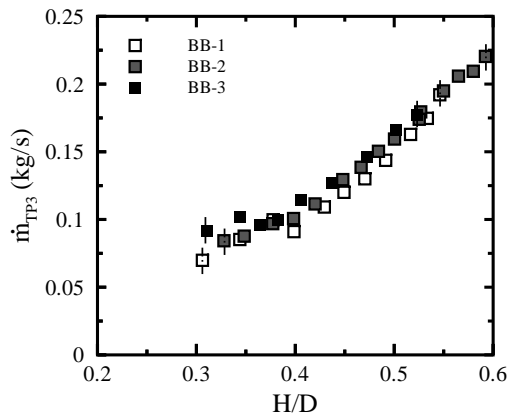
The inlet and branch two-phase quantities are presented in relation to the interface height, H at $\lambda/D = -5$. Since an interfacial liquid gradient exists along the inlet, according to Fig. 4.2, this makes it difficult to compare the absolute values of H and X_3 with other studies. By non-dimensionalizing H with the critical height at the



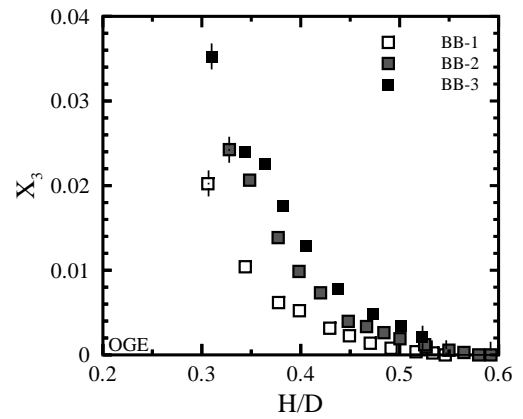
(a) Inlet superficial liquid velocity



(b) Inlet superficial gas velocity



(c) Branch two-phase mass flow rate



(d) Branch quality

Figure 4.10: Two-phase distribution at the bottom branch in relation to the interface height at $\lambda/D = -5$.

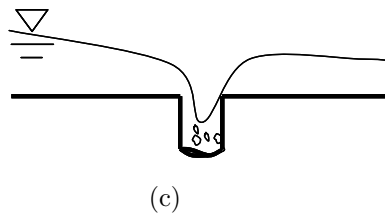
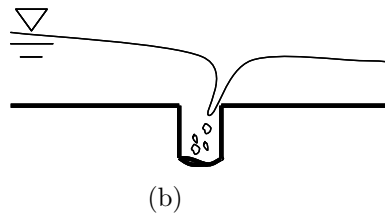
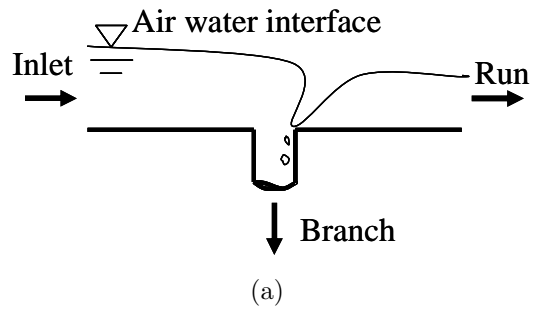


Figure 4.11: Sketches of observed air spout development during two-phase flow in the bottom branch with decreasing interface height from (a) to (c).

OGE as,

$$H^+ = \frac{H}{H_{OGE}}, \quad (4.4)$$

the measured values of X_3 have been shown to collapse together (Smoglie and Reimann, 1986; Hassan et al., 1997). For cases BB-1 and BB-2 the critical height can be found directly from Fig. 4.10, whereas H_{OGE} for case BB-3 was not achieved due to the regime transition from smooth-stratified to slug flow. This can be remedied using the relationship developed from the separator calibration in Eq. (4.1) along with the critical height relationship developed in Eq. (4.2) to estimate the anticipated value of H_{OGE} . At $\Delta P = 68.94$ kPa the corresponding value of \dot{m}_{L3} is 0.253 kg/s, which results in $Fr_d = 32$. Using Eq. (4.2) at $Fr_d = 32$, the expected value of H_{OGE} is found to be 32.1 mm.

The branch quality is presented in Fig. 4.12 as a function of the dimensionless height, H^+ . The effect of ΔP is dissipated when H is scaled with H_{OGE} , and the values of X_3 collapse together at each corresponding value of H^+ . Interestingly, the results were found to agree well with Smoglie and Reimann (1986)'s correlation, even though there are stark differences between the length scales used in the two studies ($L/D, d/D, \lambda/D$). Comparison with Hassan et al. (1997) showed that X_3 is approximately 40 to 50% lower in the region where $0.5 < H^+ < 0.7$. This may be attributed the size and shape of the air spout at the branch inlet. The sketches in Fig. 4.11(a) and (b) show that the liquid flow area at the branch inlet is much larger than that of the gas phase. This is because the air spout, due to the momentum of the inlet liquid flow, was squeezed against the side of the branch. This caused the gas flow

area at the branch inlet to be reduced, and helps to explain why a lower two-phase quality was found. In the lower ranges of H^+ the momentum of the inlet liquid phase decreases, and the air spout is nearly symmetric about the branch, as shown in Fig. 4.11(c). In stagnant reservoir studies the air spout has been described as symmetrical about the branch inlet (Hassan et al., 1997). The similarity in flow structures, the symmetrical air spout, and the fact that the inlet liquid velocity approaches the stagnant case, helps to explain why Hassan et al. (1997)'s data begins to approach Smogle and Reimann (1986)'s correlation where $H^+ < 0.3$.

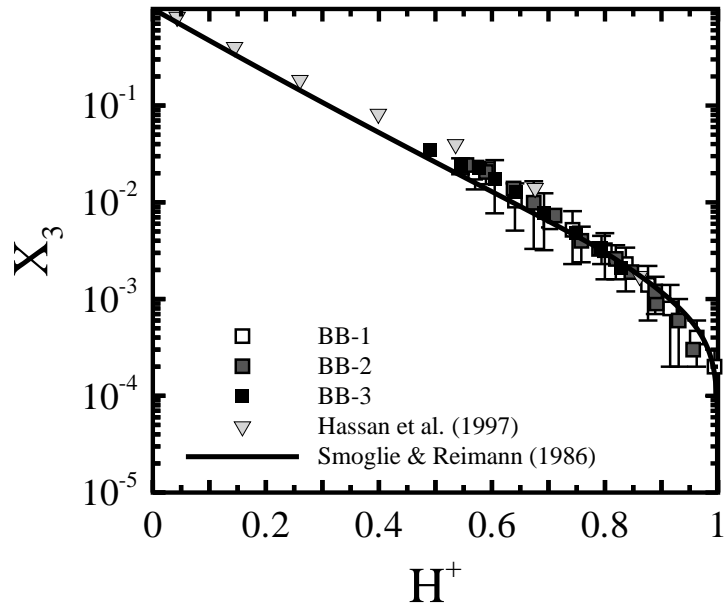


Figure 4.12: Comparison of two-phase quality in the bottom branch with Smogle and Reimann (1986) and Hassan et al. (1997).

4.3.3 Inclined Branch

Critical Height

The critical height at the onset of gas entrainment in the inclined branch was determined under co-current smooth-stratified conditions with $V_{SG1} = 0.3$ m/s, as well as quasi-stagnant conditions with $V_{SG1} = 0$ m/s and $\dot{m}_{L2} = 0$ kg/s. It is considered quasi-stagnant because the water height in the inlet-TEE and outlet-TEE were nearly identical, with less than 5% difference in H . This was achieved by closing the valve controlling \dot{m}_{L2} , allowing water to flow from the inlet-TEE and outlet-TEE into the branch. The critical height results were compared with stagnant reservoir studies in Fig. 4.13(a), accompanied by the two-phase inlet conditions in Fig. 4.13(b). The critical liquid flow distribution is presented in Fig. 4.14. At the upper limit of H_{OGE} the slug regime was observed to occur, and Fig. 4.13(b) shows that this occurred at a value of V_{SL1} that is nearly 25% higher than that of case SS-1. At the lower limit the interface height was $H/D = 0.325$, but visual observation showed that the air-water interface was nearly touching the top edge of the branch. The top edge of the branch is defined as the vertical distance from the bottom of the pipe to the upper limit of the branch, at $H/D = 0.19$, and Ahmad and Hassan (2006) also show this as the physical limit for the OGE. In effect H decreases by approximately 6.8 mm over a horizontal distance of 254 mm ($\lambda/D = -5$). Interestingly, the present data tends to converge on the stagnant results near the branch upper edge. This might be expected since V_{SL1} decreases with H/D , and consequently the air-water interface kinetic energy becomes negligible (stagnant). The present quasi-stagnant results agreed with those obtained

by Ahmad and Hassan (2006) and Hassan et al. (1997), with an average difference in H_{OGE}/D of 11%. As was the case with the bottom branch results, a much higher value of Fr_d was needed to induce OGE with a stagnant interface at a particular interface height, H_{OGE}/D . The branch mass flux is at least an order of magnitude larger than that of the run, and a correlation was developed for the critical height as,

$$\frac{H_{OGE}}{D} = 0.23Fr_d^{0.4}, \quad (4.5)$$

$$2 \leq Fr_d \leq 9.$$

Over this range between 20 to 30% of the total inlet liquid flow goes towards the branch, consequently the run mass flux, shown in Fig. 4.14, is approximately five times larger than that of the bottom branch. The critical liquid flow distribution between the run and branch was correlated as,

$$\frac{\rho_L V_{SL2}}{\rho_L V_{L3}} = 0.13Fr_d^{-0.34}, \quad (4.6)$$

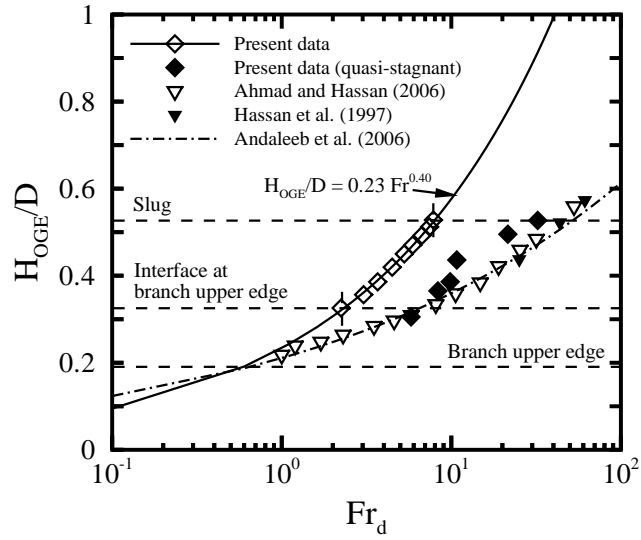
$$2 \leq Fr_d \leq 9,$$

$$\frac{\lambda}{D} = -5.$$

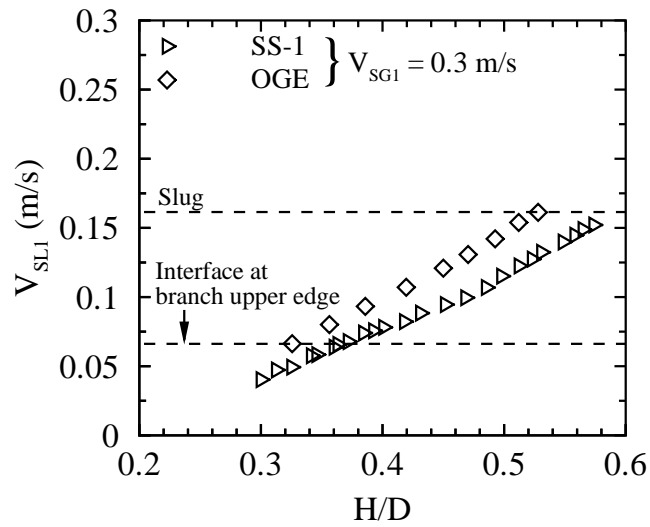
which can be used to determine the branch and run mass flow rates associated with the OGE.

Two-phase Branch Mass Flow Rate and Quality

For the three values of ΔP tested in cases IB-1, IB-2, and IB-3, with liquid only flow in the branch the corresponding values of Fr_d are found using Eq. (4.1) and Eq. (2.6)



(a) Critical height



(b) Inlet conditions

Figure 4.13: Critical conditions at the onset of gas entrainment in the inclined branch at $\lambda/D = -5$.

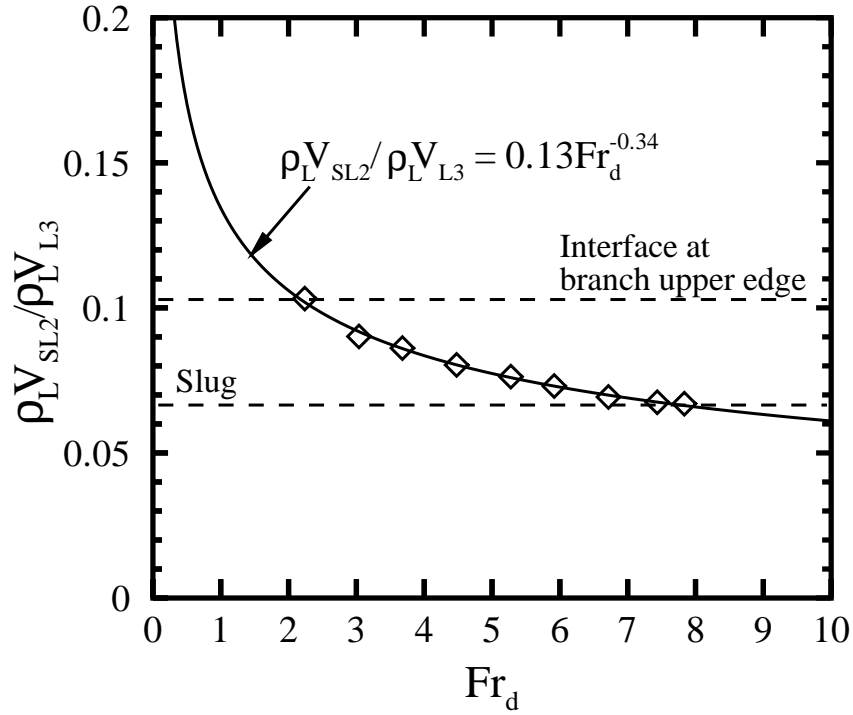


Figure 4.14: Critical liquid flow distribution between the inclined branch and run.

as 22.4, 27.6, and 32.1, respectively. The corresponding values of H_{OGE}/D using Eq. (4.5) are 0.783, 0.850, and 0.902 for cases IB-1, IB-2, and IB-3, respectively. It can be anticipated from Fig. 4.13 that at the OGE the three cases would lie within the slug regime. Therefore the upper limit for cases IB-1, IB-2, and IB-3 are expected to be met by a two-phase regime transition rather than the OGE.

The two-phase flow distribution at the inlet and branch is presented in Fig. 4.16. At the upper limit of cases IB-1 and IB-2 the slug regime was observed, while the wavy regime was observed in case IB-3. Sketches of the observed flow structure development near the branch are presented in Fig. 4.15. In Fig. 4.15(a) the air spout is shown entraining into the right side of the branch as a result of the inlet liquid momentum forcing it downstream, towards the run. As H decreased the air spout was

observed to dissipate, and air and water flowed into the branch similar to as shown in Fig. 4.15(b). Further decreasing the interface height resulted in the development of a water spout being pulled up into the branch, as in Fig. 4.15(c). The water spout was also observed to be affected by the inlet liquid momentum, and observed to entrain on the downstream side of the branch.

In all three cases the lower limit corresponds to dry-out. Figure 4.16(d) shows that dry-out occurs at a value of H/D that is higher than the critical height at the onset of liquid entrainment (OLE), as X_3 is between 0.2 and 0.3 in this range. The inlet superficial liquid velocity is shown in Fig. 4.16(a) to be up to 17% higher than case SS-1 with $H/D > 0.4$. Although V_{SG1} is up to three times higher than that of case SS-1, it was demonstrated in Fig. 4.2 that this would only yield up to a 6% increase in V_{SL1} . The increase in V_{SL1} is therefore likely attributed to the portion of liquid entering the branch - which in this case is found to be between 30 to 35% of the total inlet liquid mass flow rate. The branch two-phase mass flow rate shown in Fig. 4.16(c) is approximately 40% lower than in the bottom branch. This is attributed to the much higher portion of the gas phase in the mixture, as demonstrated by the branch quality in Fig. 4.16(d).

The inlet height, H , was non-dimensionalized according to Eq. (4.4) and the branch quality is presented as a function of H^+ in Fig. 4.17. This allows comparison with Hassan et al. (1997)'s results, which were obtained using a large stagnant air-water reservoir. In their study the authors described the air water interface, particularly the air and water spouts, as nearly symmetric about a vertical line passing through the branch center. Here, as shown in Fig. 4.15, the inlet liquid momentum

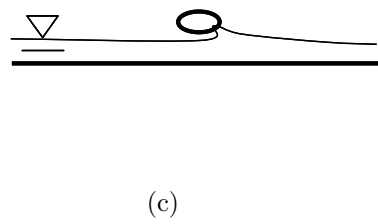
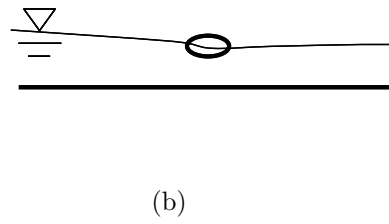
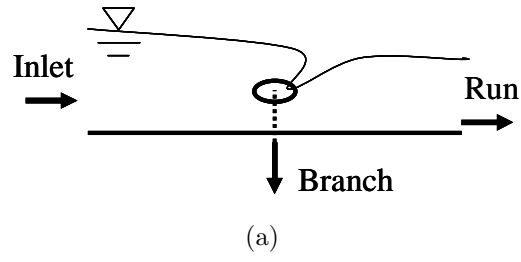
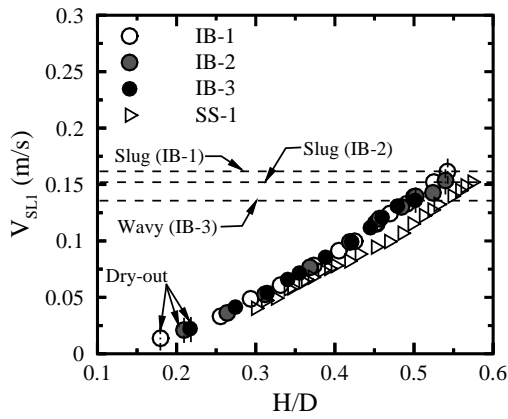
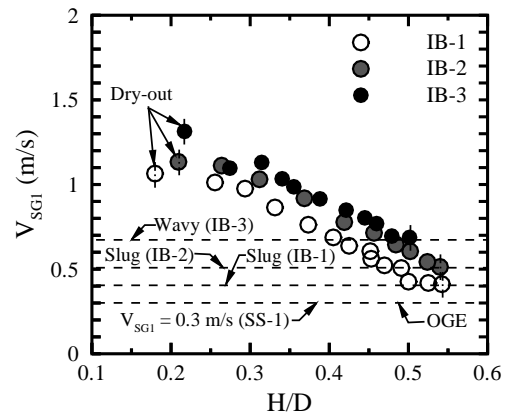


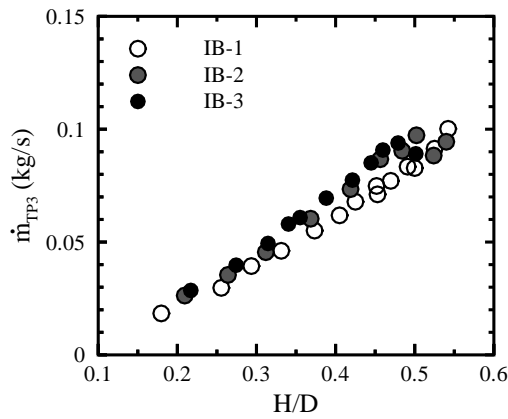
Figure 4.15: Sketches of observed air/water spout development during two-phase flow in the inclined branch with decreasing interface height from (a) to (c).



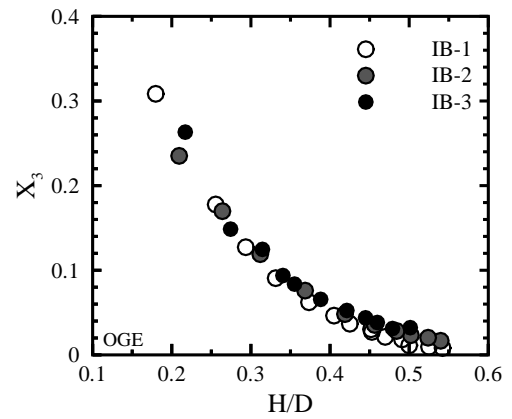
(a) Inlet superficial liquid velocity



(b) Inlet superficial gas velocity



(c) Branch two-phase mass flow rate



(d) Branch quality

Figure 4.16: Two-phase distribution at the inclined branch in relation to the interface height at $\lambda/D = -5$.

forces the air and water spouts to the run side of the branch, the effect of which is a reduction in the spout size at the branch inlet. This translates in Fig. 4.17 to a lower flow quality than Hassan et al. (1997), which is evident over the range $0.4 < H^+ < 0.7$. As H^+ decreases the inlet liquid momentum decreases and X_3 converges on Hassan et al. (1997)'s data. It is expected that as H^+ approaches 1 the two data sets will also begin to converge. This is because the portion of the air spout at the branch inlet decreases significantly, and its influence on the two-phase mass flow rate becomes less apparent as in the bottom branch case.

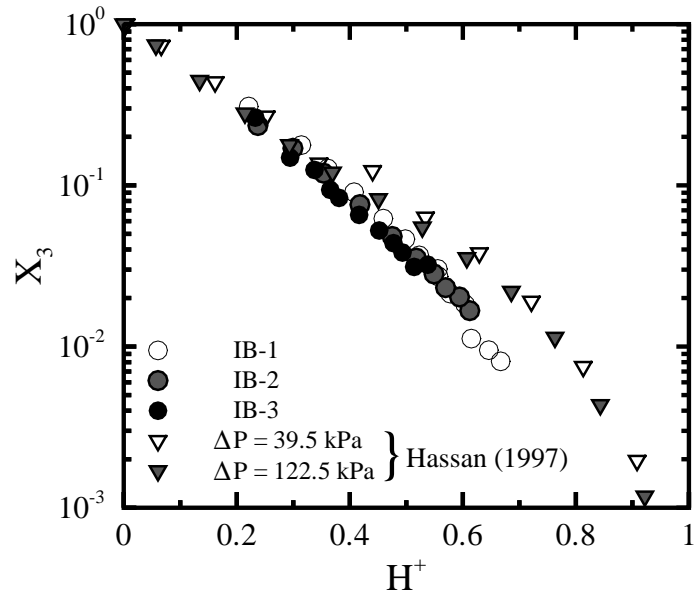
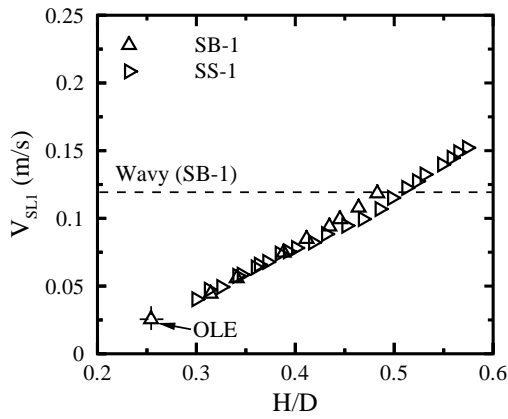


Figure 4.17: Comparison of two-phase quality in the inclined branch with Hassan et al. (1997).

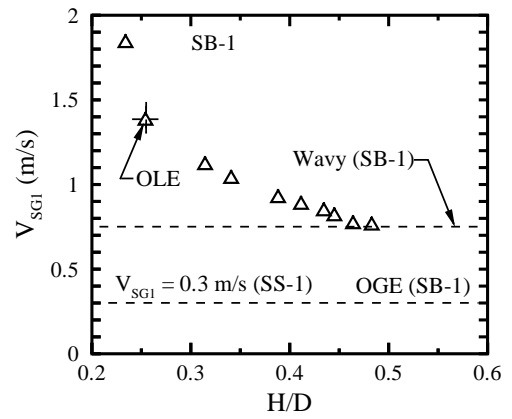
4.3.4 Side Branch

The two-phase flow distribution at the inlet and branch is presented in Fig. 4.18. Figure 4.18(a) shows that at $H/D = 0.48$ the inlet air-water interface was observed to be wavy. The upper edge of the side branch is physically located at $H/D = 0.562$, which is higher than the two-phase regime transition height. Therefore, due to the regime transition limit, the OGE could not be achieved since the interface height was always below the branch's upper edge. At the lower limit, however, the onset of liquid entrainment was encountered prior to dry-out. The OLE was found to occur at $H/D = 0.254$, and can be confirmed in Fig. 4.18(d) where $X_3 = 1$. The two-phase mass flow rate in the branch, from Fig. 4.18(c), is considerably lower than the inclined or bottom branch results but is coupled with a substantially higher branch quality, as shown in Fig. 4.18(d). The higher portion of air entering the branch translates to a much larger inlet superficial gas velocity, and is shown to be as high as 1.4 m/s in Fig. 4.18(b) which is over four times greater than case SS-1. The inlet superficial liquid velocity is marginally higher than case SS-1; a maximum increase of approximately 10% was observed at $H/D = 0.48$. Due to the presence of the wavy regime at this interface height, and the fact that the portion of liquid entering the branch is only around 12% of the total inlet liquid mass flow, interfacial shearing induced by the flowing air is likely the main contributor to the observed increase in V_{SL1} .

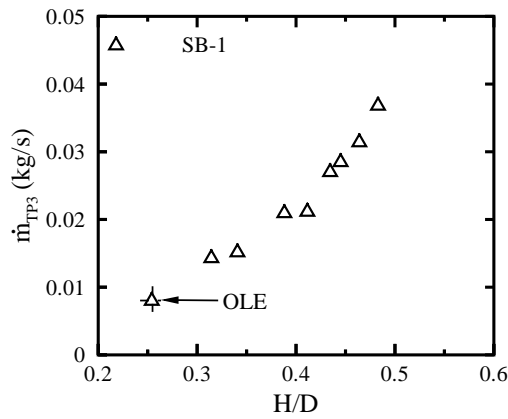
In Fig. 4.19 the OLE is compared to experimental (Maier et al., 2001a; Bowden and Hassan, 2008; Smoglie and Reimann, 1986) and theoretical (Maier et al., 2001b) investigations. Since these studies include branches on the side of a flat horizontal



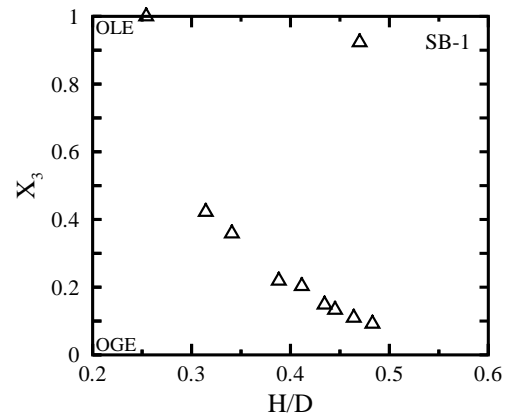
(a) Inlet superficial liquid velocity



(b) Inlet superficial gas velocity



(c) Branch two-phase mass flow rate



(d) Branch quality

Figure 4.18: Two-phase distribution at the side branch in relation to the interface height at $\lambda/D = -5$.

wall, D is therefore infinite, it is appropriate to reference the interface height from a horizontal line passing through the side branch center rather than the bottom of the pipe. The interface height relative to the side branch, H_A , is therefore,

$$H_A = H - \frac{D}{2}, \quad (4.7)$$

and the critical height at OLE is re-defined here for comparison purposes as $H_{A,OLE}$. Similar to the bottom and inclined cases, at an equivalent critical height, a lower branch Froude number is needed to induce OLE when compared to stagnant reservoir studies (Maier et al., 2001a,b; Bowden and Hassan, 2008). For example Fr_d is 20% lower when compared to Bowden and Hassan (2008), which is the closest in geometrical similarity to the present study. In the worst case the difference in Fr_d is nearly 56% when the present data is compared to Smoglie and Reimann (1986). This difference is not as severe as the inclined branch results shown in Fig. 4.13 where the stagnant reservoir values of Fr_d were between two to five times higher. The difference is attributed to the interfacial drag caused by the flowing air. At the OLE V_{SL1} is quite low, almost near dry-out in Fig. 4.18(a), however V_{SG1} is highest at 1.4 m/s. The interfacial drag forces the entraining liquid spout to one side of the branch, similar to the observations for the inclined branch in Fig. 4.15(c), and results in a thinning of the spout at the branch inlet just prior to the OLE. This consequently reduces the liquid flow area at the branch inlet, resulting in a higher branch quality.

The branch quality is compared to Smoglie and Reimann (1986)'s correlation, as well as Hassan et al. (1997)'s data in Fig. 4.20. The interface height relative to the

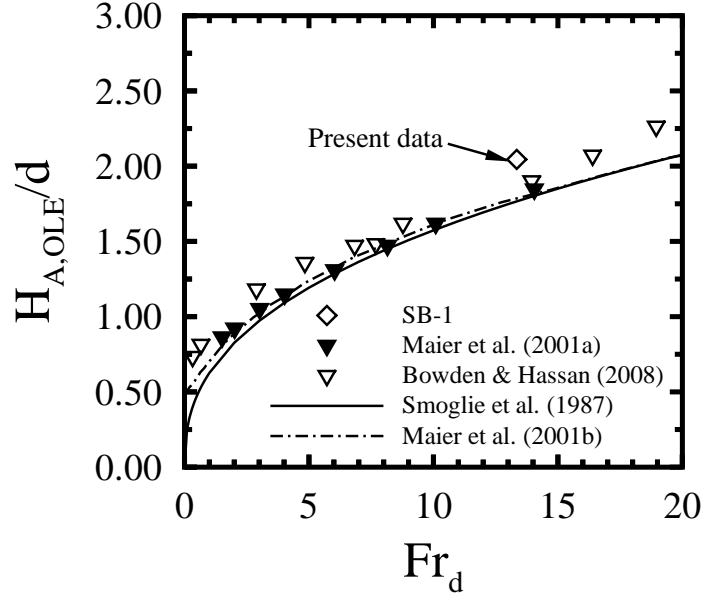


Figure 4.19: Comparison of the present critical height $\lambda/D = -5$ at the OLE in the side branch with available models and experimental data.

side branch, H_A , is scaled here using $H_{A,OLE}$ as,

$$H_A^- = \frac{H_A}{|H_{OLE}|}. \quad (4.8)$$

The present results are in very good agreement with Smogle and Reimann (1986)'s correlation, which is re-written here using the present nomenclature as,

$$X_3 = \left(\frac{1.15}{1 + \left(\frac{\rho_L}{\rho_G}\right)} \right)^{2.5H_A^-} \times \left[1 - \frac{H_A^-}{2} (1 + H_A^-) \times \left(\frac{1.15}{1 + \left(\frac{\rho_L}{\rho_G}\right)^{\frac{1}{2}}} \right)^{1-H_A^-} \right]^{\frac{1}{2}} \quad (4.9)$$

while there is poor agreement with Hassan et al. (1997)'s data, particularly where $H_A^- < 0$. This can be explained since interfacial shear causes thinning of the water spout, thereby reducing the liquid flow area at the branch inlet, which consequently increases the branch quality. In the region where $H_A^- > 0$, Hassan et al. (1997)'s data

approaches Smogle and Reimann (1986)'s correlation since the water spout dissipates as the interface approaches the branch center, as in Fig. 4.15(b), thereby reducing the influence of its size and shape on X_3 .

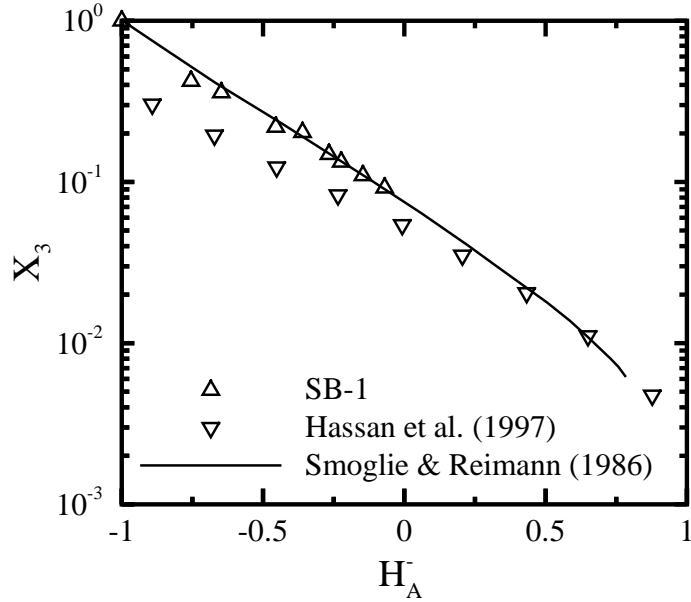


Figure 4.20: Comparison of the two-phase quality in the side branch with Smogle and Reimann (1986) and Hassan et al. (1997).

4.4 Summary

Under co-current two-phase conditions one of the consequences of a gas-liquid mixture flowing in the branch is the effect on the inlet flow regime. Under certain conditions transitions from the smooth-stratified to wavy-stratified or slug regimes were observed. Although these regimes could not be accurately controlled, in part due to their transient nature, they nevertheless have very important implications on the branch two-phase characteristics. There is evidence that a passing wave can initiate

or hinder gas entrainment, based on flow visualization, however a quantitative analysis of this phenomenon is lacking. Detailed image analysis of the phenomenon is a potential way to quantify the effects of the wavy regime on the branch two-phase flow quantities, although more exploration in this area would be needed.

The two-phase quantities, including mass flow rate and quality, were reported as a function of the liquid height within the inlet. Due to the developing nature of the flow within the inlet the measured height is dependent on the length scales of the facility. These effects are essentially smoothed out when an appropriate scaling factor is used. In this case the critical height at the onset of gas or liquid entrainment was used, which resulted in excellent agreement with the tested correlations. The consequence of this, however, is that the effect of the interfacial liquid gradient is somewhat lost in the smoothing of results. The scaling factor must be carefully assessed in order to effectively use correlations of this nature. It would be impractical to try to experimentally investigate how every scaling parameter impacts the critical height but improved analytical models could serve this purpose.

Chapter 5

Experiments with Dual

Discharging Branches at Low to

Moderate Froude Numbers

5.1 Chapter Overview

The critical height at the onset of gas entrainment in a small branch has been shown to be affected by the flow through additional branches within large stratified gas-liquid reservoirs (Ahmad and Hassan, 2006; Bowden and Hassan, 2008). In co-currently flowing gas-liquid horizontal pipes, however, the critical height can be quite different from that obtained in a stratified reservoir due to the effects of the crossflow velocities. Studies dealing with the onset of gas entrainment in multi-branch configurations, particularly where co-currently flowing two-phase pipes are concerned, are very limited. This chapter will investigate the effect of a second branch on the critical height at

the OGE in a horizontal pipe with co-currently flowing gas-liquid streams within the smooth-stratified regime.

5.2 Experimental Methodology

With a total of three branch orientations available (side/inclined/bottom), there are three possible two-branch combinations:

- Inclined and bottom branches
- Side and inclined branches
- Side and bottom branches

The fluid in each branch is either a single phase liquid or a single phase gas, and flowing with a constant mass flow rate. The branch Froude number, described in Chapter 3, is the governing dimensionless parameter to describe the related flow phenomena in the branches. Subscripts A , B , and C will be used to distinguish the branch Froude numbers as Fr_A for the side branch, Fr_B for the inclined branch, and Fr_C for the bottom branch. The OGE is expected to be related to the interface level and the branch Froude number. Subscript OGE will be used in reference to the interface height in order to distinguish the related phenomena. The two-phase flow regime is classified according to the superficial liquid, V_{SL1} , and gas, V_{SG1} , velocities within the inlet, as defined in Chapter 3. As was shown in Chapter 4, V_{SL1} is also related to the interface height since gravity is a main driving force. Therefore, where

the inlet regime is concerned the interface height will simply be denoted as H to distinguish the two-phase inlet regime data from the *OGE* data.

5.2.1 Procedures

The methodology to obtain the critical height differs from the single branch cases investigated in Chapter 4. Instead of setting the branch Froude number constant and varying the inlet height until the OGE occurs, the inlet superficial velocities (V_{SL1} , V_{SG1}) are set constant and the branch Froude numbers are slowly varied until the OGE occurs. This difference in methodology allowed more control over the OGE in the desired branch. The branch Froude number was varied at very small increments, on the order of 2 to 5% of the critical Froude number and care was taken to ensure that the OGE occurred with a steady Froude number and not due to the inertia induced by the sudden change in the branch Froude number. A typical settling time of approximately one minute was observed before classifying the state of the branch's fluid flow, i.e. the OGE or single phase.

5.2.2 Test Matrix

Five cases were tested in order to demonstrate the effects of a second active branch, these are listed in Table 5.1. The first, Case 1, examines the OGE in the inclined branch with low to moderate values of Fr_C . Case 2 tests the effect of low values of Fr_B on the OGE in the bottom branch. Case 3 presents the critical values of Fr_B and Fr_C that cause the OGE in both the inclined and bottom branches simultaneously.

Cases 4 and 5 demonstrate the effects of gas flow in the side branch using low to moderate values of Fr_A . Uncertainty estimates for the branch Froude numbers and inlet superficial velocities follow from Chapter 4.

5.3 Results and Discussion

This section is organized into three main parts. In the first section a discussion regarding the observed phenomena is presented. The discussion is accompanied by images and sketches in order to enhance the physical description of related flow phenomena and in support of the recorded quantitative data. The second section presents the recorded data of cases 1 to 5 in a concise manner. The critical height at the OGE, H_{OGE} , is presented for each case as a function of the branch's Froude number. Data is presented in order to show the effects of the second branch Froude number and the measurement location, λ , on the critical height. The third section compares the present data with applicable models and experimental data found in the literature.

5.3.1 Flow Visualization

The cases outlined in Table 5.1 were established first through extensive trials aimed at defining the related phenomena, appropriate flow ranges, and limitations. Since the methodology used during these trials was slightly different, the single branch experiments were repeated to ensure consistency with previous experiments. The discussion presented here will be on a case by case basis, following from Table 5.1, and will highlight typical visual observations of related phenomena.

Table 5.1: Test matrix of dual branch experiments.

Case	Description	Side	Branch Fluid Phase			Fr_A	Fr_B	Fr_C	OGE Branch	V_{SG1} (m/s)	V_{SL1} (m/s)
			Inclined	Bottom							
1	Dual		Liquid	Liquid		1-8	0,1,10, Fr_B	Inclined	0.3	0.05-0.15	
2	Dual		Liquid	Liquid		0,1,2	6-23	Bottom	0.3	0.05-0.15	
3	Dual		Liquid	Liquid		1-4	8-21	Inclined & Bottom	0.3	0.05-0.15	
4	Dual	Gas	Liquid		0,1,10	1-4.2		Inclined	0.3,0.4,1	0.04-0.1	
5	Dual	Gas		Liquid	0,1,10		4-21	Bottom	0.3,0.4,1	0.04-0.15	

Inclined and Bottom Branches: Cases 1 to 3

In Fig. 5.1 a sketch of dip profile development, with increasing Fr_B , is presented for the OGE in the inclined branch. The superficial inlet liquid and gas velocities are constant at 0.1 m/s and 0.3 m/s, respectively, and the air-water interface within the inlet is smooth-stratified. In Fig. 5.1 (i) there is no flow inside the branch, $Fr_B = 0$. Increasing Fr_B to 3, in Fig. 5.1 (ii), a small dip was observed to form in the air-water interface above the branch, away from the pipe wall, and slightly shifted towards the run side. As Fr_B was increased the dip was observed to grow in both depth and width. Initially the dip profile was near parabolic, however as Fr_B increased to 4.2 the dip began to form a sharp tip at its bottom until, at a certain instant, the tip collapsed into the branch causing air to entrain. At this point a portion of the dip is attached to the side of the pipe wall, as shown in Fig. 5.1 (iii). An example of the dip shape at this critical point is presented in Fig. 5.2. A similar sketch is presented in Fig. 5.3 for the dip profile development for the OGE in the bottom branch. Again V_{SL1} and V_{SG1} are constant at 0.1 m/s and 0.3 m/s, respectively, and the inlet is smooth-stratified. The branch Froude number is increased from 0 to 17 in Fig. 5.3 (i) to (iii), respectively, with the latter demonstrating the critical conditions at the OGE. The dip develops similarly to that described for the inclined branch, however, it remains detached from the side wall throughout.

Comparing Fig. 5.3 (iii) with Fig. 5.1 (iii), it can be seen that for the same inlet conditions the critical branch Froude number is affected by the branch orientation. In the bottom branch the OGE occurred with $Fr_C = 17$ while in the inclined it was

$$\begin{aligned} Fr_A = Fr_C &= 0 \\ V_{SL1} &= 0.1 \text{ m/s} \\ V_{SG1} &= 0.3 \text{ m/s} \end{aligned}$$

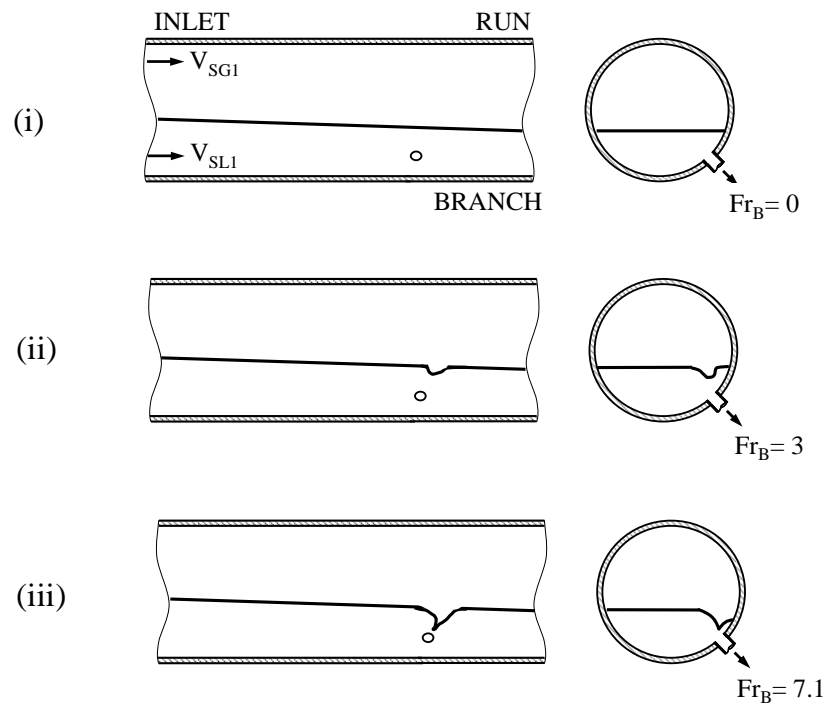


Figure 5.1: Sketches of the onset of gas entrainment at the inclined branch with constant values of V_{SL1} and V_{SG1} .

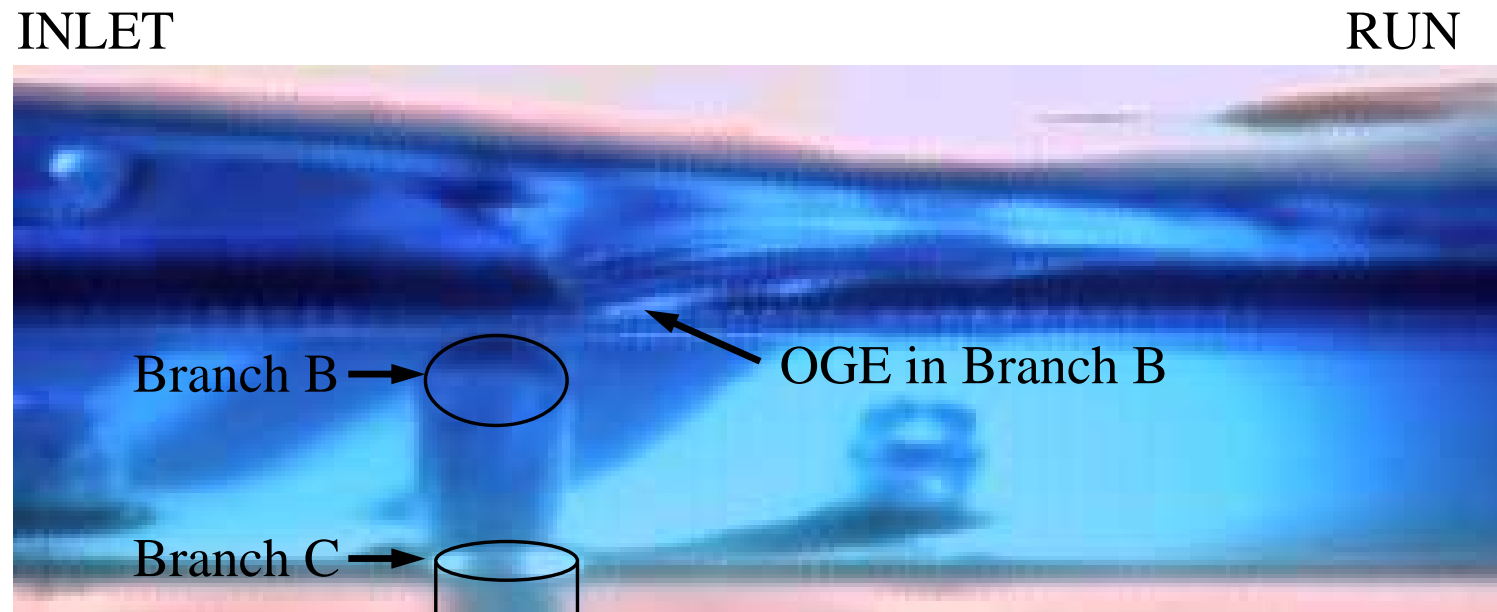


Figure 5.2: Sample image of the onset of gas entrainment at the inclined branch with a low value of Fr_C .

$$\begin{aligned} Fr_A &= Fr_B = 0 \\ V_{SL1} &= 0.1 \text{ m/s} \\ V_{SG1} &= 0.3 \text{ m/s} \end{aligned}$$

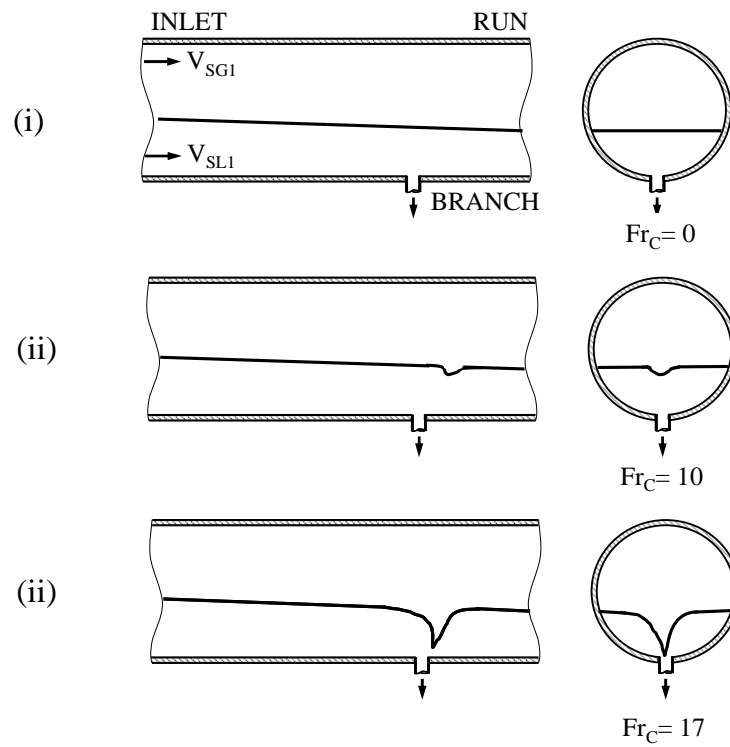


Figure 5.3: Sketches of the onset of gas entrainment at the bottom branch with constant values of V_{SL1} and V_{SG1} .

found with a much lower value, at $Fr_B = 4.2$. What this implies is that for dual discharge experiments, for a given inlet condition (V_{SL1} , V_{SG1}), the branch Froude numbers can be varied between the single branch critical limits. That is to say at $V_{SL1} = 0.1$ m/s and $V_{SG1} = 0.3$ m/s, one limit will be the OGE in the inclined branch at critical values of $Fr_B = 4.2$ and $Fr_C = 0$. The other limiting case is found with the OGE in the bottom branch at critical values of $Fr_C = 17$ and $Fr_B = 0$. During dual discharge, with values of Fr_B and Fr_C in between these limits, three distinct modes of gas entrainment are expected to occur:

- Mode 1: OGE in the inclined branch only
- Mode 2: OGE in the bottom branch only
- Mode 3: OGE in both branches simultaneously

These modes can be found through trial and error, and for various inlet conditions.

For Mode 1, and constant inlet conditions, the maximum value that Fr_C can attain is defined by the critical value at the OGE in the bottom branch. This is not a practical choice for a test value, however, since the effects of Fr_C on Mode 1 are unknown at this point. Therefore a more systematic approach is to test different values of Fr_C , below this maximum value, and find the critical value of Fr_B given constant inlet conditions.

In Fig. 5.4 the air-water interface development local to the active branches are presented with $Fr_B = Fr_C$, and $V_{SL1} = 0.15$ m/s, which is 50% higher than that discussed in the single branch examples. In Fig. 5.4(a) there is no flow in the branch. In Fig. 5.4(b) a small dip above and to the right of the inclined branch

begins to form. In Fig. 5.4(c) the dip has extended into the branch at the OGE. As the branch Froude number is increased from 0 to 7.2, the air-water interface shape changes considerably. The observed change is not only the local dip formation, but the inlet (left of the branch) and run (right of the branch) interface levels are also visibly altered. Therefore, although the inlet liquid mass flow rate is constant, the quantity of the liquid mass flowing through the branches effects the interface levels upstream of the branch. Consider that at a branch Froude number of 7.2 the liquid velocity entering the branch is around 1.8 m/s. The inlet liquid velocity will vary according to the interface height, and consider for comparison purposes that the inlet velocity is $V_{SL1} = 0.15$ m/s. This rough comparison demonstrates that the liquid velocity entering the branch is approximately an order of magnitude larger than the liquid velocity within the inlet. The liquid flowing within the inlet must therefore accelerate towards the branch in order to accomodate the much higher liquid velocity entering the branch. As the fluid accelerates towards the branch the interface level will be forced to adjust, by decreasing in height, in order to conserve the inlet liquid mass flow rate. This has obvious implications on the critical height, H_{OGE} , and precisely how the fluid accelerates in the presence of the branch flow is a point of future interest.

The discussion on the effects of Fr_C on the OGE in the inclined branch is continued by considering a case where Fr_C is greater than the critical limiting value of Fr_B but still lower than the critical limiting value of Fr_C . Consider $V_{SL1} = 0.1$ m/s, $V_{SG1} = 0.3$ m/s and $Fr_C = 10$, which was chosen since it is lower than the critical value of $Fr_C = 17$, yet higher than the critical value of $Fr_B = 4.2$. A sketch of this

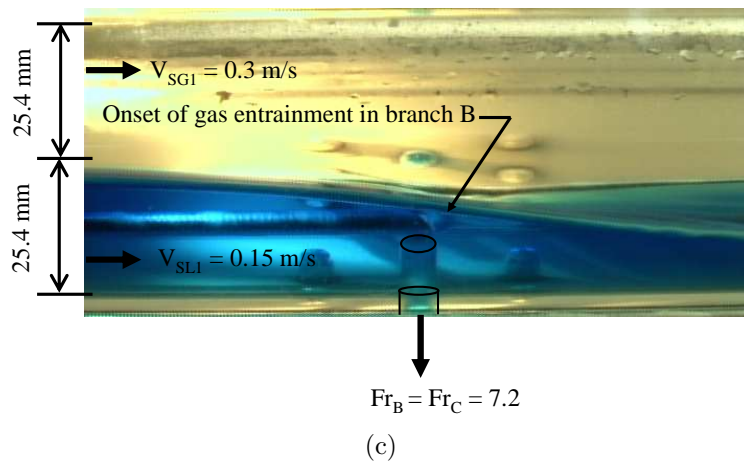
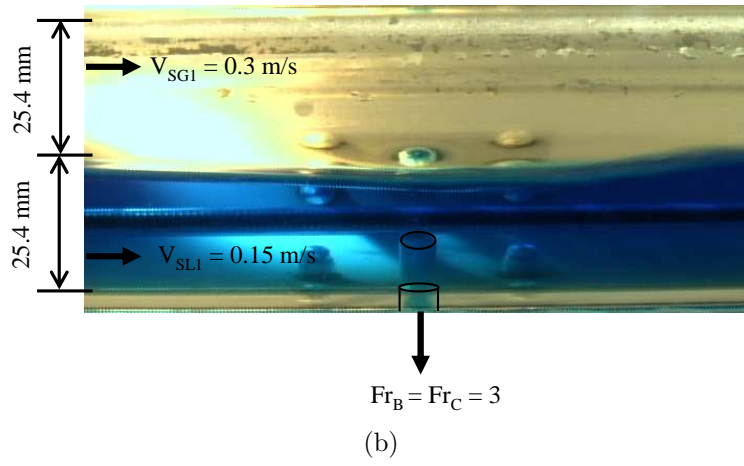
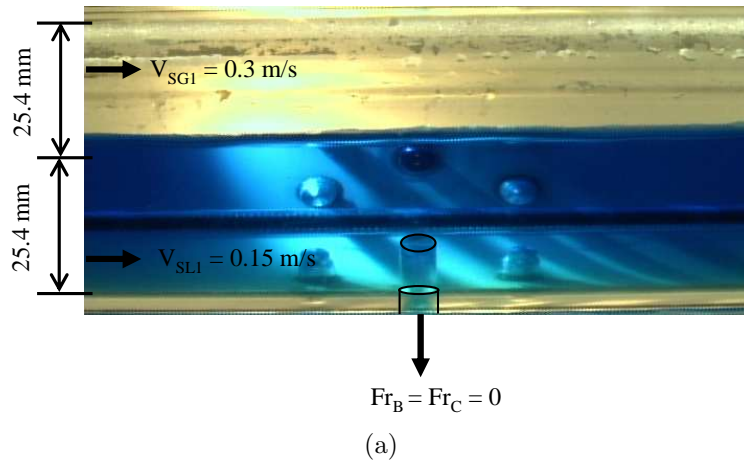


Figure 5.4: Sample images of the local air-water interface development with increasing $Fr_B = Fr_C$ and constant V_{SL1} and V_{SG1} .

case is presented in Fig. 5.5. In Fig. 5.5(i) there is only flow through the bottom branch and a dip was observed to form in the air-water interface as a result of the flow entering the branch. With a small increase in Fr_B to 2 another dip was observed to form in the interface near the inclined branch, as shown in Fig. 5.5(ii). Another small increase in Fr_B to 3.9, and the second dip collapsed into the inclined branch thereby causing the OGE, as shown in Fig. 5.5(iii). As Fr_B was increased from 0 to 3.9 there was no noticeable change in the dip near the bottom branch, however its presence affected the value of Fr_B at the OGE. In the single branch case ($Fr_C = 0$), the OGE in the inclined branch was found at $Fr_B = 4.2$, and in comparison with $Fr_C = 10$ the OGE in Fig. 5.5(iii) was found at a slightly lower value, with $Fr_B = 3.9$. One explanation for this decrease in Fr_B is that the interface level above the inclined branch was reduced due to the presence of the dip near the bottom branch. As a result a lower value of Fr_B was needed to induce air entrainment. The second explanation for this decrease is that the fluid entering the bottom branch does so at a velocity that is about two and a half times of that entering the inclined branch. The liquid must accelerate from the much slower inlet liquid stream into each branch. The acceleration of the fluid entering the bottom branch can affect the velocity of the liquid near the inclined branch dip to the point that a reduced value of Fr_B is needed to initiate the OGE.

To evaluate the effects of Fr_C further consider a constant value of $Fr_B = 2$, or half of the value needed to initiate OGE in the inclined branch in Fig.5.5, with increasing Fr_C . In Fig. 5.6 a sketch of this case is presented. In Fig. 5.6 (i) $Fr_C = 0$ and a dip appears in the interface above the inclined branch. Increasing Fr_C to 10 a second

$$Fr_C = 10$$

$$V_{SL1} = 0.1 \text{ m/s}$$

$$V_{SG1} = 0.3 \text{ m/s}$$

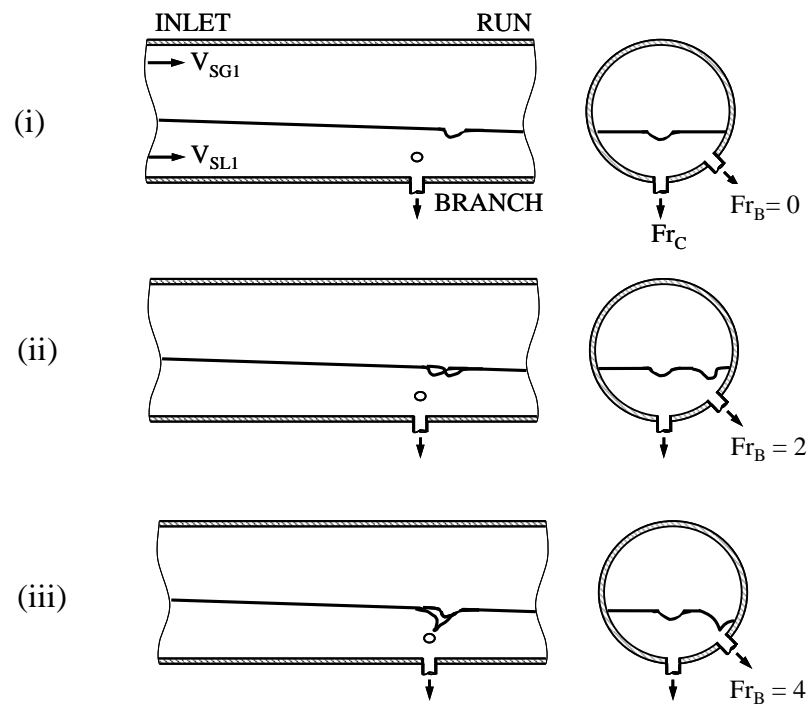


Figure 5.5: Sketches of the onset of gas entrainment at the inclined branch with a moderate value of Fr_C and constant values of V_{SL1} and V_{SG1} (Mode 1).

dip near the bottom branch forms in the interface, as shown in Fig. 5.6 (ii), which coincides with the description provided in Fig. 5.5(ii). Increasing Fr_C to 17 leads to the OGE in the bottom branch, however, the first dip does not collapse into the inclined branch. This case refers to the second mode of entrainment, that is the OGE in the bottom branch without entrainment in the inclined branch.

In order to cause the OGE in the inclined branch through an increase in Fr_C the value of Fr_B must therefore be higher than 2, Fig. 5.6(iii), but lower than the critical limit of $Fr_B = 4.2$. Consider a constant value of $Fr_B = 3.5$ while again increasing Fr_C , as shown in Fig. 5.7. In Fig.5.7(i) $Fr_C = 0$ and a dip forms in the interface above the inclined branch. Increasing Fr_C to 10 results in a second dip in the interface, as shown in Fig. 5.7(ii). By increasing Fr_C to 17 both dips were observed to collapse simultaneously into each respective branch, as in Fig. 5.7(iii). This is referred to as the third mode of gas entrainment, simultaneous entrainment in both branches. A sample image of the simultaneous OGE in both branches is presented in Fig. 5.8. In the foreground of the image is the dip just as air is about to entrain into the bottom branch, and in the background the dip as it is about to entrain in the inclined branch. Interestingly the value of Fr_B at which this occurs is found in between the other two described modes, that is, Fr_B is lower than found in Mode 1 and higher than in Mode 2 for the same inlet conditions. In summary, for a constant inlet condition (V_{SL1}, V_{SG1}), the three modes of gas entrainment may be found through trials of different combinations of the two branch Froude numbers.

$$Fr_B = 2$$

$$V_{SL1} = 0.1 \text{ m/s}$$

$$V_{SG1} = 0.3 \text{ m/s}$$

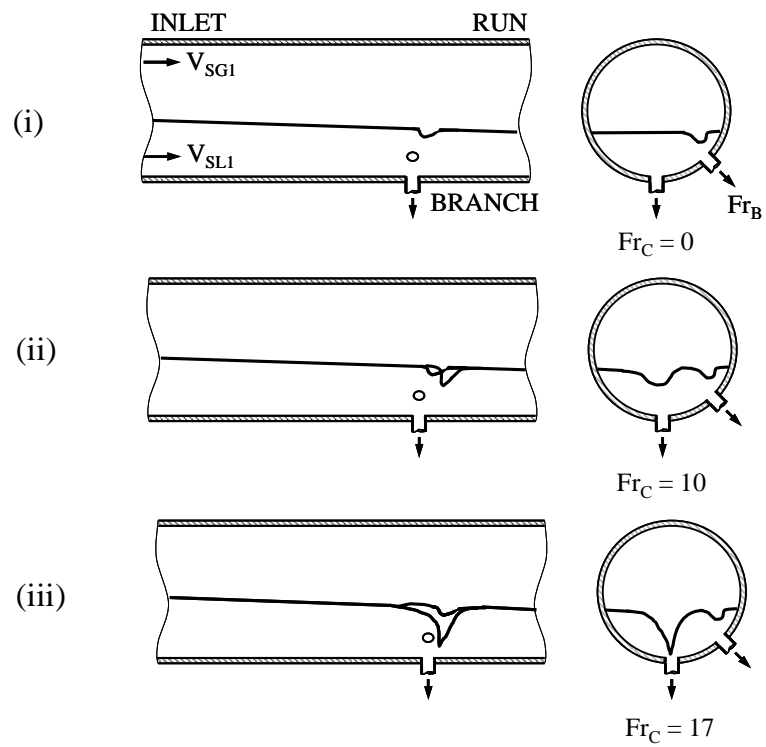


Figure 5.6: Sketches of the onset of gas entrainment at the bottom branch with a low value of Fr_B and constant values of V_{SL1} and V_{SG1} (Mode 2).

$$\begin{aligned} Fr_B &= 3.5 \\ V_{SL1} &= 0.1 \text{ m/s} \\ V_{SG1} &= 0.3 \text{ m/s} \end{aligned}$$

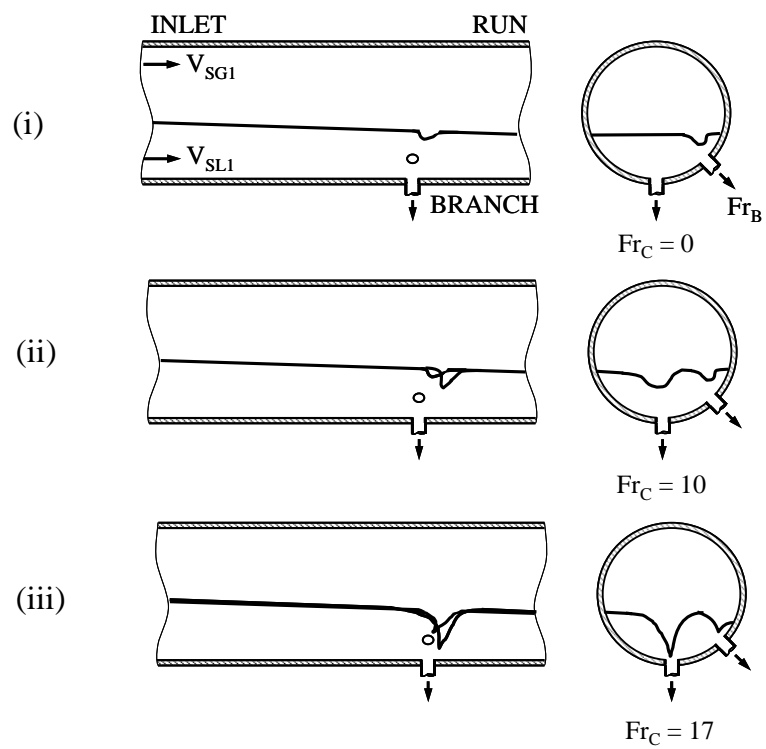


Figure 5.7: Sketches of the onset of gas entrainment at both the inclined and bottom branches with constant values of V_{SL1} and V_{SG1} (Mode 3).

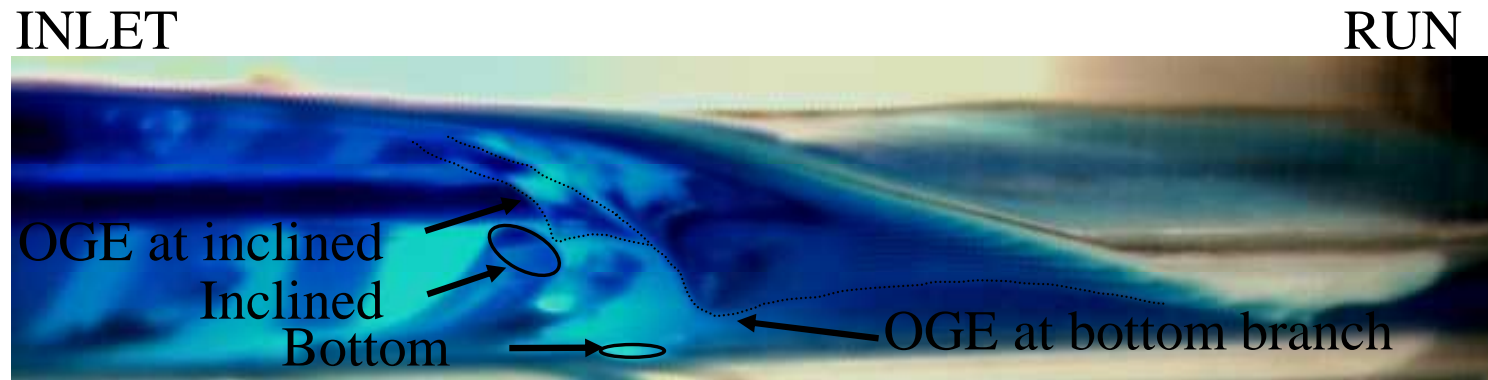


Figure 5.8: Sample image of the onset of gas entrainment at both the inclined and bottom branches (Mode 3).

Side and Inclined Branches: Case 4

As was discovered in Chapter 4 the air-water interface was always at or below the level of the side branch during single branch experimentation. As a result the flow entering the side branch consisted of either a two-phase gas-liquid mixture or single phase gas. Increasing the interface above the side branch was typically met with a regime transition boundary. It was also discussed that small to moderate increases in V_{SG1} , within the smooth-stratified regime, did not dramatically affect V_{SL1} or the interface height, H . It did however affect the regime transition boundary, and specifically in regards to the interface level where wavy or slug flows were encountered. Therefore, activating the side branch is expected to come at the expense of this regime boundary transition limitation. That is to say, increasing the gas phase Froude number in the side branch, Fr_A , will increase the inlet superficial gas velocity V_{SG1} , and ultimately affect the two-phase regime transition boundary. In addition, since the side branch will be flowing gas only, and the gas-liquid interface is always below the side branch, there is a possibility that liquid entrains into the side branch (OLE). These two phenomena, regime transition and the OLE, are expected to limit the range of Fr_A and Fr_B that can be tested. Therefore, a systematic approach was used to determine the range of these limits at constant values of V_{SL1} , by keeping Fr_A at a constant value, and determining the critical values of Fr_B for OGE in the inclined branch.

With $Fr_A = 1$, the inertia of the gas phase is on the order of gravity. In Fig. 5.9 three cases are presented for $Fr_A = 1$ at three different values of V_{SL1} . The inlet superficial gas velocity was therefore increased to 0.4 m/s, which is a small increase

over the single branch case where $V_{SG1} = 0.3$ m/s and $Fr_A = 0$. With $V_{SL1} = 0.05$ m/s the critical value of Fr_B was found to be 1.35, as shown in Fig. 5.9(i). At this point the air-water interface was considerably below the side branch inlet, and therefore no discernible effect on the OGE dip was observed. Increasing V_{SL1} to 0.08 m/s, in Fig. 5.9(ii), the critical value of Fr_B was found to be 3.2. The distance from the side branch to the air-water interface was decreased, however the OGE dip was visibly unaffected. Further increasing V_{SL1} to 0.1 m/s, as in Fig. 5.9(iii), the critical value of Fr_B was found as 4.25, which is not unlike the single branch case where $Fr_A = 0$. A low value of Fr_A seems to have little effect on the critical value of Fr_B to induce the OGE in the inclined branch. In addition, the small increase in V_{SG1} did not visibly affect the inlet regime, as it remained relatively smooth-stratified throughout.

Increasing Fr_A to a moderate value of 10, as in Fig. 5.10, showed that both the OLE and a regime transition can occur simultaneously. The inlet superficial gas velocity is increased to 1 m/s as a result of $Fr_A = 10$, which is over three times more than the single branch case, where $V_{SG1} = 0.3$ m/s. In Fig. 5.10(i), $V_{SL1} = 0.05$ m/s, and the critical value of Fr_B to cause OGE in the inclined branch was found to be 1.5, which is 10% higher than the single branch case. The air-water interface within the inlet remains relatively smooth, and at this point the OGE dip was not observed to be affected by the air flowing in the side branch. Increasing V_{SL1} to 0.08 in Fig. 5.9(ii), however, showed that very small interfacial waves, less than 0.5 mm in height, began to form on the air-water interface within the inlet. Closer inspection showed that the OGE dip was oscillating vertically with Fr_B below the critical value

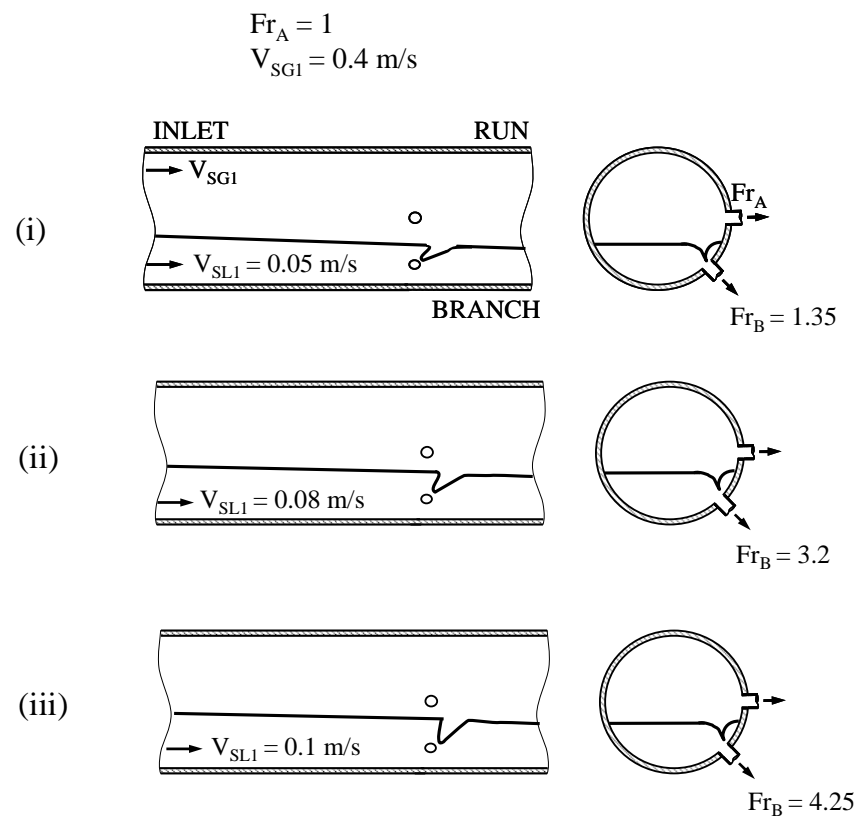


Figure 5.9: Sketches of the onset of gas entrainment at the inclined branch with a low value of Fr_A and variable inlet conditions.

of 3.5. Consequently, on the low peak of the oscillation air began to entrain into the inclined branch, and as the upper peak was approached air stopped entraining. The waves seemed to generate as a result of interfacial shear within the inlet, however, the oscillations at the dip seem to also be caused by the gas flowing into the side branch. To illustrate this in a simple way, consider that the two branches are on opposite sides of the air-water interface, and in effect apply competing forces on the interface. The inclined branch flow pulls the interface down, while the side branch pulls the interface up. Therefore, the small interfacial waves observed within the inlet could be the result of the dip oscillation emanating outwards rather than interfacial shear induced by the flowing gas phase within the inlet. Increasing V_{SL1} to 0.1 m/s, as shown in Fig. 5.10(iii), the interfacial waves within the inlet increased in size and frequency, approximately 0.5 to 1 mm in height. The wave frequency was such that it was beyond the capability of the digital camera, and images could not be captured to provide a more accurate description. A critical value of $Fr_B = 5$ was found to cause the OGE in the inclined branch, and at the same time the liquid was observed to be pulled up into the side branch. Just below the critical value of Fr_B , the OGE dip oscillations intensified as a result of the shortened distance between the side branch and the air-water interface. Compared to the single branch case, a slightly higher value of Fr_B was needed in order to induce the OGE in the inclined branch. This can be explained through the analogy of competing forces at the interface. With a reduction in the distance to the interface the gas flowing into the side branch exerts a greater upward force on the interface. In order to induce the OGE the liquid flowing into the inclined branch must therefore compensate with an increase in the downward

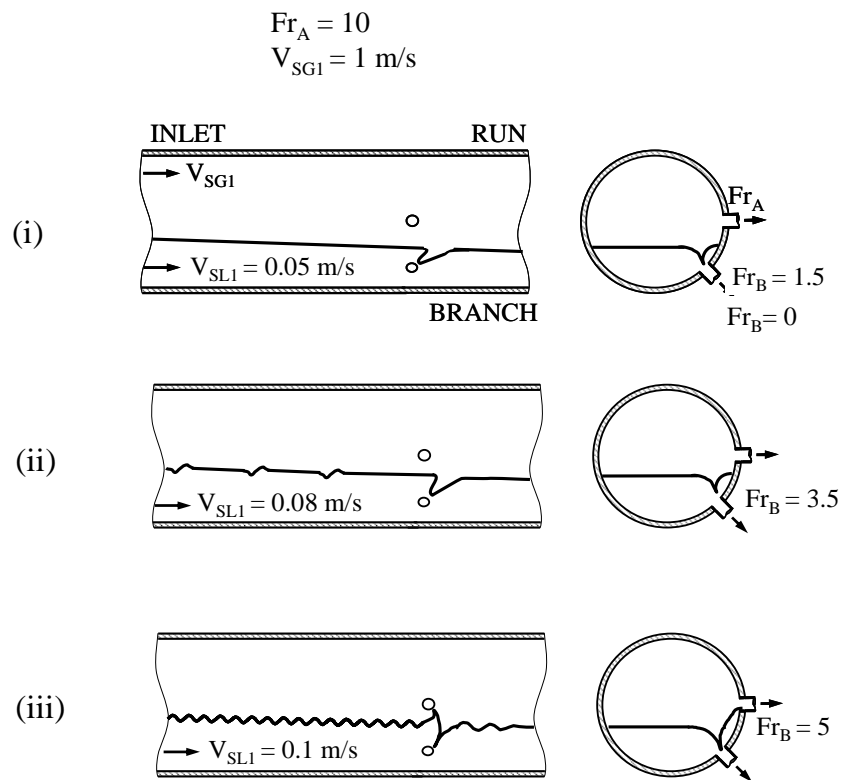


Figure 5.10: Sketches of the onset of gas entrainment at the inclined branch with a moderate value of Fr_A and variable inlet conditions.

force (Fr_B).

Side and Bottom Branches: Case 5

At low values of Fr_A , as was observed with the inclined branch, there is no appreciable change in the OGE mechanism in the bottom branch. Moderate values of Fr_A however, produce similar phenomena as found with the inclined branch. A value of $Fr_A = 10$ was used to test values of V_{SL1} at 0.05 m/s, 0.1 m/s and 0.15 m/s. The inlet superficial gas velocity is $V_{SG1} = 1$ m/s. The critical Froude number in the bottom branch was found for the associated flow conditions, and sketches of the related phenomena are provided in Fig. 5.11. In Fig. 5.11(i), with $V_{SL1} = 0.05$ m/s, the critical Froude number is found to be $Fr_C = 6$. The air-water interface within the inlet is relatively smooth, and there is minimal observed effect of the air flow through the side branch on the OGE dip. Increasing V_{SL1} to 0.1 m/s, in Fig. 5.11(ii), the OGE dip is shown to oscillate vertically, causing transient entrainment of the air in the bottom branch with Fr_C below the critical value. Increasing Fr_C to 12.9 resulted in steady entrainment. This is in contrast to the single branch case, with same V_{SL1} , where the critical Froude number was found as $Fr_C = 17$. Small waves were apparent on the air-water interface within the inlet, and as described for the inclined branch case, the initial wave formation could be a result of the OGE dip oscillations or interfacial shear. Increasing V_{SL1} to 0.15 m/s however, as shown in Fig. 5.11(iii), the wave height and frequency was found to intensify. The wave height was approximately 1 mm, and was suspected to be caused by the interfacial shear of the flowing gas phase within the inlet. The OGE dip oscillates vertically with transient entrainment of air

in the branch at values of Fr_C below the critical value. At a value of $Fr_C = 19.1$ the OGE was steady in the bottom branch. The air-water interface was close enough for a spout of water to be pulled up into the side branch.

The inlet flow regime has an impact on the critical branch Froude number as seen when comparing the bottom and inclined branch single and dual cases. Waves can be formed by either the OGE dip oscillation or interfacial shear induced by the flowing gas within the inlet. Using the bottom branch case illustrated in Fig. 5.11(iii) as an example, the transition from the wavy to slug regime will occur as V_{SG1} is increased, keeping V_{SL1} constant. This phenomenon is illustrated in Fig. 5.12. In Fig. 5.12(i) the flow conditions are as described in the bottom branch case, in Fig. 5.11(iii), that is for $V_{SL1} = 0.15$ m/s and $V_{SG1} = 1$ m/s. If V_{SG1} is increased, by either increasing Fr_A or increasing the gas mass flow rate in the run, \dot{m}_{G2} , the wave height can grow to the point where it touches the top of the pipe, as shown in the left side of Fig. 5.12(ii). Liquid accumulates behind the wave front causing a slug of liquid to form, as shown in Fig. 5.12(iii). The pressure difference on either side of the slug causes it to flow rapidly towards the low pressure side, from the inlet towards the run. This phenomenon was also observed in the single branch studies examined in Chapter 4.

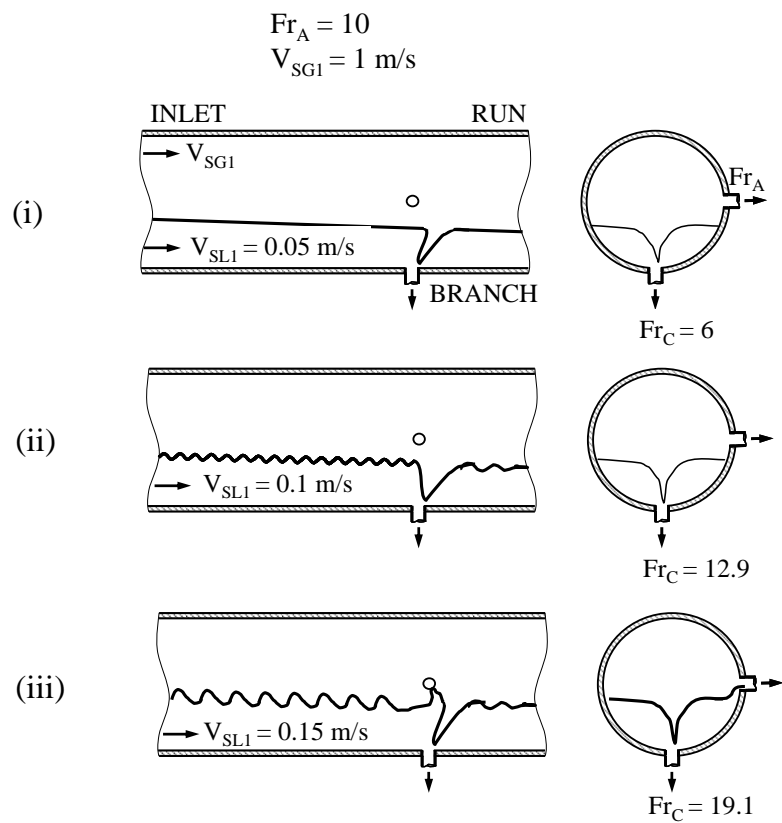


Figure 5.11: Sketches of the onset of gas entrainment at the bottom branch with a moderate value of Fr_A and variable inlet conditions.

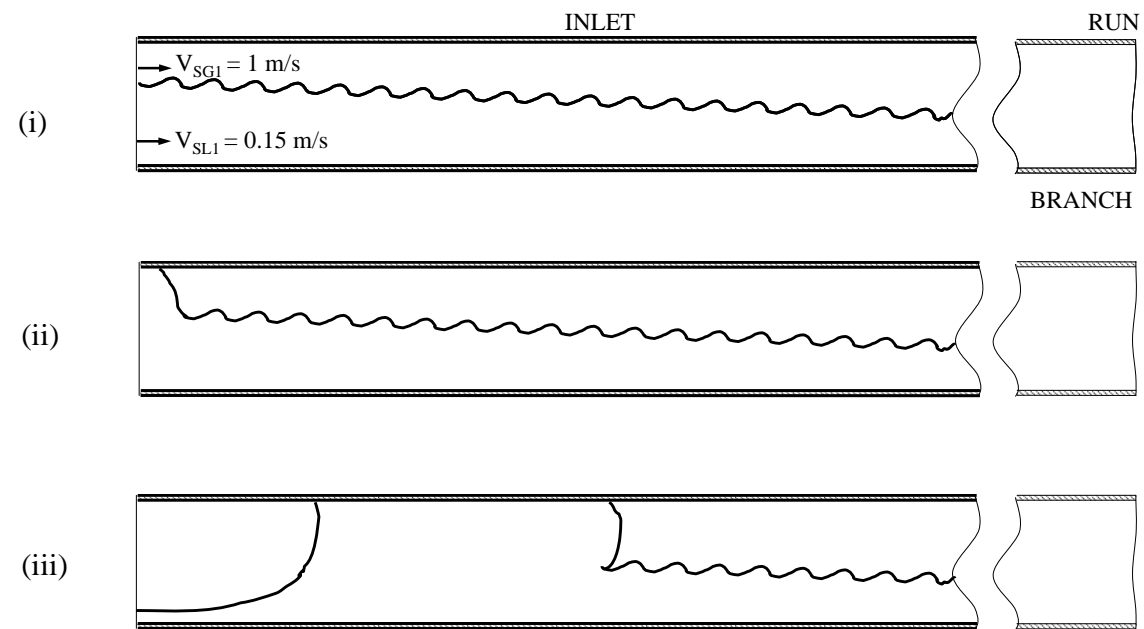


Figure 5.12: Sketches of the inlet flow during wavy to slug regime transition.

5.3.2 Critical Conditions at the Onset of Gas Entrainment

This section presents the results obtained from cases described in Table 5.1. The results are presented in Figs. 5.13 to 5.30. Each figure presents the relationship between the critical height (H_{OGE}/D), branch Froude numbers (Fr_A , Fr_B , Fr_C), and measurement location (λ/D) on the onset of gas entrainment in the inclined and bottom branches. In addition, each figure presents the relationship between the inlet height (H/D) measurement location (λ/D) and inlet superficial liquid and gas velocities, V_{SL1} and V_{SG1} , respectively.

To help interpret the figures presented in this section it is emphasized that H_{OGE}/D and H/D refer to the same measured interface height. These heights are measured relative to the bottom of the horizontal pipe at three distinct inlet locations measured relative to the branch, where λ/D equals -36, -17.5 and -5. Traditionally the critical height is measured relative to the branch inlet (Ahmad and Hassan, 2006; Bartley et al., 2008) since the phenomena is expected to be related to the vertical distance above the branch. This referencing methodology is practical in cases where the measured gas-liquid interface is stationary however in flowing systems it is more practical to adopt the channel bottom as the reference frame. The reason for this is that it allows the related OGE phenomena to be more readily correlated to the inlet conditions.

For example, at a branch Froude number of 8 the critical height at $\lambda/D = -5$ is found to be $H_{OGE}/D = 0.5$ in Fig. 5.13(a). Moving to Fig. 5.13(b), it can be found that at this interface height V_{SL1} is approximately 0.14 m/s, with $V_{SG1} = 0.3$

m/s constant from Table 5.1. From this single data point the superficial velocities can be used to compare the observed two-phase flow regime with existing empirical models, such as presented in Fig. 4.5. Alternatively, local inlet quantities that are dependent on the flow area, such as the average fluid phase velocities, or Reynolds and cross-flow Froude numbers, can be evaluated. These quantities may be used as empirical boundary conditions in future models, such as providing an estimate of the interfacial kinetic energy, or used to select appropriate models in order to estimate wall friction terms within the inlet.

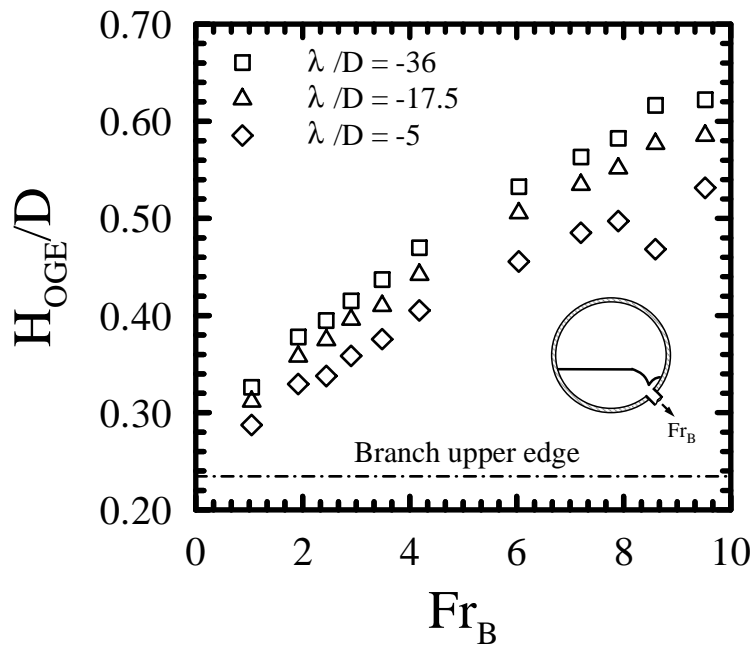
Methodology Validation: Single Branch Test

Measurements of the onset of gas entrainment in the inclined and bottom branches, which were investigated in Chapter 4, were repeated using the refined methodology outlined in §5.2 in order to verify that it yields similar results. The results are presented in Figs. 5.13 to 5.15.

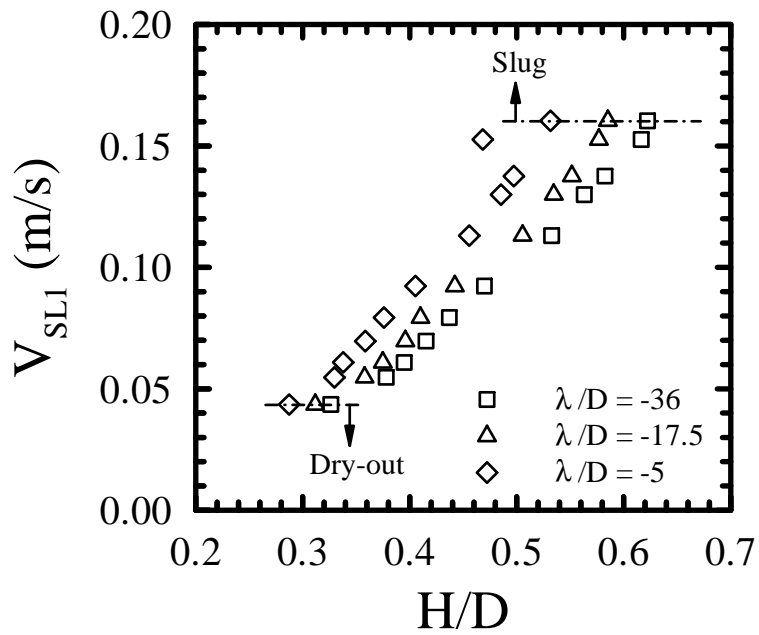
The critical conditions at the onset of gas entrainment in the inclined and bottom branch are presented in Figs. 5.13 and 5.14, respectively. In Figs. 5.13(a) and 5.14(a) the critical height is presented at the three locations upstream of the branch. In general, the further upstream of the branch the higher the value of H_{OGE}/D . The effect of branch orientation can be evaluated through use of the traditional referencing method employed in recent literature, that is the critical height is the vertical distance between the branch and two-phase interface (Ahmad and Hassan, 2006; Bartley et al., 2008). There is no change to the bottom branch critical height value, however for the inclined branch the reference height is at $H_{OGE}/D = 0.146$, which coincides with the

vertical distance from the bottom of the pipe to the inclined branch center. This value must be subtracted from the values of H_{OGE}/D in Fig. 5.13(a). For example with the inclined branch at $\lambda/D = -5$ and $Fr_B = 9.5$, the critical height is $H_{OGE}/D = 0.531$. The vertical distance from the branch center to the air-water interface, at this Froude number, is found to be $H_{OGE}/D = 0.385$, or alternatively 19.55 mm. Alternatively for the bottom branch case, and the same branch Froude number, the critical height is $H_{OGE}/D = 0.35$. The resulting vertical distance from the branch center to the air-water interface is 17.78 mm, a difference of 2.25 mm or $H_{OGE}/D = 0.044$. These two critical values occur at significantly different values of V_{SL1} , in the inclined branch it is found as 0.16 m/s while in the bottom branch as 0.07 m/s. As a result the liquid superficial velocity on the run side is found to be 0.125 m/s for the inclined branch and 0.034 m/s for the bottom branch. The run liquid superficial velocity is found as the difference in the inlet and branch liquid mass flow rates divided by the liquid density and total cross-sectional area of the pipe. What this points to is that although the critical heights found using the traditional referencing method are similar, the velocity at the interface can be quite different. From the modeling perspective, this would translate to differences in the interfacial kinetic energy terms at the inlet and dip.

The effect of measurement location, λ/D , can be evaluated by comparing two branch Froude numbers. For example in Fig. 5.13(a), at $Fr_B = 1$, comparing the three values of H_{OGE}/D a decrease of 0.04 is found between the height measured at $\lambda/D = -36$ with that at -5. On the other hand at $Fr_B = 9.5$ a reduction in H_{OGE}/D of 0.085 is found. This is because the air and water flow co-currently within the

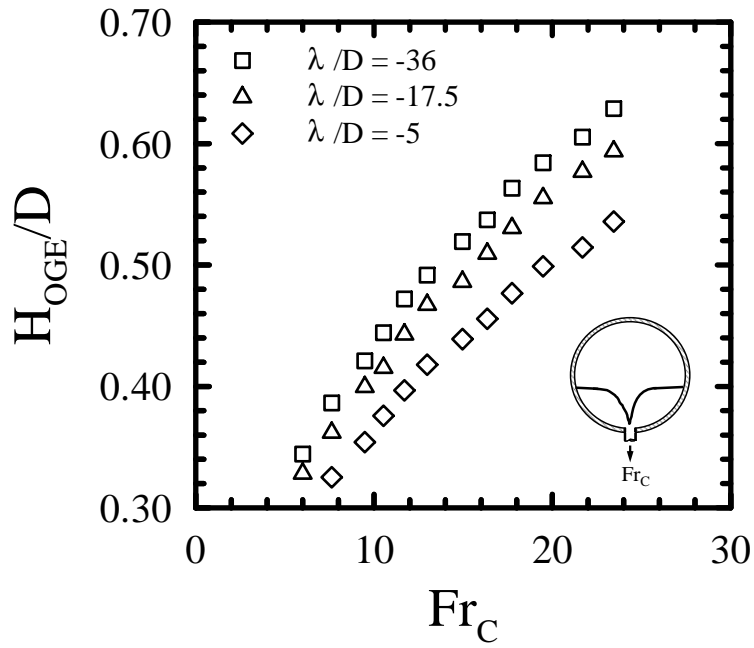


(a) Critical height

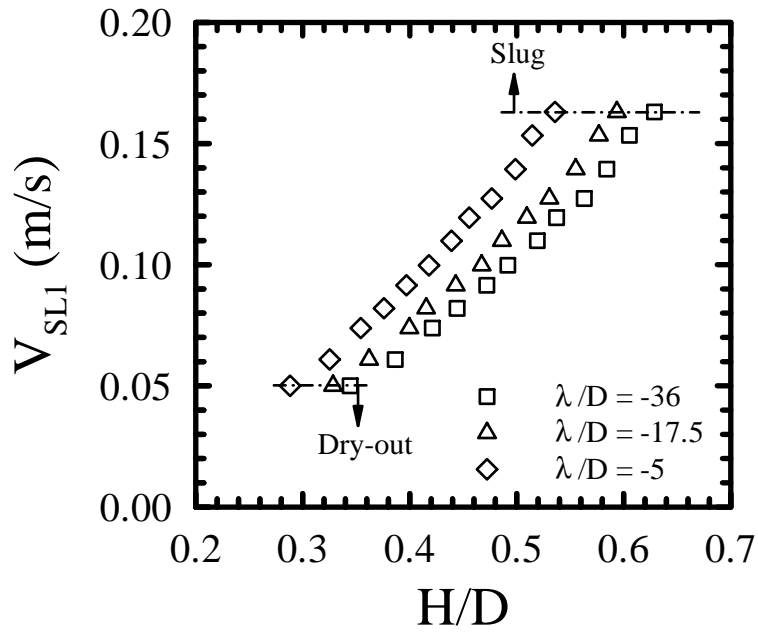


(b) Inlet conditions

Figure 5.13: The onset of gas entrainment at the inclined branch demonstrating the effect of measurement location, λ .



(a) Critical height



(b) Inlet conditions

Figure 5.14: The onset of gas entrainment at the bottom branch demonstrating the effect of measurement location, λ .

inlet, towards the branch, and as the fluid accelerates from the inlet towards the run a gradient in the interface height is naturally formed along the length of the pipe (Sadatomi et al., 1993). This is collaborated by Fig. 5.13(b) where the lowest interfacial gradient is found at the lowest inlet liquid superficial velocity, around $V_{SL1} = 0.04$ m/s, and the highest gradient at the upper limit where $V_{SL1} = 0.16$ m/s.

At the lower limit the portion of liquid that remains downstream of the branch, flowing into the run, is reduced to the point that accurate measurements of the run liquid mass flow rate using the outlet-TEE separator could not be performed. This lower limit is referred to as dry-out. At this lower limit the fluid velocity is also reduced, and begins to approach stagnation conditions, and therefore a smaller interfacial gradient is expected. Between the lower and upper limit the interface is in the smooth-stratified regime. Increasing V_{SL1} beyond the upper limiting value will cause a fast moving slug to propagate from the inlet to the run. The slug forms without wave formation, as the value of $V_{SG1} = 0.3$ m/s is relatively low, and the slug is a consequence of the smooth interface touching the top of pipe near the mouth of the inlet pipe where the liquid suddenly accelerates from a stagnant region. The upper and lower limits are not exact values, but represent the beginning of transition regions and where accurate measurements are not viable with the current experimental setup.

The effect of the measurement methodology is presented in Fig. 5.15. The two correlations developed in Chapter 4 for the critical height at the OGE in the inclined and bottom branches are presented along with the data recorded using constant inlet conditions (V_{SL1} , V_{SG1}) in the present chapter. Measurements at $\lambda/D = -5$ are shown since the correlations were developed from data at these locations. For the inclined

and bottom branches mean relative errors of 6.4% and 3.0% were found, respectively, when comparing the correlation and experimental values of H_{OGE}/D over the range of branch Froude numbers. The mean relative error was calculated as,

$$MRE(\%) = 100 \times \frac{1}{N} \sum_{i=1}^N \left| \frac{H_{OGE}(Experiment)_i - H_{OGE}(Correlation)_i}{H_{OGE}(Experiment)_i} \right| \quad (5.1)$$

In absolute terms this translates to a maximum error of approximately 1.5 mm at the highest Froude numbers. In Chapter 4 the uncertainty in H_{OGE} was estimated as 1 mm, and is subject to the observers own perception of the beginning of gas entrainment. Since the observer did not change in this case the incurred error is likely due to the differences in methodology.

A further comparison between the methodologies is presented for the inlet superficial liquid velocity in Fig. 5.15(b). The inclined and bottom branch data obtained using the constant inlet condition method is presented at two locations, $\lambda/D = -36$ and -5 , in comparison to the data obtained in Chapter 4 using the previous methodology. The present data shows that there is a marginal difference between the inclined and bottom branch data, a maximum difference of approximately 5%. The maximum uncertainty in V_{SL1} was estimated in Chapter 4 as 14%, so the difference is within the expected experimental uncertainty.

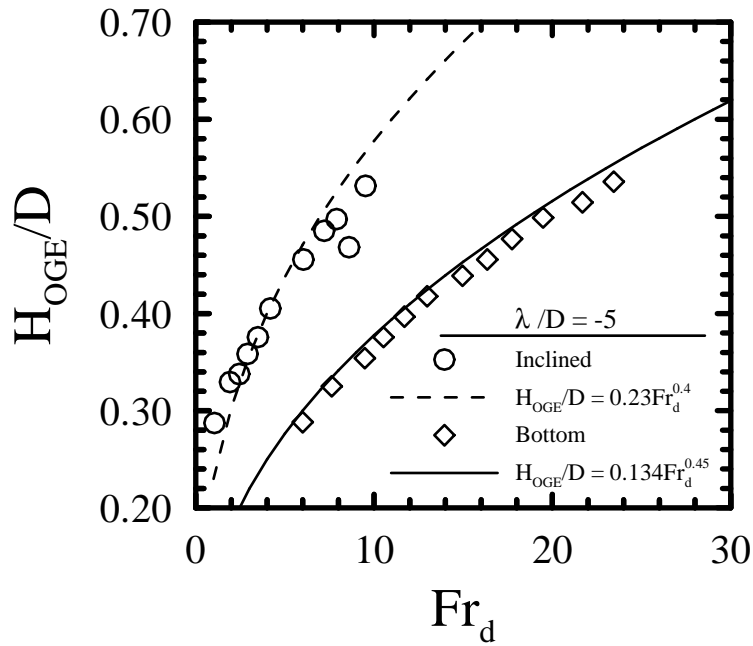
A more significant difference is found between the inclined and bottom branch data using the previous method from Chapter 4. The difference is on the order of 0.005 to 0.01 m/s, which translates to a maximum difference of approximately 20%, and is higher than the estimated uncertainty in V_{SL1} . Therefore the difference

observed in V_{SL1} is more likely due to the methodology rather than an effect of the branch flow conditions. The refined methodology of setting the inlet flow conditions constant (V_{SL1}, V_{SG1}) and varying the branch Froude number until the OGE occurs yields similar results with the previous method. There is, however, better control over the experiment, as evidenced in comparisons of V_{SL1} , and therefore this method is preferred and will be used throughout the dual branch cases.

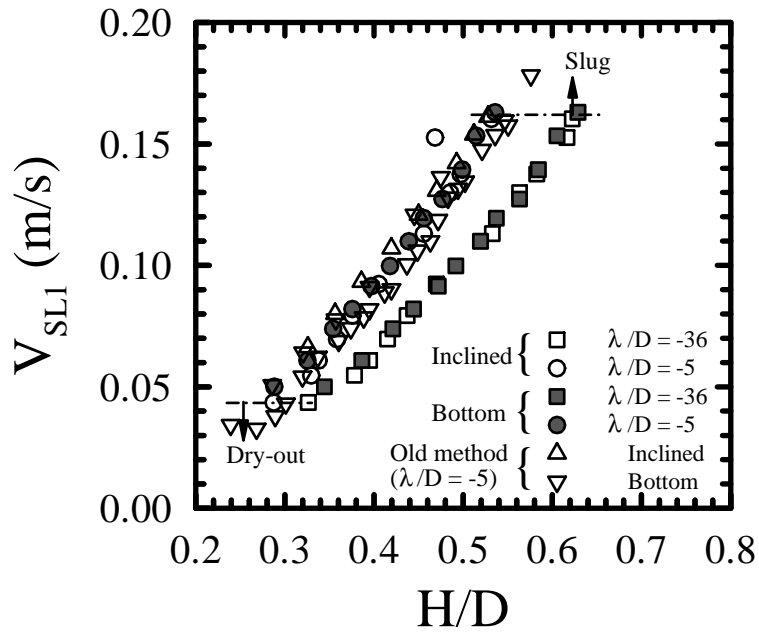
Case 1

The effect Fr_C on the OGE in the inclined branch is presented in Figs. 5.16 to 5.19. The first three figures demonstrate the effect of measurement location, λ/D , at constant values of Fr_C , while the fourth figure shows the effect of Fr_C at $\lambda/D = -5$.

In Fig. 5.16 a value of $Fr_C = 1$ was used, this is considered a low value since the ratio between the branch fluid inertia and gravity are on the same order of magnitude. As shown in Fig. 5.16(a), the range of Fr_B tested is always greater than or equal to one, and therefore the inclined branch Froude number is dominant in the liquid side flow field. Setting Fr_C equal to Fr_B , as in Fig. 5.17, the inclined branch Froude number is no longer dominant. However since it is located above the bottom branch, and is therefore closer to the air-water interface, air was always entrained into the inclined branch. At the upper limit, between $6 \leq Fr_B \leq 7$, a second dip was visible in the air-water interface near the bottom branch. Increasing Fr_C to 10, as in Fig. 5.18, ensured that it would dominate over the entire range of Fr_B . With $Fr_B > 1.2$ the OGE was observed to occur in the inclined branch with a second visible dip near the bottom branch. As Fr_B decreased from 7 the second dip near the bottom branch



(a) Critical height

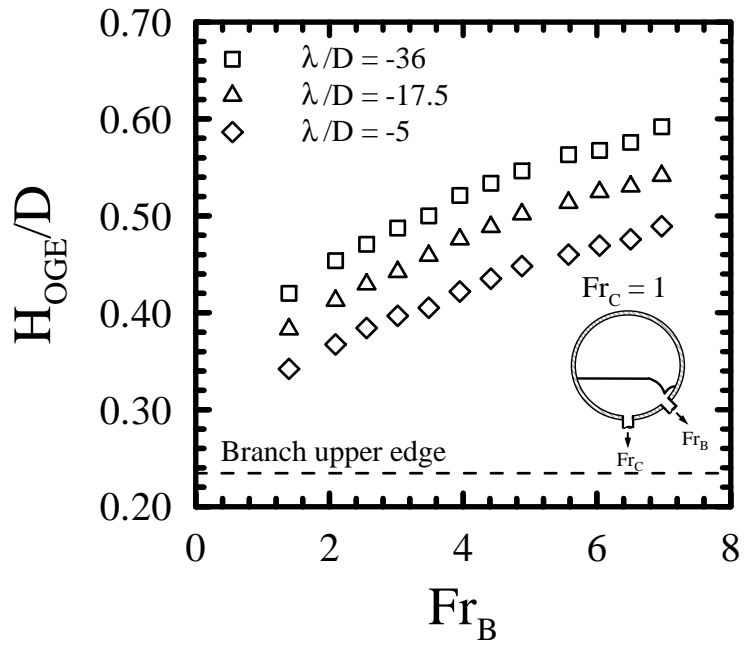


(b) Inlet conditions

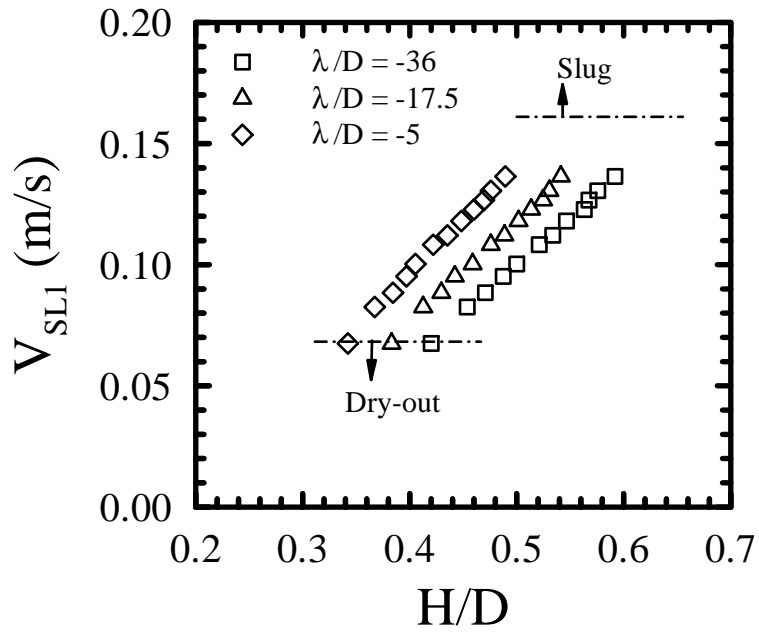
Figure 5.15: Effect of branch orientation and measurement methodology on the critical conditions at the onset of gas entrainment.

was observed to grow in size until, at $Fr_B = 1.2$, the second dip collapsed and air began to entrain into the bottom branch. At the same instant that air entrained in the bottom branch air also began to entrain into the inclined branch. This point is designated as Mode 3 in Fig. 5.18, which becomes the lower measurement limit at a value of V_{SL1} that is above dry-out. Comparing Figs. 5.16 to 5.18 with the single branch case in Fig. 5.13, there is a noticeable increase in the critical height at any measurement location as Fr_C increases. There is no significant change in the two-phase regime, the inlet is smooth-stratified, and values of V_{SL1} are comparable at the upper limit where the slug regime is encountered. The lower limit is affected however, and dry-out typically occurs at a much lower value of V_{SL1} than found with Mode 3. In all cases the interfacial development is presented according to the three measurement locations at $\lambda/D = -36, -17.5$ and -5 .

To demonstrate the effect of Fr_C on H_{OGE} , and V_{SL1} , the results recorded at $\lambda/D = -5$ are presented in Fig. 5.19. In general increasing Fr_C leads to an increase in H_{OGE}/D . This result is sensible since Fr_C provides an additional downward force, which is analogous to increasing Fr_B in the single branch case ($Fr_C = 0$). Somewhat surprising is that even at low values of Fr_C the effect on the critical height is evident. For example, comparing the $Fr_C = 0$ and $Fr_C = 1$ results in Fig. 5.19(a), the critical height is shown to increase where $Fr_B \leq 6$, it is most pronounced at low values of Fr_B , specifically where $Fr_B \leq 3$. In this low range H_{OGE}/D with $Fr_C = 1$ is higher than the single branch case ($Fr_C = 0$) by approximately 0.04. By comparison increasing Fr_B by a value of 1, over the same range of the single branch case, yields an increase in H_{OGE}/D of approximately 0.04. Therefore, the increase in the critical



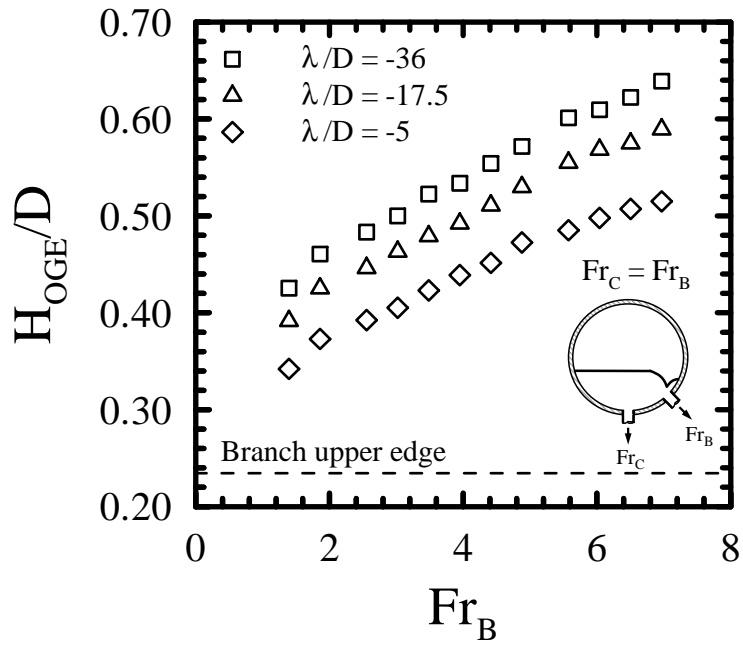
(a) Critical height



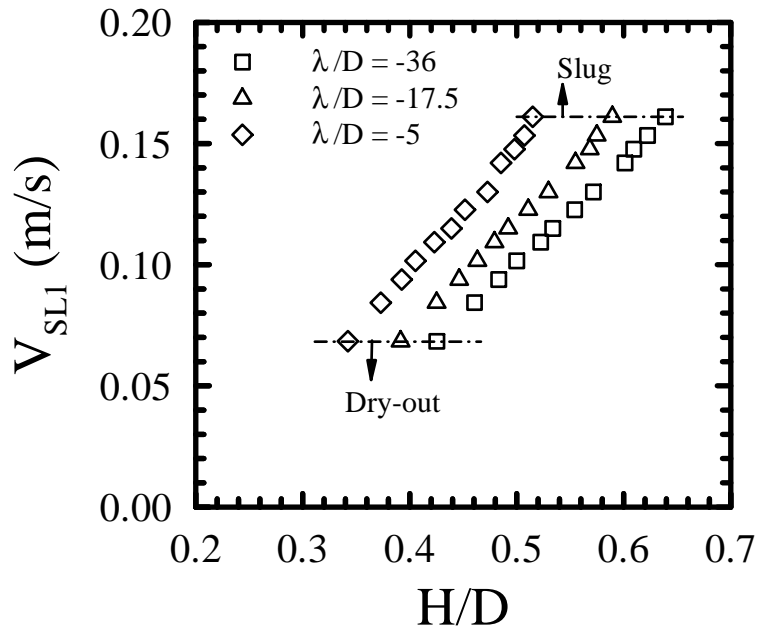
(b) Inlet conditions

Figure 5.16: Effect of measurement location, λ , on the OGE in the inclined branch with $Fr_C = 1$ (Mode 1).

height is sensible since an increase in Fr_B by 1 in the single branch case shows a similar increase, albeit over a limited range, in comparison to the dual branch case with $Fr_C = 1$. This is not to suggest that the effect of Fr_C on the critical height is this simple, as similar comparisons at higher values of Fr_C do not demonstrate the same linear behavior. For example, increasing Fr_C from 1 to 10 over the same low range of Fr_B yields an increase in H_{OGE}/D between 0.02 and 0.04, as Fr_B increases the effect of Fr_C on H_{OGE}/D diminishes. The increase in H_{OGE}/D is comparatively quite low to that exhibited with $Fr_C = 1$. A simple physical explanation for this is that the bottom branch flow provides an assisting downward force as well as a competing lateral force, which pulls the dip in its direction and away from the inclined branch. The lateral force becomes more significant with values of Fr_C well above Fr_B , which helps explain why at low values of Fr_B the increase in H_{OGE}/D between the $Fr_C = 1$ and $Fr_C = 10$ results are marginal. The effect of Fr_C on V_{SL1} is presented in Fig. 5.19 at two different locations, $\lambda/D = -36$ and $\lambda/D = -5$, respectively, and for simplicity only the minimum and maximum values of Fr_C are shown. Far upstream of the branch at $\lambda/D = -36$, over the entire range of H/D there is little or no effect of Fr_C on V_{SL1} . Physically this implies that far upstream the local average liquid velocity remains unaffected by the liquid flow accelerating into the branches. On the other hand, closer to the branch at $\lambda/D = -5$, and with a constant inlet liquid superficial velocity, the associated liquid height is shown to decrease with increasing Fr_C . This decrease in the liquid height, keeping V_{SL1} constant, points to an increase in the local average velocity. Therefore the acceleration of the liquid entering the branch affects the local velocity of the fluid five pipe diameters away, but has negligible influence

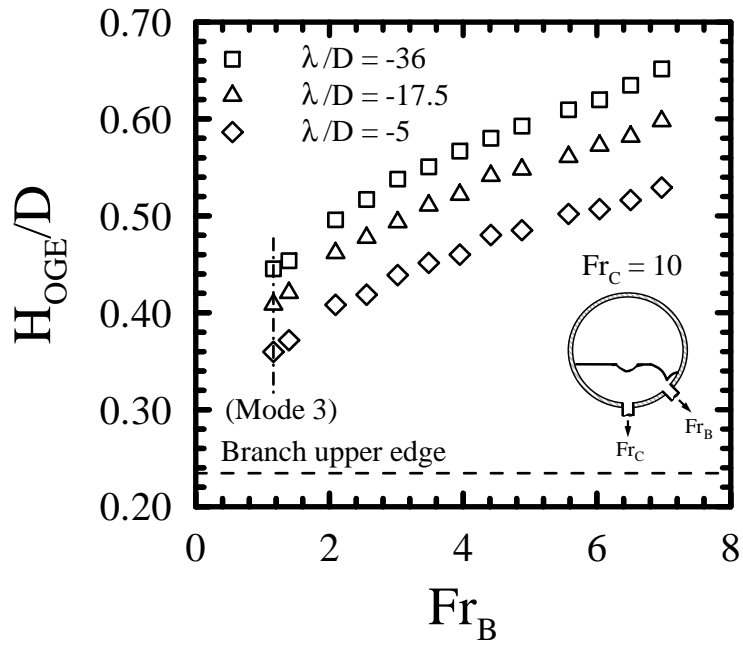


(a) Critical height

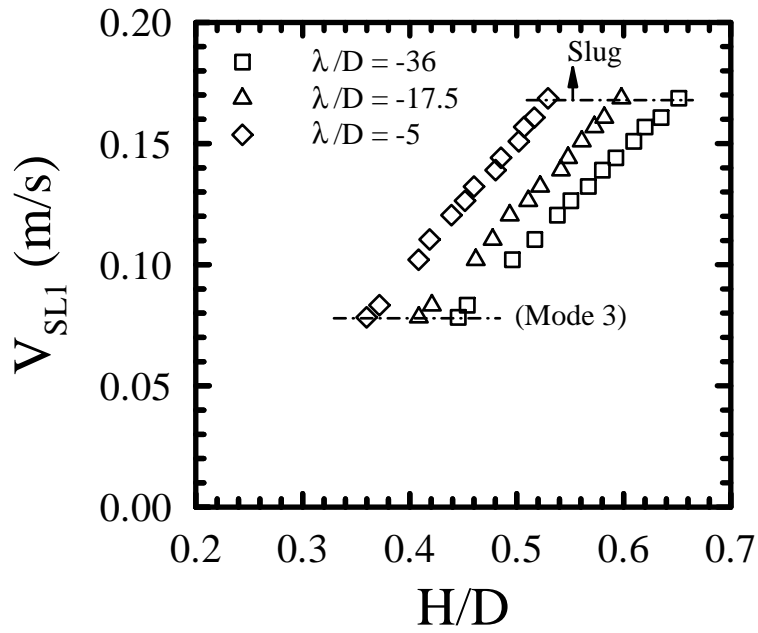


(b) Inlet conditions

Figure 5.17: Effect of measurement location, λ , on the OGE in the inclined branch with $Fr_C = Fr_B$ (Mode 1).



(a) Critical height



(b) Inlet conditions

Figure 5.18: Effect of measurement location, λ , on the OGE in the inclined branch with $Fr_C = 10$ (Mode 1).

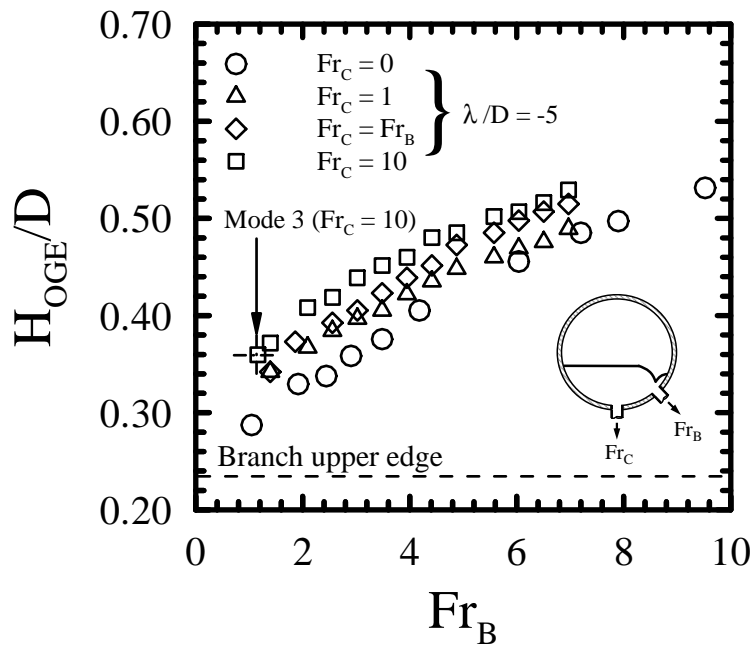
further upstream, at 36 pipe diameters. From a modeling point of view the critical height must be referenced according to a local velocity which may or may not be influenced by the fluid acceleration induced by the branch flow.

Case 2

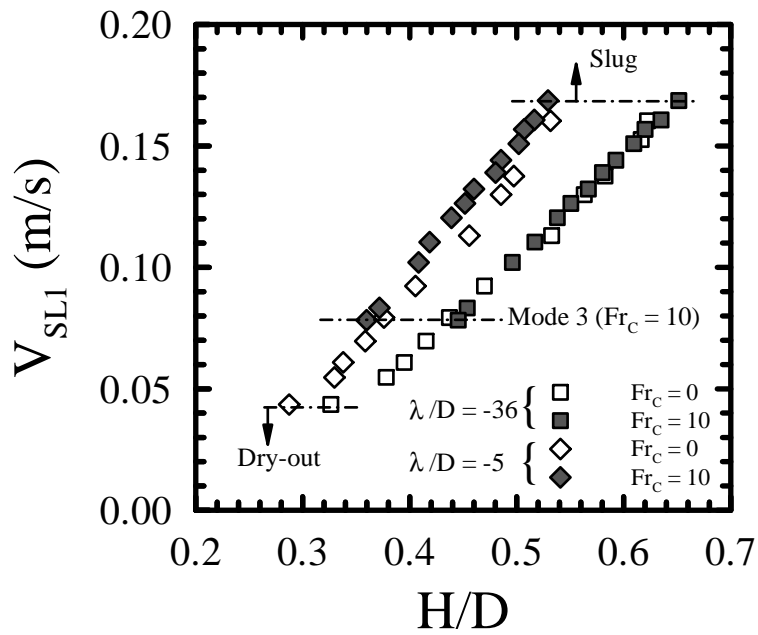
The second mode was described as the OGE in the bottom branch with liquid flowing in the inclined branch, this mode is investigated in Case 2. The effect Fr_B on the OGE in the bottom branch is presented in Figs. 5.20 to 5.22. The first two figures demonstrate the effect of measurement location, λ/D , at constant values of Fr_B , while the third figure shows the effect of Fr_B at $\lambda/D = -5$.

The single branch case in Fig. 5.14 showed a range of Fr_C between 6 and 24, and from Fig. 5.18 at $Fr_C = 10$ a value of $Fr_B = 1$ resulted in the OGE in both branches. At the lower limit, where $Fr_C = 6$, a value of $Fr_B < 1$ is necessary to ensure that the OGE occurs in the bottom branch only. With values of Fr_B lower than 1, however, gravity and surface tension forces become increasingly dominant over the branch fluid inertia (Bowden and Hassan, 2008). Decreasing Fr_B below 1 is a moot point if the effects of Fr_B on the OGE in the bottom branch are to be investigated. A value of $Fr_B = 1$ is therefore presented in Fig. 5.20 while a value of $Fr_B = 2$ is presented in Fig. 5.21.

Comparing the critical height measurements in Figs. 5.20 and 5.21 it is apparent that increasing Fr_B from 1 to 2 results in a shift in the dual onset point (Mode 3). With $Fr_B = 1$, Mode 3 is found with $Fr_C = 10$ as expected, while with $Fr_B = 2$ the dual onset point occurs at $Fr_C = 13$, with the difference in H_{OGE}/D of 0.06, or



(a) Critical height



(b) Inlet conditions

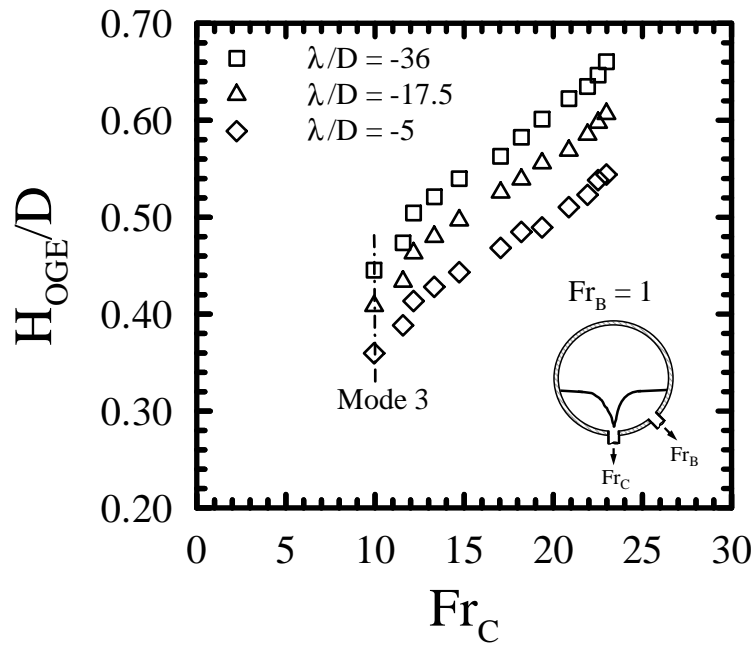
Figure 5.19: Effect of Fr_C on the OGE in the inclined branch at $\lambda/D = -5$ (Mode 1).

3.05 mm, at $\lambda/D = -5$. Mode 3 is therefore the lower limit of V_{SL1} in both cases, since lower values of V_{SL1} can only come as a result of decreasing H/D in this gravity driven liquid flow scenario. The two-phase inlet regime is smooth-stratified in both cases with the exception at the upper limit, around $V_{SG1} = 0.16$ m/s slug flow occurs. There is a marginal effect of Fr_B on the critical height, as shown in Fig. 5.22, however it is within the experimental uncertainty of H_{OGE}/D and can therefore be considered negligible. The main effect is the increase in H_{OGE}/D where the dual onset occurs. The effect on the inlet superficial liquid velocity is also negligible, from Fig. 5.22, which is shown in comparison to the single branch measurements ($Fr_B = 0$) at the location closest to the branch ($\lambda/D = -5$).

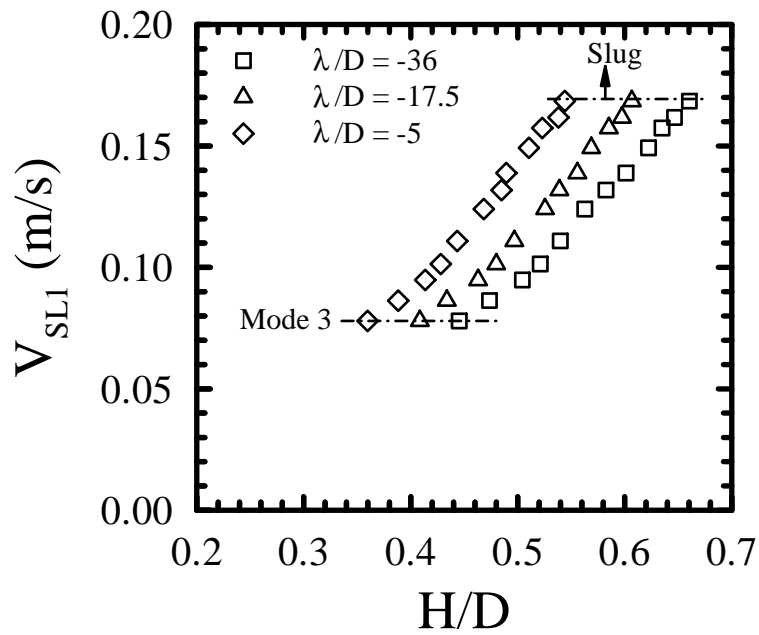
Case 3

Cases 1 and 2 presented the critical conditions of the first and second modes of gas entrainment during dual discharge. The third mode of gas entrainment, that is entrainment in both branches simultaneously, was observed under very limited conditions. The critical relationship between the associated flow conditions ($V_{SL1}, V_{SG1}, Fr_B, Fr_C$) and the critical height, H_{OGE}/D is investigated here. To obtain these points the procedure is similar to the previous two cases however, with the modification that both branch Froude numbers are slowly varied until the desired phenomenon occurs.

The critical conditions for the third mode are presented in Fig. 5.23 as a triple point curve. The branch Froude numbers are presented on the two ordinate axes with

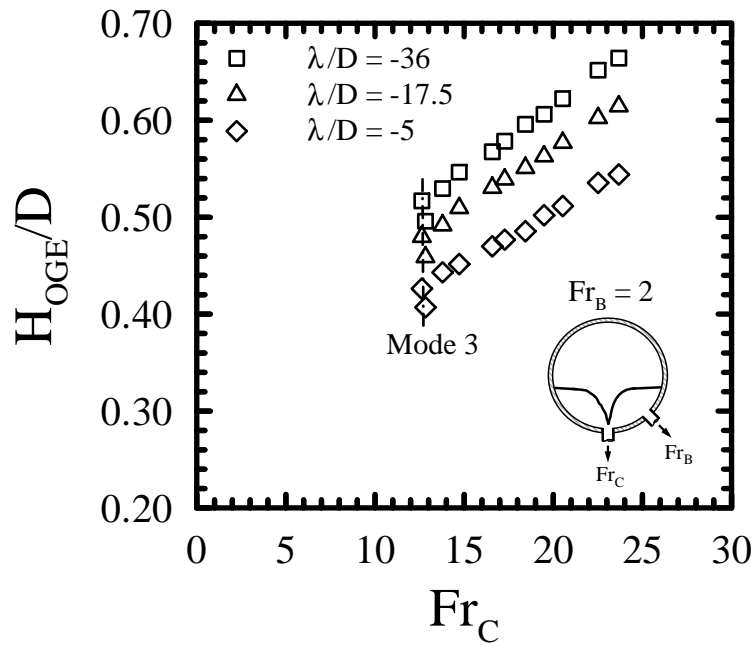


(a) Critical height

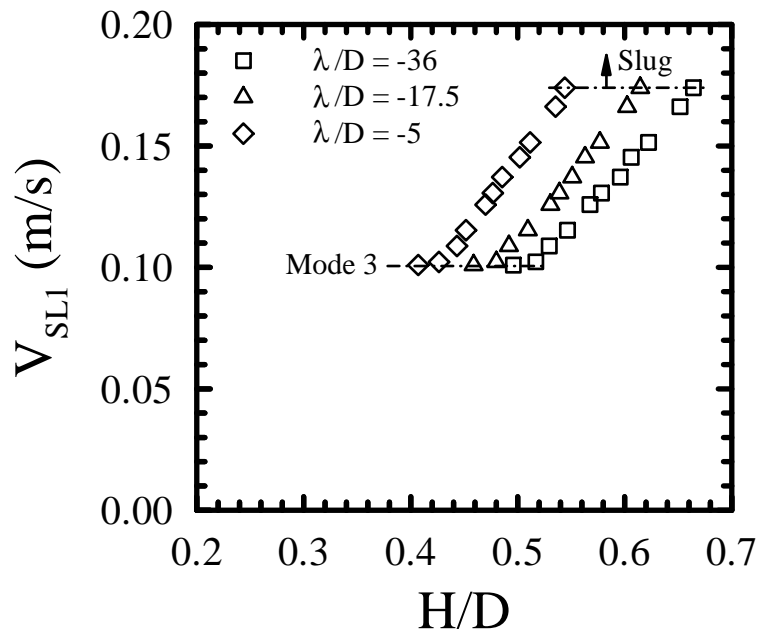


(b) Inlet conditions

Figure 5.20: Effect of measurement location, λ , on the OGE in the bottom branch with $Fr_B = 1$ (Mode 2).

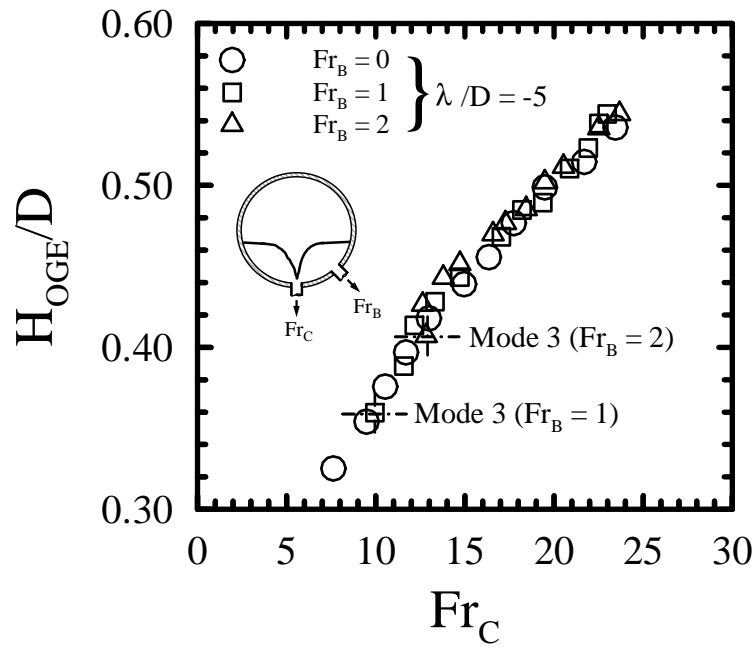


(a) Critical height

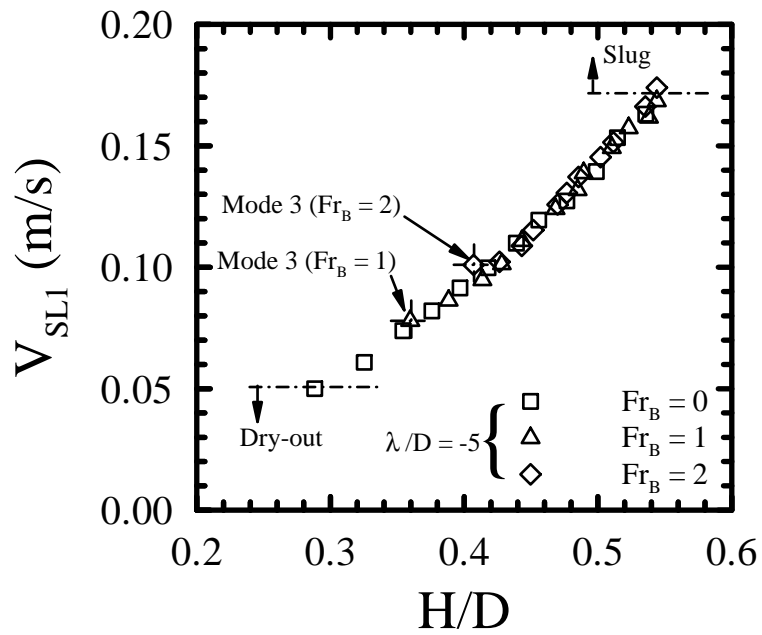


(b) Inlet conditions

Figure 5.21: Effect of measurement location, λ , on the OGE in the bottom branch with $Fr_B = 2$ (Mode 2).



(a) Critical height

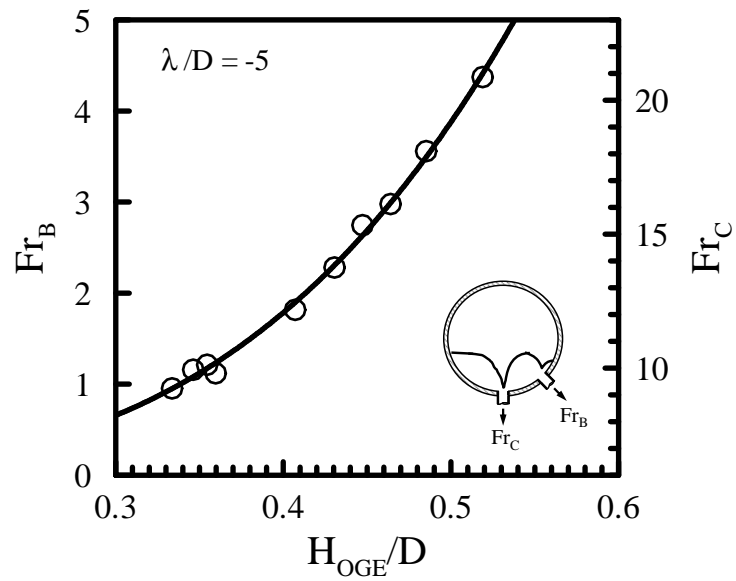


(b) Inlet conditions

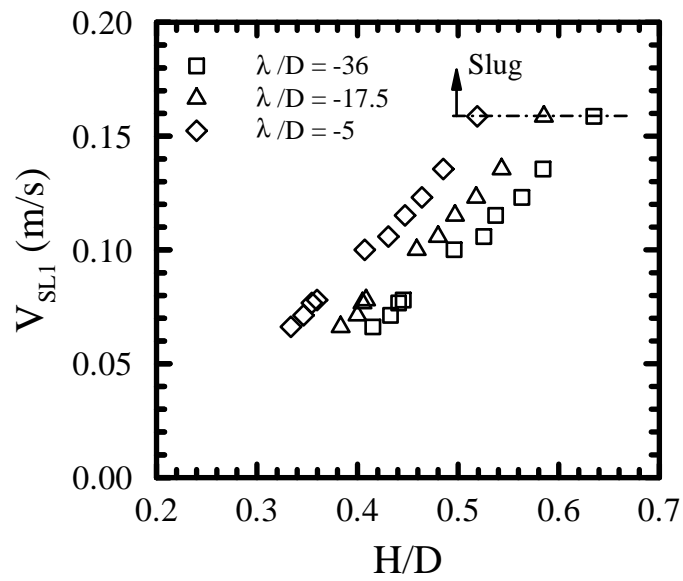
Figure 5.22: Effect of Fr_B on the OGE in the bottom branch at $\lambda/D = -5$ (Mode 2).

the corresponding inlet height presented along the abscissa. Only the height measurements obtained at $\lambda/D = -5$ are presented, but similar curves may be obtained for the other two locations. The recorded values span the full physical range, with the lower limit coinciding with $Fr_B = 1$ in Fig. 5.23(a) and the upper limit relating to the transition of the smooth-stratified to the slug regime in Fig. 5.23(b).

To help interpret the third mode of entrainment results, a map of the three modes was developed in Fig. 5.24. This was done by combining results from Cases 1 and 2, along with the results from Case 3. The symbols connected by dashed lines indicate a constant inlet condition; V_{SL1} is used since H is known to vary with the measurement location. A smooth curve is drawn through the dual onset data points identified in Fig. 5.23. Above this line the OGE occurs in the bottom branch, while below this line it occurs in the inclined branch. Along a constant V_{SL1} line the split of liquid mass flow rate between the two branches is indicated by values of Fr_B and Fr_C , respectively. Taking $V_{SL1} = 0.1$ m/s as an example, the first symbol on the left ordinate axis indicates the single branch case where $Fr_B = 0$ and OGE is in the bottom branch. With increasing Fr_B along the dashed line the transition boundary is encountered around $Fr_B = 3.75$. At this point the OGE occurs in both branches. Between $Fr_B = 0$ and $Fr_B = 3.75$, Fr_C does not vary significantly, as expected due to the relatively low values of Fr_B in comparison to Fr_C . Increasing Fr_B to the right of the transition curve the OGE occurs in the inclined branch only. There is a significant reduction in Fr_C , from 18 to 0, over a relatively small increase in Fr_B , from 3.75 to 7.2. The final right most data point on the dashed line is the single inclined branch case where $Fr_C = 0$.



(a) Critical height at $\lambda/D = -5$



(b) Inlet conditions

Figure 5.23: Critical conditions at the simultaneous OGE in the inclined and bottom branches (Mode 3).

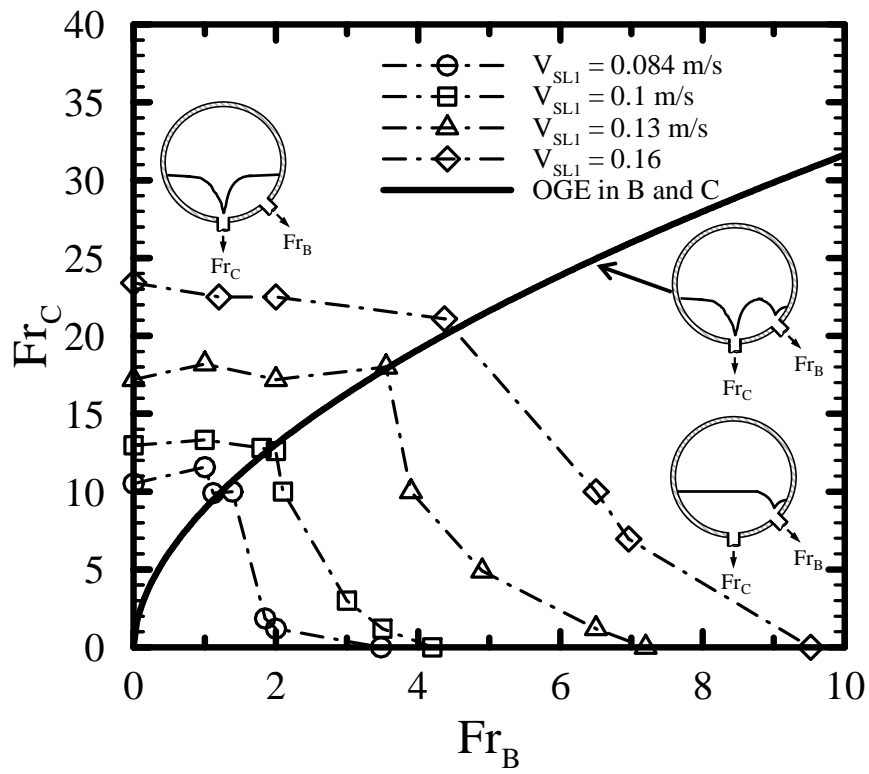


Figure 5.24: Map of dual onset conditions in the inclined and bottom branches (Modes 1, 2 and 3).

Case 4

The critical height is measured at various points using differential pressure transducers. These devices have a very low response time and are not intended for transient measurements. As a result there is an additional uncertainty introduced into the measurement of the critical height in the presence of small waves using these devices. Waves were estimated to be on the order of 0.5 to 1 mm in height. Coupling this with the uncertainty estimate under steady conditions, using the method outlined by Kline and McClintock (1953), results in an uncertainty of 1.4 mm when small waves are present. If waves were observed to cause unreasonably high fluctuations on the differential pressure gages, or in the run liquid mass flow rate, \dot{m}_{L2} , the measurements were classified as having low accuracy and were rejected from the data set. This same reasoning was used in reference to Case 5 below.

The effect of Fr_A on the OGE in the inclined branch, Case 4, is presented here. The air-water interface is located between the two branches, with air flowing in the side branch and water flowing in the inclined branch. The effect of measurement location is presented in Fig. 5.25 with $Fr_A = 1$ and in Fig. 5.26 with $Fr_A = 10$. Air and water flow co-currently within the inlet and split at the branch, with the remainder flowing into the run. Increasing the side branch gas Froude number increases the inlet superficial gas velocity above the initial condition ($V_{SG1} = 0.3$ m/s). A value of $Fr_A = 1$ increases V_{SG1} to 0.4 m/s while a value of $Fr_A = 10$ increases V_{SG1} to 1 m/s. The consequence, as discussed in the flow visualization section, is that the two-phase inlet regime may become wavy-stratified.

The height of the lower edge of the side branch, and the height of the inclined branch upper edge, are included in the figures to provide a physical reference to which the measurements can be compared against. In Fig. 5.25(a) the furthest two measurement points upstream from the branch, $\lambda/D = -36$ and -17.5 , with $Fr_B = 4.2$, indicates that the air-water interface is above the side branch entrance. As the water accelerates from the inlet towards the run the interface height gradually decreases, and measurements show that closer to the branches the interface is actually below the side branch entrance. Local to the branch however, due to the OGE dip shape, the interface can be considerably lower than the side branch entrance. The inertia of the flowing gas phase entering the side branch is insufficient to cause the water to entrain into the branch in this case. With an increase in Fr_A to 10 however, in Fig. 5.26(a), there is a small reduction in H_{OGE}/D at $\lambda/D = -36$ and -17.5 in comparison to the side branch edge at $Fr_B = 4.2$. Increasing Fr_B to 5, the interface height at the OGE in the inclined branch increases to the point that the water begins to entrain into the side branch (OLE). Under these conditions however, small waves begin to form within the inlet, as indicated in Fig. 5.26(b).

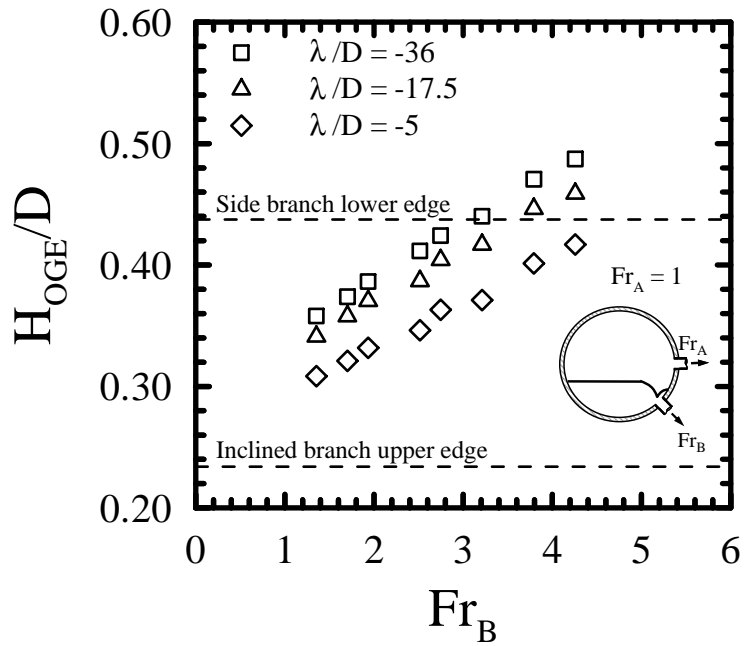
The effect of Fr_A on H_{OGE}/D , at $\lambda/D = -5$, is presented in Fig. 5.27. The critical height is shown to be unaffected below $Fr_B < 4$, where the interface remains relatively smooth. Above this, between $4 \leq Fr_B \leq 5$, an increase in Fr_A shows a marginal change in the critical height, for example at $Fr_B = 4.2$ a decrease in H_{OGE}/D of 0.02 (1.02 mm) is observed. This value happens to be close to the wavy regime transition, and is lower than the estimated uncertainty, and therefore is considered as data scatter resulting from the presence of small waves. There is little

effect of increasing V_{SG1} on V_{SL1} as shown in Fig. 5.27(b). The main difference is that at $V_{SG1} = 1$ m/s wavy flow occurs near $V_{SL1} = 0.1$ m/s while at $V_{SG1} = 0.4$ m/s, the inlet air-water interface remains smooth-stratified.

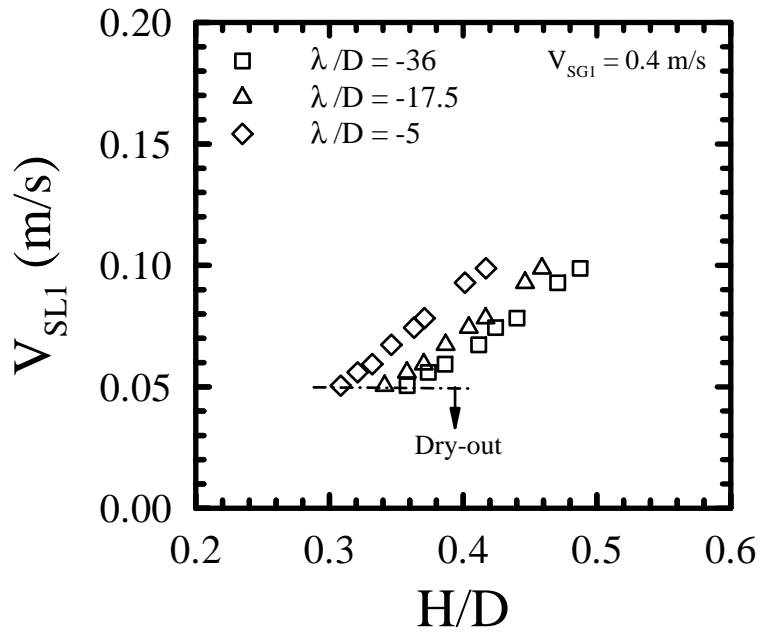
Case 5

The same values of Fr_A were tested at the OGE in the bottom branch, the effect of measurement location is presented in Fig. 5.28 and Fig. 5.29 at values of $Fr_A = 1$ and 10, respectively. The effect of Fr_A on H_{OGE}/D and V_{SL1} is presented in Fig. 5.30 at $\lambda/D = -5$.

Interestingly, at values of $Fr_C \geq 14$ the critical height is shown to be above the side branch lower edge at all upstream locations, however water did not entrain into the side branch. The reason for this is that the dip formed by the water flowing in the bottom branch causes a significant decrease in the local interface height, as shown in Fig. 4.6. With a low value of $Fr_A = 1$ the inertia of the air flowing into the side branch is insufficient to pull the flowing water into the branch. At $Fr_A = 10$, however, the air flowing into the side branch has enough inertia to pull the water up into the branch at approximately $H_{OGE}/D = 0.53$ ($\lambda/D = -5$). As was found in Case 4, increasing Fr_A to 10 causes the inlet superficial gas velocity to increase to 1 m/s. The air-water interface within the inlet began to exhibit small waves at around $V_{SL1} = 0.1$ m/s, similar to Case 4, with $H_{OGE}/D = 0.43$, however the OLE in the side branch did not occur until around $H_{OGE}/D = 0.53$ ($\lambda/D = -5$). The wave height visibly increased as H/D increased above 0.43, therefore between $0.43 \leq H_{OGE}/D \leq 0.53$ the air-water interface went through a transition from smooth-stratified to wavy-stratified. The slug

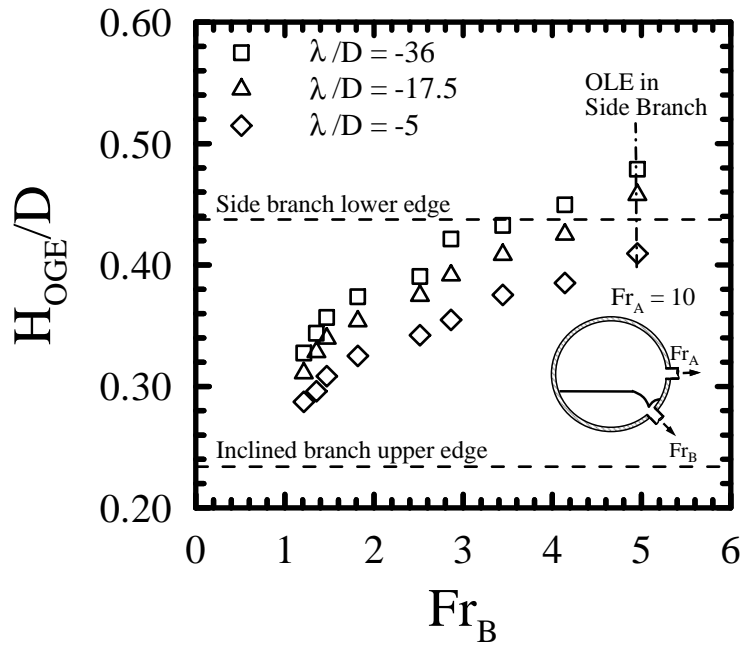


(a) Critical height

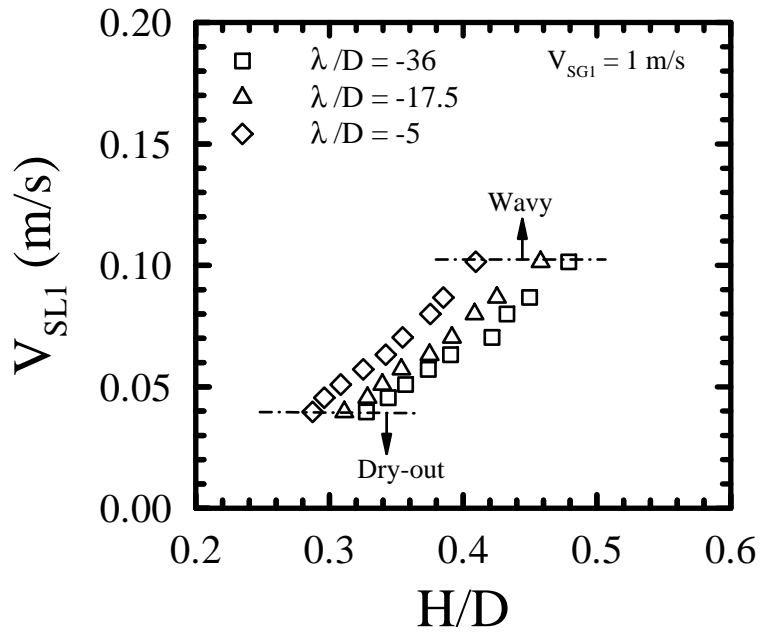


(b) Inlet conditions

Figure 5.25: Effect of measurement location, λ on the OGE in the inclined branch with $Fr_A = 1$.

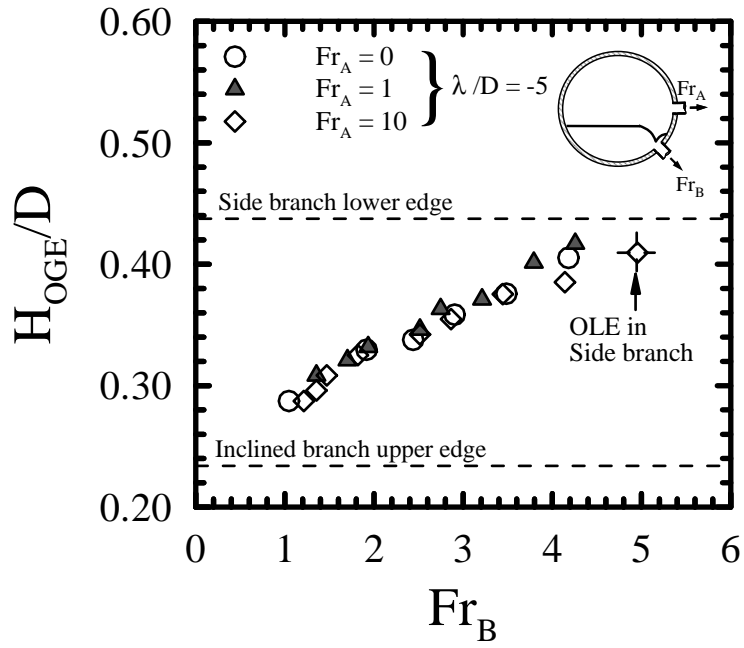


(a) Critical height

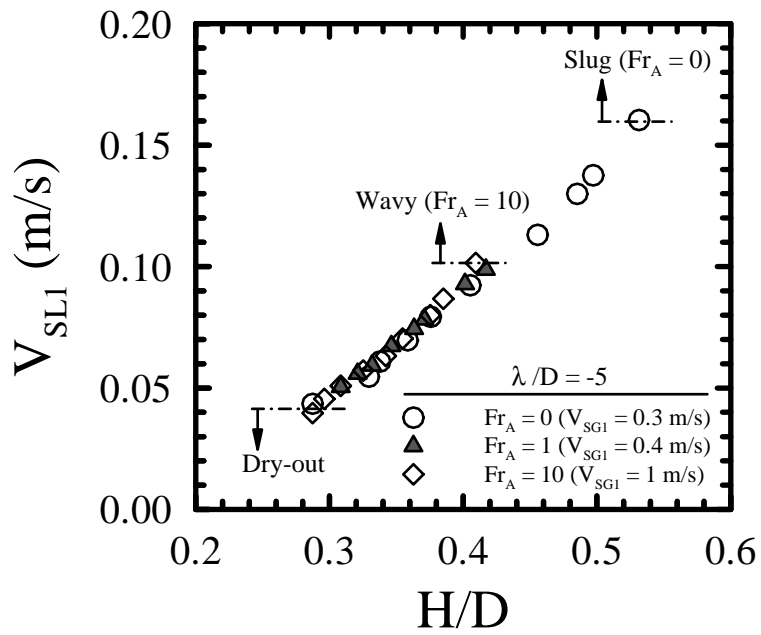


(b) Inlet conditions

Figure 5.26: Effect of measurement location, λ on the OGE in the inclined branch with $Fr_A = 10$.



(a) Critical height



(b) Inlet conditions

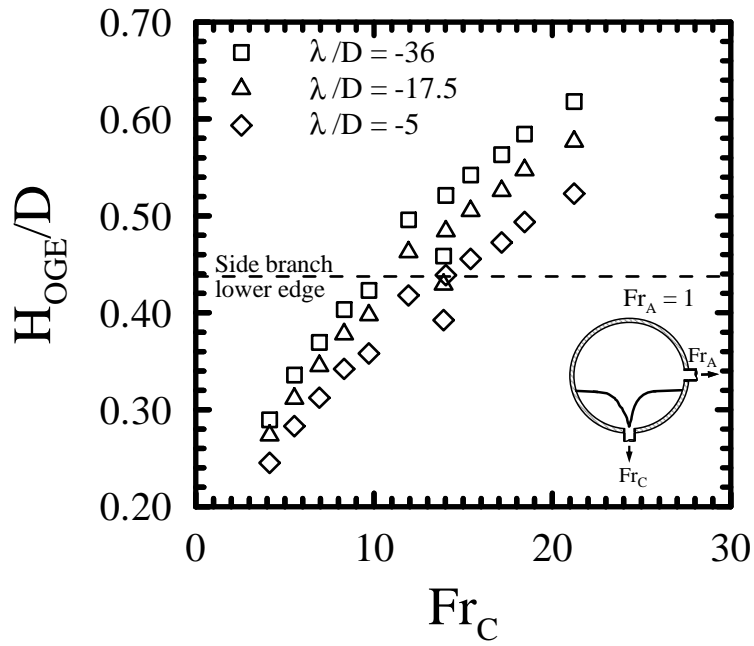
Figure 5.27: Effect of Fr_A on the OGE in the inclined branch at $\lambda/D = -5$.

regime at the upper limit, depicted in Figs. 5.28(b) and 5.29(b), comes as a result of two different interface conditions. With $V_{SG1} = 0.4$ m/s the air-water interface was smooth-stratified while with $V_{SG1} = 1$ m/s it was wavy-stratified. Similar to Case 4, there is no significant effect of Fr_A on H_{OGE}/D in the bottom branch. Minor differences do occur at higher values of V_{SL1} and V_{SG1} , but these are due to data scatter caused by the wavy interface, as shown in Fig. 5.30. The main effect of Fr_A is on the inlet two-phase regime transition. With $Fr_A = 0$ and 1, the inlet superficial gas velocity is relatively low, and therefore the interface remains smooth-stratified.

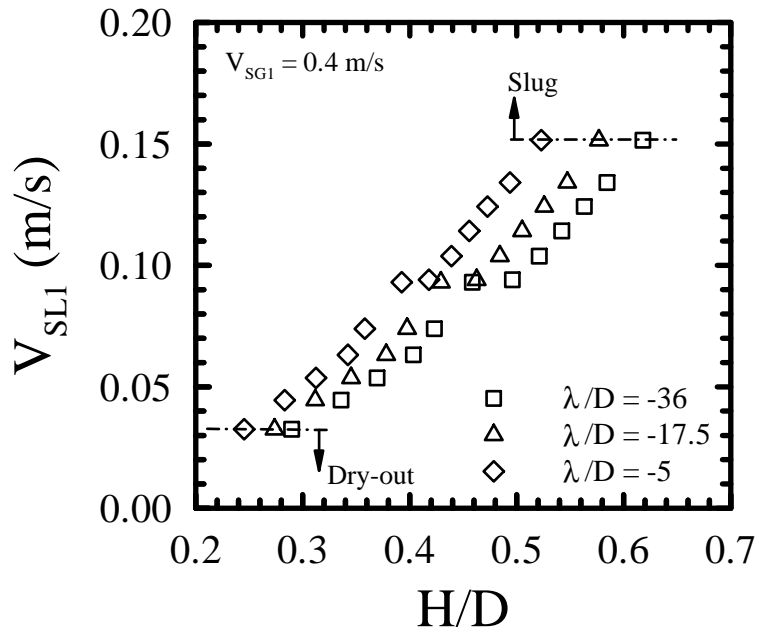
5.3.3 Comparison with Existing Studies

In this section the present dual experimental results are compared with existing theoretical models, empirical correlations, and experimental data sets. Comparison to existing single branch studies were covered in Chapter 4, however these were limited to comparisons for the specific branch orientations. A recent study by Bartley et al. (2008) demonstrated the effect of branch orientation on the critical height in a single branch. For completeness, the present single branch results are compared with Bartley et al. (2008)'s results. The dual branch comparisons cover the three modes of gas entrainment. In Fig. 5.32 and 5.33 comparison of the Mode 1 (Case 1) results are presented, in Fig. 5.34 comparison of the Mode 2 results (Case 2) are presented, and in Fig. 5.34 comparison of the Mode 3 results are presented.

Several studies were conducted using flat walls (Parrott et al., 1991; Hassan, 1995; Bartley et al., 2008), with the critical height being referenced to the branch center.

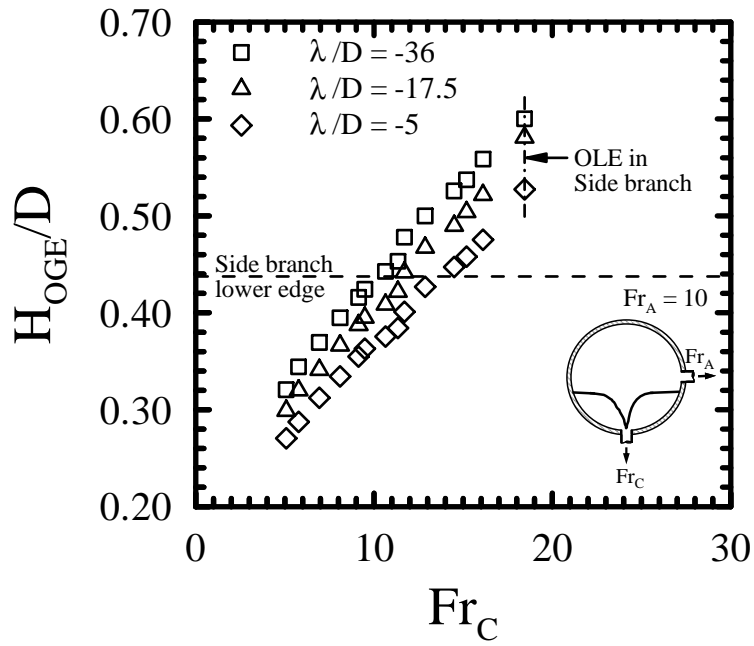


(a) Critical height

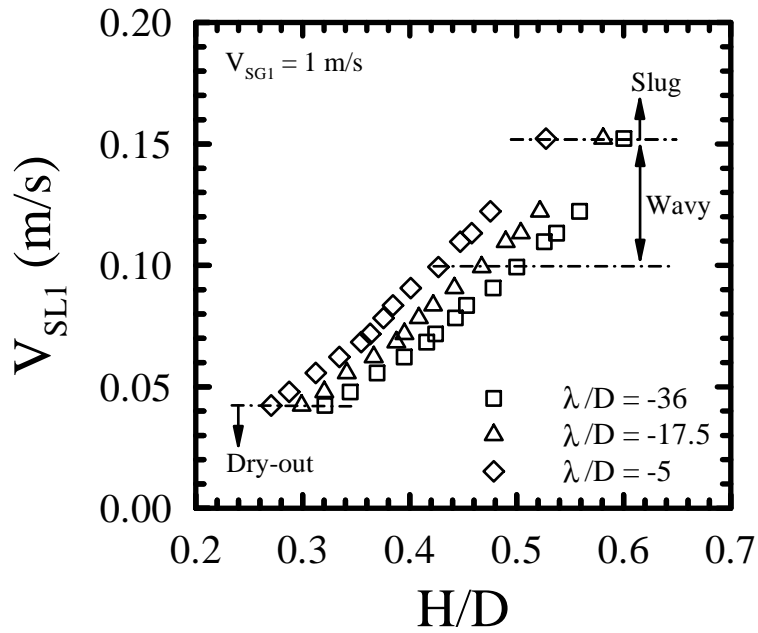


(b) Inlet conditions

Figure 5.28: Effect of measurement location on the OGE in the bottom branch with $Fr_A = 1$.

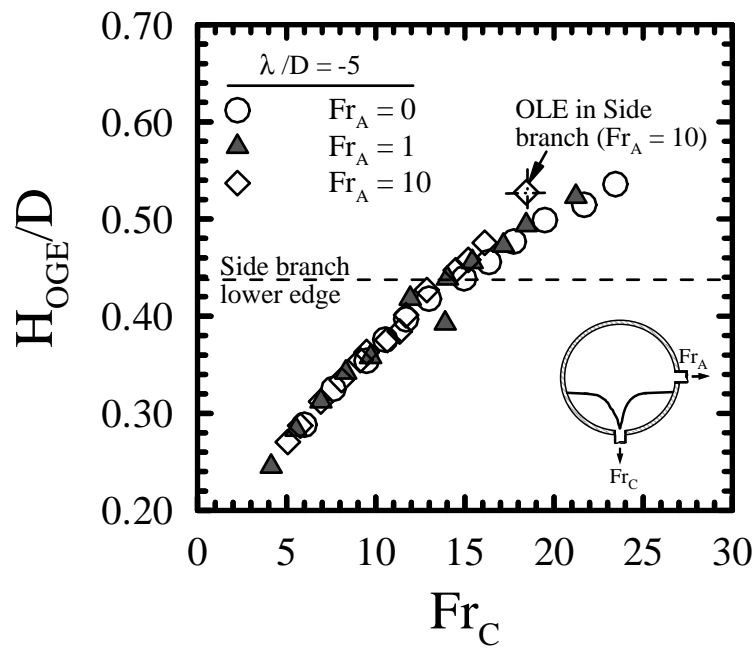


(a) Critical height

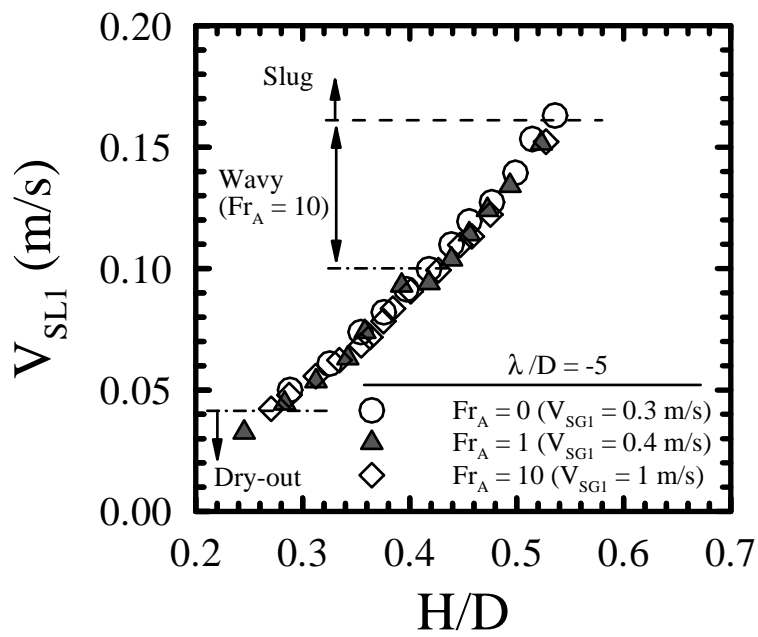


(b) Inlet conditions

Figure 5.29: Effect of measurement location on the OGE in the bottom branch with $Fr_A = 10$.



(a) Critical height



(b) Inlet conditions

Figure 5.30: Effect of Fr_A on the OGE in the bottom branch at $\lambda/D = -5$.

To provide useful comparisons the critical height is presented in this section using the same referencing method, with the only change coming to the inclined branch results.

In order to achieve this a constant defined by,

$$\frac{D}{2} - \frac{D}{2} \sin \frac{\pi}{4} \quad (5.2)$$

is subtracted from the critical height H_{OGE} value, and then non-dimensionalized using the branch diameter, d , as H_{OGE}/d .

Single Branch: Effect of Branch Orientation

Bartley et al. (2008) performed experiments with a 6.35 mm branch that was machined perpendicularly into a flat wall, and exposed to a large stratified air-water reservoir. Their test section design was unique since it permitted the flat wall to be oriented at various angles above and below the interface. They examined the critical height at the onset of gas and liquid entrainment at the various wall angles. They developed an empirical correlation for the OGE according to,

$$\frac{H_{OGE}}{d} = 0.475 Fr^{0.444}, \quad (5.3)$$

for a flat vertical wall, or an inclination of 0 degrees from vertical. They found that the critical height only varied by a maximum of 15% for a vertical, inclined, or horizontal wall over a range of low, moderate, and high branch Froude numbers.

Two data sets were selected for comparison, the horizontal wall (bottom oriented

branch), and inclined wall (inclined branch at 30 degrees from horizontal) results. These are presented in Fig. 5.31 along with the present critical height measurements using the inclined and bottom branches. Examining the data sets from each study individually first, it is evident that there is similarity in the effects of branch inclination, with the difference in H_{OGE}/D within 10% at overlapping Froude numbers. Comparing the two studies however, for either branch orientation, the critical height is significantly higher in the present results than found in Bartley et al. (2008). The reason for this difference is due to the inlet liquid crossflow velocity. This can be illustrated by considering that the inlet superficial liquid velocity decreases with decreasing height. At low values of H_{OGE}/d the present data approaches stagnation conditions, as $V_{SL1} \rightarrow 0$, and consequently converges on the stagnant reservoir critical height results provided by Bartley et al. (2008). Take for example a branch Froude number of 20, the approximate difference in H_{OGE}/d between Bartley et al. (2008) and the present results is on the order of $H_{OGE}/d = 2$, or more simply 12.7 mm. On the other hand at a branch Froude number of 2, the difference decreases to $H_{OGE}/d = 0.7$, or 4.4 mm. Between these points V_{SL1} decreases from 0.14 m/s to nearly 0.05 m/s. The effect of the inlet crossflow velocity is also applicable to the dual branch cases.

Dual Discharging Branches: Modes 1, 2, and 3

Parrott et al. (1991) had conducted experiments with two 6.35 mm diameter branches machined perpendicularly into a flat vertical wall, the branches were located in the same vertical plane. They tested several vertical separating distances between the

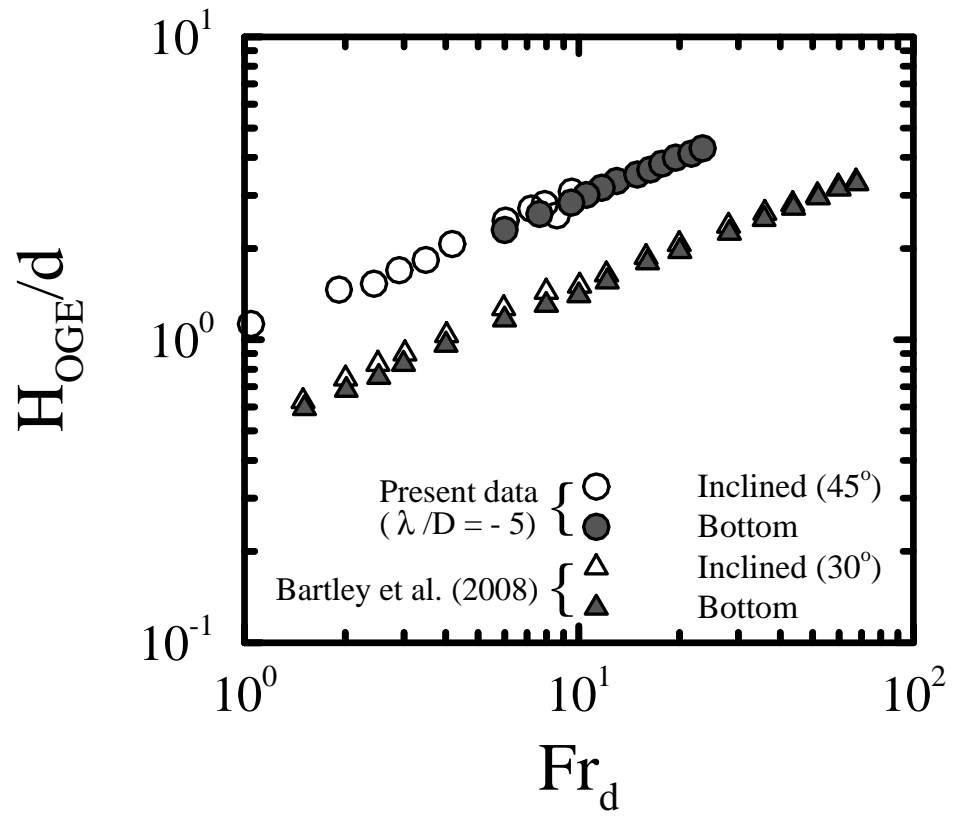


Figure 5.31: Effect of branch orientation on the OGE in comparison to Bartley et al. (2008).

two branches, l/d , and developed an empirical correlation to depict the critical height at the OGE in the upper branch (Mode 1) based on the two branch Froude numbers and separating distance. Their correlation is reproduced here as,

$$\frac{H_{OGE}}{d} = 0.887 \left[Fr_B + Fr_C \exp \left\{ -2.52 \left(\frac{l}{d} \right)^{1.1} Fr_B^{-0.22} Fr_C^{-0.16} \right\} \right]^{0.334}. \quad (5.4)$$

The upper and lower branch Froude numbers are defined as Fr_B and Fr_C , respectively, in order to be consistent with the present nomenclature. The authors also examined the critical branch Froude numbers needed to induce gas entrainment in the bottom branch only (Mode 2) or both branches simultaneously (Mode 3). They developed a map using the two branch Froude numbers and outlined the transition regions between the three modes.

Hassan (1995) performed similar experiments on a flat vertical wall, using similar separating distances. They developed an empirical correlation for the OGE in the upper branch, where $Fr_B = Fr_C$, as,

$$\frac{H_{OGE}}{d} = 0.57 \left[\left(1 + \exp \left\{ -1.96 \left(\frac{l}{d} \right)^{1.2} Fr_B^{-0.32} \right\} Fr_B \right) \right]^{0.4}. \quad (5.5)$$

Hassan (1995) also performed experiments using a semi-circular wall in close dimensional similarity to the present study, and presented a limited set of data points for the OGE in the inclined branch. Later, Ahmad and Hassan (2006) expanded this data set over a wider range of Froude numbers.

More recently Saleh (2008) developed an analytical model for one, two, and three

branches mounted on a curved surface exposed to a large stratified gas-liquid reservoir. The model was based on a two-fluid separated flow approach which considered a potential flow field local to the branches. Their results included branch inclinations at 45 and 90 degrees down from horizontal, which coincide to the inclined and bottom branch orientations used in the present study. Their model could be used to determine the critical height of the three modes of gas entrainment using the inclined and bottom branches, and presented several results to this effect.

The critical height results for Mode 1, the OGE in the inclined branch with flow in the bottom branch, are compared to these aforementioned studies in Figs. 5.32 and 5.33. The measurement point closest to the branch at $\lambda/D = -5$ was used for comparison purposes. The objective of these comparisons is to demonstrate the effects of Fr_C on the critical height in a stagnant and a co-currently flowing gas-liquid regime. In general for all studies increasing Fr_C leads to an increase in H_{OGE}/d . A simple physical explanation for this is that the inertia of the liquid flowing into the bottom branch provides an additional downward force on the gas-liquid interface. The result is that the flow through the inclined branch does not need to provide as much downward force on the interface to induce entrainment, this is seen as a reduction in Fr_B at a constant H_{OGE}/d . Another general observation in these two figures is that for similar branch Froude numbers in a co-currently flowing pipe the OGE occurs with a higher critical height than in a stagnant reservoir. The reason for this, as explained for the single branch cases, is due to the effect of the inlet liquid crossflow velocity.

As $Fr_B \rightarrow 0$, and with a constant value of Fr_C , the single bottom branch flow

configuration is approached. Therefore, as this lower limit is approached ($Fr_B = 0$) the critical height should approach the value for the OGE in the bottom branch at the particular value of Fr_C . With $Fr_C = 10$ the present results demonstrate this behavior, the corresponding value of H_{OGE}/d for the OGE in the bottom branch acting alone is 1.76. In comparison at $Fr_B = 1.2$, the left most point in Fig. 5.32, the value of H_{OGE}/d is 1.71, which is in very good agreement with the critical height in the bottom branch only. Parrott et al. (1991)'s correlation also demonstrates this behavior, as seen by the gradual reduction in the slope of the $Fr_C = 10$ curve, with decreasing Fr_B , this is in comparison to the $Fr_C = 0$ curve which has a constant slope on the log-log scale. At the upper limit, as $Fr_B \rightarrow 100$ all three studies demonstrate that low and moderate values of Fr_C becomes less significant in comparison to Fr_B , and the critical height collapses on the $Fr_C = 0$ result.

These limiting values are different in scenarios where both branches have the same Froude number, as in Fig. 5.32. A simple explanation for this is that the strength of each branch relative to the other remains practically unchanged. In this case the main parameters affecting the OGE would be related to the geometry and positioning of the branches relative to the gas-liquid interface, as has been demonstrated in earlier studies (Parrott et al., 1991; Hassan, 1995). In single branch cases, both stagnant gas-liquid reservoirs and co-currently flowing gas-liquid channels, the critical height has been found to be related to the branch Froude number to the power of 0.4. On a log-log scale, as in the figure, this power relationship is exhibited by a line of constant slope. The critical height of the present data, with $Fr_C = Fr_B$, is best fit by an exponent of 0.39. In comparison, the stagnant gas-liquid reservoir studies exhibit

similar relationships and the majority can be fit using the branch Froude number with exponents varying between 0.39 to 0.44. Included in this comparison is Bartley et al. (2008)'s correlation for a single branch, which was best fit using an exponent of 0.44. This special case can therefore be explained in a simple way, the effect of Fr_C on the OGE in the inclined branch is a proportional increase in the critical height with $Fr_B^{0.4}$. The proportionality constant is expected to be dependent on geometrical constraints, as was found in correlations by Parrott et al. (1991) and Hassan (1995). No attempt was made to correlate the present data since the inlet conditions are contingent on the channel dimensions, and more experimental data would be needed to investigate the effects of different values of L and D .

In the case of Mode 2, the OGE in the bottom branch with $Fr_B > 0$, little effect was found on the critical height at low values of Fr_B . Saleh (2008)'s model is capable of predicting the critical height for Mode 2 in a stagnant gas-liquid reservoir. They presented a sample of these results for moderate values of Fr_B , a sample of their results have been included in Fig. 5.34 for comparison purposes. Their results show that with $Fr_B = 30$, the effect is an increase in H_{OGE}/d , however, this is someone misrepresented over the range of Fr_C since at $Fr_C = 10$, the OGE would be expected in the inclined branch rather than bottom branch. Their dual onset results at $Fr_B = 30$, however, more appropriately show that the OGE will occur in both branches at nearly $Fr_C = 100$. What this means is that over the range of Fr_C presented in their results, the OGE occurs in the inclined rather than the bottom branch. The effect of Fr_B on H_{OGE} is not lost however, as an increase in the critical height is reasonably expected. Their single branch result is also included, and shows

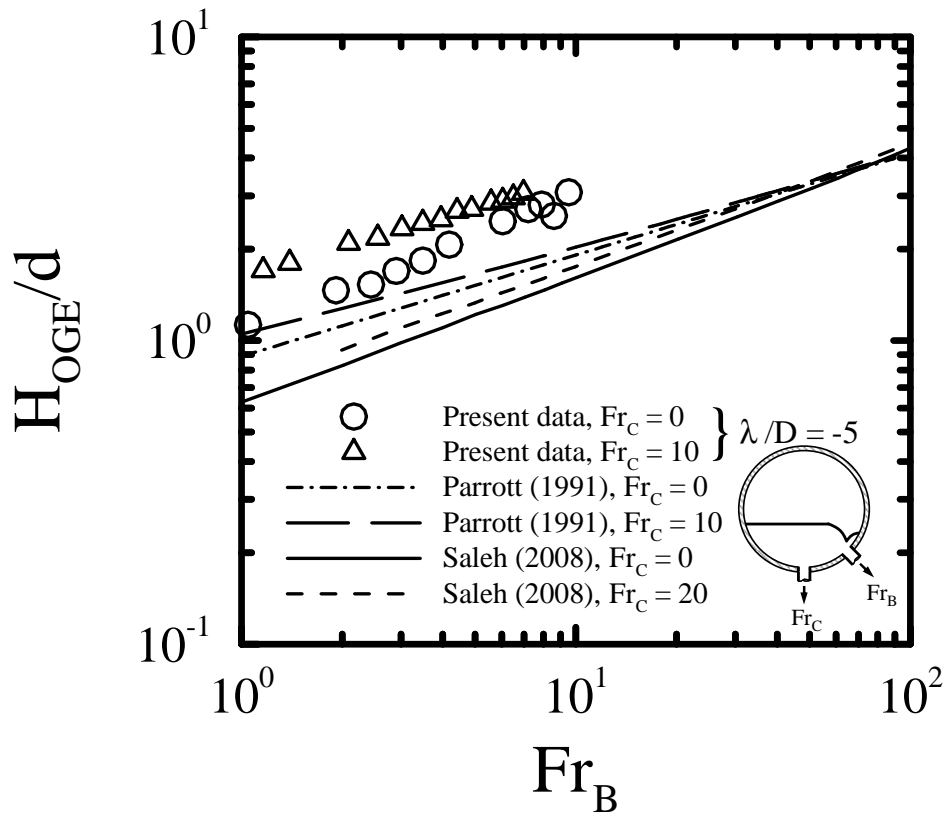


Figure 5.32: Effect of Fr_C on the OGE in the inclined branch at $\lambda/D = -5$ in comparison to published models and data (Mode 1).

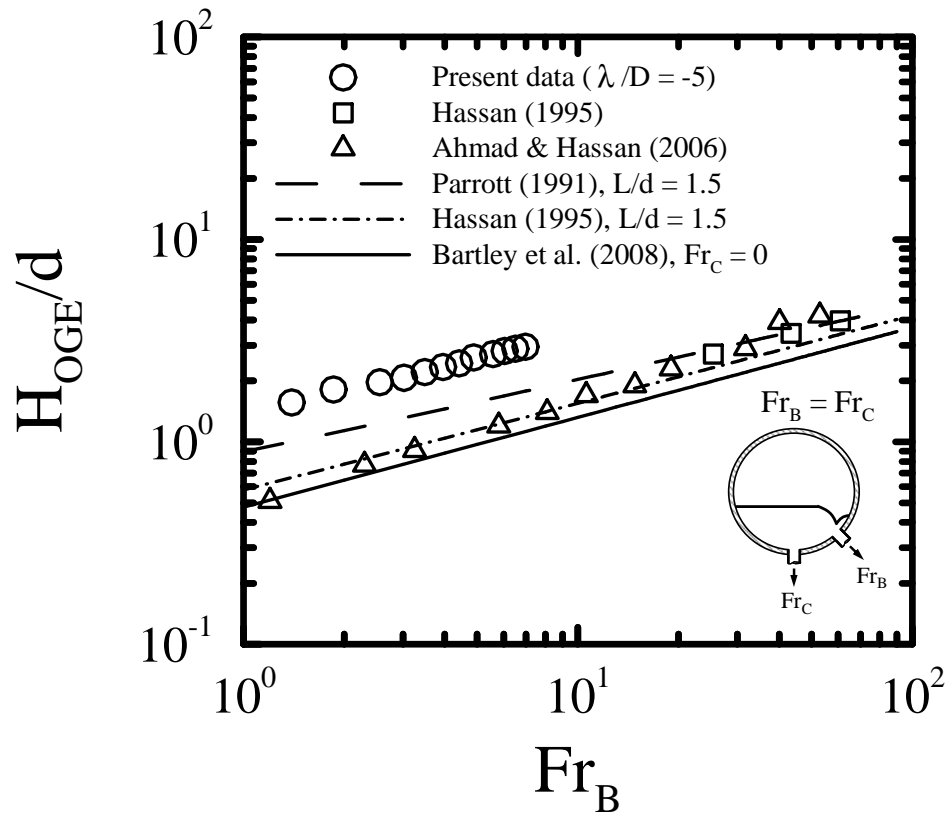


Figure 5.33: The OGE in the inclined branch with $Fr_B = Fr_C$ at $\lambda/D = -5$ in comparison to published models and data (Mode 1).

good agreement in comparison to Bartley et al. (2008)'s experimental data at the bottom oriented branch, differences between these two results could be attributed to differences in geometry and the uncertainty of measurements. Also shown in the figure is Smoglie and Reimann (1986)'s correlation for the OGE in a single branch exposed to a co-currently flow gas-liquid regime, their critical height was recorded at approximately $\lambda/D = -2.5$. Since the critical height is not dramatically affected by Fr_B , the present results agree well with their correlation.

Comparing the present data with Saleh (2008)'s prediction of the dual onset conditions of Mode 3, in Fig. 5.35, the value of Fr_C at any Fr_B is consistently lower than their prediction. The reason for this decrease in Fr_C is due to the liquid cross-flow velocity, which provides an additional force at the dip. In a simple way, the liquid crossflow velocity assists the OGE. This results in the bottom branch needing to apply a smaller force to induce the OGE - read as a reduction in Fr_C . The effect of geometry is quite significant, and is seen by comparing measurements obtained by Parrott et al. (1991) with Saleh (2008)'s prediction. Parrott et al. (1991) found that very small values of Fr_B , below 1, were needed to induce the OGE in both branches. Since both branches were located in the same vertical plane, any dip formed as a result of the bottom branch would pass almost immediately in front of the upper branch. This is in contrast to the present study, where two separate dips were observed to form in the air-water interface due to the lateral shift of the branches.

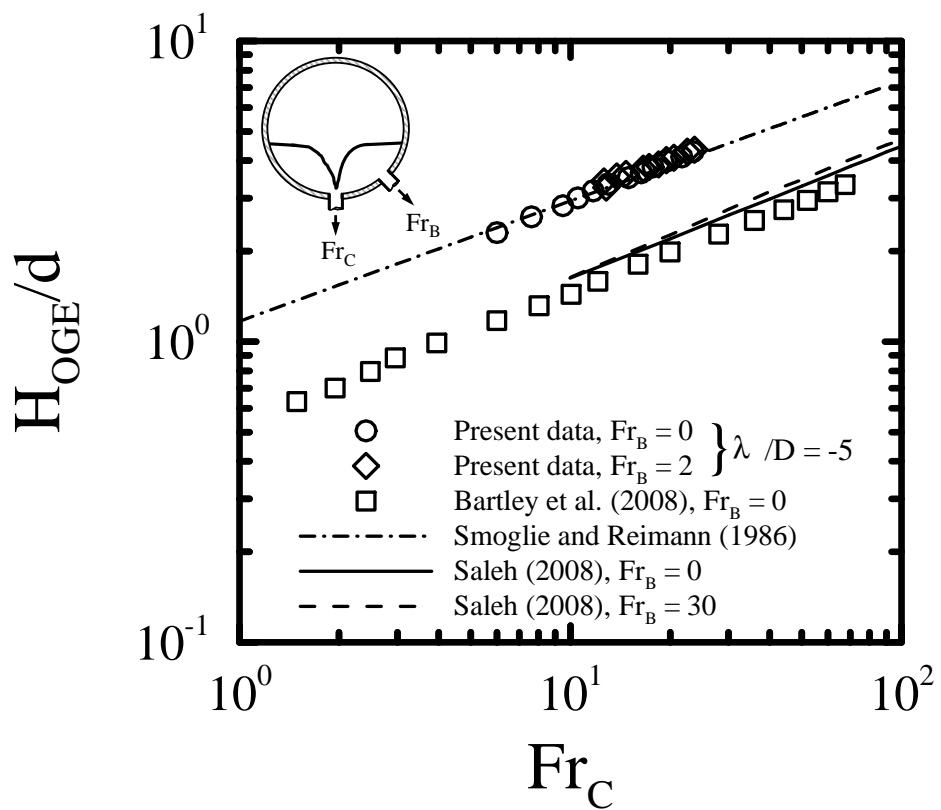


Figure 5.34: Effect of Fr_B on the OGE in the bottom branch at $\lambda/D = -5$ in comparison to published models and data (Mode 2).

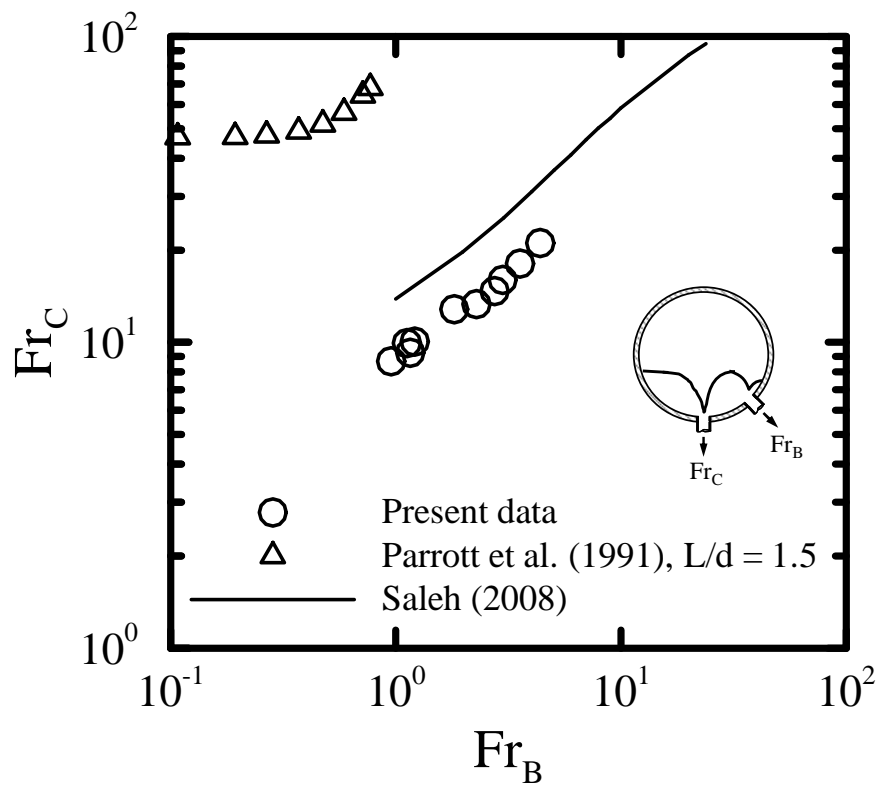


Figure 5.35: Comparison of simultaneous gas entrainment in the inclined and bottom branches with published models and data (Mode 3).

5.4 Summary

Two active branches, initially flowing liquid only, exposed to a stratified gas-liquid regime have shown to produce three different modes of gas entrainment. The mode is dependent on the branch Froude numbers, as well as the inlet conditions. If the branch where the OGE is expected to occur has a significantly higher Froude number than the second active branch, for example an order of magnitude or more, a minor effect will be found on the critical conditions. Conversely, the opposite is true if the branch where OGE occurs has a significantly lower branch Froude number than the second branch. Although the dual onset conditions were presented as a smooth curve, it is expected that there is a high variability near this region, as the interfacial instability describing the OGE is affected by the relative strengths of each branch flow, as well as the inlet liquid superficial velocity.

To complement the onset of gas entrainment mode map developed in this study, additional investigations on geometrical effects are needed. Differences in the channel and branch diameter, length of the inlet channel, and inclination of channel from horizontal, are expected to affect the inlet conditions such as interface height and fluid phase velocity.

Chapter 6

Theoretical Analysis of the Onset of Gas Entrainment

6.1 Chapter Overview

This chapter presents analytical modeling of the onset of gas entrainment (OGE) in small branches exposed to a flowing gas-liquid regime. The sections in this chapter discuss the various stages that were undertaken to model the OGE phenomenon. Both the successes and pitfalls encountered in this process are discussed. The chapter begins by modeling OGE in a single branch installed on a semi-infinite horizontal plane. The objective of this preliminary study was to incorporate liquid crossflow into an established model that was successfully used for predicting OGE in a large stratified reservoir. Section 6.3 focuses on the criteria incorporated in the model which were used to predict the OGE critical dip. This discussion is extended in §6.4 with the incorporation of a second branch, and outlines limitations of the OGE criterion.

6.2 Single Branch on a Semi-infinite Horizontal Plane

6.2.1 Problem Description

The geometry considered here is presented in Fig. 6.1. A single circular downward branch, with a diameter d , is installed on a flat horizontal wall. The origin of the Cartesian co-ordinate system ($x = 0, y = 0, z = 0$) is located at the center of the branch inlet, with the vertical, y co-ordinate, shown perpendicular to the branch inlet. A semi-infinite stratified two-phase region, of heavier and lighter fluids, exists above the branch. Here the heavier fluid is considered as the liquid phase, subscript L , with density ρ_L , and the lighter fluid as the gas phase, subscript G with density ρ_G . The heavier fluid initially flows through the branch with a mass flow rate of \dot{m}_{L3} . The bulk liquid flow which passes parallel to the flat wall, called herein crossflow, enters with a mass flow rate of \dot{m}_{L1} and exits through the run with \dot{m}_{L2} . The two-phases extend towards infinity in the x and z directions and are bounded at $y = 0$ by the solid wall. The heavier fluid flows with a uniform velocity, U , throughout the domain in the positive x -direction. The lighter fluid phase is considered stagnant.

With single phase liquid flow through the branch, and the inlet liquid height well above the branch inlet, the two-phase interface is flat. As the gas-liquid interface height is reduced a vortex-free dip begins to form in the interface, as shown in Fig. 6.1. The dip is located at point B ($x = b, y = h, z = 0$). A small reduction in the interface height causes the dip to suddenly collapse into the branch, resulting in

both gas and liquid to flow into the branch. This sudden collapse of the interface is termed the onset of gas entrainment and it occurs at a critical interface height called H_{OGE} . The sudden collapse of the interface is a result of the liquid acceleration at point B , the lowest point of the dip, exceeding that of gravity (Ahmed et al., 2003). The inlet liquid momentum causes the critical dip to shift downstream by a distance of $x = b$. The existence of the dip shift is based on earlier photographic evidence of the phenomena by Reimann and Khan (1984) and Smoglie and Reimann (1986), although not explicitly discussed in their studies. The dip shift will be considered in the development of the present model.

Flow Field Simulation

The flow field is considered quasi-steady, incompressible, inviscid, and irrotational, with negligible surface tension. These assumptions reduce the problem to a potential flow which is governed by forces of inertia and gravity. The steady continuity equation, in Cartesian coordinates (x, y, z) , with the velocity vector \mathbf{V} described by,

$$\mathbf{V} = u\mathbf{i} + v\mathbf{j} + w\mathbf{k}, \quad (6.1)$$

is,

$$\frac{\partial u}{\partial x} + \frac{\partial v}{\partial y} + \frac{\partial w}{\partial z} = 0. \quad (6.2)$$

The irrotationality condition can be satisfied through the definition of a scalar potential function, ϕ , which is related to the velocity through,

$$\mathbf{V} = \frac{\partial\phi}{\partial x}\mathbf{i} + \frac{\partial\phi}{\partial y}\mathbf{j} + \frac{\partial\phi}{\partial z}\mathbf{k}, \quad (6.3)$$

or in a more convenient compact form using the differential operator, ∇ , as,

$$\mathbf{V} = \nabla\phi, \quad (6.4)$$

where,

$$\nabla = \frac{\partial}{\partial x}\mathbf{i} + \frac{\partial}{\partial y}\mathbf{j} + \frac{\partial}{\partial z}\mathbf{k}. \quad (6.5)$$

Inserting the definition of the potential function into the continuity equation in Eq. (6.2) produces Laplace's well known differential equation as,

$$\frac{\partial^2\phi}{\partial x^2} + \frac{\partial^2\phi}{\partial y^2} + \frac{\partial^2\phi}{\partial z^2} = 0, \quad (6.6)$$

which is an elliptic type linear homogeneous partial differential equation. A linear combination of two solutions, say ϕ_I and ϕ_{II} , is also a solution as,

$$\phi = \phi_I + \phi_{II}. \quad (6.7)$$

The branch flow can be simulated by a three-dimensional point-sink intersected

by a flat wall, which produces a hemi-spherical flow area. The radial velocity, V_{Ld} , is uniformly distributed along this area at any radius, r , according to,

$$V_{Ld} = -\frac{\dot{m}_{L3}}{2\pi\rho_L r^2}. \quad (6.8)$$

The minus sign indicates that the velocity is directed towards the branch origin, at $r = 0$. Assuming that a potential function exists, ϕ_I , and the flow is uniquely radial towards the sink, it can be shown that,

$$\phi_I = \frac{\dot{m}_{L3}}{2\pi\rho_L r}, \quad (6.9)$$

where it is convenient in this case to describe the potential function in Cartesian co-ordinates using,

$$r = \sqrt{x^2 + y^2 + z^2}, \quad (6.10)$$

which results in,

$$\phi_I = \frac{\dot{m}_{L3}}{2\pi\rho_L\sqrt{x^2 + y^2 + z^2}}. \quad (6.11)$$

With a semi-infinite domain, the crossflow velocity is assumed to have a uniform horizontal profile, U , aligned parallel to the x -direction. Assuming that a potential function exists, ϕ_{II} , following Schetz and Fuhs (1996) it can be shown that,

$$\phi_{II} = Ux. \quad (6.12)$$

The superposition of these two known potential functions, using the linearity theorem in Eq. (6.7), results in the three dimensional flow field being represented by,

$$\phi = \frac{\dot{m}_{L3}}{2\pi\rho_L\sqrt{x^2 + y^2 + z^2}} + Ux. \quad (6.13)$$

Equilibrium along the Gas-Liquid Interface

The potential flow field allows Bernoulli's equation to be applied along the gas-liquid interface between two convenient points, namely A and B . On the liquid side it can be defined using the difference in static pressure, P , between points A and B ($P_{LA} - P_{LB}$) as,

$$P_{LA} - P_{LB} = \frac{\rho_L(V_{LB}^2 - V_{LA}^2)}{2} + \rho_L g(h - H_{OGE}). \quad (6.14)$$

Similarly, on the lighter fluid phase side, which is considered stagnant, the pressure difference can be expressed as,

$$P_{GA} - P_{GB} = \rho_G g(h - H_{OGE}). \quad (6.15)$$

At any point along the gas-liquid interface the pressure in either fluid phase must be equal (White, 1991). Combining the right hand sides of Eq.'s (6.14) and (6.15) results in,

$$V_{LB}^2 = V_{LA}^2 - \frac{2\Delta\rho}{\rho_L}g(h - H_{OGE}), \quad (6.16)$$

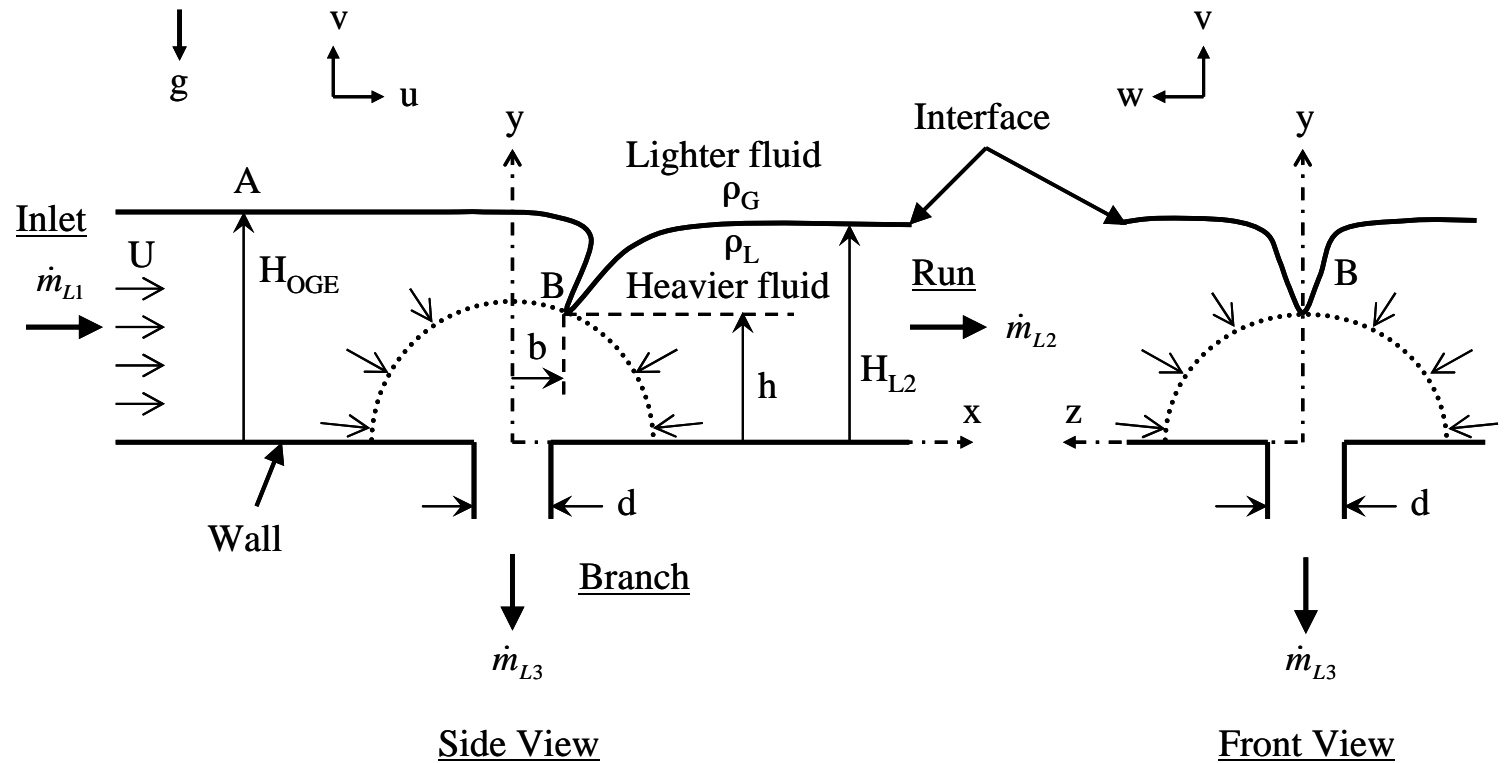


Figure 6.1: Geometry and coordinate system.

where $\Delta\rho = \rho_L - \rho_G$, is the difference in density between both fluid phases. The liquid velocity at point B can be found from the magnitude of the velocity vector as,

$$V_{LB} = (u_{LB}^2 + v_{LB}^2 + w_{LB}^2)^{\frac{1}{2}}. \quad (6.17)$$

The liquid velocity at point B is found by inserting the potential function definition from Eq. (6.4) and the co-ordinates of point B ($x = b, y = h, z = 0$) as,

$$u_{LB} = \left. \frac{\partial\phi}{\partial x} \right|_{(x=b, y=h, z=0)} = U - \frac{\dot{m}_{L3}b}{2\pi\rho_L(b^2 + h^2)^{\frac{3}{2}}}, \quad (6.18)$$

$$v_{LB} = \left. \frac{\partial\phi}{\partial y} \right|_{(x=b, y=h, z=0)} = -\frac{\dot{m}_{L3}h}{2\pi\rho_L(b^2 + h^2)^{\frac{3}{2}}}, \quad (6.19)$$

$$w_{LB} = \left. \frac{\partial\phi}{\partial z} \right|_{(x=b, y=h, z=0)} = 0, \quad (6.20)$$

Considering that $V_{LA} = U$, and substituting Eq.'s (6.17) to (6.20) into Eq. (6.16), it can be shown that,

$$\frac{H_{OGE}}{d} = \frac{h}{d} + \frac{Fr_d^2}{128} \left(\frac{d^4}{(b^2 + h^2)^2} \right) - \frac{Fr_d Fr_U}{8} \left(\frac{bd^2}{(b^2 + h^2)^{\frac{3}{2}}} \right). \quad (6.21)$$

where the branch Froude number Fr_d is defined by,

$$Fr_d = \frac{4\dot{m}_{L3}}{\pi(gd^5\rho_L\Delta\rho_L)^{\frac{1}{2}}}, \quad (6.22)$$

and introducing the crossflow Froude number, Fr_U defined as,

$$Fr_U = \frac{U}{\sqrt{gd}} \left(\frac{\rho_L}{\Delta\rho} \right)^{\frac{1}{2}}. \quad (6.23)$$

Equation (6.21) demonstrates that the critical inlet height, H_{OGE} is governed by the Froude number, which is a ratio of inertial to gravitational forces. There are three unknowns in Eq. (6.21), namely, H_{OGE} , h , and b , which requires two additional equations to close the system.

Onset of Gas Entrainment Criterion

When the vertical acceleration, a_y , of point B is equivalent to the gravitational acceleration, g , the interface becomes unstable thereby causing the dip to collapse into the branch (Ahmed et al., 2003; Andaleeb et al., 2006; Saleh et al., 2009). The onset of gas entrainment criterion can therefore be stated as,

$$a_y \Big|_B = -g. \quad (6.24)$$

The vertical acceleration of any point, following White (1991), is,

$$a_y = \frac{\partial v}{\partial t} + u \frac{\partial v}{\partial x} + v \frac{\partial v}{\partial y} + w \frac{\partial v}{\partial z}. \quad (6.25)$$

With steady state, and no variation in the x or z directions, the acceleration of point B can be obtained through substitution of the potential function definition from Eq.

(6.4) into Eq. (6.25) as,

$$a_y \Big|_{(x=b, y=h, z=0)} = \left(\frac{\partial \phi}{\partial y} \frac{\partial^2 \phi}{\partial y^2} \right). \quad (6.26)$$

Taking the second derivative of ϕ with respect to y yields,

$$\frac{\partial^2 \phi}{\partial y^2} = \frac{\dot{m}_{L3}}{2\pi\rho_L(x^2 + y^2 + z^2)^{\frac{3}{2}}} \left(\frac{3y^2}{(x^2 + y^2 + z^2)} - 1 \right). \quad (6.27)$$

Substituting Eq. (6.19) and Eq. (6.27) into Eq. (6.26) evaluated at point B , and equalizing it with $-g$ as in Eq. (6.24), it can be shown that,

$$Fr_d^2 \left(\frac{hd^5}{(b^2 + h^2)^3} - \frac{3h^3d^5}{(b^2 + h^2)^4} \right) + 64 \left(\frac{\rho_L}{\Delta\rho} \right) = 0. \quad (6.28)$$

Offset Distance Criterion

The third equation is proposed by considering that the dip is stationary in the x -direction. This occurs as a result of the point-sink and uniform flow velocities having equal magnitudes, and opposite directions, at point B . The criterion may be expressed as,

$$\frac{\partial \phi_I}{\partial x} \Big|_{x=b, y=h, z=0} = \frac{\partial \phi_{II}}{\partial x} \Big|_{x=b, y=h, z=0}, \quad (6.29)$$

or substituting the definitions of ϕ_I and ϕ_{II} yields,

$$\frac{\dot{m}_{L3}x}{2\pi\rho_L(x^2 + y^2 + z^2)^{\frac{3}{2}}} \Big|_{x=b, y=h, z=0} = U. \quad (6.30)$$

Evaluating this equation at point B it can be shown that,

$$Fr_U - \frac{Fr_d}{8} \left(\frac{d^2 b}{(b^2 + h^2)^{\frac{3}{2}}} \right) = 0. \quad (6.31)$$

Special Case ($Fr_U = 0$)

When the crossflow Froude number is zero ($Fr_U = 0$) the physical model reduces to a single branch in a large two-phase reservoir. This implies that the offset distance, b , is uniquely zero. The number of unknowns is reduced to two, requiring only two equations to close the system. A quick check of Eq. (6.31) verifies that with $Fr_U = 0$, and $Fr_d > 0$, the offset distance must be $b = 0$. With $b = 0$, Eq. (6.28) reduces to,

$$\frac{h}{d} = 0.5 Fr_d^{0.4} \left(\frac{\Delta\rho}{\rho_L} \right)^{0.2}, \quad (6.32)$$

and substituting this into Eq. (6.21) results in,

$$\frac{H_{OGE}}{d} = Fr_d^{0.4} \left(\frac{1}{2} \left(\frac{\Delta\rho}{\rho_L} \right)^{0.2} + \frac{1}{8} \left(\frac{\rho_L}{\Delta\rho} \right)^{0.8} \right). \quad (6.33)$$

If the lighter fluid density is negligible, that is $\Delta\rho \cong \rho_L$ then Eq. (6.33) is reduced to,

$$\frac{H_{OGE}}{d} = 0.625 Fr_d^{0.4}. \quad (6.34)$$

6.2.2 Results and Discussion

The model consists of three non-linear equations, Eqs. (6.21), (6.28), and (6.31),

respectively, with three unknowns, these being the critical inlet height, H_{OGE} , and the location of the dip at $x = b$, and $y = h$. These unknowns are governed by the applied flow conditions defined by the branch and crossflow Froude numbers, Fr_d and Fr_U , respectively. The system of equations was evaluated numerically through the use of MatLab 7.0's built in *fsolve* function. The branch Froude number, Fr_d , was tested between 0.1 and 100, while the crossflow Froude number, Fr_U , ranged between 0 and 1. With these parameters, residuals in each of the three equations were 1×10^{-11} or less.

The special case, where $Fr_U = 0$, along with cases of $Fr_U = 0.2, 0.4,$ and 0.8 are presented in Fig. 6.2. The $Fr_U = 0$ case shows the highest critical height for any combination of Fr_d or Fr_U . This implies that any imposed constant crossflow velocity will decrease the critical height. For a constant crossflow Froude number, Fr_U , as the branch strength, Fr_d , increases the curve approaches the $Fr_U = 0$ line. Physically, this means that the branch becomes increasingly dominant in the flow field. At lower branch Froude numbers ($Fr_d < 10$) the influence of the crossflow Froude number is more pronounced. The variation of the dip height, h/d , is presented in Fig. 6.3. The trend is similar to that of H_{OGE}/d shown in Fig.6.2. The ratio of the critical height to dip height, H_{OGE}/h , is presented in Fig.6.4 - demonstrating the effects of crossflow and branch strengths, Fr_U and Fr_d , respectively. The $Fr_U = 0$ line shows a constant value where $H_{OGE}/h = 1.25$, and is consistent with an earlier point-sink analysis for a side branch on a flat vertical wall with no imposed crossflow (Ahmed et al., 2003). For cases with crossflow the effect of Fr_U is a decrease in H_{OGE}/h for all Fr_d . At low values of Fr_d , H_{OGE}/h decreases dramatically with $Fr_U = 0.8$ and

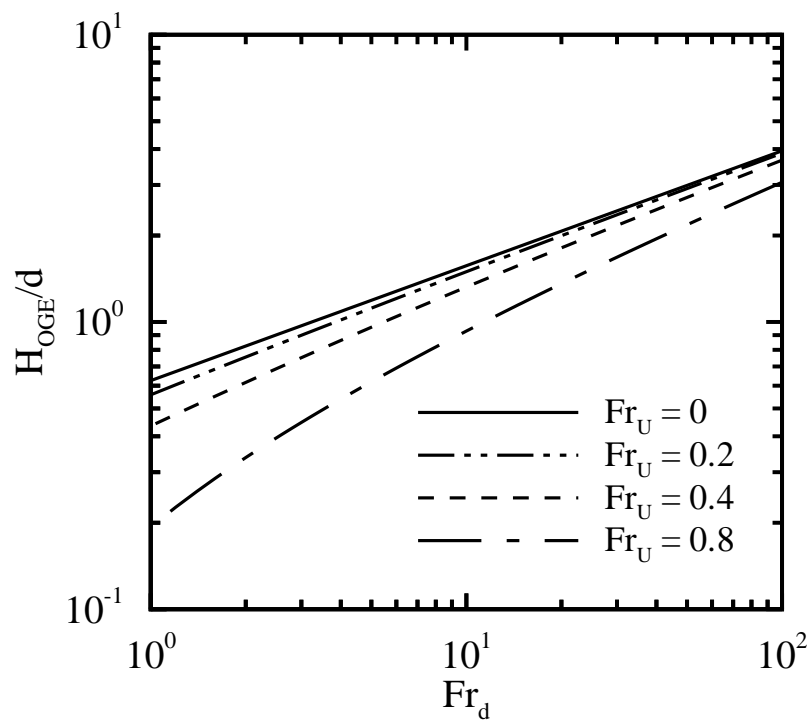


Figure 6.2: Effect of Fr_U on the critical height H_{OGE}/d .

indicates that values of $H_{OGE}/h < 1$ were found. Values of H_{OGE}/h lower than 1 violate the physics of the problem because it implies the dip is located above the gas-liquid interface. A value of $H_{OGE}/h = 1$, as Fr_d approaches zero, would be physically more appropriate since it implies the dip disappears from the two-phase interface - substitution of $Fr_d = 0$ into Eq. (6.21) yields the same conclusion. The shift in the dip location downstream of the branch centerline was defined at $x = b$. The effects of Fr_d and Fr_U on b/d (b was non-dimensionalized with the branch diameter d) are shown in Fig. 6.5. An increase in crossflow strength, Fr_U , demonstrates an increase in b/d , which comes as a result of a shift in the stagnation point obtained from Eq. (6.31). On the other hand, the results indicate that an increase in branch strength, Fr_d , also results in an increase in the dip offset distance, b/d . While an increase in b/d with Fr_d might not be implicit, this trend can be explained with the aid of Fig. 6.6. This figure highlights the behavior of the dip location using a ratio of dip offset distance and dip height, b/h . As the branch strength, Fr_d , increases the result is a decrease in b/h . As Fr_d increases it becomes the dominant player in the flow field and, as a result, forces the dip to move closer to the y -axis resulting in a decrease of b/h .

Control Volume Analysis

A control volume approach is used in order to evaluate the crossflow mass flow rate at the inlet and exit of the domain. This step is necessary in order to compare with published experimental data which typically cite the crossflow term as a mass flow rate. The analysis is presented for cases with an imposed liquid flow, i.e. $Fr_U > 0$.

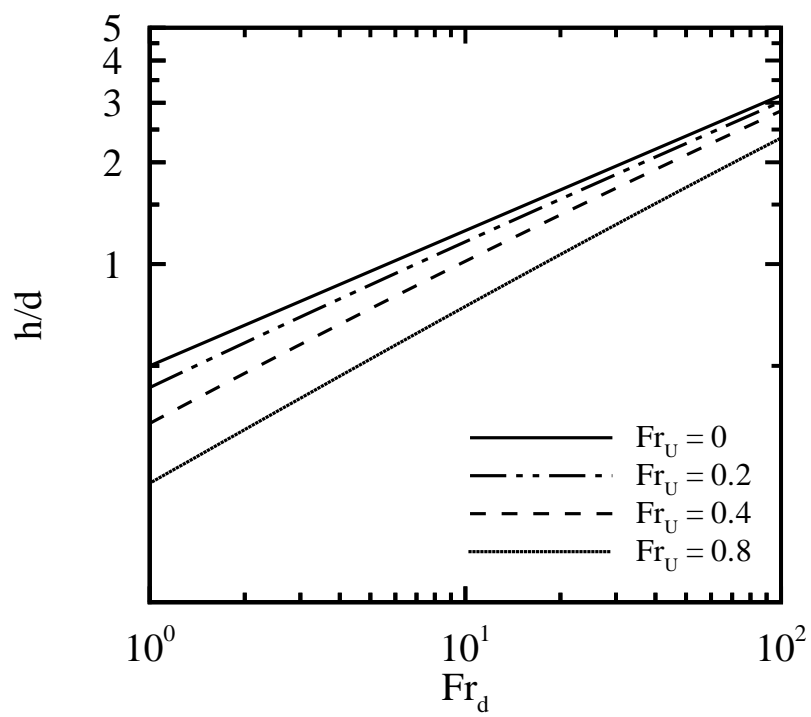


Figure 6.3: Variation of the dip height, h/d .

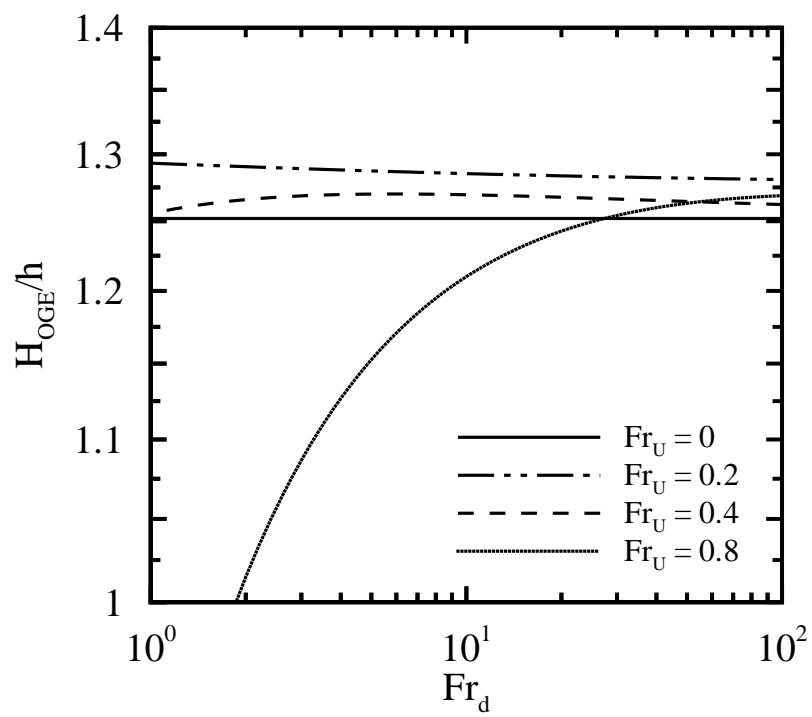


Figure 6.4: Variation of H_{OGE}/h .

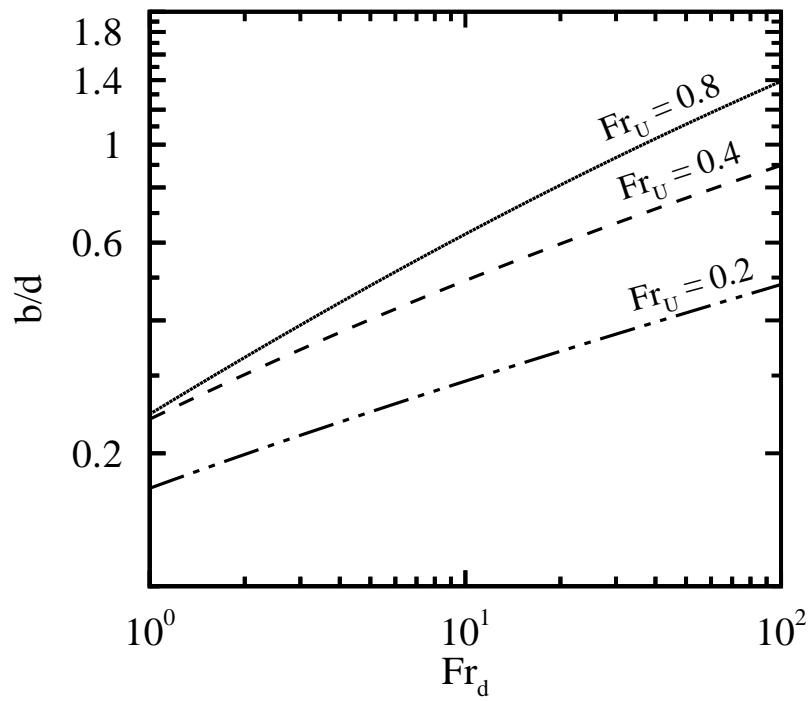


Figure 6.5: Variation of the dip offset distance, b/d .

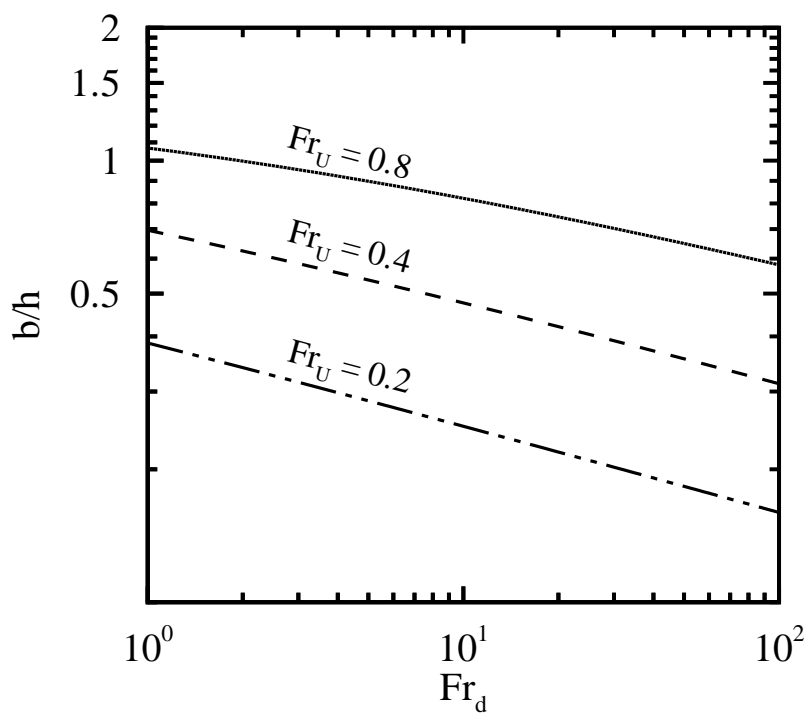


Figure 6.6: Variation of the offset distance, b , with the dip height, h .

The bottom wall is assigned a finite size in the z -direction, called the plate width, W , so the liquid cross-sectional areas at the inlet ($x \rightarrow -\infty$) and exit ($x \rightarrow \infty$) can be defined. This follows from considering the inlet mass flow rate, \dot{m}_{L1} as,

$$\dot{m}_{L1} = \rho_L(H_{L1}W)V_{L1}, \quad (6.35)$$

the outlet (run) mass flow rate (\dot{m}_{L2}) as,

$$\dot{m}_{L2} = \rho_L(H_{L2}W)V_{L2} \quad (6.36)$$

and the branch mass flow rate (\dot{m}_{L3}) as,

$$\dot{m}_{L3} = \rho_L\left(\frac{\pi d^2}{4}\right)V_{L3}. \quad (6.37)$$

The liquid velocity passing through each of the three control surfaces, defined as V_L , is assumed to have a uniform profile. Subscripts 1, 2, and 3 denote the inlet, run, and branch, respectively. The liquid height at the inlet and run are defined as H_{L1} and H_{L2} , respectively. The cross-sectional areas of the liquid phase at the inlet and run are therefore $H_{L1}W$, and $H_{L2}W$, respectively. Considering the conservation of mass from the definitions in Fig. 6.1 the resulting liquid mass flow rates at the inlet, \dot{m}_{L1} , run, \dot{m}_{L2} , and branch, \dot{m}_{L3} are conserved as,

$$\dot{m}_{L1} = \dot{m}_{L2} + \dot{m}_{L3}. \quad (6.38)$$

The definition of \dot{m}_{L3} could be found in terms of the branch Froude number by rearranging Eq. (6.22) using,

$$\dot{m}_{L3} = \frac{Fr_d}{4}(\pi\sqrt{gd^5\rho_L\Delta\rho}). \quad (6.39)$$

At the onset of gas entrainment $H_{L1} = H_{OGE}$ and $V_{L1} = U$. To find the liquid velocity through the run control surface, V_{L2} , consider the definition of the velocity field from the potential function, as $x \rightarrow \infty$, which results in $V_{L2} \rightarrow U$. The inlet and run mass flow rates can be rewritten as a function of the crossflow Froude number using Eq. (6.23) as,

$$\dot{m}_{L1} = \rho_L(H_{OGE}W)Fr_U\sqrt{gd}, \quad (6.40)$$

and,

$$\dot{m}_{L2} = \rho_L H_{L2} W Fr_U \sqrt{gd}. \quad (6.41)$$

Inserting these definitions into the conservation of mass in Eq. (6.38), and rearranging in terms of the liquid height in the run, H_{L2} , result in,

$$\frac{H_{L2}}{d} = \frac{H_{OGE}}{d} - \frac{\pi}{4} \left(\frac{d}{W} \right) \left(\frac{\Delta\rho}{\rho_L} \right)^{\frac{1}{2}} \left(\frac{Fr_d}{Fr_U} \right). \quad (6.42)$$

The equation states that the run liquid height, H_{L2} , will be less than the inlet critical liquid height, H_{OGE} , if the plate width, W , has a finite size. As the plate width approaches infinity the run liquid height, H_{L2} , approaches the inlet value of H_{OGE} .

If a positive real value of the run liquid height, H_{L2} , is found from Eq. (6.42) -

given that the crossflow and branch Froude numbers are positive and non-zero, and the plate has a finite size, W - then the run mass flow rate, \dot{m}_{L2} , will have a real positive value. If a run liquid height of $H_{L2} = 0$ is found it implies that there is no flow ($\dot{m}_{L2} = 0$) passing through the run control surface. Furthermore, negative values of H_{L2} imply that the run mass flow rate, \dot{m}_{L2} , is also negative. In such a case the liquid flow direction is reversed and is flowing into (*-ve x-direction*) the control volume at the run control surface rather than flowing out (*+ve x-direction*). By inserting $H_{L2} = 0$ into Eq. (6.42), and rearranging the equation, the limit where this flow reversal occurs can be defined as,

$$\left. \frac{H_{OGE}}{d} \right|_{H_{L2}=0} = \frac{\pi}{4} \left(\frac{d}{W} \right) \left(\frac{\Delta\rho}{\rho_L} \right)^{\frac{1}{2}} \left(\frac{Fr_d}{Fr_U} \right). \quad (6.43)$$

A sample of flow conditions causing flow reversal are shown in Fig. 6.7 with $d/W = 0.05$ and $\Delta\rho = \rho_L$.

Comparison with Earlier Experimental Studies

Experiments conducted without any imposed crossflow, $Fr_U = 0$, are representative of the special case derived in Eq. (6.33). Both quasi-steady (Hassan et al., 1997; Ahmad and Hassan, 2006; Bowden and Hassan, 2007) and unsteady (Lubin and Springer, 1967; Abdalla and Berenyi, 1969) experimental results have been reported, and are presented in Fig.6.8. The present model agrees well with the experiments with $Fr_U = 0$ and demonstrates a 30% range of maximum error. It is interesting to note, however, that the maximum deviation occurs at either low ($Fr_d < 1$) or high ($Fr_d > 100$)

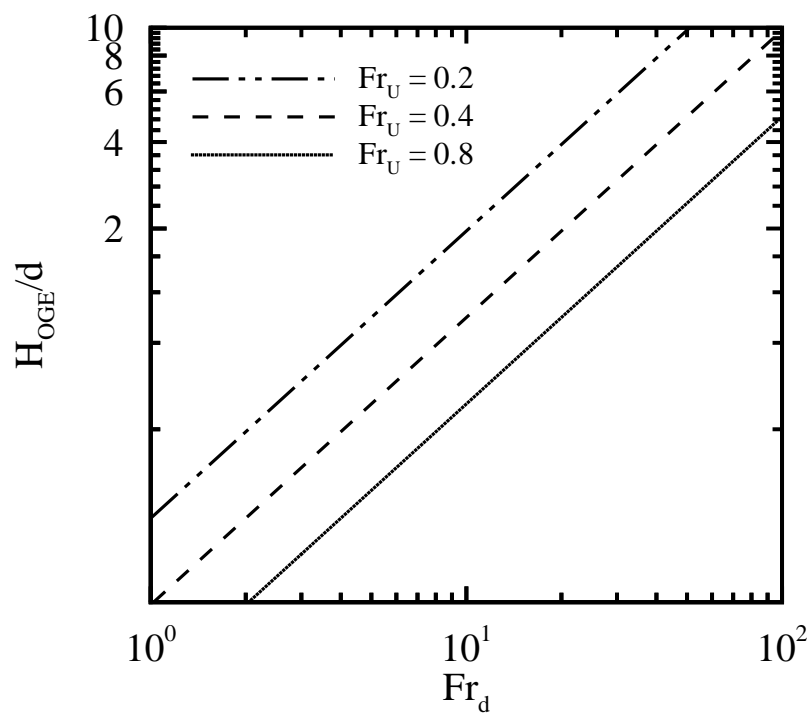


Figure 6.7: Example of critical values causing flow reversal ($d/W = 0.05$).

branch Froude numbers. It is possible to speculate that in these ranges the critical height is influenced by additional forces that are not considered by the branch Froude number. Aside from the methodologies used by these experimental studies to record the critical height (quasi-steady versus unsteady) there are also significant differences in the two-fluids used (gas-liquid and liquid-liquid), as well as the geometry of the test sections. All things considered, the agreement helps to validate the point-sink approach, which includes the inviscid, incompressible, irrotational, quasi-steady and negligible surface tension assumptions used in the development of the present model. The analytical model developed by Andaleeb et al. (2006) is also presented in Fig. 6.8. Their prediction lies on the same line as the present study with less than 1% deviation for $Fr_d > 0.1$.

The effects of crossflow on the critical height are presented in Fig. 6.9 by comparing correlations developed from selected quasi-steady experimental studies. These correlations are presented in the figure with the benchmark case with no imposed crossflow, $Fr_U = 0$, as described by Eq. (6.34). There is poor agreement between these correlations and the present model, which is particularly true at high branch Froude numbers. The results presented in Fig. 6.2 demonstrated that as Fr_d increased the model predictions converged to the $Fr_U = 0$ case. The convergence at $Fr_U = 0$ is physically appropriate since the branch flow becomes dominant over the crossflow. The experimentally derived correlations presented in Fig. 6.9, however, do not converge to the $Fr_U = 0$ prediction as Fr_d increases, but rather run parallel or even diverge.

There is also a large discrepancy between the correlations regarding the effects of

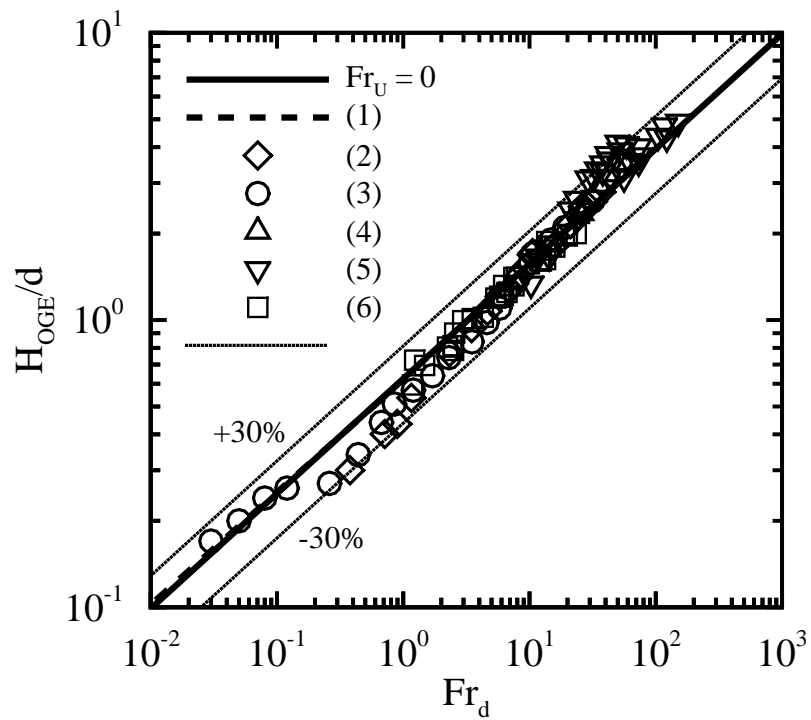


Figure 6.8: Comparison of the special case model ($Fr_U = 0$) with theoretical work of (1)Andaleeb et al. (2006), (2) and experimental work of (2)Bowden and Hassan (2007), (3)Ahmad and Hassan (2006), (4)Hassan et al. (1997), (5)Abdalla and Berenyi (1969), and (6)Lubin and Springer (1967).

crossflow on the critical inlet height. Comparing with the benchmark case, $Fr_U = 0$, two of the correlations indicate that crossflow causes the critical height to increase (Smoglie and Reimann, 1986; Schrock et al., 1986) while the remaining three correlations indicate a decrease in H_{OGE} (Maciaszek and Micaelli, 1990; Yonomoto and Tasaka, 1991; Kowalski and Krishnan, 1987). Maciaszek and Micaelli (1990) had explained that liquid crossflow caused the vortex-free gas core formation to be suppressed which resulted in a substantial decrease in critical height. They had tested run liquid velocities up to 3 m/s, which was substantially higher than the approximately 0.36 m/s liquid velocity reported by Smoglie and Reimann (1986), and attributed this difference to the sharp decrease in critical height. The present model corroborates Maciaszek and Micaelli (1990)'s findings that an imposed liquid crossflow, $Fr_U > 0$, decreases the critical height for a given branch Froude number, Fr_d , - as was verified in Fig. 6.2. The critical height predicted by their correlation is presented in Fig. 6.10 for a range of momentum fluxes using a selected crossflow value of $Fr_U = 0.8$. The critical height predicted by the present model is also presented in this figure.

The correlation developed by Yonomoto and Tasaka (1991) includes a ratio of the run to inlet mass flow rates as a compensating factor for crossflow effects. This correlation is presented in Fig. 6.11 for a range of mass flow rate ratios using a selected value of $Fr_U = 0.6$. Their experiments were conducted using a square (190mm by 190mm) channel with a single downward branch ($d/W = 0.052, 0.079, \text{ and } 0.105$). Using the conservation of mass it is possible to compare the present model with their correlation for a range of mass flow rate ratios.

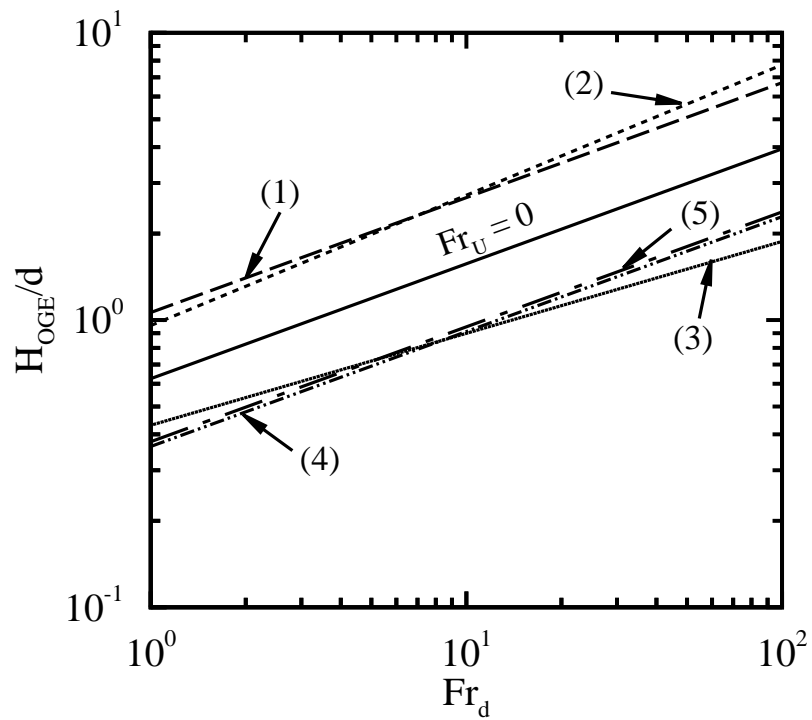


Figure 6.9: Effect of crossflow with comparison to experimentally derived correlations by (1)Smoglie and Reimann (1986), (2)Schrock et al. (1986), (3)Kowalski and Krishnan (1987), (4)Maciaszek and Micaelli (1990), and (5)Yonomoto and Tasaka (1991).

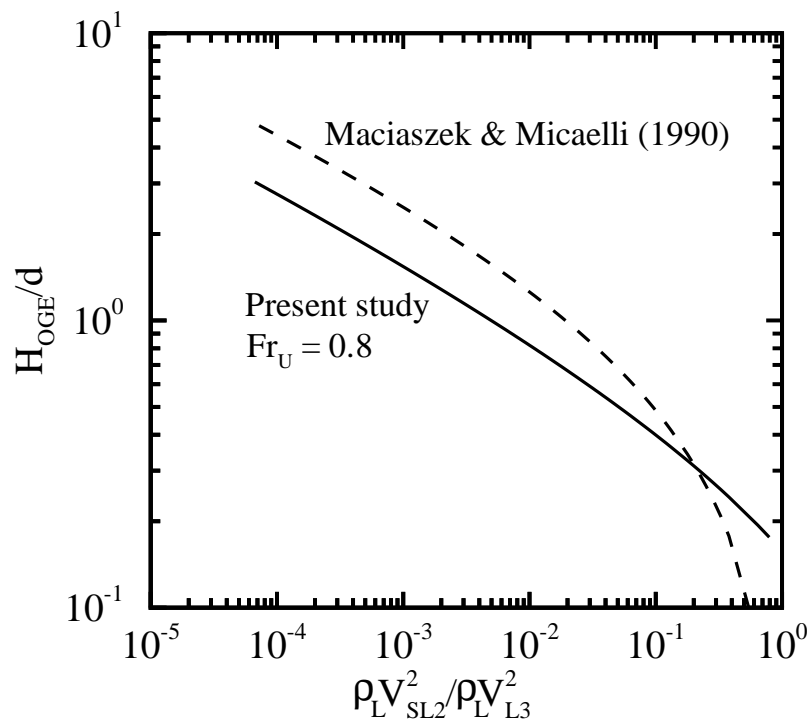


Figure 6.10: Comparison of the point-sink model with experimentally derived correlation compensating for crossflow effects (Maciaszek and Micaelli, 1990).

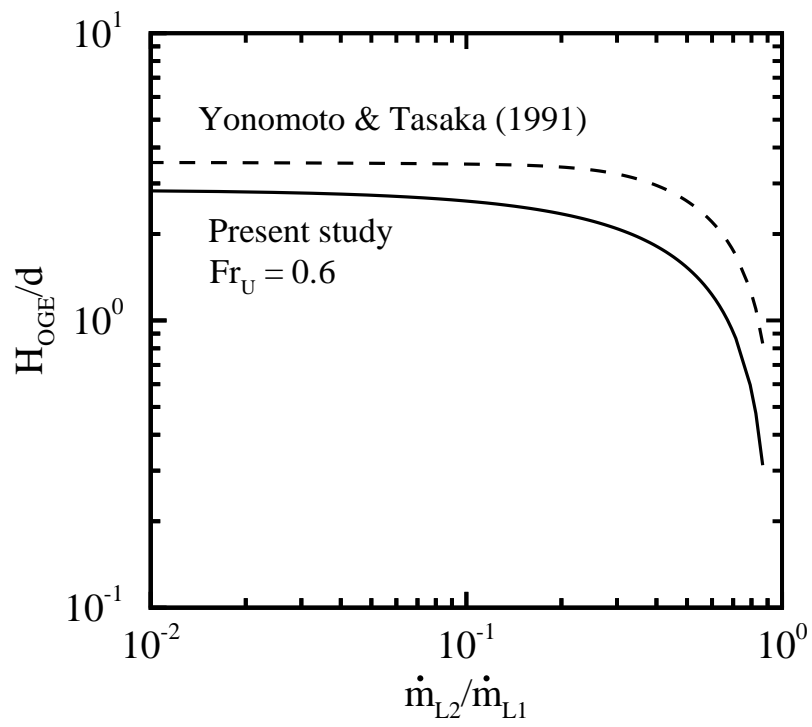


Figure 6.11: Comparison with Yonomoto and Tasaka (1991)'s correlation compensating for crossflow effects.

6.3 The OGE Criterion in Crossflow

6.3.1 Problem Description

The onset of gas entrainment was predicted analytically in §6.2 using two distinct criteria to define the dip location. In the first, the onset of gas entrainment was found assuming that the dip was located at a point where the vertical acceleration, a_y , was equivalent to gravity. The second criterion stated that the dip was located where the sink and crossflow velocities produced a horizontal stagnation point, i.e. the resultant velocity was equivalent to the vertical velocity component. The total potential function is a linear combination of the point-sink, ϕ_I , and uniform crossflow velocity, ϕ_{II} , potential functions. The velocity components are found from the gradient of the total potential function, as in Eq. (6.4), where the unit vectors in (x, y, z) directions are denoted as $(\mathbf{i}, \mathbf{j}, \mathbf{k})$ with magnitudes of (u, v, w) . The kinetic energy term, V_{LB}^2 , at the lowest point of the dip ($x = b, y = h, z = 0$) follows from Eq. (6.17) as,

$$V_{LB}^2 \Big|_{(x=b, y=h, z=0)} = \left[\left(U - \frac{\dot{m}_{I3} b}{2\pi \rho_L (b^2 + h^2)^{\frac{3}{2}}} \right)^2 + \left(\frac{\dot{m}_{I3} h}{2\pi \rho_L (b^2 + h^2)^{\frac{3}{2}}} \right)^2 \right]. \quad (6.44)$$

The squared velocity term on the left hand side of Eq. (6.44) also arises naturally, in §6.2.1, when Bernoulli's equation is applied on either side of the gas-liquid interface following from Eq. (6.16). The interface height at point A is H_{OGE} , while the interface height at the lowest point of the dip, point B , is h . The liquid kinetic energy term at point B, V_{LB}^2 , is therefore a function of the upstream kinetic energy at point A , V_{LA}^2 , and interfacial heights, h , and H . If the crossflow velocity, U , is considered uniform

and constant over the entire domain, as was the case in §6.2, Eq. (6.16) may be re-written here as,

$$V_{LB}^2 = U^2 + 2g \frac{\Delta\rho}{\rho_L}(H - h). \quad (6.45)$$

Craya (1949)'s Criterion

Craya (1949) defined the criterion for the onset of liquid entrainment (OLE) in a small branch from a large stratified gas-liquid reservoir ($U = 0$). It stated that the kinetic energy at point B obtained from Bernoulli's equation should be equivalent to that found when simulating the branch flow as a point-sink. Craya (1949) cited that three distinct solutions were possible when scanning a range of dip heights, h , for a given branch mass flow rate, \dot{m}_{L3} and the stagnant interface height (in this case H_{OGE}) as:

- Case 1: Eq. (6.45) and Eq. (6.44) do not intersect anywhere (No solution)
- Case 2: Eq. (6.45) and Eq. (6.44) intersect at two distinct values of h (Non-critical)
- Case 3: Eq. (6.45) and Eq. (6.44) intersect at a single value of h (Critical solution)

Craya (1949) indicated that Case 3 was representative of the OLE problem, which was satisfied when Eq. (6.45) and Eq. (6.44) were tangent as,

$$\left. \frac{dV_{LB}^2}{dh} \right|_{Eq.(6.45)} = \left. \frac{dV_{LB}^2}{dh} \right|_{Eq.(6.44)}. \quad (6.46)$$

Applying this methodology to the simple OGE case of a single branch in a large stratified gas-liquid reservoir ($U = 0$), the dip is located vertically above the branch at point B ($b = 0, h, z = 0$). The kinetic energy term in Eq. (6.44) can therefore be shown to reduce to,

$$V_{LB}^2 = \frac{\dot{m}_{L3}^2}{4\pi^2 \rho_L^2 h^4}. \quad (6.47)$$

The derivative of Eq. (6.47) with respect to h yields,

$$\frac{dV_{LB}^2}{dh} = \frac{-\dot{m}_{L3}^2}{\pi^2 \rho_L^2 h^5}. \quad (6.48)$$

Similarly, finding the derivative of Eq. (6.45) with respect to h , where H_{OGE} is constant and $U = 0$, yields,

$$\frac{dV_{LB}^2}{dh} = -2g \frac{\Delta\rho}{\rho_L}. \quad (6.49)$$

Combining Eq. (6.48) and (6.49) it can be shown that the dip height is related to the branch Froude number as,

$$\frac{h}{d} = 0.5 Fr_d^{0.4}. \quad (6.50)$$

This result was also found when using the acceleration based criterion in §6.2.1, where $\Delta\rho \cong \rho_L$ in Eq. (6.32). Substituting the relationship for the dip height back into Eq. (6.45) leads to the stagnant interface height, H_{OGE} , being related to the branch Froude number as found earlier in Eq. (6.33). Craya (1949)'s criterion is therefore capable of predicting the onset of gas entrainment in the simple stagnant stratified gas-liquid reservoir case. It is therefore instructive to investigate this criterion for the crossflow problem described in §6.2.1.

Rather than imposing a criterion for the offset distance, b , it is assumed here that a solution will exist somewhere along a line defined by a constant ratio of b/h . Doing so relaxes the dip height solution thereby allowing Craya (1949)'s criterion to be isolated, and investigated more readily. The range tested here is,

$$0 \leq \frac{b}{h} \leq 0.8 \quad (6.51)$$

A constant crossflow velocity of 0.25 m/s and a branch Froude number of 10 were chosen as test conditions. Solutions were obtained numerically, using a trial and error approach, while scanning a wide range of values of h and H_{OGE} . A sample of the solutions are presented here.

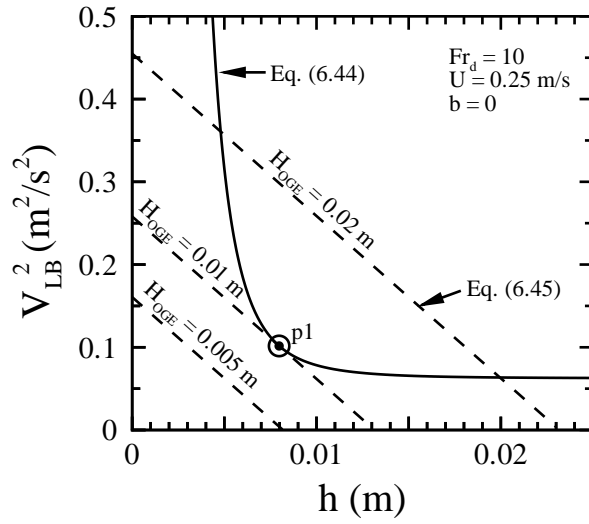
6.3.2 Results and Discussion

Equations (6.44) and (6.45) are presented as a function of the dip height, h , in Fig. 6.12. A ratio of $b/h = 0$ is presented in Fig. 6.12(a), and a ratio of $b/h = 0.5$ in Fig. 6.12(b). In each figure three inlet heights, H_{OGE} , are tested in order to demonstrate the three cases described by Craya (1949) above. In Fig. 6.12(a) an inlet height of $H_{OGE} = 0.05$ m represents Case 1, as there is no intersection of Eq. (6.45) and (6.44). An example of Case 2 is represented at an inlet height of $H_{OGE} = 0.02$ m, as h is found to equal either 0.00473 m or 0.02 m. Case 3, the critical solution, is found with an inlet height of $H_{OGE} = 0.01$ m and a single dip height of $h = 0.008$ m. The intersection of the two equations is labeled as $p1$. A critical solution is also found at a ratio of $b/h = 0.5$ in Fig. 6.12(b), with an inlet height of $H_{OGE} = 0.0066$

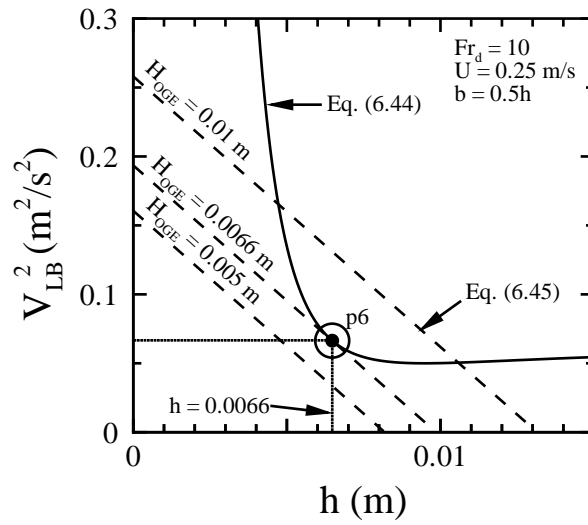
m and a corresponding dip height of $h = 0.0066$ m. This point is labeled as $p6$. These two points represent the physical limits of the solution. In the case of $p1$ the dip is located vertically above the branch, since $b/h = 0$. At $p6$ a solution is found where $H_{OGE} = h$; in effect, the dip becomes virtually non-existent as the interface is flat between points A and B . Numerical solutions where $h > H_{OGE}$ were found, however these are not physically appropriate since they indicate a dip located above the stagnant interface. These solutions were therefore ignored.

A selection of six points that were found to satisfy Eq. (6.46) are presented within the horizontal and vertical velocity fields, and corresponding kinetic energy field, in Fig. 6.14. The critical points are presented in each figure with the upper and lower physical limits labeled at $p1$ and $p6$, respectively. The contours represent the magnitude of each variable with the vector field superimposed to demonstrate the flow direction. The streamline that divides the flow going into the branch, or downstream towards the run, is denoted as the stagnation streamline. This streamline was found to pass through a stagnation point at $x = 0.00715$ m and $y = 0$. This point can be observed in Fig. 6.14(c), where $V_{LB}^2 \rightarrow 0$, denoted by the dark blue contour region. Alternatively, the branch is located at the center of the dark red contour region, where $V_{LB}^2 \rightarrow \infty$. To the left, and below the stagnation streamline, the liquid flows uniquely to the branch while everywhere else it flows towards the run.

All the critical points are found in the region to the left of the stagnation streamline. These points are also located well above the contour defined by $\partial\phi_I/\partial x = \partial\phi_{II}/\partial x$ in Fig. 6.14(a), which is a statement of the proposed offset distance criterion from Eq. (6.29). The proposed offset distance criterion is not simultaneously

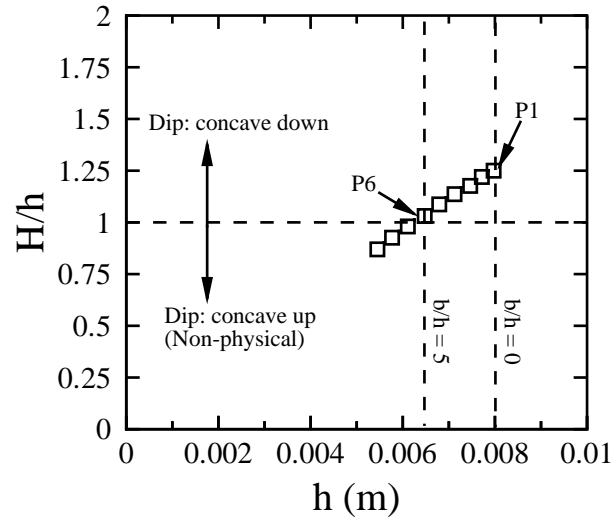


(a) $b/h = 0$

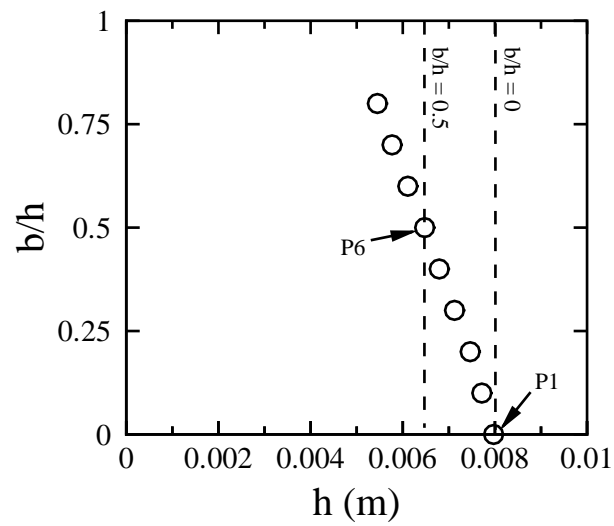


(b) $b/h = 0.5$

Figure 6.12: Evaluating Craya (1949)'s criterion at two different dip angles under crossflow $U = 0.25 \text{ m/s}$.

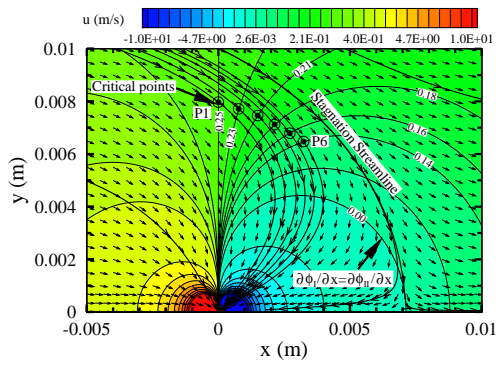


(a) Predicted upstream height relative to the dip height, H_{OGE}/h

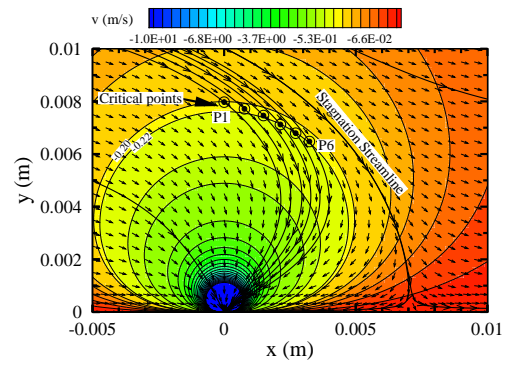


(b) Predicted dip offset distance relative to the dip height, b/h

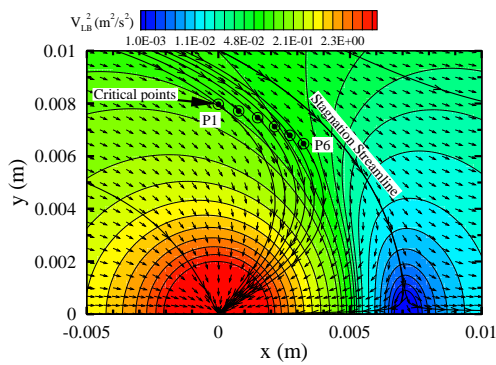
Figure 6.13: Predicted critical points using Craya (1949)'s criterion.



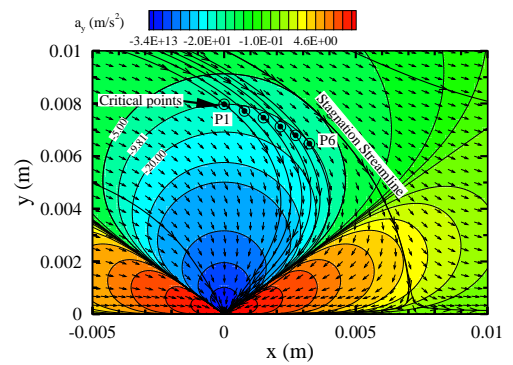
(a) Horizontal velocity field



(b) Vertical velocity field



(c) Kinetic energy field



(d) Vertical acceleration field

Figure 6.14: Location of critical points obtained using Craya (1949)'s criterion within the flow field.

satisfied with Craya (1949)'s criterion. The vertical velocity presented in Fig. 6.14(b) shows a marginal variation of $v = -0.20$ and $v = -0.22$ between $p1$ and $p6$, respectively. This vertical velocity, and its gradient in the vertical direction, were used in the acceleration based OGE criterion in Eq. (6.26). It is therefore useful to compare the six predicted points using Craya (1949)'s criterion with the vertical acceleration field defined by Eq. (6.26). As can be seen in Fig. 6.14(d), only $p1$ and $p6$ coincide exactly with the $a_y = -9.8 \text{ m/s}^2$ contour. The points in between these two limits are shown to lie just below the $a_y = -9.8 \text{ m/s}^2$ contour.

One of the fundamental differences between Craya (1949)'s criterion and the acceleration based criterion used earlier in Eq. (6.26) is that the former is insensitive to the inlet conditions. Therefore, it is possible to find a solution for a critical dip using the acceleration based criterion that can not be coupled to the inlet conditions through Bernoulli's equation. Craya (1949)'s criterion on the other hand explicitly defines the exchange of energy between the inlet and the critical dip in their criterion. In both instances however, coupling the critical dip and upstream conditions can be problematic if the crossflow velocity is not constant at points A and B , as will be discussed in more detail later in Chapter 7.

Horizontal Gradients in the $a = -g$ Criterion Under Crossflow Conditions

A consequence of using the vertical acceleration criterion described in Eq. (6.26) is that the crossflow velocity U vanishes from the OGE criterion when the horizontal,

x -direction, gradients are neglected. The horizontal convection term is,

$$u \frac{\partial v}{\partial x} = \frac{\partial \phi}{\partial x} \frac{\partial}{\partial x} \left(\frac{\partial \phi}{\partial y} \right). \quad (6.52)$$

Including the horizontal convection term, the vertical acceleration at any point $p(x, y, z)$ becomes,

$$a_y \Big|_{p(x,y,z)} = \frac{\partial \phi}{\partial x} \frac{\partial}{\partial x} \left(\frac{\partial \phi}{\partial y} \right) + \frac{\partial \phi}{\partial y} \frac{\partial^2 \phi}{\partial y^2} \Big|_{p(x,y,z)}. \quad (6.53)$$

In some cases the horizontal convection term may be negligible, for example when the dip is located directly above the simulated branch - this comes as a result of $u \rightarrow 0$ when $b \rightarrow 0$. This is a reasonable assumption for the stagnant reservoir model. However, when the dip is not located directly above the branch, the horizontal convection term is not negligible.

To test this a value of $U = 0.25$ m/s is imposed in Eq. (6.53), the resulting acceleration field is shown in Fig. 6.15. Comparing this with Fig. 6.14(d), it is evident that the shape of the $a = -9.8$ m/s² contour changes quite dramatically. This has direct implications on the OGE criterion, since it can be satisfied anywhere along this contour where $b \geq 0$. For example, at $p6$ in Fig. 6.14(d) $a_y = -9.8$ m/s², however in Fig. 6.15 at the same point $a_y = -4.3$ m/s², or a difference of 56%. This reasoning lead to the inclusion of the horizontal convection term in the analysis presented in Chapter 7.

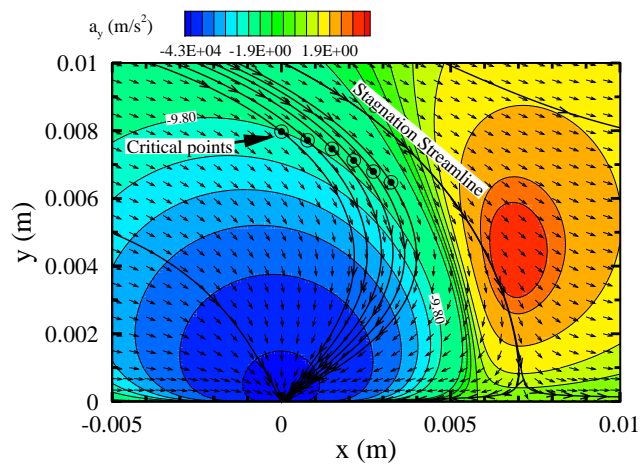


Figure 6.15: Vertical acceleration field including the gradients in the x-direction.

6.4 The OGE Criterion for Two Branches

The geometry considered in this section is presented in Fig. 6.16. Two branches of diameter, d , are installed on a flat inclined wall. The wall inclination, β , varies between 0 and 90 degrees, and the branches are separated by a center-to-center distance, L_S . The origin of the co-ordinate system ($x = 0$, $y = 0$, $z = 0$) is located at the center of branch II 's inlet. The branches are exposed to a semi-infinite stratified two-phase environment of heavier and lighter fluids. The heavier fluid is considered as the liquid (subscript L) phase and the lighter fluid as the gas (subscript G) phase. The fluid phase densities are ρ_L and ρ_G . The heavier fluid initially flows through branches I and II with mass flow rates of \dot{m}_{L3-I} and \dot{m}_{L3-II} , respectively. To investigate the effect of a second branch, consider that the crossflow velocity of the heavier fluid is zero, $U = 0$, and that the lighter fluid phase is negligible.

Flow Field Simulation

The flow field is considered steady, incompressible, inviscid, and irrotational, with negligible surface tension. These assumptions reduce the problem to a potential flow which is governed by forces of inertia and gravity. The three-dimensional continuity equation, in Cartesian co-ordinates (x, y, z), reduces to Eq. (6.2). The irrotationality condition is satisfied when a scalar potential function, ϕ , is defined such that the velocity is defined through Eq. (6.4). Substitution of the scalar potential function into the continuity equation yields the well known Laplace's equation, as in Eq. (6.6). A characteristic of this elliptic type partial differential equation is that a solution can

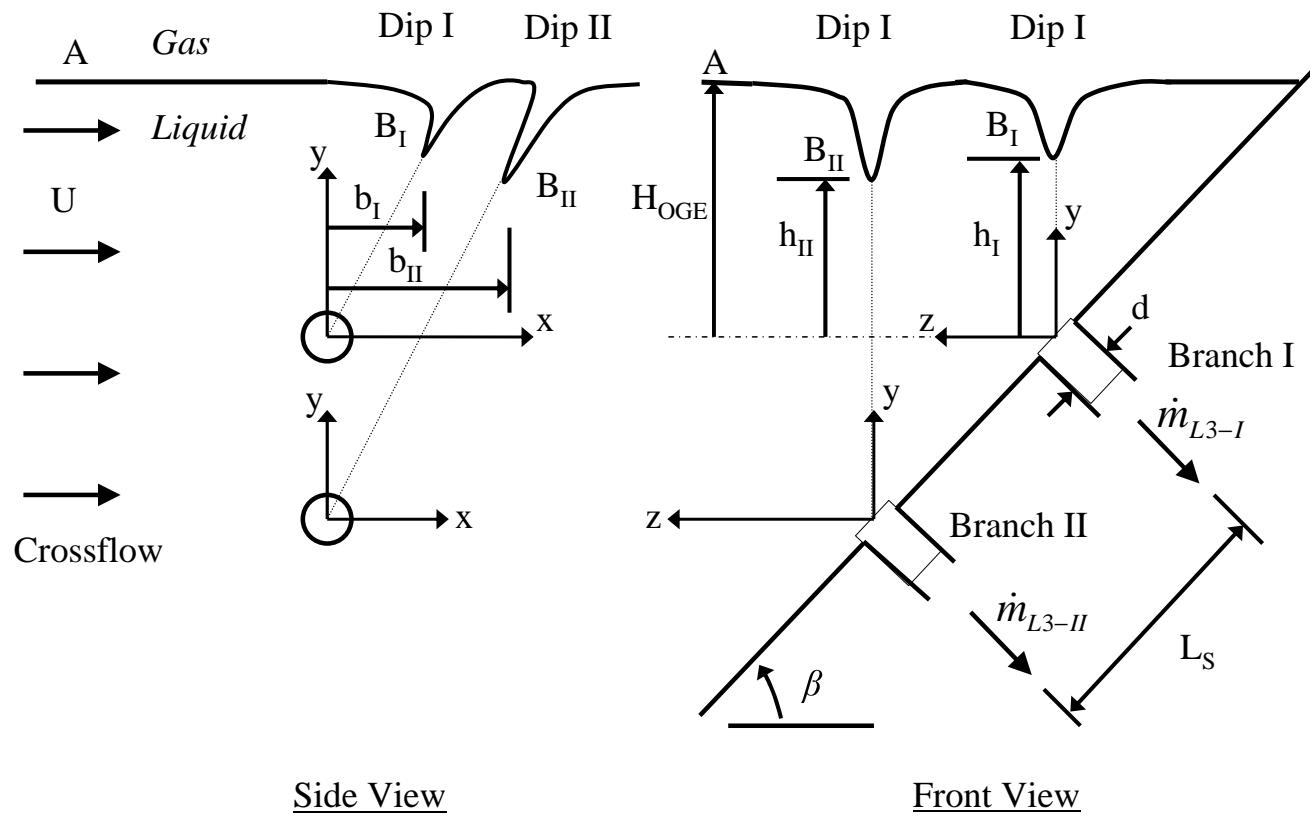


Figure 6.16: Geometry and flow conditions.

be a linear combination of two or more solutions, say ϕ_I , and ϕ_{II} , which can be written as,

$$\phi = \phi_I + \phi_{II}. \quad (6.54)$$

Potential flow theory has provided well-known solutions to Laplace's equation for point-sinks and uniform flows. By simulating each branch as a point-sink with a hemi-spherical flow area the linearity theorem in Eq. (6.54) can be applied. For the configuration presented in Fig. 6.16 the point-sink potential functions of branches I and II can be described following Schetz and Fuhs (1996) as,

$$\phi_I = \frac{\dot{m}_{L3-I}}{2\pi\rho_L\sqrt{x^2 + (y - L_s \sin \beta)^2 + (z + L_s \cos \beta)^2}} \quad (6.55)$$

and,

$$\phi_{II} = \frac{\dot{m}_{L3-II}}{2\pi\rho_L\sqrt{x^2 + y^2 + z^2}} \quad (6.56)$$

Onset of Gas Entrainment Criterion

The onset of gas entrainment criterion follows from Eq. (6.24), with the vertical direction denoted by the y -axis. In single branch scenarios Eq. (6.26) has been shown to provide a reasonable prediction of the gas entrainment dip height, h in stagnant reservoirs. One of the pitfalls of using this criterion in two-branch arrangements, as will be discussed later, is that it can be difficult to distinguish which branch induces the OGE without additional reasoning.

Considering that the total potential function, ϕ , is a linear combination of solutions, from Eq. (6.54), the total vertical acceleration, a_y , can be found to be,

$$a_y = \frac{\partial\phi_I}{\partial y} \frac{\partial^2\phi_I}{\partial y^2} \left(1 + \frac{\partial\phi_{II}}{\partial\phi_I}\right) + \frac{\partial\phi_{II}}{\partial y} \frac{\partial^2\phi_{II}}{\partial y^2} \left(1 + \frac{\partial\phi_I}{\partial\phi_{II}}\right) \quad (6.57)$$

The first term on the right hand side of Eq. (6.57) represents the total vertical acceleration produced if branch I acted alone in the flow field. For example, substituting $\phi_{II} = 0$ into Eq. (6.57) reduces the bracketed expressions to a value of 1, and consequently Eq. (6.57) reduces to the single branch expression in Eq. (6.26). A similar result would be found if branch II acted alone, substituting $\phi_I = 0$. The term in each bracketed expression represents the relative change in one branch's potential function with the other. The bracketed term scales the contributed acceleration from each respective branch to the total acceleration. Since the vertical velocity, v , is defined using the potential function definition in Eq. (6.4), as $v = \partial\phi/\partial y$, the term contained within the brackets can be conveniently written as a ratio of vertical velocities, v , through the chain rule. Defining the vertical acceleration for branch I as a_I and for branch 2 as a_{II} where,

$$a_I = \frac{\partial\phi_I}{\partial y} \frac{\partial^2\phi_I}{\partial y^2} \quad (6.58)$$

and,

$$a_{II} = \frac{\partial\phi_{II}}{\partial y} \frac{\partial^2\phi_{II}}{\partial y^2} \quad (6.59)$$

results in,

$$a_y = a_I \left(1 + \frac{v_{II}}{v_I}\right) + a_{II} \left(1 + \frac{v_I}{v_{II}}\right), \quad (6.60)$$

where,

$$v_I = \frac{\partial \phi_I}{\partial y} \quad (6.61)$$

and,

$$v_{II} = \frac{\partial \phi_{II}}{\partial y}. \quad (6.62)$$

The OGE criterion, following from Eq. (6.24), results in the right hand side of Eq. (6.60) being equal to $-g$ at a single location within the flow field, denoted as point B (the lowest point of the dip). While this criterion is sufficient for single branch conditions it may not suffice for predicting the three modes that have been observed experimentally by Parrott et al. (1991):

- Mode 1: OGE in branch I only
- Mode 2: OGE in branch II only
- Mode 3: OGE in branches I and II

Mode 1 was predominantly observed in Parrott et al. (1991)'s study, as branch I was located above branch II in the same vertical plane, and OGE tended to occur in the branch closest to the interface. In certain instances however, the gas phase would be pulled into the lower branch with the air core by-passing the upper branch (Mode 2). This was usually the result of the flow rate in branch II being much greater than that in branch I ($Fr_{II} \gg Fr_I$). Slowly increasing the flow rate in branch I, keeping the flow rate in branch II constant, showed that the gas phase would eventually entrain in both branches simultaneously (Mode 3). Parrott et al. (1991)'s

experiments showed that two dips can form in the gas-liquid interface during dual branch scenarios. Theoretically this implies that two points in the flow field, B_I and B_{II} from Fig. 6.16, respectively, satisfy the OGE criterion in Eq. (6.24). Considering that each dip forms in the region above the branch, limitations arise as,

$$L_s \rightarrow 0, \quad (6.63)$$

and,

$$\begin{aligned} \beta &= 90^\circ \\ L_s &> 0. \end{aligned} \quad (6.64)$$

The two dips are located within the flow field at points B_I and B_{II} for branch I and branch II, respectively. From Fig. 6.16, using the assigned coordinate system, these points are defined at:

$$B_I \left\{ \begin{array}{l} x = b_I \\ y = h_I + L_S \sin \beta \\ z = -L_S \cos \beta \end{array} \right. \quad (6.65)$$

and,

$$B_{II} \left\{ \begin{array}{l} x = b_{II} \\ y = h_{II} \\ z = 0 \end{array} \right. \quad (6.66)$$

This section investigates the OGE criterion for dual branch cases, and looks specifically to the limitations resulting from Eq. (6.63) and Eq. (6.64). The branch strength

is represented by the branch Froude number, following from Eq. (6.22) for branches I and II as Fr_I , and Fr_{II} , respectively. To predict the dip locations there are a total four unknowns, these are h_I , b_I , h_{II} , and b_{II} . For the purpose of this study, the offset distance term, b , will be considered negligible, which arises from $U = 0$. The dips are therefore located vertically above each branch, by their respective dip heights, h . The separating distance, L_S , is varied between 0 to $10d$ while the wall inclination angle, β , is varied between 0 degrees (*horizontal wall*) and 90 degrees (*vertical wall*).

6.4.1 Results and Discussion

Single Branch

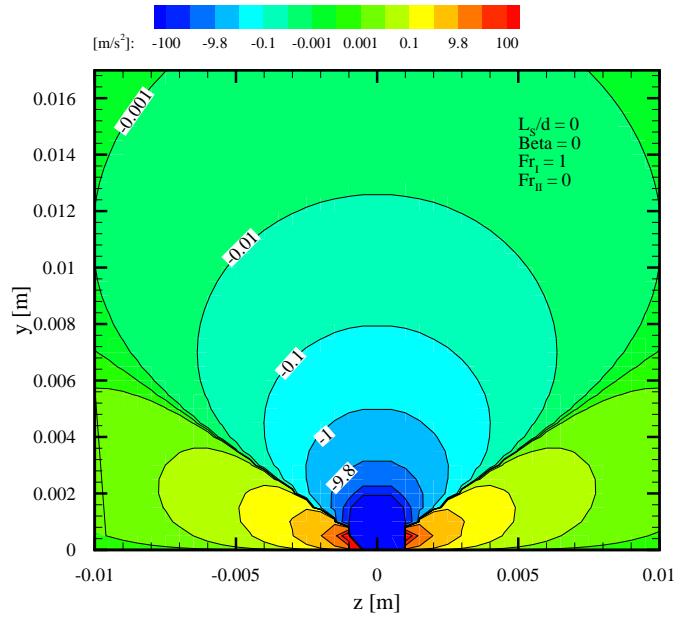
A typical vertical acceleration field of a single branch case is presented in Fig. 6.17(a), for $Fr_I = 1$. The acceleration is shown to dramatically increase as the branch inlet is approached at the origin ($x = 0, y = 0, z = 0$). The acceleration contour corresponding to the gravitational acceleration is shown to extend vertically until $y = 3.175$ mm. This corresponds to the predicted vertical location of the dip height, h_I . The corresponding critical height following from Eq. (6.33), was found to be 3.968 mm. The acceleration profile along a vertical line passing through the branch inlet ($x = 0, z = 0$) is presented in Fig. 6.17(b) for $Fr_I = 1$ and 20. The absolute value of the acceleration is used in order to present the profile on a log scale. Increasing the branch Froude number increases the acceleration magnitude at any y . Increasing the branch Froude number from 1 to 20 lead to an increase in the dip height from 3.175 mm to 10.52 mm. Alternatively, the critical height, H_{OGE} , yields an increase from 3.96 mm

to 13.15 mm.

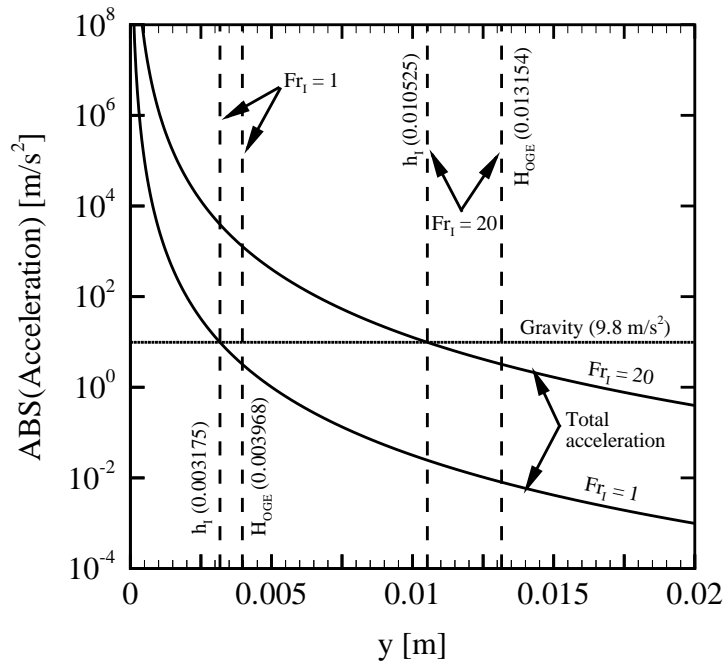
Two branches in the Same Horizontal Plane

The vertical acceleration field resulting from adding a second branch in the domain along the same horizontal plane ($\beta = 0$) is presented in Fig. 6.18. In this case the second branch has $Fr_{II} = 20$ with its origin located at $(0,0,0)$ while $Fr_I = 1$ and located at $(0,0,-12.7\text{mm})$. The spacing between the branches is 12.7 mm ($L_S/d = 2$). Two distinct contours are observed where the acceleration is equivalent to gravity (-9.8 m/s^2). The contour on the left hand side is located near branch I, while the other is located near branch II. The area and maximum height achieved by branch II's contour is significantly larger than that of branch I - as might be expected since $Fr_{II} \gg Fr_I$. The dip height above branch I was found to be $h_I = 3.26 \text{ mm}$, which is 2.7% larger than the single branch case presented in Fig. 6.17 for $Fr_I = 1$. This demonstrates the effect that branch II has on the vertical acceleration local to branch I. On the other hand the effect of branch I on branch II's acceleration field is negligible. Comparing with the single branch case, where $Fr_{II} = 20$, it was found that h_{II} changes by around 0.1%. The branch with the highest Froude number will therefore have the greatest influence on the acceleration field local to the other branch.

It was found that increasing the separating distance, L_S/d , reduced these effects. Conversely, as the separating distance decreases, or Fr_{II} increases, branch II's effect on the acceleration field surrounding branch I increases. It can increase to the point where the contours begin to merge together, for example as seen along the $a_y = -0.1$



(a) Sample vertical acceleration field, $Fr_I = 1$



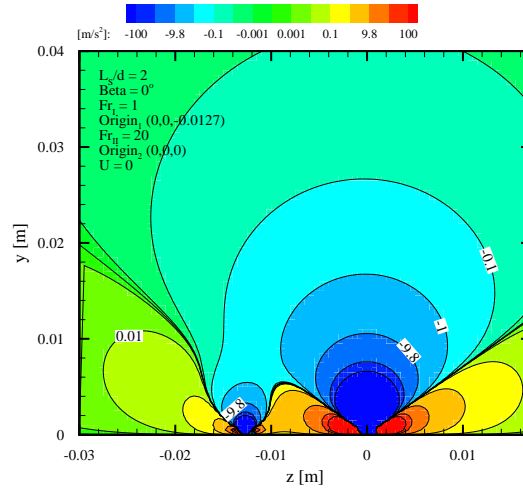
(b) Acceleration profile extracted at $x = 0, z = 0$, along $y \geq 0$

Figure 6.17: Effect of Fr_I on the vertical acceleration for a single branch.

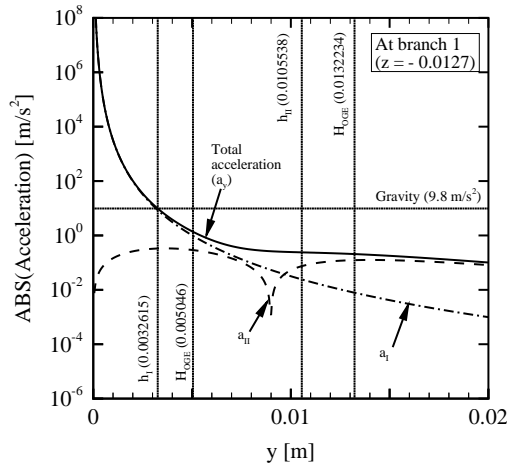
m/s^2 contour. If the $a_y = -g(9.8m/s^2)$ contours merge this implies that the OGE criterion does not in itself distinguish which branch is responsible for the formation of each dip at h_I and h_{II} . This is because the total acceleration, a combination of acceleration fields induced by both branches, defines the OGE criterion.

The acceleration profile along a vertical line passing through each branch is presented in Fig. 6.18(a) and Fig. 6.18(b) for branches I and II, respectively. The total acceleration, a_y from Eq. (6.60) is presented along with the acceleration resulting from each branch acting alone, a_I and a_{II} , respectively. At h_I in Fig. 6.18(a), a_{II} is shown to be approximately an order of magnitude smaller than a_I . As the vertical distance above the branch increases beyond h_I it can be seen that a_I diverges from a_y , while at $y > 0.008$ m a_{II} begins to converge on a_y . At $y = 0.02$ m, where the $a_y = -0.1 m/s^2$ contour was shown to merge in Fig.6.18(a), the difference between a_y and a_{II} is approximately 20%. At the same location, a_I is shown to be two orders of magnitude smaller than a_y . In Fig. 6.18(b) a_{II} is nearly identical to a_y , and a_I is several orders of magnitude smaller than a_y . The dip and critical heights obtained for each branch are also presented in Fig. 6.18. The critical stagnation height is found following the methodology in §6.2.1 using the predicted dip conditions, specifically h and V_B^2 .

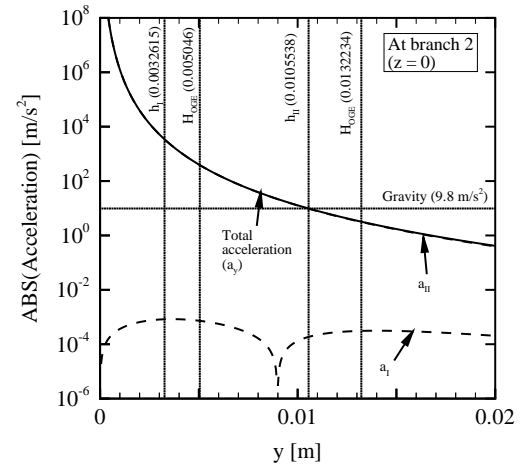
When the separating distance, L_S/d , is reduced to the point where the $a_y = -9.8 m/s^2$ contours merge, branch II causes a dramatic increase in the vertical acceleration above branch I, and consequently the dip height, h_I . The OGE criterion at branch I, can therefore be significantly influenced by branch II. Since the dip height at branch II is much larger than branch I's however, a comparison of the dip heights reveals



(a) Acceleration field



(b) Profile at branch I



(c) Profile at branch II

Figure 6.18: Vertical acceleration resulting from two branches in the same horizontal plane, with $Fr_I = 1$, $Fr_{II} = 20$ and $L_s/d = 2$.

that OGE will likely occur at branch II before it occurs at branch I. Reducing the separating distance until $L_S = 0$ produces a flow field represented by the single branch case where the Froude number is sum of the two branch Froude numbers, $Fr_d = Fr_I + Fr_{II}$. In such a scenario a single dip is created and OGE occurs in both branches simultaneously. Although this scenario is practically impossible - two branches can not occupy the same physical space - it is used to illustrate the limitations of the OGE criterion. Another dual branch scenario arises when the two branch Froude numbers are equal. The dip heights and critical heights produced are identical, as are the acceleration profiles above the branches, which results in OGE in both branches simultaneously.

Two branches in a vertical plane

Presented in Fig. 6.19 is the onset of gas entrainment prediction where the two branches are aligned in the same vertical plane ($\beta = 90^\circ$). The secondary branch Froude number is constant, $Fr_{II} = 56.7$, while Fr_I is varied. The branch separating distance is constant at $L_S/d = 1.5$. This case is representative of the experimental study performed by Parrott et al. (1991) which described OGE in branch I while branch II was active. Their measurements were performed by recording the vertical distance from the tip of the liquid meniscus to the branch centerline (H_m) and the vertical distance from the free surface to the branch centerline (H_f). In effect, the difference between these two readings is the meniscus height, which may vary according to fluid and surface conditions. Parrott et al. (1991)'s data is also presented in Fig. 6.19 for comparison. The trend of the prediction is well suited to the experiments,

however, it under-predicts H_m while over-predicting H_f . In absolute terms, Parrott et al. (1991) quoted a meniscus height of approximately 3 mm, meaning that the difference between the prediction and H_m , or H_f , is approximately 1.5 mm. It is reasonable to expect that this small deviation will be within the bounds of experimental uncertainty.

Parrott et al. (1991) reported experimental evidence that supported the three different modes of the OGE. From their experiments two dips can be produced however, from the theoretical point of view, using the OGE criterion only a single dip can be produced with two branches in the same vertical plane. This comes as a direct consequence of assuming that the dip lies vertically above the branch. Typical acceleration fields are presented in Fig. 6.20 and 6.21 to further illustrate this point.

The acceleration field produced when $L_S/d = 5$ for $Fr_I = 1$ and $Fr_{II} = 20$ is presented in Fig. 6.20(a). The vertical acceleration profile passing through both branch centers is presented in Fig. 6.20(b). Two distinct contours are shown where the acceleration is equal to gravity ($a_y = -9.8 \text{ m/s}^2$). These two contours are shown to originate from each of the two branches, the upper at branch I and the lower at branch II. These two contours correspond to the intersection where $a_y = -g$ in Fig. 6.20(b). In this arrangement the highest dip location seemingly corresponds to branch I, and would result in OGE in this branch. The acceleration profile also seems to support OGE in branch I since a_I is approximately equal to a_y at the highest dip point. Since two distinct locations are found where $a_y = -g$, OGE will occur in the branch with the highest h - as was the case in the horizontal plane arrangement. Decreasing the branch spacing, L_S/d , will cause the two acceleration fields to merge.

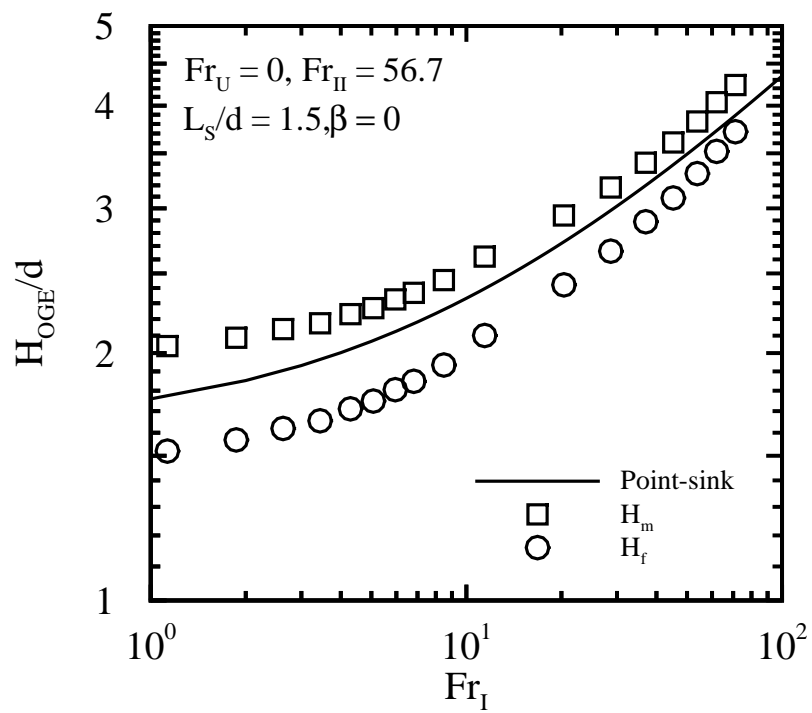
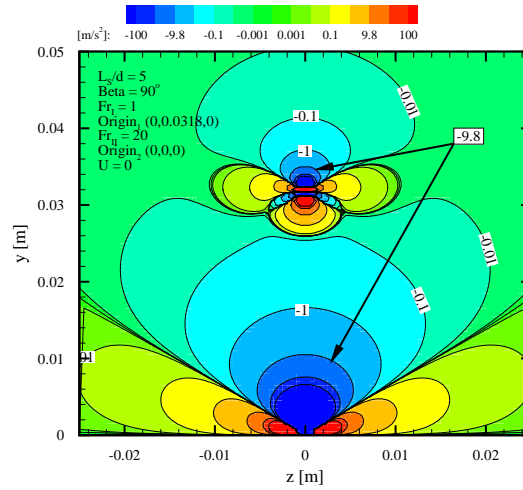
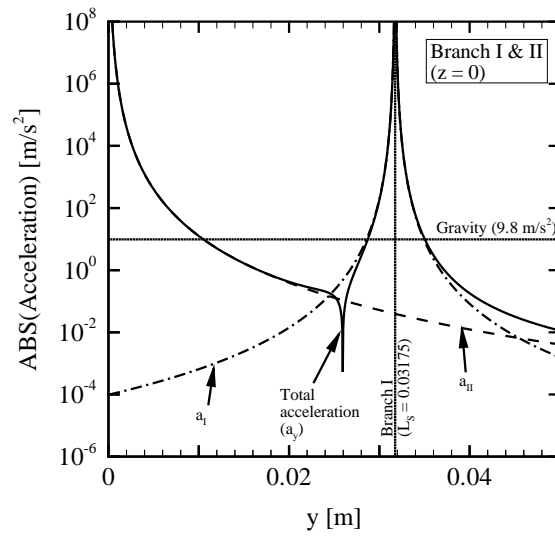


Figure 6.19: Onset of gas entrainment in branch I with $Fr_{II} = 56.7$ compared with Parrott et al. (1991)'s experiments.

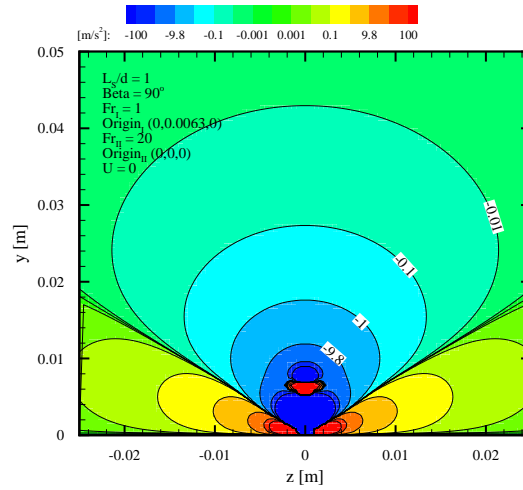


(a) Vertical acceleration field

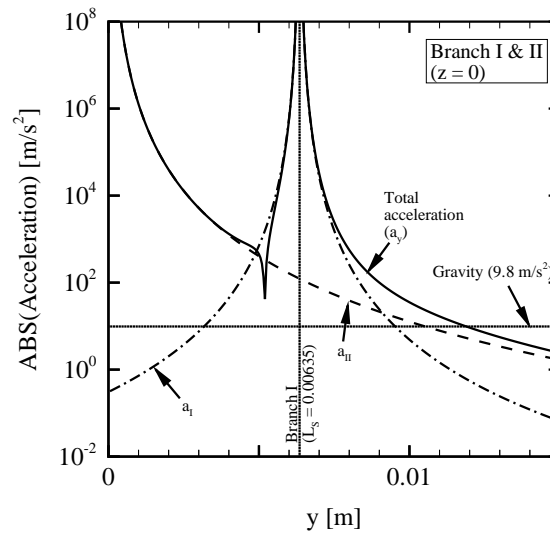


(b) Acceleration distribution along $z = 0$

Figure 6.20: Acceleration field of two branches in the same vertical plane with $L_S/d = 5$.



(a) Vertical acceleration field



(b) Acceleration distribution along $z = 0$

Figure 6.21: Acceleration field of two branches in the same vertical plane with $L_S/d = 1$.

If the spacing is sufficiently small, but keeping $L_S > 0$, a single contour where $a_y = -g$ will exist.

The resulting acceleration field from a reduction in L_S/d , from 5 to 1, is presented in Fig. 6.21. The branch spacing causes the two $a_y = -9.81 \text{ m/s}^2$ contours from Fig. 6.20 to merge into a single contour in Fig. 6.21. The acceleration profile along a vertical line passing through both branch centers is presented in Fig. 6.21(b). The effect of reducing the branch separating distance is that a single point exists where the acceleration is equal to gravity, which implies the existence of a single dip. In this case the OGE criterion alone does not distinguish at which branch gas entrainment occurs. As seen from Fig. 6.21(b), where $a_y = 9.81 \text{ m/s}^2$, a_{II} is shown to be much larger than a_I and would seem to imply that OGE is in branch II. The fact that a_{II} is larger than a_I is not sufficient evidence to establish which branch OGE occurs in. This limitation requires that further considerations of the OGE criterion are required in order to predict the conditions causing the three modes of gas entrainment.

6.5 Summary

Section 6.2 outlines a novel theoretical model to predict the critical height at the onset of gas entrainment in a single downward branch with liquid crossflow. The model demonstrated that the OGE phenomenon was governed by the branch and crossflow Froude numbers. Comparison of the critical height from the benchmark case with both quasi-steady and unsteady experimental data showed good agreement with a maximum deviation of 30%. Empirical correlations for the critical height derived from flowing stratified channels, however, demonstrated significant discrepancies with regards to the effects of crossflow on the critical height. These studies typically omitted details of the inlet conditions, and more specifically, the relationship between the critical height and the inlet liquid mass flow rate. As a result, the crossflow velocity term could not be appropriately defined in their particular cases. This lack of data had provided part of the motivation to experimentally investigate the OGE phenomenon in a single branch, as described in Chapter 4. Furthermore, the assumed constant crossflow velocity throughout the analytical domain was not representative of the experimental findings in Chapters 4 and 5. Due to interfacial liquid gradients within the inlet, and the shape of the OGE dip, the crossflow velocity requires a local definition. Sections 6.3 and 6.4 provided considerations, and improvements, to the OGE criterion used in §6.2 in the presence of a liquid crossflow velocity term, or a second branch. It was found that the proposed offset distance criterion may lead to erroneous results. The next chapter explores the use of empirical boundary conditions to address the definitions of the local crossflow velocity, and the offset distance.

Chapter 7

Semi-Empirical Modeling of the Onset of Gas Entrainment

7.1 Chapter Overview

Modeling the OGE in Chapter 6 was based on an unconfined geometry - a branch in a semi-infinite medium. A constant horizontal liquid crossflow velocity was imposed throughout the entire domain to simulate a flowing stratified gas-liquid regime. This boundary condition, however, posed a challenge when attempting to compare the predictions with experiments since in reality the crossflow velocity is not constant, and should be defined locally. The present study improves upon the earlier analysis by modeling the branch within a confined horizontal channel, and defines the crossflow velocity locally at two distinct locations. To simplify the analysis a square cross-section was employed, which allowed the velocity field to be modeled using well known potential functions, following from Chapter 6. Empirical closure relations were found

to be needed, and provided the motivation for performing a series of experiments on the OGE phenomenon. Experiments were performed using a branch installed at the bottom of a horizontal pipe with a flowing stratified gas-liquid regime within the inlet, upstream of the branch. A digital imaging technique was incorporated in order to determine the critical dip location, as well as the interfacial liquid profile upstream of the branch.

7.2 Feasibility Study: Semi-Empirical Methods

One of the challenges associated with theoretically modeling the onset of gas entrainment, in Chapter 6, was establishing the criteria needed to predict the critical dip location relative to the branch. This is particularly true when there is an imposed liquid crossflow, since the dip is no longer located directly above the branch, but rather shifted a finite offset distance downstream. Digital imaging has been used in the past to quantify gas-liquid interfacial features, and more specifically, the steady dip profile at a bottom branch in a large stratified reservoir (Saleh et al., 2009). Technical challenges aside, Saleh et al. (2009) demonstrated it was feasible to record the steady dip profile using digital imaging.

7.2.1 Problem Description

In their paper Saleh et al. (2009) used digital imaging to capture the side projection of a steady dip at a bottom oriented branch from a large stratified gas-liquid reservoir. The measurements were needed in order to quantify the effects of surface tension in

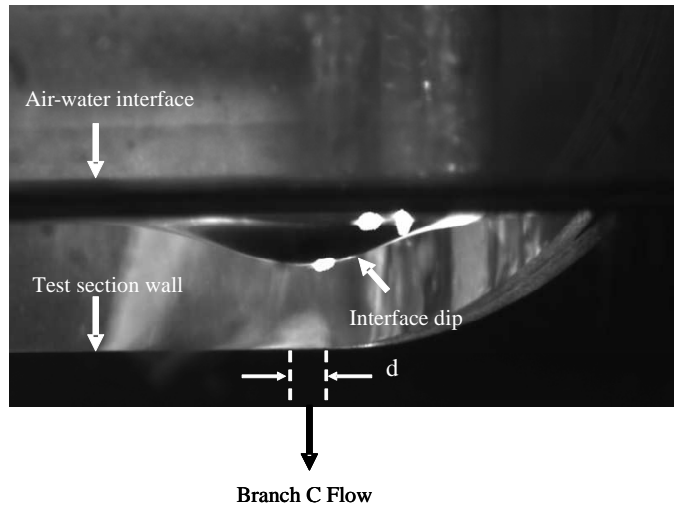
their semi-empirical model. They were interested in the dip's shape and curvature rather than the dip location, since they were able to determine it analytically using the OGE criterion following from Eq. (6.24). A sample image is shown in Fig. 7.1(a), and a schematic of the problem is shown in Fig. 7.1(b). The measurements included a digitized planar map of the dip profile (the side projection) in x, y coordinates. The lowest point of the critical dip, referred to here as the vertical height h in Fig.7.1(b), has been cited as the critical link needed to predict the OGE or OLE phenomena in stratified reservoirs (Craya, 1949; Soliman and Sims, 1991; Ahmed et al., 2003; Andaleeb et al., 2006).

7.2.2 Analysis and Results

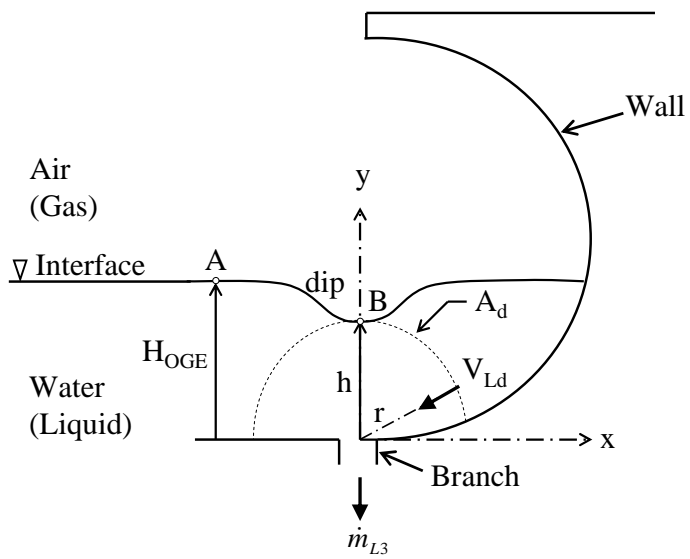
In their analysis Saleh et al. (2009) argued that the OGE dip height was predicted when the vertical acceleration at the lowest point of the dip was equivalent to the gravitational acceleration. The criterion was then coupled with a two-fluid separated flow model that was derived using Bernoulli's equation on either side of the gas-liquid interface, similar to the procedure outlined in Chapter 6. In effect the critical stagnation height, H_{OGE} , is found as a function of the dip height and dip kinetic energy, V_{LB}^2 as,

$$H_{OGE} = h + \frac{\rho_L}{\Delta\rho} \frac{V_{LB}^2}{2g}. \quad (7.1)$$

In order to find V_{LB}^2 , the branch flow can be simulated as a point-sink, and in effect the fluid flows radially inward to the branch center. The flow area control surface (A_d) becomes hemi-spherical, as shown in Fig. 7.1(b), where at any radial



(a) Image courtesy of Saleh et al. (2009)



(b) Problem description

Figure 7.1: Steady dip in a stagnant two-phase reservoir at a bottom oriented branch.

distance, r , the liquid velocity is uniformly distributed over the entire surface. The liquid velocity, V_{Ld} , over the control surface area, A_d , at any r , can be found using the branch liquid mass flow rate, \dot{m}_{L3} , as

$$V_{Ld} = \frac{\dot{m}_{L3}}{\rho_L A_d}, \quad (7.2)$$

where for a hemi-sphere of radius r ,

$$A_d = 2\pi r^2. \quad (7.3)$$

At the onset of gas entrainment the lowest point of the dip is h and A_d has a radius $r = h$, assuming that the dip is oriented directly above the branch. The critical dip velocity, V_{LB} , or more conveniently the kinetic energy term V_{LB}^2 , can be determined by re-arranging Eq. (7.2) while substituting $r = h$ as,

$$V_{LB}^2 = \left(\frac{\dot{m}_{L3}}{2\pi\rho_L h^2} \right)^2. \quad (7.4)$$

Saleh et al. (2009) reported both the free surface height, H_{OGE} , as well as the side projection of the dip profile for three branch Froude numbers. The dip height for these branch Froude numbers can be found and used to determine the kinetic energy at the lowest point of the dip using Eq. (7.4). The dip height was extracted from their data and is reproduced here in Table 7.1. Substituting V_{LB}^2 from Eq. (7.4) into Eq. (7.1), the stagnation height can be determined. This is done in order to compare with the measured values of H_{OGE} in Table 7.1. The calculated values are also shown

in Table 7.1; the results demonstrate that H_{OGE} is predicted with a mean absolute error of 11%. Simulation of the branch as a point-sink, coupled with measurements of h , yields a reasonable prediction of the critical height. Digital imaging therefore provides a reasonable method for defining the critical dip location. It can be used as an alternative method to purely theoretical analysis in the prediction of the onset of gas entrainment.

Table 7.1: Saleh et al. (2009)'s data for OGE in a bottom branch

Fr_d	H_{OGE} (Experiment) (mm)	h (Experiment) (mm)	$\frac{\Delta\rho V_{LB}^2}{2g\rho L}$ (Eq. (7.4)) (mm)	H_{OGE} (Eq. (7.1)) (mm)	Error (H_{OGE}) (%)
1.2	5.52	2.68	2.07	4.75	13.9
6.9	8.45	7.66	1.12	8.78	3.9
31.6	16.62	13.88	2.16	16.04	3.5

7.3 Reduced T-Junction With Co-current Stratified Gas-Liquid Flow

7.3.1 Theoretical Analysis

Problem Description

A horizontal channel with a square cross-section of side length D is shown in Fig. 7.2 to have a bottom oriented branch of diameter d . The branch inlet is the origin of the Cartesian coordinate system ($x = 0, y = 0, z = 0$). Liquid flows into the branch with a mass flow rate of \dot{m}_{L3} , and flows out of the run as \dot{m}_{L2} . Gas flows out of the run with a mass flow rate of \dot{m}_{G2} . Subscripts L and G are used to denote the liquid and gas phases, while subscripts $1, 2$ and 3 denote the inlet, run, and branch, respectively. The gas-liquid interface in the inlet is considered to be smooth-stratified and the interfacial shear induced by the gas phase is assumed to be negligible. The liquid side is assumed to be quasi-steady, incompressible, inviscid, and irrotational, with negligible surface tension.

A steady dip is observed to form in the gas-liquid interface with its lowest point at B ($x = b, y = h, z = 0$) at the onset of gas entrainment. Applying Bernoulli's equation on the gas side from a location within the inlet, at point A ($x = -\lambda, y = H_{OGE}, z = 0$), and point B results in,

$$P_{GA} - P_{GB} = \rho_G g(h - H_{OGE}) + \frac{\rho_G}{2}(V_{GB}^2 - V_{GA}^2). \quad (7.5)$$

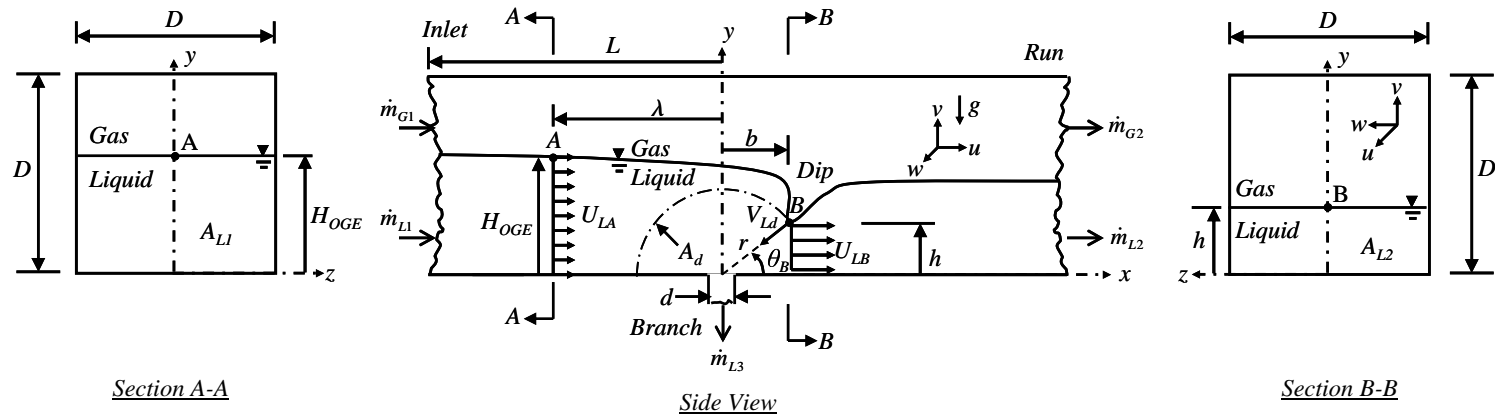


Figure 7.2: Theoretical problem description.

The static pressure is defined as P , the density as ρ , gravitational acceleration as g , the height of the interface at point A relative to the bottom of the channel as H_{OGE} , and at point B as h . Subscripts A and B are used to denote the two interfacial points. The kinetic energy of the gas phase is considered negligible and therefore,

$$\frac{\rho_G}{2}(V_{GB}^2 - V_{GA}^2) = 0. \quad (7.6)$$

Similarly, for the liquid phase, applying Bernoulli's equation between point A and B yields,

$$P_{LA} - P_{LB} = \rho_L g(h - H_{OGE}) + \frac{\rho_L}{2}(V_{LB}^2 - V_{LA}^2). \quad (7.7)$$

Thermodynamic equilibrium is assumed on either side of the gas-liquid interface ($P_{LA} = P_{GA}$, $P_{LB} = P_{GB}$) which requires that,

$$P_{LA} - P_{LB} = P_{GA} - P_{GB}. \quad (7.8)$$

Setting the right hand sides of Eq. (7.5) and (7.7) equivalent to each other, and re-arranging to solve for the liquid phase kinetic energy at point B , V_{LB}^2 , yields,

$$V_{LB}^2 = 2g \frac{(\rho_L - \rho_G)}{\rho_L} (H_{OGE} - h) + V_{LA}^2. \quad (7.9)$$

Assuming that the local liquid velocity profile at the inlet, U_{LA} , is horizontal and uniform, the kinetic energy term at the interface, V_{LA} , can be determined by,

$$V_{LA}^2 = U_{LA}^2 = \left(\frac{\dot{m}_{L1}}{\rho_L A_{L1}} \right)^2, \quad (7.10)$$

where the liquid flow area, A_{L1} , is a product of the channel width, D , and liquid height, H_{OGE} , as,

$$A_{L1} = H_{OGE}D. \quad (7.11)$$

The inlet liquid mass flow rate, \dot{m}_{L1} , is a summation of the run, \dot{m}_{L2} , and branch, \dot{m}_{L3} , mass flow rates through conservation of mass as,

$$\dot{m}_{L1} = \dot{m}_{L2} + \dot{m}_{L3}. \quad (7.12)$$

Substituting Eq. (7.10), (7.11) and (7.12) into Eq. (7.9) yields,

$$V_{LB}^2 = 2g \left(\frac{\Delta\rho}{\rho_L} \right) (H_{OGE} - h) + \left(\frac{\dot{m}_{L2} + \dot{m}_{L3}}{\rho_L H_{OGE}D} \right)^2 \quad (7.13)$$

For any given flow condition (\dot{m}_{L2} , \dot{m}_{L3}) there are three unknowns in Eq. (7.13), namely V_{LB}^2 , H_{OGE} , and h .

Simulation of the Liquid Side Flow Field at the Dip

As the liquid approaches the branch from the inlet, it splits partially into the branch and partially into the run, as shown in Fig. 7.2. The dip is the linking point between the branch and run flows, having a kinetic energy of V_{LB}^2 and height, h , as defined in Eq. (7.13). The assumptions about the liquid side flow field (quasi-steady, incompressible, inviscid, and irrotational) lead to a potential flow problem, which is governed by the forces of inertia and gravity. At any point the resultant liquid velocity is described through the three components (u,v,w) as,

$$\mathbf{V} = u\mathbf{i} + v\mathbf{j} + w\mathbf{k}, \quad (7.14)$$

where $(\mathbf{i},\mathbf{j},\mathbf{k})$ are unit directional vectors in (x,y,z) . According to White (1991), the three-dimensional steady incompressible continuity equation reduces to,

$$\frac{\partial u}{\partial x} + \frac{\partial v}{\partial y} + \frac{\partial w}{\partial z}, \quad (7.15)$$

and the irrotationality criterion is satisfied when a potential function, ϕ , is defined such that,

$$\mathbf{V} = \frac{\partial \phi}{\partial x}\mathbf{i} + \frac{\partial \phi}{\partial y}\mathbf{j} + \frac{\partial \phi}{\partial z}\mathbf{k}. \quad (7.16)$$

Inserting the definition of the potential function in Eq. (7.16) into the continuity equation in Eq. (7.15) yields Laplace's equation,

$$\frac{\partial^2 \phi}{\partial x^2} + \frac{\partial^2 \phi}{\partial y^2} + \frac{\partial^2 \phi}{\partial z^2} = 0. \quad (7.17)$$

which is an elliptic type linear homogeneous partial differential equation. A linear combination of two solutions (superposition), ϕ_I and ϕ_{II} , is also a solution through,

$$\phi = \phi_I + \phi_{II}. \quad (7.18)$$

Simulating the branch flow as a three-dimensional point-sink intersected by a flat horizontal wall produces a hemi-spherical flow area, A_d in Fig. 7.2, whose radius, r , is defined by,

$$r = (x^2 + y^2 + z^2)^{\frac{1}{2}}. \quad (7.19)$$

The velocity, V_{Ld} , is uniformly distributed along the hemi-spherical flow area, and may be defined as,

$$V_{Ld} = \frac{\dot{m}_{L3}}{\rho_L A_d}, \quad (7.20)$$

where for a hemi-spherical flow area,

$$A_d = 2\pi r^2, \quad (7.21)$$

and at point B the critical radius is defined as,

$$r = (b^2 + h^2)^{\frac{1}{2}}. \quad (7.22)$$

Following Schetz and Fuhs (1996), the potential function describing the radial flow into the hemi-spherical flow area is defined by,

$$\phi_I = \frac{\dot{m}_{L3}}{2\pi\rho_L(x^2 + y^2 + z^2)^{\frac{1}{2}}}. \quad (7.23)$$

The local crossflow velocity induced by the run flow, at the dip, is assumed to have a uniform horizontal profile, U_{LB} . Its magnitude is found as a quotient of the liquid mass flow rate in the run and the liquid flow area beneath the dip. The resulting potential function is therefore found, following from Schetz and Fuhs (1996), as,

$$\phi_{II} = U_{LB}x, \quad (7.24)$$

where,

$$U_{LB} = \frac{\dot{m}_{L2}}{\rho_L A_{L2}}, \quad (7.25)$$

at the dip. The liquid flow area beneath the dip is a product of the dip height h and channel width D , as,

$$A_{L2} = hD. \quad (7.26)$$

The total potential function to describe the local flow at the dip, using superposition theorem in Eq. (7.18), is found to be,

$$\phi_I = \frac{\dot{m}_{L3}}{2\pi\rho_L(x^2 + y^2 + z^2)^{\frac{1}{2}}} + \phi_{II} = U_{LB}x, \quad (7.27)$$

which is similar to the definition used in Chapter 6, however the crossflow velocity at

the dip and inlet are defined locally through Eqs. (7.10) and (7.25), using the channel geometry and flow conditions. The velocity components at the dip are found through the first derivatives of Eq. (7.27), following from Eq. (7.16), and evaluated at point B with $(x = b, y = h, z = 0)$ as,

$$u_{LB} = \left. \frac{\partial \phi}{\partial x} \right|_{(x=b, y=h, z=0)} = \frac{\dot{m}_{L2}}{\rho_L h D} - \frac{\dot{m}_{L3} b}{2\pi \rho_L (b^2 + h^2)^{\frac{3}{2}}}, \quad (7.28)$$

$$v_{LB} = \left. \frac{\partial \phi}{\partial y} \right|_{(x=b, y=h, z=0)} = -\frac{\dot{m}_{L3} h}{2\pi \rho_L (b^2 + h^2)^{\frac{3}{2}}}, \quad (7.29)$$

$$w_{LB} = \left. \frac{\partial \phi}{\partial z} \right|_{(x=b, y=h, z=0)} = 0, \quad (7.30)$$

The velocity field is symmetrical about the $x - y$ plane, and subsequently $w_{LB} = 0$ in Eq. (7.30). The offset distance term, b , comes as a result of the transverse liquid momentum forcing the dip downstream towards the run. With the velocity components defined at point B , through Eq. (7.28) to (7.29), V_{LB}^2 can be found as,

$$V_{LB}^2 = u_{LB}^2 + v_{LB}^2 + w_{LB}^2, \quad (7.31)$$

which is derived from the squared length of the velocity vector, $V = (u^2 + v^2 + w^2)^{\frac{1}{2}}$.

Substituting the first derivatives into Eq. (7.31) results in,

$$V_{LB}^2 = \left(\frac{\dot{m}_{L2}}{\rho_L h D} - \frac{\dot{m}_{L3} b}{2\pi \rho_L (b^2 + h^2)^{\frac{3}{2}}} \right)^2 + \left(-\frac{\dot{m}_{L3} h}{2\pi \rho_L (b^2 + h^2)^{\frac{3}{2}}} \right)^2, \quad (7.32)$$

which provides a definition for the left hand side of Eq. (7.13) in terms of b , h , \dot{m}_{L2} , and \dot{m}_{L3} .

The steady vertical acceleration, a_y , at any point in the liquid side flow field can be found from White (1991) using the velocity vector components (u, v, w) in the Cartesian coordinate system (x, y, z) through,

$$a_y = u \frac{\partial v}{\partial x} + v \frac{\partial v}{\partial y} + w \frac{\partial v}{\partial z}. \quad (7.33)$$

The definition in Eq. (7.33) is a function of only convective terms, and the local acceleration is negligible due to the quasi-steady assumption. The criterion to predict the dip instability at the onset of gas entrainment is defined from the vertical acceleration at point B ($x = b, y = h, z = 0$) being equivalent to gravity as,

$$a_y \Big|_{(x=b, y=h, z=0)} = -g. \quad (7.34)$$

The acceleration due to gravity is given by $-g$ (-9.81 m/s^2), with the negative sign indicating that it is acting in the negative y -direction. Substituting the potential function definition in Eq. (7.16) into Eq. (7.33), the onset criterion becomes,

$$\left[\frac{\partial \phi}{\partial x} \frac{\partial}{\partial x} \left(\frac{\partial \phi}{\partial y} \right) + \frac{\partial \phi}{\partial y} \frac{\partial}{\partial y} \left(\frac{\partial \phi}{\partial y} \right) + \frac{\partial \phi}{\partial z} \frac{\partial}{\partial z} \left(\frac{\partial \phi}{\partial y} \right) \right] \Big|_{(x=b, y=h, z=0)} = -g, \quad (7.35)$$

with partial derivatives of $\partial\phi/\partial y$ evaluated at point B found to be,

$$\frac{\partial}{\partial x} \left(\frac{\partial\phi}{\partial y} \right) \Big|_{x=b, y=h, z=0} = \frac{3\dot{m}_{L3}bh}{2\pi\rho_L(b^2 + h^2)^{\frac{5}{2}}}, \quad (7.36)$$

$$\frac{\partial}{\partial y} \left(\frac{\partial\phi}{\partial y} \right) \Big|_{x=b, y=h, z=0} = \frac{3\dot{m}_{L3}h^2}{2\pi\rho_L(b^2 + h^2)^{\frac{5}{2}}} - \frac{\dot{m}_{L3}}{2\pi\rho_L(b^2 + y^2)^{\frac{3}{2}}}, \quad (7.37)$$

$$\frac{\partial}{\partial z} \left(\frac{\partial\phi}{\partial y} \right) \Big|_{x=b, y=h, z=0} = 0. \quad (7.38)$$

Substituting the first and second derivative definitions from Eq. (7.28) to (7.30) and Eq. (7.36) to (7.38) into Eq. (7.35), the resulting equation describing the onset of gas entrainment criterion can be found to be,

$$\frac{5}{4} \frac{\dot{m}_{L3}^2}{\rho_L^2 \pi^2} \left[\frac{h^3 - b^2h}{(b^2 + h^2)^4} \right] + \frac{3}{2} \frac{\dot{m}_{L2}\dot{m}_{L3}}{\rho_L^2 \pi D} \left[\frac{b}{(b^2 + h^2)^{\frac{5}{2}}} \right] = -g \quad (7.39)$$

Closure Relations and Solution Methodology

The model to predict the onset of gas entrainment phenomenon in a flowing horizontal channel is defined by the system equations provided by Eq. (7.13), (7.32) and (7.39). These three equations have four unknowns, H_{OGE} , h , b , and V_{LB} , with applied flow conditions defined by \dot{m}_{L2} and \dot{m}_{L3} .

In stratified co-current gas-liquid channel flow the inlet liquid height and mass flow rate are coupled, driving forces include gravity, interfacial shear induced by the flowing gas phase, and wall shear stresses (Sadatomi et al., 1993). The division of the inlet liquid mass flow rate between the branch and run at H_{OGE} - the inlet liquid height - is expected to share a particular relationship, and a closure equation is needed

to satisfy this requirement. This relationship is referred to here as the critical liquid flow distribution, and for a specific geometry (D, d, L) it can be described in a simple way as a ratio of the run and branch liquid superficial mass fluxes, $\rho_L V_{SL2}/\rho_L V_{L3}$.

The momentum of the run liquid flow forces the dip downstream while the branch flow forces the dip back towards its entrance. The resultant of these two opposing forces is that the steady dip is offset in the positive x -direction (downstream) by a distance, b . The dip position relative to the branch is related to the height and offset distance through the dip angle, θ_B , as shown in Fig. 7.2, which is defined as,

$$\theta_B = \tan^{-1}\left(\frac{h}{b}\right). \quad (7.40)$$

An additional closure equation is needed to determine the relationship between the dip angle and liquid momentum ratio of the run and branch flows as,

$$\theta_B = f\left(\frac{\rho_L U_{LB}^2}{\rho_L V_{LB}^2}\right) \quad (7.41)$$

The critical liquid flow distribution and dip angle relationships are particular to the T-junction design, which necessitates that the closure equations be empirically derived. An experimental investigation was conducted for this purpose, as described in the following section, in order to determine the form of these two closure equations.

The model solution is a two step process. In the first step the dip characteristics (position, velocity, and acceleration) are evaluated using values of \dot{m}_{L2} , \dot{m}_{L3} , and θ_B that were determined through empirical closure relations. The OGE criterion in

Eq. (7.39) was evaluated numerically using an in-house code where the radius of the hemi-spherical branch flow area was restricted to,

$$0 < r < \frac{D}{2}, \quad (7.42)$$

since the side wall is a physical limit at $D/2$. The root of Eq. (7.39), the dip location (b, h) , was found using an algorithm to verify that the acceleration at the given point did not exceed 1% of the gravitational value (-9.81 m/s^2). The dip kinetic energy, V_{LB}^2 , was then evaluating by substituting b and h into Eq. (7.32). In the second step, V_{LB}^2 and h are coupled with \dot{m}_{L2} and \dot{m}_{L3} in Eq. (7.13) to solve for the remaining unknown, the upstream liquid height, H_{OGE} . This was done numerically whereby Eq. (7.13) was scanned over a range limited by,

$$h < H_{OGE} < D. \quad (7.43)$$

An algorithm was implemented to search for roots where V_{LB}^2 from Eq. (7.32) was within 1% of the value found using Eq. (7.13).

7.3.2 Experimental Methodology

A facility was established that incorporated a horizontal pipe with a single downward oriented branch. The square cross-section used in the development of the theoretical model, as shown in Fig. (7.2), was not a practical choice for the experimental investigation. Mechanical design constraints were imposed, due to elevated operating

pressures, in order to improve operational safety. To avoid expected stress raisers at the sharp corners, and potential mechanical failure points, a circular cross-section design was employed.

Digital imaging was used to record the liquid interface within the acrylic test section using a 3-CCD (charge coupled device) Sony progressive scan digital camera, 640×3480 pixels, coupled with an objective lens. The camera output was connected to a National Instruments image acquisition module and an in house LabVIEWTM code was used to control the acquisition and storing of the images. The camera was arranged such that the CCD plane was parallel to the flat side of the test section, and blue dye was added to the water to enhance visualization of the interface. A linear scale (mm resolution) was used to scale the image plane.

Calibration

Water was first added to the inlet-TEE until the outlet-TEE was filled to the same level. With all rotameter valves closed, and the ball valve downstream of the branch closed, air was added to the inlet-TEE to a static set-point pressure of P_1 . With the camera aligned to view the side of the test section, as shown in Fig. 7.3, the image plane was focused on the region of interest (ROI). The linear scale is shown within the ROI and permits the image to be spatially calibrated. The image resolution was typically around 0.125 mm/pixel. The image coordinate system (x', y') are corrected to coincide with the coordinate system (x, y, z) in Fig. 7.2. This is done by first taking an image of a static interface and extracting points along the interface in order to determine the interface's inclination relative to the image plane. A linear fit

is applied to the points along the static interface as,

$$y' = x' \frac{\Delta y'}{\Delta x'} + Constant, \quad (7.44)$$

where the slope of the fitted data points is $\Delta y'/\Delta x'$. If the slope is non-zero the y -coordinate is corrected to ensure a zero slope in the image ROI by,

$$y'_{corrected} = y' - x' \frac{\Delta y'}{\Delta x'}. \quad (7.45)$$

In most cases images of the static interface had a slope on the order of 1×10^{-2} , and the corrected slope was on the order of 1×10^{-5} . The image plane co-ordinate system (x', y') is then translated using a known reference location so that all points are taken relative to the branch origin at $(x = 0, y = 0, z = 0)$.

Methodology Validation: Smooth-stratified Flow without an Active Branch

The needle valves connected to the rotameters were then opened, allowing air (\dot{m}_{G2}) and water (\dot{m}_{L2}) to flow out of the outlet-TEE. The water level in the outlet-TEE was then permitted to drop well below the run level, resulting in a difference in water level between the inlet and outlet-TEE reservoirs. This caused water to flow through the test section. The water flow rate supplied to the inlet-TEE was then adjusted to compensate for the outflow of water. Steady-state was achieved when the water level in the outlet-TEE and the inlet-TEE were observed to be constant. Images of the smooth-stratified air-water interface were recorded at steady-state conditions, and

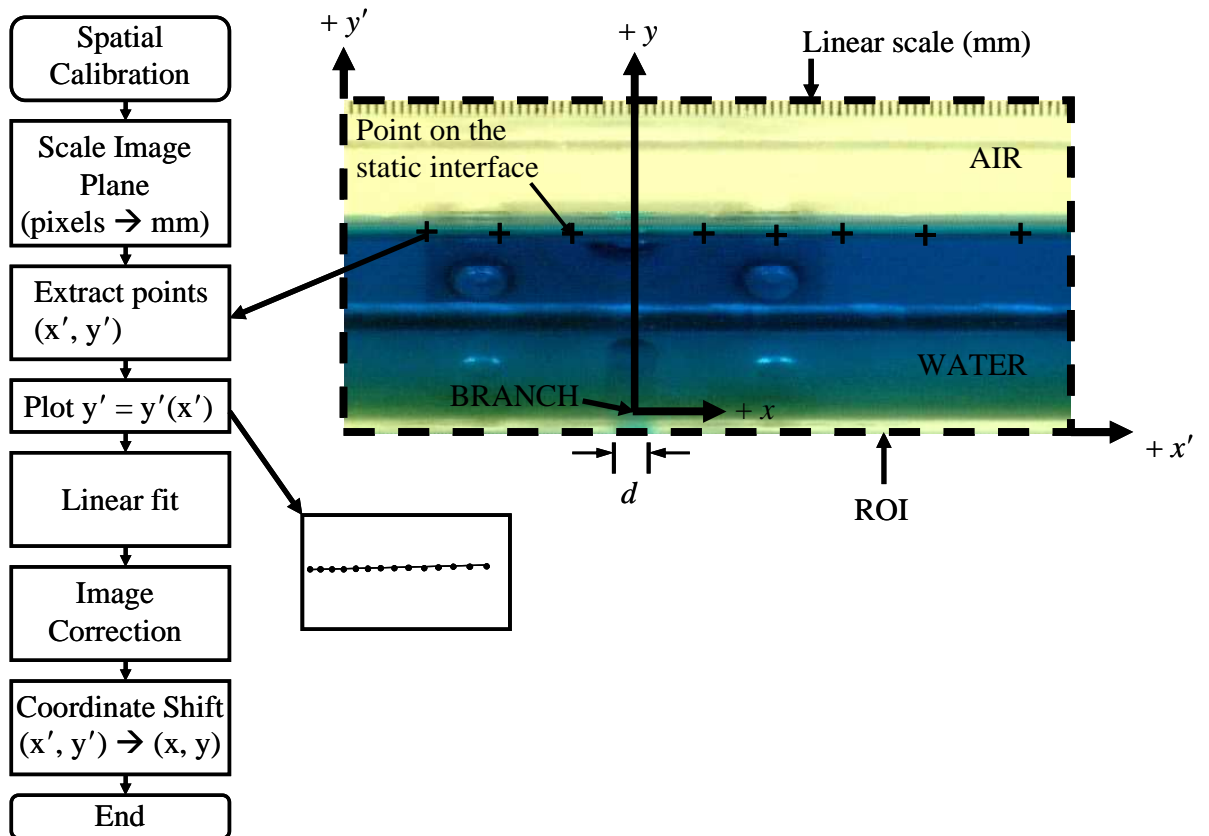


Figure 7.3: Image calibration.

points along the interface were extracted digitally through inspection. Two cases were tested, as shown in Table 7.2, with water flowing within the horizontal pipe without an active branch. The inlet was smooth-stratified in both cases, with an inlet superficial gas velocity, V_{SG1} , of 0.3 m/s used in both cases, and a liquid superficial velocity of 0.13 m/s in Case 1 and 0.061 m/s in Case 2.

The interface profiles obtained through image analysis were then compared against those obtained from the differential pressure transducers in order to validate the imaging methodology, as shown in Fig. 7.4. To estimate the uncertainty of the imaging method the interface height obtained from image analysis is compared with those obtained from transducer measurements. Assuming that the liquid interface varies linearly between $\lambda/D = -17.5$ and $\lambda/D = 17.5$, a conservative estimate of the maximum error between the imaging and transducer measurements is found to be approximately 0.45 mm in Case 1, and 0.62 mm in Case 2. Perspective distortion and the size of the liquid meniscus at the channel wall are observed to increase as the interface height decreases, and accounts for the discrepancy between the two cases.

Table 7.2: Test matrix.

Case	Description	P_1 (kPa)	λ/D	Fr_d	V_{SG1} (m/s)	V_{SL1} (m/s)
1	No Branch	206	-17.5 to +17.5	0	0.3	0.13
2	No Branch			0		0.06
3	OGE			18		0.13
4	OGE			13		0.095
5	OGE			11.3		0.085
6	OGE			7.9		0.06
7	OGE		-5 and -17.5	1 to 30		0.013 to 0.18

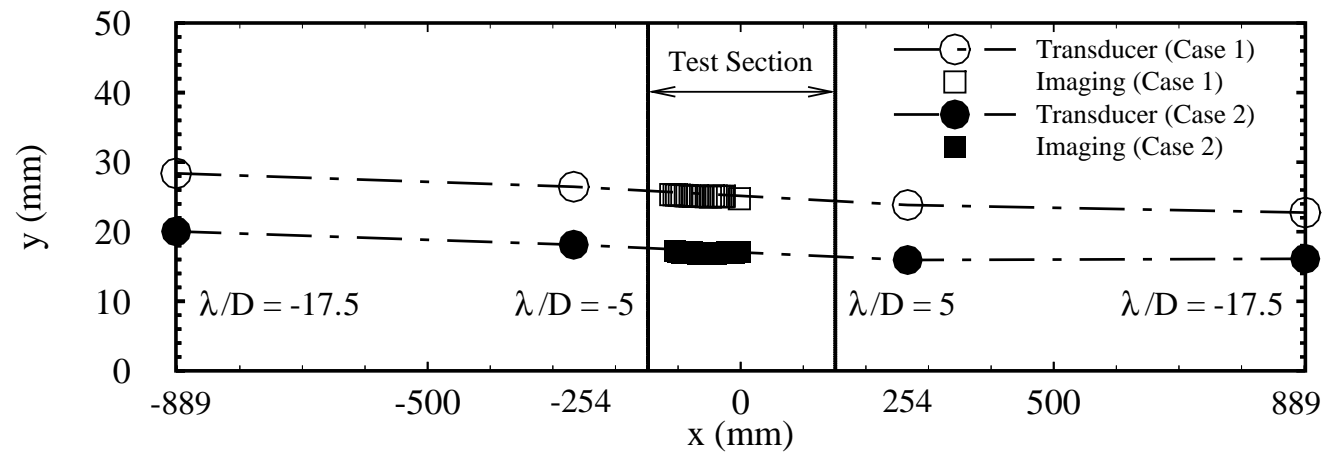


Figure 7.4: Comparison between imaging and transducer measurements under smooth-stratified conditions.

Critical Dip at the Onset of Gas Entrainment

With steady smooth-stratified conditions achieved, the branch was next activated. The branch liquid flow rate, \dot{m}_{L3} , was slowly increased, while the run liquid flow, \dot{m}_{L2} , was slowly decreased. The inlet liquid mass flow rate, \dot{m}_{L1} , remained steady while these two liquid flow rates were adjusted. The branch liquid mass flow rate was increased until a steady stream of air was observed to flow into the branch. The critical conditions at OGE were then recorded, including H_{OGE} , P_1 , \dot{m}_{L2} , \dot{m}_{G2} , and \dot{m}_{L3} .

With OGE established, a sequential set of images of the phenomenon were recorded at a liquid height just prior to OGE in order to visualize the steady dip flow structure. The number of images captured was typically around 20. A sample image of the steady dip is shown in Fig. 7.5. The raw image was then calibrated and the interfacial liquid profile extracted digitally. This was achieved by selecting points along the interface by visual inspection, as shown in Fig. 7.5.

The variables tested are summarized in Table 7.2. The OGE experiments scanned the maximum and minimum allowable inlet water heights, and consequently inlet flow rates, in the facility. Cases 3 to 6 have an active branch flow Froude number. The liquid interface is recorded using image analysis in these four cases in conjunction with the traditional point-measurements provided by the differential pressure transducers. It was not practical to employ digital imaging at every branch Froude number as refraction at lower Froude numbers was observed to cause appreciable imaging distortion. Four branch Froude numbers were therefore selected, where the

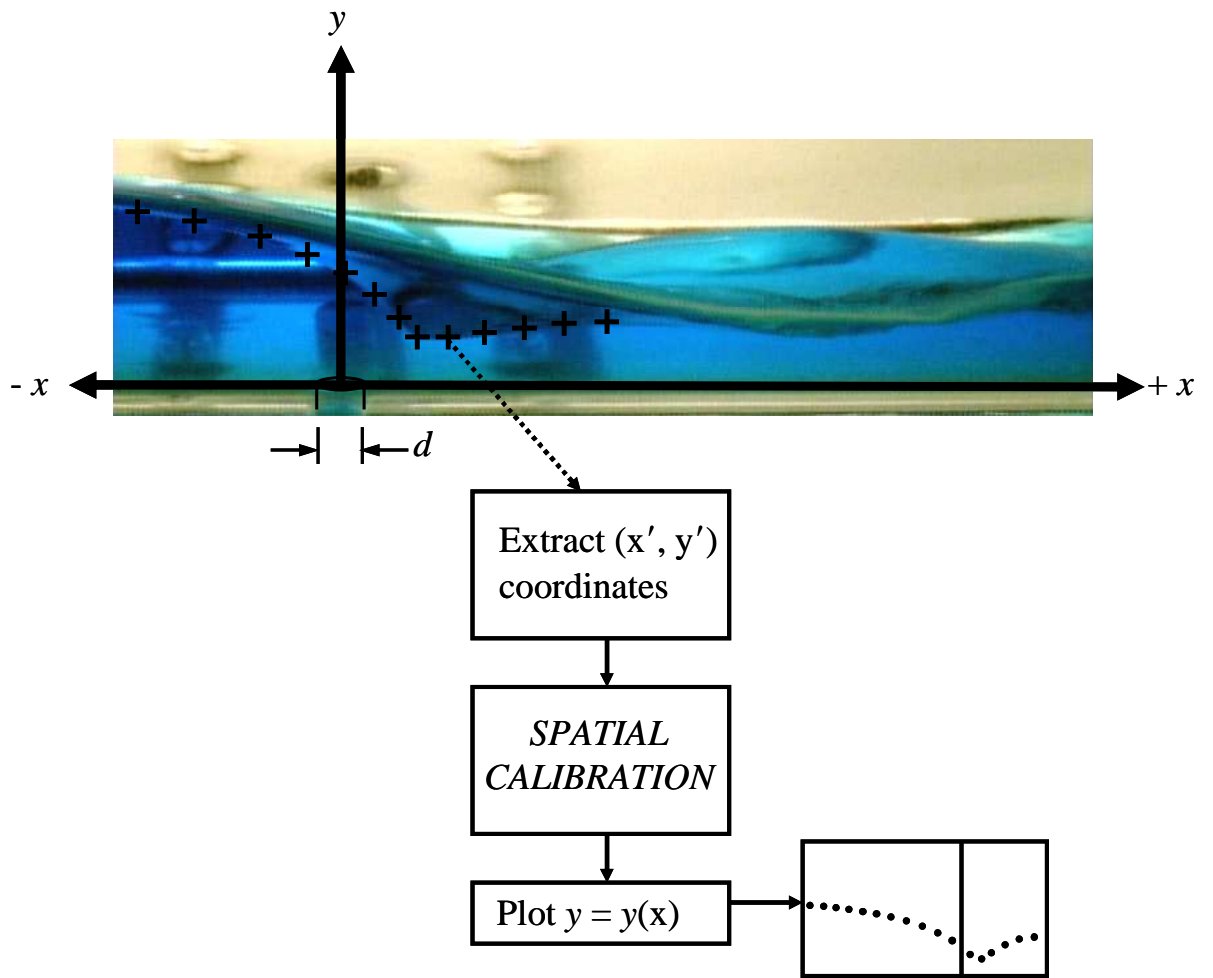


Figure 7.5: Digitization of the critical dip profile.

interface could be recorded using image analysis with reasonable certainty. Case 7 scans the full range of branch Froude numbers and provides measurements of the liquid height in the inlet by transducer measurement only ($\lambda/D = -5, -17.5$). The inlet was maintained in the smooth-stratified regime using a superficial gas velocity of 0.3 m/s in all cases. The liquid superficial velocity for each case is also included in Table 7.2. The allowable operating pressure deviation from the set-point value was 6.8 kPa with an instrument uncertainty of 0.83 kPa. The instrument uncertainty in measuring the liquid height using a transducer was 0.165 mm, and the maximum uncertainty in the liquid Froude number, following Kline and McClintock (1953) was estimated at 5%.

7.3.3 Results and Discussion

Empirical Closure Relations

Critical Liquid Flow Distribution

The critical liquid flow distribution was determined by scanning the full range of allowable branch Froude numbers, from Case 7, and recording the corresponding branch and run mass flow rates at OGE. The branch mass flow rate, \dot{m}_{L3} , is a function of the branch diameter, d , while the run mass flow rate, \dot{m}_{L2} , is a function of the pipe diameter, D . By dividing each of the liquid mass flow rates by the total flow areas the critical flow distribution may be represented in terms of a ratio of superficial mass fluxes, $\rho_L V_{SL2}/\rho_L V_{L3}$. The critical flow distribution is shown in Fig. 7.6 and is

correlated here as,

$$\frac{\rho_L V_{SL2}}{\rho_L V_{L3}} = 0.02 Fr_d^{-0.16} \quad (7.46)$$

$$1 \leq Fr_d \leq 30.$$

Multiplying Eq. (7.46) by the ratio D^2/d^2 yields the ratio of flow rates, $\dot{m}_{L2}/\dot{m}_{L3}$.

The total inlet mass flow rate, \dot{m}_{L1} , was observed to vary proportionally with the inlet height, and this observation was collaborated by Reimann and Khan (1984). They presented the inlet liquid mass flow rate at the maximum and minimum liquid heights, and based on this, the critical distribution was estimated from their measurements. Since they investigated two different branch diameters, 6 mm and 12 mm, respectively, the effect of d/D could be presented more readily. The critical flow distribution extracted from Reimann and Khan (1984)'s results are also presented in Fig. 7.6. Decreasing d/D leads to a decrease in the ratio $\rho_L V_{SL2}/\rho_L V_{L3}$. This is expected since a smaller branch diameter requires less liquid flow rate to achieve the same branch Froude number.

Dip Characteristics

The images presented in Fig. 4.6 showed the typical development of the gas entrainment flow structure in the bottom branch. In Fig. 4.6(a) the image depicts the formation of the steady dip, typical of the vortex-free gas entrainment phenomenon. In this instance the inlet liquid height, and branch and run flow rates, have achieved steady state. The dip structure remains relatively stable. Increasing the branch Froude number, or alternately reducing the inlet height, typically less than 1 mm,

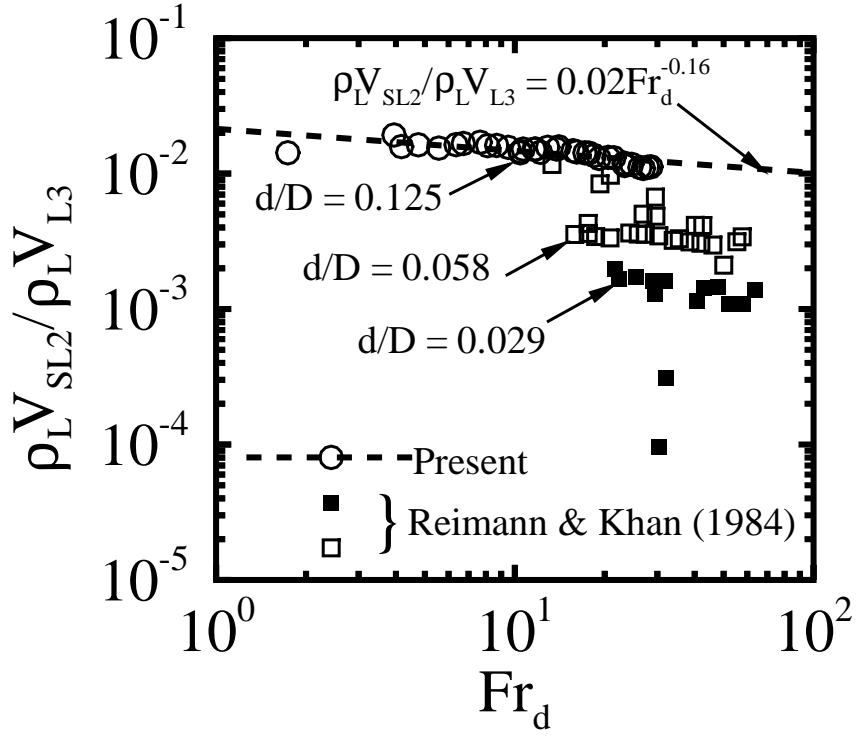


Figure 7.6: Critical liquid flow distribution between run and branch.

resulted in air entrainment into the branch, as was shown in Fig. 4.6(b). Initially entrainment was observed to be transient as the dip experienced a sudden collapse into the branch and then quickly reformed. As the liquid height was decreased further, the gas phase began to steadily entrain into the branch. The visualization method used to depict the OGE does cause a bias uncertainty in the measurement of the critical height, and is estimated to be 1 mm, as it is dependent on the observer's perception of the OGE phenomenon.

The development of the OGE dip profile is presented in Fig. 7.7 for a branch Froude number of 18. The profiles represent the side projection of the steady dip. As the inlet liquid height decreases the dip becomes more pronounced and eventually a sharp tip is formed at the lowest point of the dip at around $x = 6$ mm, and $y = 5.9$

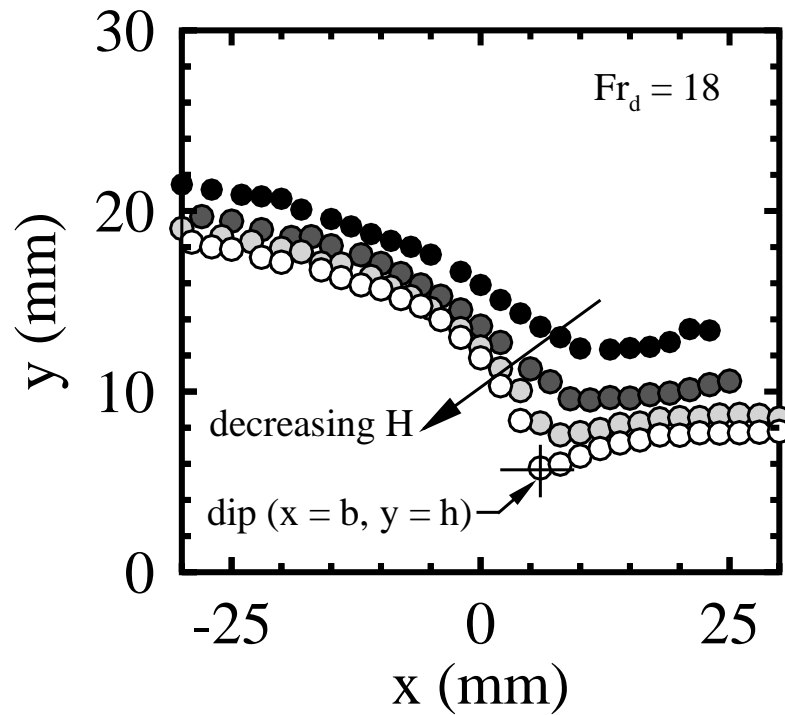


Figure 7.7: Example of the development of the steady OGE dip profile.

mm. This location is the critical dip location where $x = b$, and $y = h$ in Fig. 7.2. The dip flow structure was observed to be nearly symmetric about the $x - y$ plane passing through the branch, as assumed in the model development. Lowering the inlet height further resulted in the dip break-up described in Fig. 4.6(b). Measurements of the steady dip profile, just prior to dip break-up, were conducted for a total of four different Froude numbers.

The steady dip profiles obtained at branch Froude numbers of 18, 13, 11.4, and 7.9 are presented in Fig. 7.8(a) and accompanied by the transducer measurements obtained upstream ($\lambda/D = -5, -17.5$) and downstream ($\lambda/D = 5, 17.5$) of the branch in Fig. 7.8(b). The dip angle was calculated for each Froude number, following Eq. (7.40), and presented in relation to the run to branch momentum ratio in Fig.

7.9. Since the channel has a circular cross-section the dip crossflow velocity, U_{LB} , is determined from Eq. (7.26) with a liquid flow area, A_{L2} , represented by a circle intersected by a horizontal chord along $y = h$, as shown in Fig. 7.10, and from Zwillinger (1996),

$$A_{L2} = \frac{D^2}{4} \cos^{-1} \left(\frac{D-2h}{D} \right) - \left(\frac{D}{2} - h \right) \sqrt{Dh - h^2}. \quad (7.47)$$

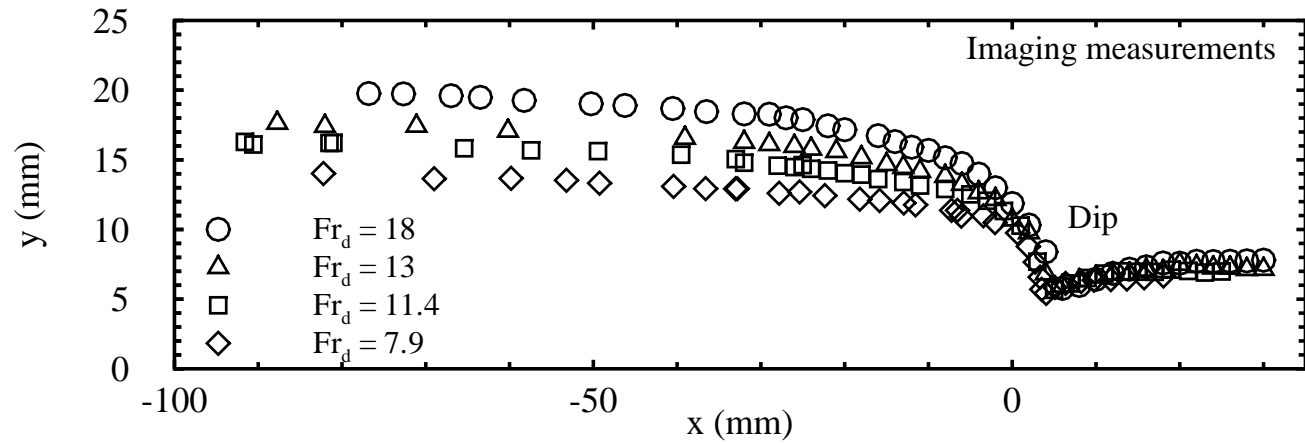
Similarly, the uniformly distributed liquid velocity, V_{Ld} , is determined from Eq. (7.20) however the branch flow area, A_d , is represented as the intersection between a sphere and cylinder, as shown in Fig. 7.10, and following Saleh (2008),

$$A_d = 2\pi(b^2 + h^2) - 4(b^2 + h^2)^{0.5} \int_0^{(b^2+h^2)^{0.5}} \arctan \left(\frac{1}{\sqrt{\frac{D^2}{(b^2+h^2)-y^2} - 1}} \right) dy. \quad (7.48)$$

The dip velocity magnitude, V_{LB} , is found as a vector summation of the run and branch components as,

$$V_{LB} = [(U_{LB} - V_{Ld} \cos \theta_B)^2 + (V_{Ld} \sin \theta_B)^2]^{\frac{1}{2}}. \quad (7.49)$$

The measured critical dip location is presented in Table 7.3, and the calculated velocities are presented in Table 7.4. In Fig. 7.9, at the limit where $\rho_L U_{LB}^2 / \rho_L V_{Ld}^2 = 0$, Saleh (2008) showed that without an imposed liquid crossflow velocity the dip is located vertically above the branch at $\theta_B = 90$ degrees. Increasing $\rho_L U_{LB}^2 / \rho_L V_{Ld}^2$ demonstrated that the dip angle decreases as a result of the run liquid momentum



(a) Dip profiles and air-water interface using imaging

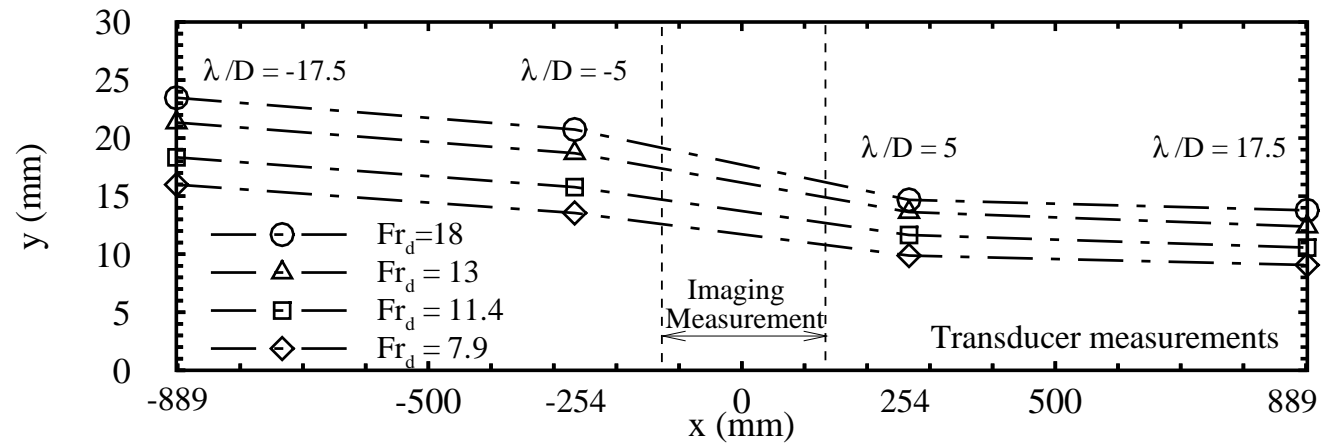
(b) Air-water interface within the *Inlet* and *Run* using differential pressure transducers

Figure 7.8: Air-water interface at the onset of gas entrainment including the steady dip.

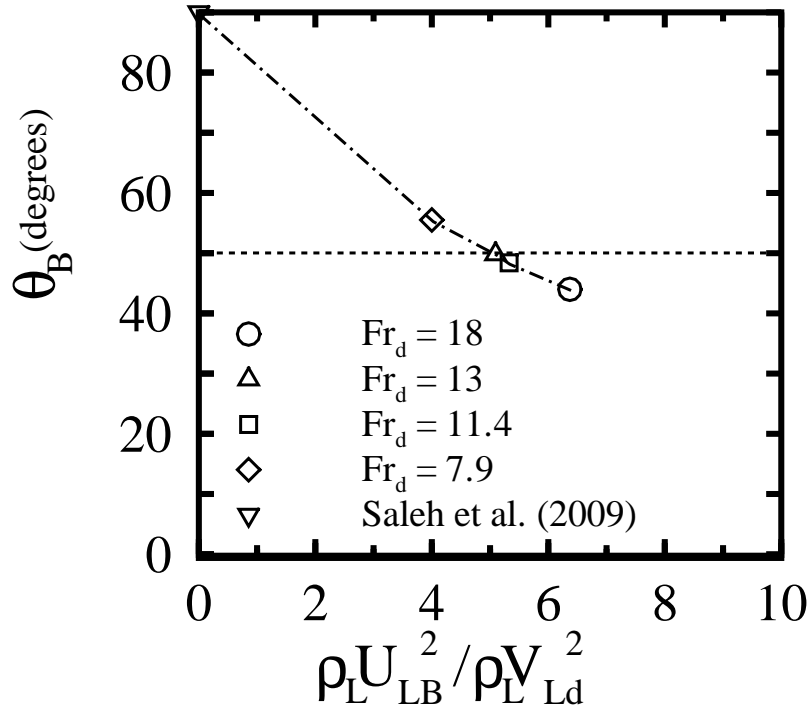


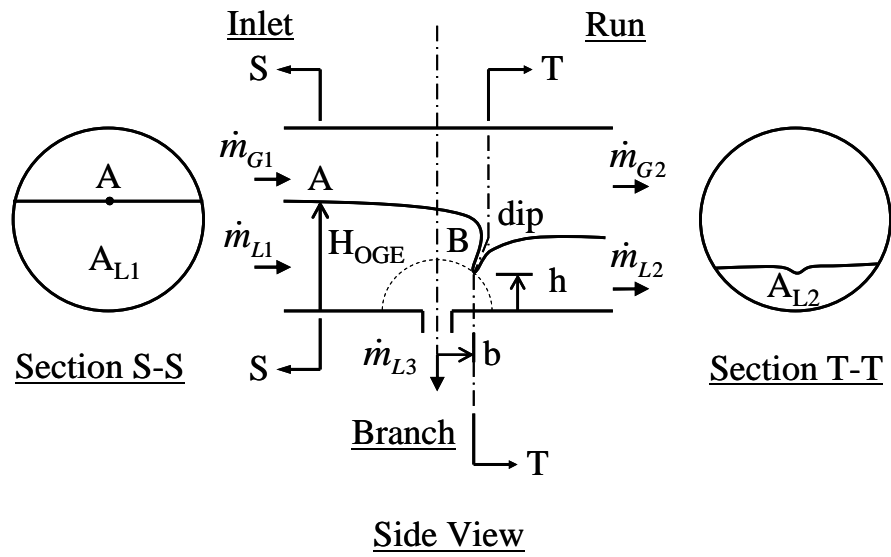
Figure 7.9: Relationship between the dip angle and dip momentum flux ratio.

forcing the dip downstream, which is corroborated by the trend of the data presented in Fig. 7.9.

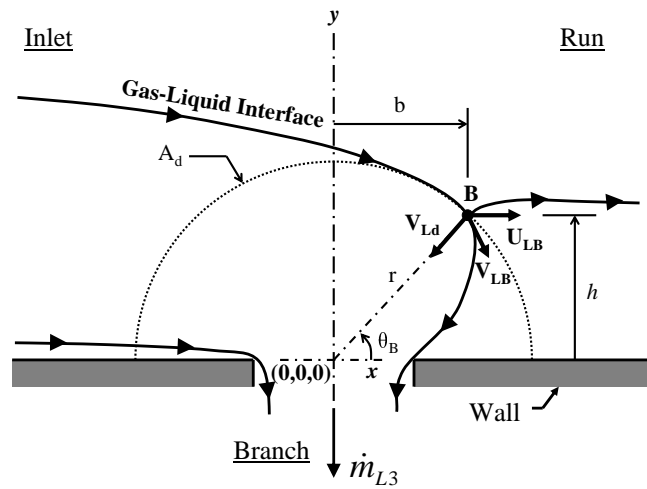
Using the semi-empirical dip velocities from Table 7.4 the dip offset distance criterion proposed in Chapter 6 can be evaluated. The criterion stated that the dip offset distance could be found at a stagnation point where the horizontal component of branch velocity, $V_{Ld} \cos \theta_B$, and horizontal crossflow velocity, U_{LB} , were equal as,

$$V_{Ld} \cos \theta_B = U_{LB}. \quad (7.50)$$

From this criterion the magnitude of V_{LB} becomes the vertical component of V_{Ld} as, $V_{Ld} \sin \theta_B$. The results are presented in Fig. 7.11, and demonstrate that in all



(a) Inlet/Run/Branch



(b) Local to the branch

Figure 7.10: Problem description for OGE in a bottom branch from a cylindrical channel.

Table 7.3: Measured critical dip location for OGE in a bottom branch

Fr_d	h (mm)	b (mm)	θ_B (degrees)
7.9	5.33	3.66	55.5
11.4	5.58	4.91	48.6
13	6.04	5.08	50.0
18	5.79	5.99	44.0

cases the run crossflow velocity is approximately three to four times higher than the branch horizontal velocity. Consequently, this helps to disprove the criterion used to determine the offset distance, b , in Chapter 6. Since h is common to both V_{Ld} and U_{LB} , the criterion could only be satisfied by an under-predicted value of b . In which case, the effect U_{LB} on the dip location is not represented appropriately. The number of measurements points was insufficient for developing a confident relationship between the dip angle and momentum ratio. The dip angle was seen to vary between 40 to 60 degrees over the four tested Froude numbers. For this reason three dip angles were selected to test as closure relations for the theoretical model, these correspond to values of $\theta_B = 40, 50,$ and 60 degrees.

Table 7.4: Calculated Dip Velocities

Fr_d	V_{Ld} (m/s)	U_{LB} (m/s)	V_{LB} (m/s)
7.9	0.253	0.506	0.418
11.4	0.279	0.644	0.505
13	0.284	0.641	0.507
18	0.355	0.896	0.687

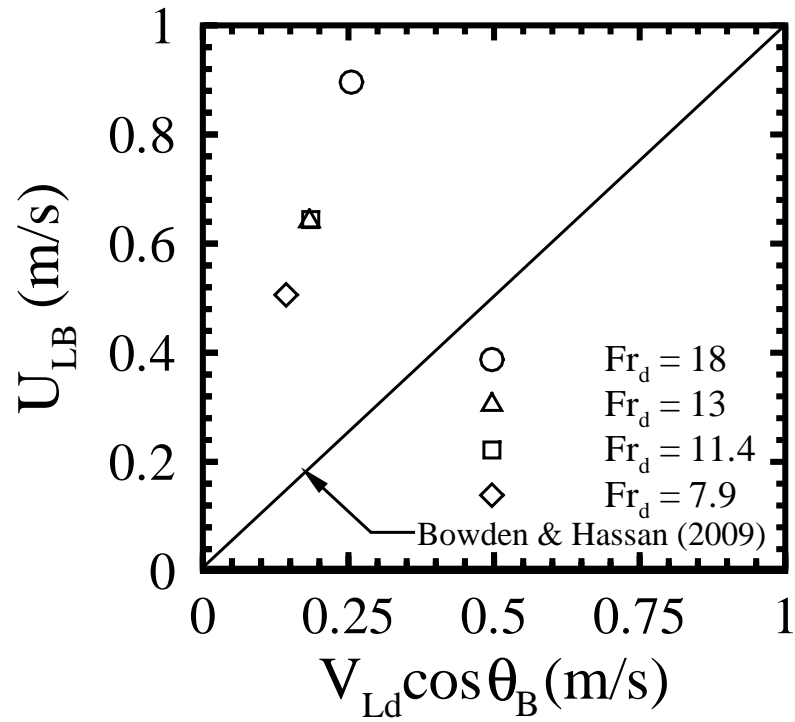


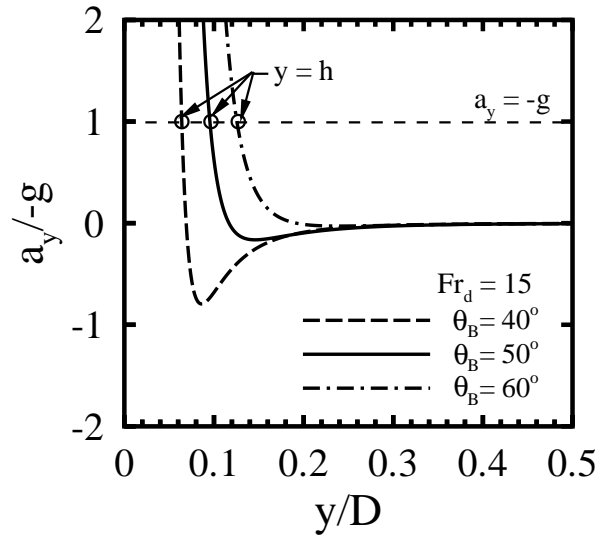
Figure 7.11: Calculated horizontal velocities at the dip.

Model Predictions

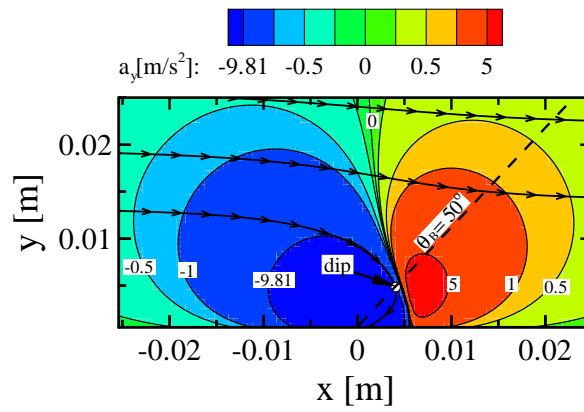
Using Eq. (7.46) as an empirical boundary condition, the onset of gas entrainment criterion in Eq. (7.39) is used to determine the dip height, h by scanning three dip angles, $\theta_B = 40, 50$ and 60 degrees. By evaluating Eq. (7.39) for a single branch Froude number and over a range of heights, y , as shown in Fig. 7.12(a), a single root is found where the acceleration is equivalent to gravity for each dip angle. For example, for a branch Froude number of $Fr_d = 15$, and a dip angle of 50 degrees, the predicted dip height corresponds to $h = 4.9$ mm. Increasing the dip angle is shown to increase the predicted dip height. This can be explained through the acceleration field presented in Fig. 7.12(b) for $Fr_d = 15$, $\theta_B = 50$, and $h = 4.9$

mm. The acceleration field is asymmetrical about the x -axis due to the imposed crossflow velocity from Eq. (7.25). The dip criterion is satisfied anywhere along the $a_y = -9.81 \text{ m/s}^2$ contour. At a dip angle of 50 degrees, a single point can be defined along this contour as the dip location.

The locus of dip heights, as a function of the branch Froude number and dip angle, is presented in Fig. 7.13(a). The analytical prediction of h is compared in the figure with experimental results. The results show that h is predicted at a dip angle of around 60 degrees for the majority of experimental data points, although the majority of the measured dip angles were found to be 50 degrees or below. There are important implications from this observation which are linked to differences incurred by the theoretical and experimental geometries, and more specifically the square and circular cross-sections. Firstly, the uniform sink velocity, V_{Ld} , is affected due to differences in A_d and secondly, U_{LB} is affected due to differences in A_{L2} . These differences can compound to dramatically influence the dip kinetic energy term, V_{LB}^2 . For example, a square channel with $Fr_d = 11.4$, $h/D = 0.109$, and $\theta_B = 60$ degrees, results in a dip kinetic energy of $0.10 \text{ m}^2/\text{s}^2$. On the other hand, the cylindrical channel results in Table 7.4 shows that for $Fr_d = 11.4$, $h/D = 0.109$, and $\theta_B = 48$ degrees, the calculated dip kinetic energy term can be calculated to be $0.255 \text{ m}^2/\text{s}^2$, or 2.5 times greater than the square channel value. Since V_{LB}^2 is one of the major terms in Eq. (7.13), and h is equal in both cases, it can be expected that the corresponding value of H_{OGE} for both geometries can be dramatically affected by the geometrical differences. Therefore, the inlet height for a cylindrical channel was evaluated semi-empirically, and discussed later in reference to Fig. 7.17.

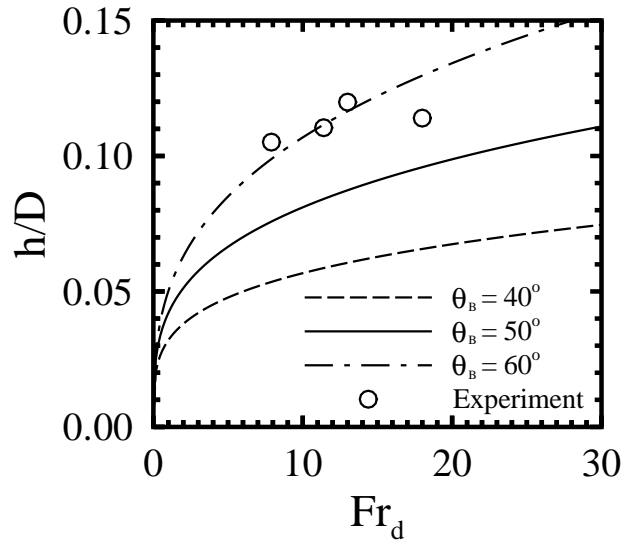


(a) Dip height in relation to θ_B

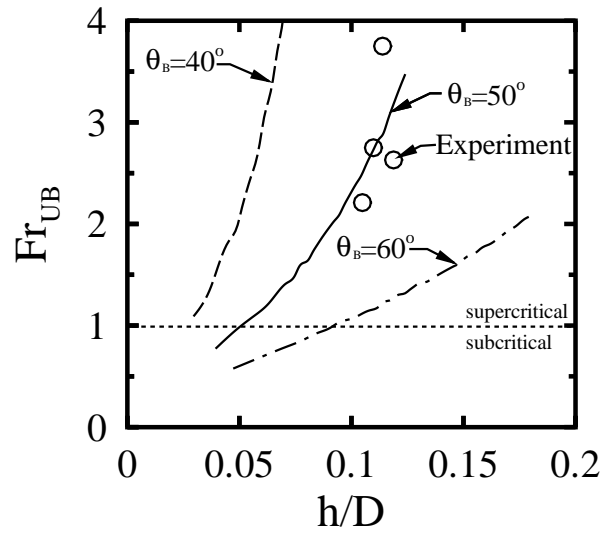


(b) Local acceleration field with $\theta_B = 50$ degrees

Figure 7.12: Prediction of the critical dip with $Fr_d = 15$.



(a) Dip height



(b) Crossflow Froude number

Figure 7.13: Comparison between predictions at the critical dip and experiments.

The predicted dip crossflow Froude number, Fr_{UB} , is presented in Fig. 7.13(b) as a function of the dip height. The dip crossflow Froude number is re-defined here as,

$$Fr_{UB} = \frac{U_{LB}}{(hg)^{\frac{1}{2}}}, \quad (7.51)$$

which is used extensively in the study of open channel flows Chow (1959). It is a ratio of the run liquid inertia to gravitational acceleration. Knowing h and Fr_{UB} the dip crossflow velocity, U_{LB} , can be determined from Fig. 7.13(b) and Eq. (7.51). In general, the crossflow Froude number reveals three distinct types of flow regimes (Chow, 1959):

- $Fr_{UB} = 1$ Critical flow
- $Fr_{UB} < 1$ Subcritical flow
- $Fr_{UB} > 1$ Supercritical flow

For any flow rate the coupling of the liquid height and velocity may have three unique solutions defined by these flow regimes. Physically, a subcritical flow possesses a lower velocity and higher liquid height than a supercritical flow. Supercritical flows can also result in a flow phenomenon known as a hydraulic jump, where the flowing fluid returns to a subcritical state through a sudden expansion of the liquid flow area (Chow, 1959). For a dip angle of 50 degrees and $h/D > 0.05$, the flow regime is shown to be supercritical, while the same regime is found for the 60 degree dip angle and $h/D > 0.1$. The corresponding values of Fr_{UB} obtained from experiments are shown to be uniquely supercritical, and the majority of points are predicted

near $\theta_B = 50$ degrees, similar to the experimental values. To interpret this result, consider for example that the cylindrical and square channels share the same value of Fr_{UB} at $h/D = 0.109$. In the cylindrical channel, for $Fr_{UB} = 2.74$, the run mass flow rate corresponds to $\dot{m}_{L2} = 0.078$ kg/s, while in the square channel it is 0.172 kg/s. The higher run mass flow rate in the square channel comes as a consequence of the larger liquid flow area, A_{L2} , since h is the same for both geometries. Interestingly, experiments showed a secondary phenomenon whereby a steady liquid stream emanated from the dip, flowing in the direction of the run. This phenomenon is shown in Fig. 4.6(a), just to the right of the dip. With gas entrainment, the phenomenon was dissipated, as shown in Fig. 4.6(b). Since the run flow is shown to be supercritical at the dip, one possible explanation for this observed phenomenon is that a type of hydraulic jump is produced, and has also shown to occur in earlier images of OGE in a bottom branch captured by Reimann and Khan (1984).

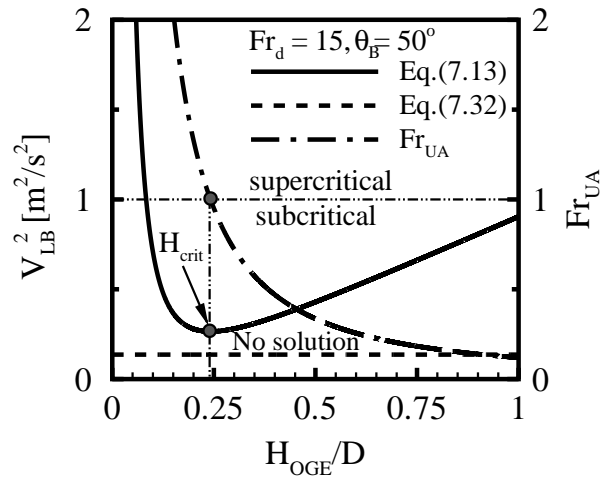
The character of Eq. (7.13) as a function of the upstream height, H , is shown in Fig. 7.14(a). The figure presents the predicted dip kinetic energy from Eq. (7.13) and from the potential field in Eq. (7.32). In the case of a large stagnant reservoir, a comparison of kinetic energies between the tip of the OLE spout and static interface was used to predict the critical height (Soliman and Sims, 1991, 1992). The critical height being the vertical distance from the branch to the static interface, which follows from Craya (1949)'s original analysis. The critical height is then found as a single root where the dip kinetic energy obtained from the statement of Bernoulli's equation and the potential field are equal, with Eq. (7.13) and (7.32) being tangent to each other at the root. The same methodology was employed in this study, however, no root

was found when the upstream velocity was non-zero, as seen in the figure. This can come as a consequence of an under-predicted value of the dip kinetic energy, or inlet liquid mass flow rate. The inlet velocity, U_{LA} , is presented using the inlet crossflow Froude number, Fr_{UA} ,

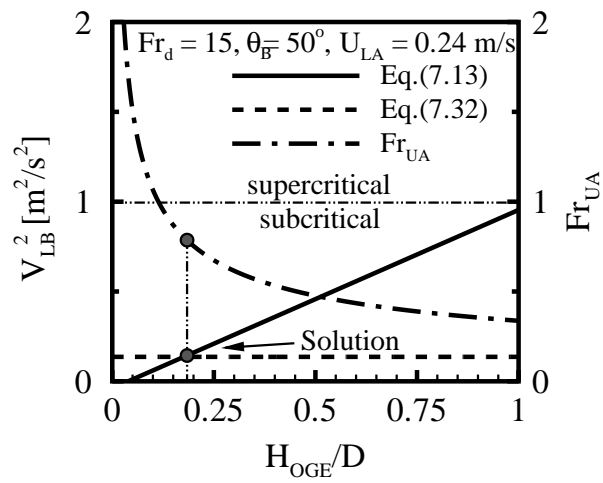
$$Fr_{UA} = \frac{U_{LA}}{(gH_{OGE})^{\frac{1}{2}}}, \quad (7.52)$$

which possesses the same physical characteristics to Fr_{UB} in that the flow regime could be critical, subcritical, or supercritical depending on its value. The inlet velocity is imposed in Eq. (7.13) implicitly as a function of the inlet height, using Eq. (7.10). The consequence is that the inlet velocity is dominant in Eq. (7.13) at low values of H_{OGE} , and becomes less significant as H_{OGE} increases. The effect is seen in the figure as Eq. (7.13) decreases to a minimum value at H_{crit} . This minimum peak value is significant from a physical standpoint in that it represents the transition from subcritical to supercritical flow regimes as evidenced by the corresponding value of $Fr_{UA} = 1$. If the functional relationship between the upstream height and velocity are relaxed, that is the upstream velocity is imposed explicitly rather than implicitly, a solution can be found in the form of a single root, as shown in Fig. 7.14(b). The difference between Fig. 7.14(a) and 7.14(b) is that the upstream velocity, U_{LA} , is set constant at 0.24 m/s in the latter.

In order to find a solution to Eq. (7.13) an empirical function for the average upstream velocity, U_{LA} , was developed. This was done following Eq. (7.10) using the recorded values of the upstream height and flow rate, and where the inlet flow area, A_{L1} , is represented by a circle intersected by a horizontal chord along $y = H_{OGE}$, as



(a) Inlet velocity defined as a function of the inlet height



(b) Inlet velocity defined explicitly as $U_{LA} = 0.24$ m/s

Figure 7.14: Comparing the dip kinetic energy obtained from Eq. (7.9) and (7.32).

shown in Fig. 7.10, through,

$$A_{L1} = \frac{D^2}{4} \arccos\left(\frac{D - 2H_{OGE}}{D}\right) - \left(\frac{D}{2} - H_{OGE}\right) \sqrt{DH_{OGE} - H_{OGE}^2}. \quad (7.53)$$

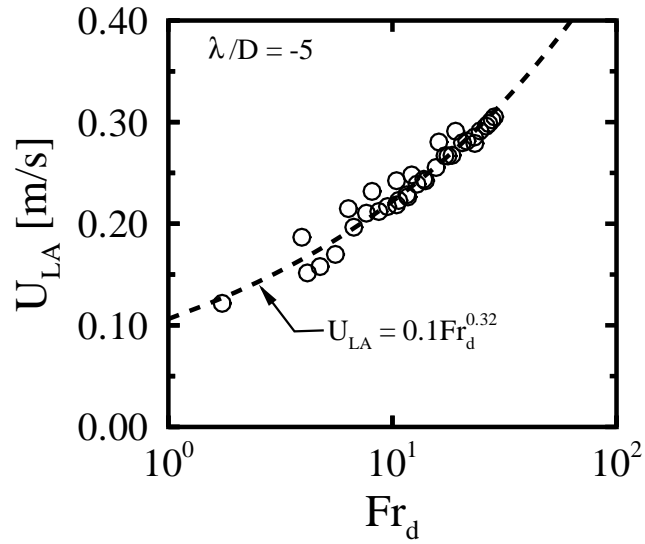
To evaluate this equation, the value of the upstream height was taken at a distance of $\lambda/D = -5$. The resulting local average velocity is shown in Fig. 7.15(a) as a function of Fr_d and was fit by,

$$U_{LA} = 0.1Fr_d^{0.32} \quad (7.54)$$

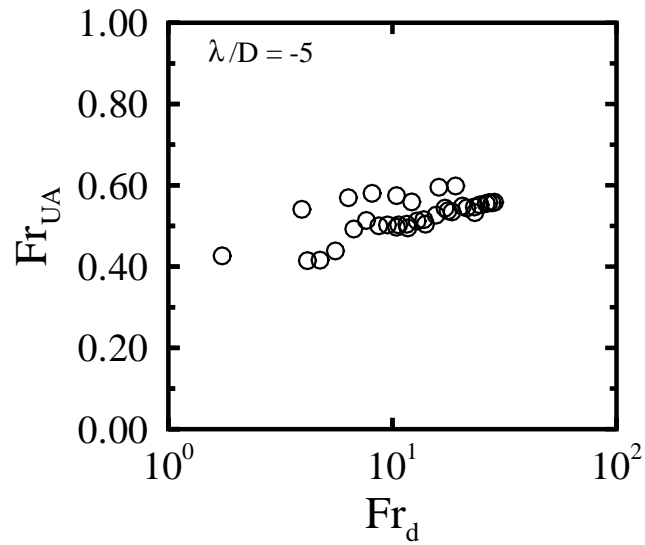
$$1 \leq Fr_d \leq 30.$$

Over the range of H_{OGE} the flow is subcritical with Fr_{UA} ranging between 0.4 and 0.6, as shown from Fig. 7.15(b). The resulting locus of solutions for the upstream heights, as a function of Fr_d , is presented in Fig. 7.16 and is shown in comparison to the actual upstream height recorded at $\lambda/D = -5$. The upstream height is not well predicted from the square channel analysis over the three dip angles tested, and the error is on the order of approximately 50% for a dip angle of 50 degrees. As was mentioned earlier, the dip kinetic energy is significantly different as a result of geometrical differences, which in this case translated to a high error in the prediction of the inlet height. Therefore an alternate method is needed to validate the upstream height prediction.

The inlet height may also be determined semi-empirically for the circular channel from Eq. (7.9) since the dip position (b, h) was recorded experimentally, the inlet velocity ($V_{LA} = U_{LA}$) is known from Fig. 7.15(a), and the dip velocity (V_{LB}) was calculated in Table 7.4. The calculated values of each term in Eq. (7.9) are



(a) Inlet average velocity



(b) Inlet crossflow Froude number

Figure 7.15: Inlet flow conditions at $\lambda/D = -5$.

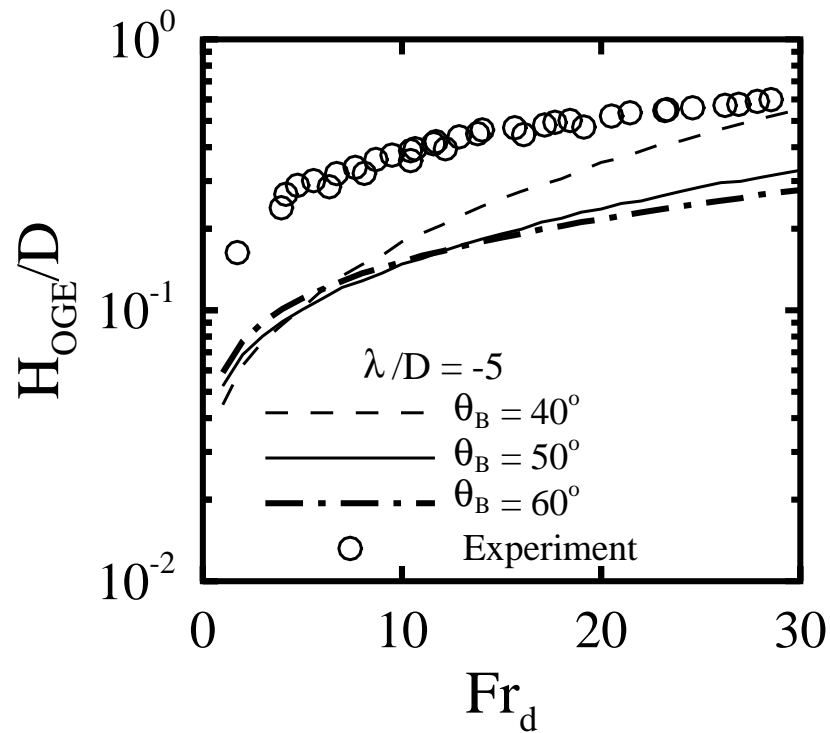


Figure 7.16: Critical height prediction.

tabulated in Table 7.5. The results are also presented in Fig. 7.17 in comparison to the square channel results, which were calculated using the same dip angles and inlet velocity. There is a significant improvement in the prediction of the inlet critical height, H_{OGE} , using the circular channel, as might be anticipated, and the error in relation to experimental values is within 20%. Several factors contribute to this error, including geometrical differences, and the omission of energy changes due to shear and inertial effects. The interfacial liquid gradient in horizontal channels with co-current gas-liquid flow has been shown to be well predicted when wall friction and interfacial shearing are considered (Sadatomi et al., 1993).

Table 7.5: Calculation of the critical height using Eq.(7.9)

Fr_d	H_{OGE} (Experiment) (mm)	h (mm)	$\frac{\Delta\rho V_{LA}^2}{2g\rho_L}$ (mm)	$\frac{\Delta\rho V_{LB}^2}{2g\rho_L}$ (mm)	H_{OGE} (Calculated) (mm)	Error (H_{OGE}) (%)
7.9	16.39	5.33	1.91	8.89	12.31	24.9
11.4	19.26	5.58	2.41	12.95	16.12	16.3
13	20.41	6.04	2.62	13.05	16.47	19.3
18	23.55	5.79	3.22	23.98	26.54	12.7

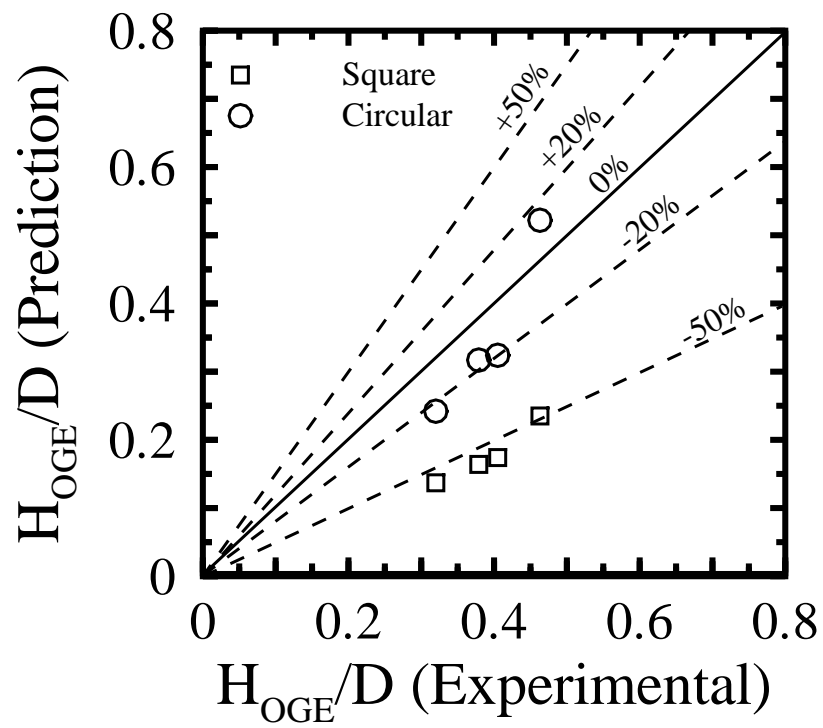


Figure 7.17: Effect of channel geometry on the critical height prediction.

7.4 Summary

Experiments have shown that the stratified air-water flow is hydrodynamically developing within the inlet region. This results in an interfacial liquid gradient within the inlet region, and consequently, a single unique critical height to characterize the onset of gas entrainment phenomenon is un-realistic. This is in contrast to the stagnant reservoir case where a single critical height is reasonable. Experiments also showed that the dip structure is dependent on the imposed flow conditions. The dip angle was recorded over a limited range of Froude numbers and treated as a constant in the theoretical predictions. In reality, this is not the case, as the dip position, size, and orientation are expected to be influenced by the momentum ratio between the run and branch flows. The analytical model was shown to predict the dip height; however the inlet height could not be predicted without an empirical function to describe the inlet velocity. Differences between the theoretical and experimental geometries were quantified, and in some cases shown to be substantial, as in the case of the dip kinetic energy. Semi-empirical prediction of the inlet height, using the appropriate geometrical constraints, showed a considerable improvement over the square cross-section results. The dip and inlet region were coupled through Bernoulli's equation and consequently the effects of wall and interfacial shear, as well as inertial effects due to the velocity profile development, were neglected.

Chapter 8

Conclusions and Future Directions

8.1 Conclusions and Contributions

A state-of-the-art facility has been developed in order to investigate the related two-phase (gas-liquid) phenomena in small branches on a horizontal channel. The test section was designed for the purpose of flow visualization local to the branch, as well enable quantitative measurements through digital imaging technologies. The test section incorporated three branches at 0, 45, and 90 degrees down from horizontal and the facility was designed to support both single and multi-branch discharge experiments. Two types of gravitational based flow separators were incorporated into the facility design in order to measure the mass flow rates of the gas and liquid flowing through the branch and run.

Extensive experimental data were reported in Chapter 4 on the related two-phase phenomena resulting from co-current separated gas-liquid flow in single side, inclined, and bottom oriented branches. The relationship between the air-water interface

height, the pressure drop across the branch, and the two-phase branch and inlet quantities was reported. These included the branch two-phase mass flow rate and quality, as well as the inlet superficial velocities of the gas and liquid phases. The critical conditions at the onset of two-phase flow were identified, namely the onsets of gas and liquid entrainment, and then the relationship between the interface height and branch single phase Froude number was reported for the inclined and bottom oriented branch. The majority of data corresponded to a smooth-stratified regime within the inlet, but increases in the inlet superficial gas velocity by flow into the branch were shown to induce transitions to the wavy-stratified and slug flow regimes.

These initial results revealed that the interface height was influenced by the measurement location within the inlet region. Non-dimensionalizing the interface height with the critical height was shown to dampen the effect of measurement location, as well as the effect of crossflow velocity within the inlet. Comparisons of the relationship between the dimensionless interface height and the two-phase branch quality demonstrated good agreement with earlier studies, which included co-currently flowing and stagnant stratified gas-liquid regimes. Comparisons between the critical height at the onset of gas entrainment with empirical and theoretical models developed in large stagnant two-phase reservoirs supported the effect of crossflow velocity and measurement location. The result was that a lower branch Froude number was required, at a specific interface height, to induce the onset of gas entrainment.

The effects a second active branch at low and moderate Froude numbers were investigated in Chapter 5. Extensive experimental data were reported, relating the critical liquid interface height, at three locations within the inlet, to the branch Froude

numbers and inlet superficial liquid and gas velocities. The effect of fluid phase in the second branch was also reported, with the second branch either above or below the air-water interface. In the first configuration, with liquid flowing in both branches, three distinct cases were observed. The onset of gas entrainment could occur in the top branch only, the bottom branch only, or both branches simultaneously. From these measurements a novel map of the three cases was developed, showing the relationship between the inlet superficial liquid velocity and branch Froude numbers. In the second configuration, with gas flowing in the second branch, the main effects were observed to occur in relation to the inlet two-phase regime, specifically the transitions to wavy-stratified and slug regimes. In limited cases, the onset of gas and liquid entrainment was observed, and these points were shown to exist near the inlet two-phase regime transition. Comparisons to earlier studies showed consistency in relation to the effects of the second branch, however, these were limited to models and experimental data developed for large stagnant two-phase stratified reservoirs.

A theoretical model to predict the critical height at the onset of gas entrainment in a flowing stratified gas-liquid regime was developed in Chapter 6. To the best of the authors knowledge this was the first attempt in open literature at modeling the effects of the inlet crossflow velocity on the onset of gas entrainment. The model was developed following an established methodology for large stagnant gas-liquid reservoirs. Comparisons to earlier studies were limited, due to availability of experimental data, and presented the need for local measurements of the critical dip and inlet velocity. Analysis was provided regarding the inaccuracy of the proposed onset of gas entrainment criterion at a single branch in cases of liquid crossflow. Alternatives

were explored for the onset of gas entrainment from established studies dealing with liquid entrainment. In addition, limitations of the proposed onset of gas entrainment criterion were explored for dual branch configurations in flat vertical or horizontal planes.

A semi-empirical model was developed in Chapter 7 for the onset of gas entrainment in a single branch on the bottom of a square channel to address some of the challenges and inaccuracies faced in pure theoretical analysis. A digital imaging technique was developed to record the location of the critical dip relative to the branch at four branch Froude numbers. This information was then used to determine the relationship between the dip angle and liquid momentum flux ratio between the run and branch flows. The dip angle, coupled with appropriate mass flow rates, were used as empirical boundary conditions in the prediction of the dip height and dip crossflow velocity. Predictions were comparable to measured and calculated values, however, inaccuracies were identified to be due to differences in experimental and modeled geometries. The dip prediction was coupled with the inlet through a two-fluid statement of Bernoulli's equation. It was shown that the local inlet velocity needed to be defined in order to find a solution for the inlet critical height. Using the measured average velocity the resulting prediction showed an average error of 50% with experiments. Incorporating the cylindrical channel geometry, however, showed an improvement in the prediction of the critical height to within 20% error.

8.2 Future Directions

This study has shown that the related two-phase phenomena in small branches are coupled to the two-phase conditions within the channel inlet. Under smooth-stratified flow conditions, the inlet liquid mass flow rate is primarily gravity driven, while the inlet gas phase mass flow rate is pressure driven. The inlet conditions are dependent on the channel geometry (length, diameter), orientation (horizontal, slightly inclined), material, as well as the two operating fluids. Such parametric studies are therefore needed in co-current, and even counter-current, two-phase flow configurations. Broadening the scope of tested inlet conditions will lead to improved models of the related phenomena, for example for the critical height at the onset of gas entrainment, which are currently limited to very specific geometries.

The facility was developed with multi-branch experiments in mind, however only dual branch scenarios were investigated in the present study. Even these dual branch cases were limited mainly to the bottom and inclined branches, due to the maximum air-water interface heights that could be tested within the smooth-stratified regime. Furthermore, experiments were limited only to the beginning of two-phase flow, mainly because increasing the branch flow quality affected the two-phase inlet regime transition. The branch two-phase mass flow rate and quality will be affected by flow through additional branches, however, some modifications to the present facility are needed in order to conduct such experiments.

Increased hydraulic resistances should be tested, between the branch inlet and separator, in order to limit the two-phase mass flow rate in the branch. This will

consequently provide more control over the inlet superficial gas velocity, and moreover, the two-phase regime transitions. This can be achieved by increasing the length of the connecting pipe, as well as decreasing its diameter, between the branch and separator. Lower two-phase branch mass flow rates will require increased sensitivity of the separators, which can be achieved by reducing the overall volume of the separator, for the gas side, and diameter, for the liquid side.

Two-phase regime transitions affected the ability to measure the run liquid and gas mass flow rates at the outlet-TEE, which is essentially a gravity based flow separator, with the run liquid flow directly draining into it. The reason for this is that measurement of the run flow quantities required a steady air-water interface within the outlet-TEE, and transient regimes, waves and slugs, caused significant disturbances at this interface. To counteract this, two modifications are recommended. First, the individual mass flow rates of the gas and liquid phases should be measured at the inlet rather than at the run. This can be achieved by moving all related flow meter devices before the inlet-TEE. Second, the outlet-TEE should be replaced by a second air-water separator, similar to that used for the branch. This will require design trials, to accommodate the expected mass flow rate ranges and regime transitions, however it will permit measurements within the wavy-stratified, and slug regimes. Transient regimes, such as wavy-stratified flow, will also require high frequency response devices to measure the interface height. Potential candidates for such measurements include direct measurement, such as parallel wire capacitance devices, or indirect non-intrusive devices, such as high speed digital cameras.

The present test section was designed with digital imaging technologies in mind,

and specifically for local velocity measurements using particle image velocimetry. These measurements were not performed in the present study, however they are needed in order to quantify the effects of liquid branch flow on the liquid velocity distribution within the inlet. Coupling local measurements of the liquid velocity and interface height would provide a thorough description of the inlet conditions. These measurements would enhance future models by providing local velocity distributions for use as empirical boundary conditions, which would replace locally averaged values. Local velocity measurements could also provide important boundary layer information which could be used to describe the local shear stresses at the wall and interface. Such quantities are important in determining appropriate models to use in evaluating wall and interfacial friction factors, which can further improve models related to the critical height by accounting for hydrodynamic losses within the inlet. Future models should investigate the effect of branch orientation on the critical height in crossflow scenarios. The present study was limited to a single bottom oriented branch, however analytical and semi-empirical methodologies developed in this study could be adapted for this purpose. Models for predicting the branch two-phase branch mass flow rate and quality are highly limited, and are typically purely empirical or semi-empirical. Analytical models could broaden the range of geometries, and flow conditions, for a variety of applications.

To approach realistic header/feeder systems, additional branches should be investigated downstream of the main branch. This would be particularly interesting since the interface shape is dramatically different on either side of the branch. This study focused on the inlet region, which was mainly smooth-stratified, however on the run

side a variety of flow phenomena, including hydraulic jumps, wakes and vortices, were observed. These phenomena can lead to dramatic changes in the downstream branch mass flow rate and two-phase quality.

References

- Abdalla, K. and Berenyi, S. Vapor ingestion phenomenon in weightlessness. Technical Report NASA TN D-5210, National Aeronautics and Space Administration, Lewis Research Center, 1969.
- Adrian, R. Twenty years of particle image velocimetry. *Experiments in Fluids*, 39: 159–19, 2005.
- Ahmad, T. and Hassan, I. Experimental investigation of the onset of gas entrainment from a stratified two-phase region through multiple branches mounted on a curved surface. *ASME Journal of Fluids Engineering*, 128:726–733, 2006.
- Ahmed, M. Theoretical analysis of the onset of gas entrainment from a stratified two-phase region through two side-oriented branches mounted on a vertical wall. *ASME Journal of Fluids Engineering*, 128:131–141, 2006.
- Ahmed, M., Hassan, I., and Esmail, N. Modeling the onset of gas entrainment through a finite-side branch. *ASME Journal of Fluids Engineering*, 125:902–909, 2003.

- Ahmed, M., Hassan, I., and Esmail, N. The onset of gas pull-through during dual discharge from a stratified two-phase region: Theoretical analysis. *Physics of Fluids*, 16:3385–3392, 2004.
- Andaleeb, A., Hassan, I., Saleh, W., and Ahmad, T. Modeling the onset of gas entrainment from a stratified two-phase region through branches on a curved surface. *ASME Journal of Fluids Engineering*, 128:717–725, 2006.
- Andersen, A., Bohr, T., Stenum, B., Juul Rasmussen, J., and Lautrup, B. Anatomy of a bathtub vortex. *Physical Review Letters*, 91:104502–1 – 104502–4, 2003.
- Ardron, K. and Bryce, W. Assessment of horizontal stratification entrainment model in RELAP5/MOD2 by comparison with separate effects experiments. *Nuclear Engineering and Design*, 122:263–271, 1990.
- Armstrong, K., Parrott, S., Sims, G., Soliman, H., and Krishnan, V. Theoretical and experimental study of the onset of liquid entrainment during dual discharge from large reservoirs. *International Journal of Multiphase Flow*, 18:217–227, 1992.
- Azzopardi, B. The effect of the side arm diameter on the two-phase flow split at a “T” junction. *International Journal of Multiphase Flow*, 4:509–512, 1984.
- Azzopardi, B. Phase separation at T-junctions. *Multiphase Science and Technology*, 11:223–329, 1999.
- Azzopardi, B. and Whaley, P. The effect of flow patterns on two-phase flow in a T junction. *International Journal of Multiphase Flow*, 5:491 – 507, 1982.

- Baker, O. Simultaneous flow of oil and gas. *Oil Gas Journal*, 128:726–733, 1954.
- Banerjee, S. and Nieman, R. Fundamental studies on heavy water reactor thermal hydraulics. In *Heat Transfer in Nuclear Reactor Safety*, pages 49–86, 1982.
- Bartley, J., Soliman, H., and Sims, G. Experimental investigation of the onsets of gas and liquid entrainment from a small branch mounted on an inclined wall. *International Journal of Multiphase Flow*, 34:905–915, 2008.
- Bartley, J., Soliman, H., and Sims, G. Experimental investigation of two-phase discharge from a stratified region through a small branch mounted on an inclined wall. *International Journal of Multiphase Flow*, 36:588–597, 2010.
- Baum, M. and Cook, M. Gas entrainment at the free surface of a liquid: Entrainment inception at a vortex with an unstable gas core. *Nuclear Engineering and Design*, 32:239–245, 1975.
- Bowden, R. and Hassan, I. Incipience of liquid entrainment from a stratified gas-liquid region in multiple discharging branches. *Journal of Fluids Engineering*, 130:011301–011311, 2008.
- Bowden, R. and Hassan, I. Flow field characterization at the onset of gas entrainment in a single downward discharge using particle image velocimetry. *ASME Journal of Fluids Engineering*, 129:1565–1576, 2007.
- Bowden, R. and Hassan, I. Modeling the onset of gas entrainment in a single downward discharge from a stratified gas-liquid region with liquid crossflow. *Journal of Fluids Engineering, ASME*, 131:0313041 – 0313048, 2009.

- Chow, V. *Open Channel Hydraulics*. McGraw-Hill, New York, USA, 1959.
- Craya, A. Theoretical research on the flow of nonhomogeneous fluids. *La Houille Blanche*, 4:44–55, 1949.
- Das, G., Das, P., and Azzopardi, B. The split of stratified gas-liquid flow at a small diameter T-junction. *International Journal of Multiphase Flow*, 31:514–528, 2005.
- El-Shaboury, A., Soliman, H., and Sims, G. Two-phase flow in a horizontal equal-sided impacting tee junction. *International Journal of Multiphase Flow*, 33:411–431, 2007.
- Gardner, G. Co-current flow of air and water from a reservoir into a short horizontal pipe. *International Journal of Multiphase Flow*, 4:375–388, 1988.
- Gariel, P. Experimental research on the flow of nonhomogeneous fluids. *La Houille Blanche*, 4:56–64, 1949.
- Ghiaasiaan, S. *Two-Phase Flow, Boiling and Condensation: In Conventional and Miniature Systems*. Cambridge University Press, New York, USA, 1 edition, 2008.
- Hanna, B. CATHENA: A thermalhydraulic code for CANDU analysis. *Nuclear Engineering and Design*, 180:113–131, 1998.
- Hassan, I. *Single, Dual and Triple Discharge from a Large Stratified, Two-phase Region Through Small Branches*. PhD thesis, University of Manitoba, Winnipeg, Manitoba, Canada, 1995.

- Hassan, I., Soliman, H., Sims, G., and Kowalski, J. Discharge from a smooth stratified two-phase region through two horizontal side branches located in the same vertical plane. *International Journal of Multiphase Flow*, 22:1123–1142, 1996a.
- Hassan, I., Soliman, H., Sims, G., and Kowalski, J. Experimental investigation of the two-phase discharge from a stratified region through two side branches oriented horizontally. *Experimental Thermal Fluid Science*, 13:117–128, 1996b.
- Hassan, I., Soliman, H., Sims, G., and Kowalski, J. Single and multiple discharge from a stratified two-phase region through small branches. *Nuclear Engineering and Design*, 176:233–245, 1997.
- Hassan, I., Soliman, H., Sims, G., and Kowalski, J. Two-phase flow from a stratified region through a small side branch. *Journal of Fluids Engineering*, 120:605–612, 1998.
- Hassan, I., Soliman, H., Sims, G., and Kowalski, J. The onset of liquid entrainment during discharge from two branches on an inclined wall. *The Canadian Journal of Chemical Engineering*, 77:433–438, 1999.
- Hassan, Y., Ortiz-Villafuerte, J., and Schmidl, W. Three-dimensional measurements of single bubble dynamics in a small diameter pipe using stereoscopic particle image velocimetry. *International Journal of Heat and Fluid Flow*, 27:817–842, 2001.
- Henry, J. Dividing annular flow in a horizontal tee. *International Journal of Multiphase Flow*, 7:343–355, 1981.

- Honan, T. and Lahey Jr., R. The measurement of phase separation in wyes and tees. *Nuclear Engineering and Design*, 64:93–102, 1981.
- Kline, S. and McClintock, F. Describing uncertainties in single sample experiments. *Mechanical Engineering*, pages 3 – 8, 1953.
- Kowalski, J. and Krishnan, V. Two-phase flow distribution in a large manifold. In *AIChE Annual Meeting*, New York, NY, 1987.
- Lorencez Gonzalez, C. *Turbulent Momentum Transfer at a Gas-Liquid Interface in a Horizontal Stratified Flow in a Rectangular Channel*. PhD thesis, University of Toronto, Toronto, Ontario, Canada, 1994.
- Lubin, B. and Hurwitz, M. Vapor pull-through at a tank drain - with and without dielectrophoretic baffling. In *Long Term Cryo-Propellant Storage in Space*, Huntsville, Ala., 1966. NASA Marshall Space Center.
- Lubin, B. and Springer, G. The formation of a dip on the surface of a liquid draining from a tank. *Journal of Fluid Mechanics*, 29:385–390, 1967.
- Maciaszek, T. and Micaelli, J. CATHARE phase separation modeling for small breaks in horizontal pipes with stratified flow. *Nuclear Engineering and Design*, 124:247–256, 1990.
- Maier, M., Soliman, H., and Sims, G. Onsets of entrainment during dual discharge from a stratified two-phase region through horizontal branches with centerlines falling in an inclined plane: Part 1 - analysis of liquid entrainment. *International Journal of Multiphase Flow*, 27:1011–1028, 2001a.

- Maier, M., Soliman, H., and Sims, G. Onsets of entrainment during dual discharge from a stratified two-phase region through horizontal branches with centerlines falling in an inclined plane: Part 2 - experiments on gas and liquid entrainment. *International Journal of Multiphase Flow*, 27:1029–1049, 2001b.
- Mandhane, J., Gregory, G., and Aziz, K. A flow pattern map for gas-liquid flow in horizontal pipes. *International Journal of Multiphase Flow*, 1:537–553, 1974.
- Margaris, D. T-junction separation modelling in gas-liquid two-phase flow. *Chemical Engineering and Processing*, 46:150–158, 2007.
- Marti, S. and Shoham, O. A unified model for stratified-wavy two-phase flow splitting at a reduced T-junction with an inclined branch arm. *International Journal of Multiphase Flow*, 23:725–748, 1997.
- Munson, B., Young, D., and Okiishi, T. *Fundamentals of Fluid Mechanics*. John Wiley & Sons, Inc., New York, USA, 4 edition, 2002.
- Nikuradse, J. Gesetzmässigkeit der turbulenten stromung in glatten rohren. Technical Report VDI-Forschungsheft 356, 1932.
- Oranje, L. Condensate behavior in gas pipelines is predictable. *Oil and Gas Journal*, 32:39–44, 1973.
- Parrott, S., Soliman, H., Sims, G., and Kowalski, V. Experiments on the onset of gas pull-through during dual discharge from a reservoir. *International Journal of Multiphase Flow*, 17:119–129, 1991.

- Persen, L. Stratified two-phase flow in circular pipes. *International Journal of Heat and Mass Transfer*, 27:1227–1234, 1984.
- Prasad, A. Stereoscopic particle image velocimetry. *Experiments in Fluids*, 29:103–116, 2000.
- Raffel, M., C., W., and Kompenhans, J. *Particle Image Velocimetry: A Practical Guide*. Springer-Verlag, New York, USA, 3 edition, 1998.
- Rea, S. and Azzopardi, B. The split of horizontal stratified flow at a large diameter t-junction. *Trans IChemE*, 79:470–476, 2001.
- Reimann, J. and Khan, M. Flow through a small break at the bottom of a large pipe with stratified flow. *Nuclear Science and Engineering*, 88:297–310, 1984.
- Riemke, R., Bayless, P., and Modro, M. Recent improvements to the RELAP5-3D code. In *ICAPP*, pages 1816–1819, Reno, NV, USA, 2006. Idaho National Laboratories.
- Rodriguez, O. and Oliemans, R. Experimental study on oil-water flow in horizontal and slightly inclined pipes. *International Journal of Multiphase Flow*, 32:323–343, 2006.
- Saba, N. and Lahey Jr., R. The analysis of phase separation phenomena in branching conduits. *International Journal of Multiphase Flow*, 10:1–20, 1984.

- Sadatomi, M., Kawaji, M., Lorencez, C., and Chang, T. Prediction of liquid level distribution in horizontal gas-liquid stratified flows with interfacial level gradient. *International Journal of Multiphase Flow*, 19:987–997, 1993.
- Sakaguchi, T., Akagawa, K., Hamaguchi, H., Imoto, M., and Ishida, S. Flow regime maps for developing steady air-water two-phase flow in horizontal tubes. *Memoirs of the Faculty of Engineering, Kobe University*, 25:191–202, 1979.
- Saleh, W., Bowden, R., Hassan, I., and Kadem, L. A hybrid model to predict the onset of gas entrainment with surface tension effects. *Journal of Fluids Engineering, ASME*, 131:011305–011315, 2009.
- Saleh, W., Bowden, R., Hassan, I., and Kadem, L. Techniques of PIV in stratified two-phase headers. *Experimental Thermal and Fluid Science*, In Press: doi:10.1016/j.expthermflusci.2010.08.009, 2010a.
- Saleh, W., Bowden, R., Hassan, I., and Kadem, L. Two-phase flow structure in dual discharges - stereo PIV measurements. *Experimental Thermal and Fluid Science*, In Press:doi:10.1016/j.expthermflusci.2010.03.005, 2010b.
- Saleh, W. *Two-Phase Flow Structure at Header-Channel Junctions: PIV Experiments and Modeling*. PhD thesis, Concordia University, Montreal, Quebec, Canada, 2008.
- Schetz, J. and Fuhs, A. *Handbook of Fluid Dynamics and Fluid Machinery: Fundamentals of Fluid Mechanics*, volume 1. Wiley, New York, USA, 1996.

- Schrock, V., Revankar, S., Mannheimer, R., Wang, C., and Jia, D. Steam-water critical flow through small pipes from stratified upstream regions. In *Eighth International Heat Transfer Conference*, volume 5, pages 2307–2311, San Francisco, CA, 1986.
- Shoham, O., Brill, J., and Taitel, Y. Two phase flow splitting in a tee junction - experiment and modeling. *Chemical Engineering Science*, 42:2667–2676, 1987.
- Smoglie, C. and Reimann, J. Two-phase flow through small branches in a horizontal pipe with stratified flow. *International Journal of Multiphase Flow*, 12:609–625, 1986.
- Soliman, H. and Sims, G. Theoretical analysis of the onset of liquid entrainment for slots of finite width. *International Journal of Heat and Fluid Flow*, 12:354–360, 1991.
- Soliman, H. and Sims, G. Theoretical analysis of the onset of liquid entrainment for orifices of finite diameter. *International Journal of Multiphase Flow*, 18:229–235, 1992.
- Taitel, Y. and Dukler, A. A model for predicting flow regime transitions in horizontal and near horizontal gas-liquid flow. *AIChE*, 22:47–55, 1976.
- Taitel, Y. and Dukler, A. Effect of pipe length on the transition boundaries for high-viscosity liquids. *International Journal of Multiphase Flow*, 4:557–581, 1987.

- Takahashi, A., Inoue, A., Aritomi, M., Takenaka, Y., and Suzuki, K. Gas entrainment at free surface of liquid, (II):onset conditions of vortex-induced gas entrainment. *Journal of Nuclear Science and Technology*, 25:245–253, 1988.
- Taylor, G. The instability of liquid surfaces when accelerated in a direction perpendicular to the planes. *Proceedings Royal Society London, Series A*, 201:192–196, 1950.
- Teclemariam, Z., Soliman, H., Sims, G., and Kowalski, J. Experimental investigation of the two-phase flow distribution in the outlets of a horizontal multi-branch header. *Nuclear Engineering and Design*, 222:29–39, 2003.
- Torgerson, D., Shalaby, B., and Pang, S. CANDU technology for generation III+ and IV reactors. *Nuclear Engineering and Design*, 236:1565–1572, 2006.
- Ullmann, A. and Brauner, N. Closure relations for two-fluid models for two-phase stratified smooth and stratified wavy flows. *International Journal of Multiphase Flow*, 32:82–105, 2006.
- Wallis, G. Critical two-phase flow. *International Journal of Multiphase Flow*, 6: 97–112, 1980.
- White, F. *Viscous Fluid Flow*. McGraw-Hill, New York, USA, 1991.
- Willert, C. and Gharib, M. Digital particle image velocimetry. *Experiments in Fluids*, 10:181–193, 1991.

- Yonomoto, T. and Tasaka, K. Liquid and gas entrainment to a small break hole from a stratified two-phase region. *International Journal of Multiphase Flow*, 17: 745–765, 1991.
- Zhang, Z. and Hugo, R. Stereo particle image velocimetry applied to a vortex pipe. *Experiments in Fluids*, 40:333–346, 2006.
- Zuber, N. Problems in modeling of small break LOCA. Technical Report NUREG-0724, Nuclear Regulatory Commission, 1980.
- Zwillinger, D. *Standard Mathematical Tables and Formulae*. CRC Press, Boca Raton, Florida, USA, 30 edition, 1996.

Appendix A

Experimental Data

A.1 Co-Current Air-Water Flow

Table A.1: Case SS-1 data

P_1 (kPa)	V_{SG1} (m/s)	V_{SL1} (m/s)	H (mm)			
			$\lambda/D =$ -36	$\lambda/D =$ -17.5	$\lambda/D =$ -5	$\lambda/D =$ +5
208.91	0.30	0.152	32.89	31.40	29.14	25.49
210.29	0.30	0.149	32.46	31.01	28.69	24.96
209.60	0.30	0.145	31.82	30.37	28.35	24.75
209.60	0.30	0.140	31.18	29.94	27.86	24.12
210.29	0.30	0.132	30.32	28.91	26.96	23.32
210.98	0.30	0.127	29.89	28.66	26.57	23.05
210.29	0.30	0.123	29.25	28.07	26.02	22.62
206.02	0.30	0.115	28.61	27.16	25.29	21.76
206.15	0.30	0.107	27.54	26.11	24.65	20.91
210.29	0.30	0.099	26.69	25.36	23.79	20.27
212.36	0.30	0.095	25.83	24.38	22.94	19.63
208.91	0.30	0.088	24.55	23.31	21.90	18.55
208.91	0.30	0.082	23.69	22.48	21.23	17.78
209.53	0.30	0.078	22.84	21.82	20.36	17.27
210.98	0.30	0.076	22.24	21.17	19.94	16.63
209.60	0.30	0.074	22.20	20.89	19.52	15.78
210.29	0.30	0.068	21.55	20.60	18.88	15.30
206.98	0.30	0.066	20.91	20.11	18.45	14.85
209.60	0.30	0.064	20.91	20.11	18.29	14.55
208.91	0.30	0.058	20.06	19.04	17.57	14.24
208.22	0.30	0.058	19.84	19.04	17.34	14.09
207.53	0.30	0.049	18.80	17.94	16.52	13.21
208.91	0.30	0.047	18.13	17.46	15.88	12.78
209.39	0.30	0.040	17.28	16.47	15.24	12.14

Table A.2: Case SS-2 data

P_1 (kPa)	V_{SG1} (m/s)	V_{SL1} (m/s)	H (mm)			
			$\lambda/D =$ -36	$\lambda/D =$ -17.5	$\lambda/D =$ -5	$\lambda/D =$ +5
210.98	1.00	0.103	25.79	24.80	23.37	19.39
210.98	1.00	0.098	24.99	24.10	22.69	18.74
210.98	1.00	0.093	24.55	23.53	22.13	18.34
210.98	1.00	0.090	23.91	22.88	21.23	17.70
210.29	1.00	0.082	22.84	21.82	20.16	16.63
210.29	1.00	0.079	22.24	21.17	19.94	15.99
210.29	1.00	0.075	21.59	20.50	19.30	15.35
210.98	1.00	0.072	21.14	20.32	18.88	15.18
210.98	1.00	0.068	20.91	19.89	18.45	14.49
211.67	1.00	0.065	20.49	19.40	18.23	14.49
208.91	1.00	0.062	20.06	19.25	17.64	14.11
208.91	1.00	0.058	19.42	18.58	17.38	13.64
207.53	1.00	0.054	18.99	18.18	16.95	13.42
212.36	1.00	0.039	16.42	15.61	14.60	11.71

A.2 Single Discharging Branch

Table A.3: Case SB-1 data

$\Delta P = 34.47 \text{ (kPa)}, R = 1052 \text{ (kg - m)}^{\frac{-1}{2}}$ $\lambda/D = -5, \dot{m}_{G2} = 0.0022 \text{ (kg/s)}$						
P_1 (kPa)	P_3 (kPa)	V_{SG1} (m/s)	V_{SL1} (m/s)	\dot{m}_{TP3} (kg/s)	X_3	H (mm)
211.67	171.89	0.757	0.118	0.0368	0.092	24.53
207.67	172.09	0.765	0.108	0.0314	0.110	23.57
210.43	173.08	0.812	0.099	0.0285	0.133	22.61
209.60	172.46	0.842	0.094	0.0270	0.149	22.07
208.77	171.99	0.880	0.085	0.0211	0.203	20.90
208.22	172.20	0.920	0.075	0.0209	0.219	19.72
208.57	172.30	1.033	0.056	0.0151	0.359	17.31
206.88	172.20	1.114	0.044	0.0143	0.423	15.97
204.08	173.54	1.377	0.025	0.0080	1.000	12.91

Table A.4: Case IB-1 data

$\Delta P = 34.47$ (kPa), $R = 1052$ (kg - m) $^{-\frac{1}{2}}$ $\lambda/D = -5$, $\dot{m}_{G2} = 0.0022$ (kg/s)						
P_1 (kPa)	P_3 (kPa)	V_{SG1} (m/s)	V_{SL1} (m/s)	\dot{m}_{TP3} (kg/s)	X_3	H (mm)
207.33	173.39	0.411	0.161	0.1002	0.0081	27.54
204.08	173.13	0.418	0.152	0.0914	0.0095	26.68
200.09	173.13	0.426	0.139	0.0828	0.0112	25.40
206.91	172.20	0.507	0.133	0.0834	0.0183	24.94
205.60	172.20	0.522	0.124	0.0771	0.0213	23.86
204.15	172.20	0.561	0.115	0.0711	0.0272	23.01
210.29	172.20	0.606	0.116	0.0749	0.0303	22.95
206.84	172.71	0.638	0.100	0.0679	0.0368	21.59
208.08	173.75	0.688	0.091	0.0618	0.0464	20.58
207.88	173.13	0.762	0.078	0.0551	0.0622	18.97
207.33	171.68	0.864	0.061	0.0461	0.0907	16.83
210.29	172.20	0.976	0.049	0.0394	0.1273	14.91
205.05	172.20	1.012	0.033	0.0297	0.1777	12.98
203.67	172.20	1.065	0.014	0.0184	0.3085	9.13

Table A.5: Case IB-2 data

$\Delta P = 51.71$ (kPa), $R = 1044$ (kg - m) $^{-\frac{1}{2}}$ $\lambda/D = -5$, $\dot{m}_{G2} = 0.0022$ (kg/s)						
P_1 (kPa)	P_3 (kPa)	V_{SG1} (m/s)	V_{SL1} (m/s)	\dot{m}_{TP3} (kg/s)	X_3	H (mm)
209.53	156.68	0.513	0.154	0.0944	0.0167	27.43
209.53	154.93	0.543	0.143	0.0883	0.0203	26.62
210.77	155.13	0.606	0.139	0.0973	0.0232	25.51
208.91	155.13	0.645	0.130	0.0904	0.0282	24.60
210.98	155.44	0.714	0.120	0.0867	0.0354	23.19
208.36	155.55	0.778	0.099	0.0734	0.0482	21.28
209.60	155.44	0.919	0.077	0.0603	0.0760	18.72
206.43	155.13	1.031	0.053	0.0455	0.1190	15.84
204.22	155.13	1.112	0.036	0.0354	0.1698	13.41
202.77	155.13	1.134	0.021	0.0263	0.2352	10.64

Table A.6: Case IB-3 data

$\Delta P = 68.94$ (kPa), $R = 1038$ (kg - m) $^{-\frac{1}{2}}$ $\lambda/D = -5$, $\dot{m}_{G2} = 0.0022$ (kg/s)						
P_1 (kPa)	P_3 (kPa)	V_{SG1} (m/s)	V_{SL1} (m/s)	\dot{m}_{TP3} (kg/s)	X_3	H (mm)
211.39	137.55	0.688	0.136	0.0891	0.0322	25.47
203.36	132.33	0.695	0.131	0.0939	0.0312	24.33
208.91	137.55	0.769	0.121	0.0908	0.0383	23.35
206.36	137.55	0.803	0.112	0.0851	0.0438	22.60
205.74	137.03	0.849	0.099	0.0774	0.0525	21.40
205.05	137.55	0.915	0.086	0.0695	0.0656	19.72
203.19	137.55	0.987	0.072	0.0608	0.0836	18.04
205.64	137.55	1.034	0.066	0.0580	0.0938	17.30
204.08	137.55	1.130	0.054	0.0494	0.1247	15.98
205.39	137.55	1.097	0.041	0.0397	0.1486	13.94
208.91	137.55	1.314	0.022	0.0286	0.2632	11.02

Table A.7: Case BB-1 data

$\Delta P = 34.47$ (kPa), $R = 1052$ (kg - m) $^{-\frac{1}{2}}$ $\lambda/D = -5$, $\dot{m}_{G2} = 0.0022$ (kg/s)						
P_1 (kPa)	P_3 (kPa)	V_{SG1} (m/s)	V_{SL1} (m/s)	\dot{m}_{TP3} (kg/s)	X_3	H (mm)
206.98	173.23	0.301	0.169	0.1921	0.0000	27.74
208.98	172.71	0.307	0.150	0.1747	0.0002	27.10
206.64	173.02	0.309	0.141	0.1628	0.0004	26.24
205.60	173.28	0.316	0.127	0.1437	0.0008	24.96
206.02	172.97	0.325	0.116	0.1300	0.0014	23.89
207.26	173.28	0.338	0.107	0.1201	0.0023	22.82
204.71	172.71	0.348	0.097	0.1092	0.0032	21.81
203.81	173.23	0.365	0.082	0.0910	0.0052	20.25
203.40	173.33	0.384	0.084	0.0998	0.0062	19.18
203.40	173.23	0.421	0.069	0.0852	0.0104	17.47
202.71	173.23	0.491	0.050	0.0699	0.0202	15.55

Table A.8: Case BB-2 data

$\Delta P = 51.71$ (kPa), $R = 1044$ (kg - m) $^{-\frac{1}{2}}$ $\lambda/D = -5$, $\dot{m}_{G2} = 0.0022$ (kg/s)						
P_1 (kPa)	P_3 (kPa)	V_{SG1} (m/s)	V_{SL1} (m/s)	\dot{m}_{TP3} (kg/s)	X_3	H (mm)
215.12	162.37	0.301	0.189	0.2204	0.0000	30.09
211.53	160.77	0.301	0.180	0.2095	0.0000	29.46
207.88	155.16	0.309	0.175	0.2059	0.0003	28.70
207.67	154.93	0.316	0.166	0.1949	0.0006	27.93
212.29	159.84	0.323	0.154	0.1795	0.0009	26.76
207.53	152.84	0.329	0.150	0.1740	0.0012	26.68
215.67	163.61	0.342	0.135	0.1594	0.0019	25.42
209.60	158.54	0.354	0.128	0.1504	0.0026	24.59
205.74	156.89	0.364	0.118	0.1385	0.0033	23.70
209.19	162.01	0.370	0.110	0.1295	0.0040	22.76
207.39	158.13	0.411	0.090	0.1115	0.0073	21.34
210.15	161.44	0.435	0.081	0.1007	0.0099	20.23
205.60	155.13	0.482	0.075	0.0969	0.0139	19.16
204.77	155.34	0.545	0.061	0.0877	0.0206	17.70
204.08	155.65	0.577	0.054	0.0843	0.0243	16.66

Table A.9: Case BB-3 data

$\Delta P = 68.94$ (kPa), $R = 1038$ (kg - m) $^{-\frac{1}{2}}$ $\lambda/D = -5$, $\dot{m}_{G2} = 0.0022$ (kg/s)						
P_1 (kPa)	P_3 (kPa)	V_{SG1} (m/s)	V_{SL1} (m/s)	\dot{m}_{TP3} (kg/s)	X_3	H (mm)
208.57	137.45	0.352	0.147	0.1774	0.0021	26.57
210.22	137.55	0.377	0.133	0.1661	0.0034	25.48
210.29	138.38	0.395	0.118	0.1461	0.0048	24.01
207.60	137.81	0.434	0.102	0.1272	0.0078	22.21
210.43	138.22	0.499	0.087	0.1142	0.0129	20.61
206.36	137.45	0.536	0.076	0.0995	0.0175	19.41
208.98	138.02	0.593	0.069	0.0962	0.0225	18.49
205.46	137.03	0.630	0.068	0.1017	0.0240	17.47
204.43	137.76	0.734	0.054	0.0915	0.0351	15.76

Table A.10: Data for the OGE in the inclined branch

P_1 (kPa)	V_{SG1} (m/s)	V_{SL1} (m/s)	Fr_B (Liquid)	H_{OGE} (mm)		
				$\lambda/D =$ -36	$\lambda/D =$ -17.5	$\lambda/D =$ -5
204.57	0.30	0.160	9.5	31.61	29.73	27.00
208.91	0.30	0.153	8.6	31.31	29.30	23.79
204.50	0.30	0.138	7.9	29.59	28.02	25.26
210.15	0.30	0.130	7.2	28.61	27.16	24.65
202.71	0.30	0.113	6.0	27.06	25.68	23.15
208.91	0.30	0.092	4.2	23.87	22.46	20.59
201.81	0.30	0.079	3.5	22.20	20.83	19.09
204.71	0.30	0.070	2.9	21.09	20.11	18.21
205.05	0.30	0.061	2.4	20.06	19.04	17.16
206.57	0.30	0.055	1.9	19.20	18.18	16.74
205.26	0.30	0.044	1.0	16.57	15.83	14.60

Table A.11: Data for the OGE in the bottom branch

P_1 (kPa)	V_{SG1} (m/s)	V_{SL1} (m/s)	Fr_C (Liquid)	H_{OGE} (mm)		
				$\lambda/D =$ -36	$\lambda/D =$ -17.5	$\lambda/D =$ -5
208.91	0.30	0.163	23.4	31.94	30.16	27.22
208.77	0.30	0.153	21.7	30.75	29.3	26.14
208.22	0.30	0.139	19.5	29.68	28.2	25.34
210.98	0.30	0.127	17.7	28.61	26.95	24.22
209.60	0.30	0.119	16.3	27.29	25.88	23.15
209.60	0.30	0.110	15.0	26.38	24.7	22.3
210.98	0.30	0.100	13.0	24.98	23.74	21.23
208.91	0.30	0.092	11.7	23.98	22.5	20.16
208.64	0.30	0.082	10.5	22.57	21.1	19.09
207.74	0.30	0.074	9.5	21.39	20.3	17.99
205.05	0.30	0.061	7.6	19.63	18.39	16.52
207.53	0.30	0.050	6.0	17.49	16.68	14.64

Table A.12: Dip profile data from Fig. 7.8(a) ($Fr_d = 18, 13$)

$Fr_d = 18$				$Fr_d = 13$			
x (mm)	y (mm)	x (mm)	y (mm)	x (mm)	y (mm)	x (mm)	y (mm)
31.00	7.35	-9.00	15.33	30.00	7.16	-11.00	14.18
30.00	7.80	-10.00	15.68	29.00	7.23	-12.00	14.27
29.00	7.57	-11.00	15.80	28.00	7.14	-13.00	14.47
28.00	7.75	-12.00	15.91	27.00	7.22	-14.00	14.60
27.00	7.54	-13.00	16.39	26.00	7.24	-15.00	14.68
26.00	7.72	-14.00	16.31	25.00	7.26	-17.00	15.06
25.00	7.45	-15.00	16.51	24.00	7.25	-18.00	15.17
24.00	7.70	-16.00	16.74	23.00	7.23	-20.00	15.39
23.00	7.62	-17.00	16.79	22.00	7.36	-21.00	15.61
22.00	7.72	-20.00	17.16	21.00	7.09	-22.00	15.78
21.00	7.58	-21.00	17.28	20.00	7.52	-24.00	15.78
20.00	7.58	-22.00	17.44	19.00	7.14	-25.00	15.83
19.00	7.41	-23.00	17.52	18.00	6.99	-26.00	15.98
18.00	7.60	-25.00	17.88	17.00	7.26	-28.00	15.94
17.00	7.41	-26.00	17.91	16.00	7.10	-29.00	16.11
16.00	7.32	-27.00	18.01	15.00	7.11	-31.00	16.20
15.00	7.25	-28.00	18.17	14.00	6.82	-32.00	16.27
14.00	7.15	-29.00	18.28	13.00	7.14	-33.92	16.25
13.00	6.82	-30.00	18.25	12.00	6.83	-39.07	16.56
12.00	6.85	-32.00	18.30	11.00	6.75	-55.50	17.13
11.00	6.48	-33.00	18.52	10.00	6.60	-60.19	17.07
10.00	6.43	-36.49	18.47	9.00	6.41	-66.98	17.31
9.00	6.26	-38.61	18.58	8.00	6.34	-71.11	17.43
8.00	5.98	-40.53	18.68	7.00	6.03	-75.43	17.46
7.00	5.85	-43.29	18.70	6.00	5.94	-82.04	17.42
6.00	5.77	-46.23	18.90	5.00	6.08	-85.90	17.54
5.00	6.78	-49.35	19.02	4.00	6.83	-87.73	17.64
4.00	8.40	-50.27	19.02	3.00	8.55	-93.70	17.77
3.00	9.53	-54.77	19.24	2.00	9.78	-100.04	18.10
2.00	10.32	-58.26	19.27	1.00	10.45	-110.88	18.44
1.00	11.29	-61.29	19.38	0.00	10.70		
0.00	11.86	-63.49	19.49	-1.00	11.45		
-1.00	12.25	-65.97	19.50	-2.00	12.17		
-2.00	13.00	-66.98	19.60	-3.00	12.12		
-3.00	13.19	-69.92	19.71	-4.00	12.65		
-4.00	13.98	-72.67	19.73	-5.00	12.83		
-5.00	14.03	-75.06	19.75	-6.00	13.26		
-6.00	14.74	-76.81	19.76	-7.00	13.31		
-7.00	14.89	-79.01	19.88	-8.00	13.82		
-8.00	15.15			-9.00	13.79		

Table A.13: Dip profile data from Fig. 7.8(a) ($Fr_d = 11.4, 7.9$)

$Fr_d = 11.4$				$Fr_d = 7.9$			
x (mm)	y (mm)	x (mm)	y (mm)	x (mm)	y (mm)	x (mm)	y (mm)
26.00	6.97	-17.00	13.82	19.18	6.86	-14.44	11.98
25.00	6.99	-18.00	13.94	18.05	6.67	-15.20	11.92
24.00	6.97	-19.00	13.90	16.82	6.62	-15.83	12.08
23.00	6.91	-20.00	14.04	15.74	6.53	-18.20	12.17
22.00	7.02	-21.00	14.01	14.71	6.54	-20.40	12.28
21.00	7.03	-22.00	14.24	13.68	6.44	-20.52	12.38
20.00	7.01	-22.90	14.52	12.65	6.50	-22.37	12.43
19.00	7.12	-23.00	14.41	11.77	6.40	-24.97	12.54
18.00	6.97	-24.00	14.36	10.74	6.41	-25.38	12.70
17.00	6.96	-25.00	14.40	9.76	6.36	-27.81	12.60
16.00	6.97	-25.02	14.62	8.92	6.32	-30.43	12.91
15.00	6.97	-26.00	14.48	8.23	6.27	-30.46	12.71
14.00	6.90	-27.00	14.53	7.35	6.27	-32.82	12.93
13.00	7.00	-28.00	14.58	6.37	6.13	-33.02	12.92
12.00	6.89	-28.78	14.83	5.73	5.94	-34.93	12.88
11.00	6.84	-30.00	14.67	5.09	5.85	-36.60	12.93
10.00	6.67	-32.00	14.79	4.45	5.70	-38.56	13.09
9.00	6.52	-33.00	15.05	4.06	5.41	-40.43	13.09
8.00	6.38	-33.00	14.77	3.66	5.32	-40.99	13.27
7.00	6.13	-38.79	15.27	3.52	5.71	-41.90	13.05
6.00	5.89	-39.52	15.37	3.42	6.10	-44.57	13.29
5.00	5.67	-44.67	15.59	3.33	6.58	-49.26	13.33
4.00	5.99	-49.44	15.63	3.08	7.12	-53.21	13.53
3.00	7.69	-50.27	15.63	2.74	7.66	-55.74	13.64
2.00	9.17	-57.43	15.68	2.35	8.19	-59.82	13.67
1.00	10.28	-61.93	15.72	1.91	8.78	-64.13	13.70
0.00	10.76	-65.42	15.83	1.38	9.32	-69.00	13.65
-1.00	11.33	-68.91	15.86	0.64	9.76	-76.35	13.79
-2.00	11.91	-76.53	16.09	-0.54	10.10	-82.22	14.02
-3.00	12.07	-81.03	16.21	-2.06	10.50	-93.24	14.28
-4.00	12.17	-81.49	16.21	-3.44	10.98	-100.59	14.33
-5.00	12.52	-85.07	16.15	-4.07	10.75	-110.60	14.49
-6.00	12.63	-87.18	16.26	-5.34	11.26		
-8.00	12.91	-90.58	16.10	-6.08	10.95		
-9.00	13.14	-91.59	16.29	-6.54	11.37		
-11.00	13.16	-97.84	16.52	-7.24	11.38		
-12.00	13.29	-104.72	16.66	-9.14	11.57		
-13.00	13.41	-104.91	16.57	-10.25	11.51		
-15.00	13.62	-112.07	16.80	-11.54	11.77		
-16.00	13.62			-12.95	11.91		

A.3 The OGE in Dual Discharging Branches

Table A.14: Dual case 1 data: OGE in the inclined branch ($Fr_C = 1$)

P_1 (kPa)	V_{SG1} (m/s)	V_{SL1} (m/s)	Fr_B (Liquid)	Fr_C (Liquid)	H_{OGE} (mm)		
					$\lambda/D =$ -36	$\lambda/D =$ -17.5	$\lambda/D =$ -5
208.50	0.30	0.136	7.0	1.2	30.07	27.50	24.86
205.88	0.30	0.131	6.5	1.2	29.25	26.95	24.17
206.15	0.30	0.127	6.0	1.2	28.83	26.65	23.84
206.36	0.30	0.123	5.6	1.2	28.61	26.09	23.37
206.84	0.30	0.118	4.9	1.2	27.76	25.49	22.77
206.77	0.30	0.112	4.4	1.2	27.11	24.82	22.11
205.95	0.30	0.108	3.9	1.2	26.47	24.17	21.44
208.91	0.30	0.100	3.5	1.2	25.40	23.31	20.59
206.91	0.30	0.095	3.0	1.2	24.76	22.46	20.16
204.08	0.30	0.088	2.6	1.2	23.91	21.82	19.52
203.19	0.30	0.083	2.1	1.2	23.05	20.96	18.66
204.36	0.30	0.067	1.4	1.2	21.34	19.46	17.38

Table A.15: Dual case 1 data: OGE in the inclined branch ($Fr_C = 10$)

P_1 (kPa)	V_{SG1} (m/s)	V_{SL1} (m/s)	Fr_B (Liquid)	Fr_C (Liquid)	H_{OGE} (mm)		
					$\lambda/D =$ -36	$\lambda/D =$ -17.5	$\lambda/D =$ -5
203.12	0.30	0.169	7.0	10.0	33.10	30.37	26.89
201.46	0.30	0.161	6.5	10.0	32.25	29.56	26.23
204.98	0.30	0.157	6.0	10.0	31.49	29.09	25.75
205.39	0.30	0.151	5.6	10.0	30.96	28.49	25.50
206.08	0.30	0.144	4.9	10.0	30.11	27.84	24.65
205.12	0.30	0.139	4.4	10.0	29.47	27.50	24.40
206.43	0.30	0.132	3.9	10.0	28.80	26.51	23.37
207.19	0.30	0.126	3.5	10.0	27.97	25.95	22.94
205.74	0.30	0.120	3.0	10.0	27.33	25.07	22.30
202.15	0.30	0.110	2.6	10.0	26.26	24.26	21.27
203.40	0.30	0.102	2.1	10.0	25.19	23.46	20.74
203.40	0.30	0.083	1.4	10.0	23.05	21.37	18.88
202.77	0.30	0.078	1.2	10.0	22.63	20.75	18.27

Table A.16: Dual case 1 data: OGE in the inclined branch ($Fr_C = Fr_B$)

P_1 (kPa)	V_{SG1} (m/s)	V_{SL1} (m/s)	Fr_B (Liquid)	Fr_C (Liquid)	H_{OGE} (mm)		
					$\lambda/D =$ -36	$\lambda/D =$ -17.5	$\lambda/D =$ -5
200.09	0.30	0.161	7.0	7.0	32.46	29.94	26.16
201.95	0.30	0.153	6.5	6.5	31.61	29.20	25.76
202.43	0.30	0.148	6.0	6.0	30.96	28.87	25.29
204.08	0.30	0.142	5.6	5.6	30.54	28.19	24.65
202.71	0.30	0.130	4.9	4.9	29.04	26.91	24.01
207.53	0.30	0.123	4.4	4.4	28.15	25.95	22.94
205.05	0.30	0.115	3.9	3.9	27.11	25.00	22.30
202.71	0.30	0.109	3.5	3.5	26.54	24.34	21.49
202.71	0.30	0.102	3.0	3.0	25.40	23.53	20.59
202.71	0.30	0.094	2.6	2.6	24.55	22.67	19.94
201.88	0.30	0.084	1.9	1.9	23.40	21.60	18.95
204.02	0.30	0.068	1.4	1.4	21.61	19.89	17.38

Table A.17: Dual case 2 data: OGE in the bottom branch ($Fr_B = 1$)

P_1 (kPa)	V_{SG1} (m/s)	V_{SL1} (m/s)	Fr_C (Liquid)	Fr_B (Liquid)	H_{OGE} (mm)		
					$\lambda/D =$ -36	$\lambda/D =$ -17.5	$\lambda/D =$ -5
205.46	0.30	0.168	23.0	1.1	33.55	30.82	27.64
204.77	0.30	0.162	22.5	1.1	32.85	30.35	27.34
204.08	0.30	0.157	21.9	1.1	32.25	29.73	26.57
207.53	0.30	0.149	20.9	1.1	31.61	28.89	25.93
207.53	0.30	0.139	19.4	1.1	30.54	28.23	24.86
209.60	0.30	0.132	18.2	1.1	29.59	27.38	24.63
207.95	0.30	0.124	17.0	1.1	28.59	26.70	23.79
208.43	0.30	0.111	14.7	1.1	27.42	25.24	22.52
208.36	0.30	0.101	13.3	1.1	26.47	24.38	21.75
206.08	0.30	0.095	12.2	1.1	25.62	23.52	21.01
204.43	0.30	0.086	11.6	1.1	24.06	22.03	19.73
202.71	0.30	0.078	9.9	1.1	22.63	20.75	18.27

Table A.18: Dual case 2 data: OGE in the bottom branch ($Fr_B = 2$)

P_1 (kPa)	V_{SG1} (m/s)	V_{SL1} (m/s)	Fr_C (Liquid)	Fr_B (Liquid)	H_{OGE} (mm)		
					$\lambda/D =$ -36	$\lambda/D =$ -17.5	$\lambda/D =$ -5
203.40	0.30	0.174	23.7	2.0	33.74	31.22	27.64
204.84	0.30	0.166	22.5	2.0	33.11	30.60	27.20
217.18	0.30	0.151	20.5	2.0	31.61	29.30	25.99
214.43	0.30	0.145	19.5	2.0	30.79	28.60	25.50
212.36	0.30	0.137	18.4	2.0	30.27	27.99	24.66
213.05	0.30	0.131	17.3	2.0	29.38	27.38	24.22
212.36	0.30	0.126	16.6	2.0	28.83	26.95	23.87
213.74	0.30	0.115	14.7	2.0	27.76	25.88	22.94
212.29	0.30	0.109	13.8	2.0	26.90	24.98	22.51
213.05	0.30	0.102	12.6	2.0	26.26	24.38	21.66
203.40	0.30	0.101	12.8	2.0	25.19	23.31	20.68

Table A.19: Dual case 3 data: OGE in the inclined and bottom branches

P_1 (kPa)	V_{SG1} (m/s)	V_{SL1} (m/s)	Fr_B (Liquid)	Fr_C (Liquid)	H_{OGE} (mm)		
					$\lambda/D =$ -36	$\lambda/D =$ -17.5	$\lambda/D =$ -5
212.36	0.30	0.159	4.4	21.1	32.25	29.73	26.36
206.15	0.30	0.136	3.6	18.1	29.68	27.59	24.65
200.78	0.30	0.123	3.0	16.0	28.61	26.31	23.57
207.53	0.30	0.115	2.7	14.7	27.29	25.24	22.72
210.29	0.30	0.106	2.3	13.3	26.69	24.38	21.87
203.40	0.30	0.100	1.8	12.8	25.19	23.31	20.68
202.71	0.30	0.078	1.1	9.9	22.63	20.75	18.27
203.40	0.30	0.077	1.2	10.1	22.39	20.57	18.01
203.40	0.30	0.071	1.2	9.3	21.98	20.31	17.59
213.74	0.30	0.066	1.0	8.7	21.09	19.46	16.95

Table A.20: Dual case 4 data: OGE in the inclined branch ($Fr_A = 1$)

P_1 (kPa)	V_{SG1} (m/s)	V_{SL1} (m/s)	Fr_B (Liquid)	Fr_A (Gas)	H_{OGE} (mm)		
					$\lambda/D =$ -36	$\lambda/D =$ -17.5	$\lambda/D =$ -5
205.26	0.40	0.099	4.3	1	24.76	23.31	21.18
206.15	0.40	0.093	3.8	1	23.91	22.67	20.39
213.05	0.40	0.078	3.2	1	22.36	21.17	18.85
210.91	0.40	0.074	2.7	1	21.55	20.53	18.45
212.22	0.40	0.067	2.5	1	20.91	19.65	17.59
211.60	0.40	0.059	1.9	1	19.63	18.82	16.86
210.63	0.40	0.056	1.7	1	18.99	18.18	16.31
206.15	0.40	0.050	1.4	1	18.19	17.33	15.67

Table A.21: Dual case 4 data: OGE in the inclined branch ($Fr_A = 10$)

P_1 (kPa)	V_{SG1} (m/s)	V_{SL1} (m/s)	Fr_B (Liquid)	Fr_A (Gas)	H_{OGE} (mm)		
					$\lambda/D =$ -36	$\lambda/D =$ -17.5	$\lambda/D =$ -5
215.81	1	0.101	5.0	10.0	24.33	23.26	20.80
212.36	1	0.087	4.1	10.0	22.84	21.60	19.57
214.77	1	0.080	3.4	10.0	21.98	20.75	19.07
214.22	1	0.070	2.9	10.0	21.41	19.89	18.02
214.43	1	0.063	2.5	10.0	19.84	19.04	17.38
213.74	1	0.057	1.8	10.0	18.99	17.97	16.52
213.67	1	0.051	1.5	10.0	18.13	17.25	15.67
214.43	1	0.046	1.4	10.0	17.47	16.68	15.04
215.12	1	0.040	1.2	10.0	16.64	15.80	14.60

Table A.22: Dual case 5 data: OGE in the bottom branch ($Fr_A = 1$)

P_1 (kPa)	V_{SG1} (m/s)	V_{SL1} (m/s)	Fr_C (Liquid)	Fr_A (Gas)	H_{OGE} (mm)		
					$\lambda/D =$ -36	$\lambda/D =$ -17.5	$\lambda/D =$ -5
210.98	0.40	0.152	21.2	1.0	31.39	29.30	26.57
213.94	0.40	0.134	18.4	1.0	29.69	27.80	25.08
211.53	0.40	0.124	17.2	1.0	28.61	26.71	24.01
217.18	0.40	0.114	15.4	1.0	27.54	25.66	23.15
206.84	0.40	0.104	14.0	1.0	26.47	24.60	22.30
208.08	0.40	0.094	11.9	1.0	25.19	23.50	21.23
215.12	0.40	0.093	13.9	1.0	23.29	21.80	19.94
212.36	0.40	0.074	9.7	1.0	21.49	20.20	18.19
213.74	0.40	0.063	8.3	1.0	20.49	19.20	17.38
210.77	0.40	0.054	6.9	1.0	18.77	17.54	15.87
212.36	0.40	0.045	5.5	1.0	17.06	15.83	14.38
212.01	0.40	0.033	4.1	1.0	14.71	13.90	12.46

Table A.23: Dual case 5 data: OGE in the bottom branch ($Fr_A = 10$)

P_1 (kPa)	V_{SG1} (m/s)	V_{SL1} (m/s)	Fr_C (Liquid)	Fr_A (Gas)	H_{OGE} (mm)		
					$\lambda/D =$ -36	$\lambda/D =$ -17.5	$\lambda/D =$ -5
213.74	1.00	0.152	18.4	10.0	30.49	29.51	26.79
208.22	1.00	0.122	16.1	10.0	28.38	26.50	24.15
204.08	1.00	0.113	15.2	10.0	27.29	25.60	23.26
205.46	1.00	0.110	14.5	10.0	26.71	24.88	22.72
206.15	1.00	0.099	12.9	10.0	25.40	23.74	21.68
208.08	1.00	0.091	11.7	10.0	24.28	22.44	20.37
208.01	1.00	0.084	11.3	10.0	23.02	21.43	19.52
208.64	1.00	0.078	10.6	10.0	22.49	20.75	19.07
208.98	1.00	0.072	9.5	10.0	21.55	20.07	18.44
206.15	1.00	0.068	9.1	10.0	21.13	19.68	18.02
205.88	1.00	0.062	8.1	10.0	20.06	18.61	16.98
205.67	1.00	0.056	6.9	10.0	18.77	17.33	15.86
206.15	1.00	0.048	5.8	10.0	17.49	16.26	14.60
206.15	1.00	0.042	5.1	10.0	16.29	15.19	13.74